HAL
open science

Numerical investigations of the strain localization in geotechnical engineering within the framework of micropolar theory

Jiangxin Liu

To cite this version:

Jiangxin Liu. Numerical investigations of the strain localization in geotechnical engineering within the framework of micropolar theory. Civil Engineering. École centrale de Nantes, 2018. English. NNT : 2018ECDN0005 . tel-01952827

HAL Id: tel-01952827

https://theses.hal.science/tel-01952827

Submitted on 12 Dec 2018

HAL is a multi-disciplinary open access archive for the deposit and dissemination of scientific research documents, whether they are published or not. The documents may come from teaching and research institutions in France or abroad, or from public or private research centers.

L'archive ouverte pluridisciplinaire **HAL**, est destinée au dépôt et à la diffusion de documents scientifiques de niveau recherche, publiés ou non, émanant des établissements d'enseignement et de recherche français ou étrangers, des laboratoires publics ou privés.

Thèse de Doctorat

Jiangxin LIU

Mémoire présenté en vue de l'obtention
du grade de Docteur de l'Ecole Centrale de Nantes
Sous le label de l'UNIVERSITÉ BRETAGNE LOIRE

École doctorale : Sciences pour l'Ingénieur

Discipline : Génie Civil
Unité de recherche : Institut de recherche en génie civil et mécanique

Soutenue le 22 Mars 2018

Etude numérique de la localisation des déformations en géotechnique dans le cadre de la théorie micropolaire

JURY

Président :	MILLET Olivier
Rapporteurs :	**SHAO Jianfu**, Professeur des Universités, Université des Sciences et Technologies de Lille 1
	LAOUAFA Farid, Ingénieur (HDR), INERIS
Examinateurs :	**MILLET Olivier**, Professeur des Universités, Universités de la Rochelle
	PAPON Aurélie, Maître de conférences, INSA Toulouse
Directeur de thèse :	**YIN Zhenyu,** Maître de conférences (HDR), Ecole Centrale de Nantes
Co-directeur de thèse :	**HICHER Pierre-Yves**, Professeur Émérite, Ecole Centrale de Nantes

Acknowledgments

This research was motivated, supervised and strongly supported by my advisors Dr. Zhenyu YIN and Prof. Pierre-Yves HICHER. Their insight, encouragement, dedication, and great personality helped me throughout this research. I am greatly thankful for both of them.

Moreover, I would like to thank the faculty who contributed to this in accepting to serve in my PhD committee, Prof. Olivier MILLET, Prof. Jianfu SHAO, Dr. LAOUAFA Farid and Dr. Aurélie PAPON; I appreciate their help and fruitful discussions. I would like to express sincere thanks to my language teacher SHIMU, who always encourages me to speak French and corrects my grammar mistakes in my manuscripts. I would like also to thank the Chinese friends Zheng LI, Jian LI, Yinfu JIN, Chaofa ZHAO, Zexiang WU, Jie YANG…, for their valuable discussions and cooperations. The help and care from Ran ZHU, Zhuang JIN, Huang WANG and Kexin YIN are also worth appreciating. Special thanks for Prof. Wenxiong HUANG for his valuable discussions. I would like to thank my officemates Benoit, George and Reda for their support and patience.

I feel very much indebted to my parents, my sisters and my wife for their love, support and endurance. I also thank my daughter Amira who makes me a caring, patient and persistent man.

Last, I want to appreciate the friendship between China and France, and I would acknowledge the financial support from China Scholarship Council.

Abstract

Most of the progressive failures of geotechnical structures are associated with the strain localization phenomenon, which is generally accompanied by strength softening. Many experimental observations show that significant rearrangements and rotations of particles occur inside the shear bands. The aim of this thesis is to investigate numerically the strain localization phenomena of granular materials. Considering the mesh dependency problems in finite element analysis caused by strain softening within the classical continuum framework, a sand model based on critical-state has been formulated within the framework of the micropolar theory, taking into account the micro rotations, and implemented into a finite element code for two dimensional problems. Then, the simulations of the shear band in biaxial tests are comprehensively studied in terms of onset, thickness, orientation, etc. At the same time, the efficiency of the micropolar approach, as a regularization technique, is discussed. This is followed by an instability analysis using the second-order work based on the micropolar continuum theory. Finally, for a wider application in simulating failures in geotechnical engineering, the 2D model has been extended to 3D model. Based on the entire study, both the 2D and 3D model demonstrate obvious regularization ability to relieve the mesh dependency problems and to reproduce reasonably the shear bands in geostructures.

Key words: Granular soils, shear band, finite element method, mesh dependency, micropolar theory, instability.

Résume

La plupart des défaillances des structures géotechniques sont associées aux phénomènes de localisation des déformations, qui s'accompagnent toujours d'un adoucissement de la résistance. De nombreuses observations expérimentales montrent que d'importants réarrangements et rotations de particules se produisent à l'intérieur des bandes de cisaillement. Cette thèse vise à étudier numériquement les phénomènes de localisation des déformations dans les matériaux granulaires. Considérant les problèmes de dépendance au maillage dans l'analyse par éléments finis dans le cadre de la modélisation continue classique, un modèle de sable basé sur l'état critique a été formulé dans le cadre de la théorie micropolaire. Un code d'élément pour les problèmes bidimensionnels a été développé dans ce cadre. Ensuite, les simulations d'essais biaxiaux ont permis d'étudier en profondeur les caractéristiques des bande de cisaillement en termes d'apparition, d'épaisseur et d'orientation, etc… Dans le même temps, l'efficacité de l'approche micropolaire, en tant que technique de régularisation, a été discutée. L'analyse de l'instabilité dans un continuum micropolaire basé sur le travail du second ordre a également été effectuée. Enfin, pour une application plus large dans la simulation des défaillances en ingénierie géotechnique, le modèle 2D a été étendu à un modèle 3D. Sur la base de l'étude, les modèles 2D et 3D ont démontré leurs capacités de régularisation pour éviter les problèmes de dépendance au maillage et reproduire raisonnablement la bande de cisaillement dans les géostructures.

Mots-clés: Sol granulaire, bande de cisaillement, méthode des éléments finis, dépendance au maillage, théorie micropolaire, instabilité.

Table content

Acknowledgments II

Abstract III

Résume IV

Table content i

List of figures v

List of tables xiii

General introduction 1

Introduction générale 3

Chapter 1 Literature Survey 5

1.1 Introduction 5

1.2 Strain localization phenomena 6

1.2.1 Engineering scale: collapse of geotechnical structures 6

1.2.2 Model scale: strain localization in model tests 9

1.2.3 Laboratory sample scale: strain localization in specimens 12

1.3 Mechanisms of strain localization 14

1.4 Theories and methods of describing strain localization 17

1.4.1 Experimental investigations 17

1.4.2 Constitutive models and theories 25

1.4.3 Numerical analysis 27

1.4.4 Non–localized regularization approaches 31

1.5 Application of micropolar theory in geotechnical engineering 46

1.5.1 Different polarized constitutive models and the applications 46

1.5.2 Internal length scale and micropolar shear modulus 48

1.6 Conclusions 51

Chapter 2 Finite Element Implementation of the Micropolar SIMSAND Model 52

2.1 Introduction 52

2.2 Introduction of micropolar SIMSAND model 53
2.2.1 Description of SIMSAND model 53
2.2.2 Extension to the micropolar SIMSAND model 56
2.2.3 Summary of model parameters 59
2.3 Finite element implementation 61
2.3.1 Formulations of UEL 61
2.3.2 Integration algorithm-cutting plane method 68
2.3.3 Numerical validations 73
2.4 Verification of the micropolar model with plane strain tests results 76
2.5 Numerical simulations of shear bands in biaxial tests 80
2.5.1 Mesh dependency of the simulated results by classical SIMSAND model 81
2.5.2 Mesh independency of the simulated results by micropolar SIMSAND model 84
2.6 Application of the micropolar model in simulating retaining wall 86
2.6.1 Mesh dependency of the simulated results by classical SIMSAND model 87
2.6.2 Mesh independency of the simulated results by micropolar SIMSAND model 90
2.7 Conclusions 93
Chapter 3 Numerical Analysis of Shear Band 94
3.1 Introduction 94
3.2 Numerical investigation of shear band by micropolar approach 94
3.2.1 Mechanical response 94
3.2.2 Shear band inclination 95
3.2.3 Shear band thickness and shear band identifications 97
3.2.4 Shear band evolution 100
3.2.5 Influence of internal length on the simulated results 101
3.2.6 Influences of the micropolar shear modulus 106
3.3 Some other advantages of the micropolar approach 112
3.4 Proposition of the regularization effectiveness ratio—l_d/l_e 117
3.5 Influencing factors on shear band and regularization effectiveness ratio 124
3.5.1 Influence of confining pressure 124

3.5.2 Influence of initial density 127
3.5.3 Influence of several key parameters 128
3.6 Conclusions 133
Chapter 4 Second-Order Work Criterion in Micropolar Theory 135
4.1 Introduction 135
4.2 Mathematical implications of instability 136
4.2.1 Material instability 136
4.2.2 Structural instability 139
4.2.3 Second-order work framework 141
4.3 Formulations of second-order work in micropolar theory 142
4.3.1 General equation of second-order work 142
4.3.2 Second-order work in classical continuum theory based FE analysis 143
4.3.3 Second-order work in micropolar theory based FE analysis 143
4.4 Discussions of second-order work in FE analysis by simulating a biaxial test 144
4.4.1 Second-order work behind the mechanical response 145
4.4.2 Comparisons of second-order work from classical model and polarized model 146
4.4.3 Mesh dependency analysis of classical model by the second-order work 148
4.4.4 Mesh independency analysis of micropolar model by the second-order work 150
4.4.5 Discussions of the contribution of micro rotations to the second-order work 153
4.5 Application of the second-order work in the analysis of a retaining wall 155
4.6 Conclusions 157
Chapter 5 Extension of the micropolar model from 2D to 3D 159
5.1 Introduction 159
5.2 Framework of the 3D micropolar theory 159
5.2.1 Equilibrium formulations 159
5.2.2 Kinematics formulations 163
5.2.3 Force stress and moment stress of a micropolar continuum 166
5.2.4 Constitutive equations for a micropolar elasticity 167
5.3 Finite element formulations 168

5.3.1 Equilibrium equations 168
5.3.2 Kinematics equations 169
5.3.3 Finite element discretization 169
5.4 FE implementation of the 3D critical state–based micropolar model 172
5.5 Numerical simulations and discussions 175
5.5.1 Element validation 175
5.5.2 Boundary value problems in plane strain condition 178
5.5.3 Boundary value problems in a real 3D condition 185
5.6 Conclusions 188
Conclusions and Perspectives 190
Conclusions 190
Perspectives 191
Appendix A: Numerical Pathological Solutions 192
Ill-posedness of static loading problems 192
Ill-posedness of dynamic loading problems 193
Appendix B: Mesh Dependency Problem within Classical Continuum Theory 195
Appendix C: Full Formulations of Micropolar Theory 198
Equilibrium equations 200
Static equilibrium 200
Dynamic equilibrium 202
Kinematics equations 204
Constitutive laws 206
Elastic models 206
Elastoplastic models 207
Appendix D: Brief Introduction of UMAT and Validation 209
Introduction of UMAT 209
Verification of UMAT 210
Appendix E: Calibration with Optimization Method 214
References 218

List of figures

Figure 1-1 Uneven settlement and the collapse of buildings: (a) Tower of Pisa; (b) residential buildings in Shanghai 6

Figure 1-2 Collapse of typical geotechnical structures: (a) landslide in San Salvador; (b) slide of a high embankment; (c) collapse of the excavation surface; (d) failure of a retaining wall 7

Figure 1-3 Major types of failure of slope: (a) rotational landslide; (b) translational landslide; (c) block slide 8

Figure 1-4 Centrifuge and typical centrifuge modellings. (a) Centrifuge machine (b) Dike model (c) Uneven settlement (d) Street pile wall 10

Figure 1-5 Progressive failure of retaining wall by geo-hazard tank model: (a) initial state; (b) formation of first shear band; (c) formation of several shear band; (d) collapse of soil 11

Figure 1-6 Soil failure under footing by geo-hazard tank model: (a) initial state; (b) formation of the triangle area under footing; (c) laterally uplift outward; (d) formation of slide surface 12

Figure 1-7 Apparatus and specimens: (a) triaxial test; (b) biaxial test 14

Figure 1-8 Stress and strain of the specimen in triaxial or biaxial test 15

Figure 1-9 Investigations of shear band with computed tomography technique: (a) observation of Desrues; (b) observation of Alshibli; (c) observation of Bésuelle 19

Figure 1-10 DEM simulations of shear band in: (a) biaxial test; (b) simple shear test 29

Figure 1-11 Standard procedure of Finite Element Analysis 30

Figure 1-12 One-dimensional viscoplastic model for example 33

Figure 1-13 Spatial average: (a) profiles of micro strain and average strain along a segment with point x in the center of a representative volume; (b) sketch of the representative volume with the center point x; (c) the representative volume near the surface of the body; (d) the weighting function for non-local averaging integral and its relation to the internal length scale l 36

Figure 1-14 Typical evolution of plastic strain distribution in strain localization of softening materials 39

Figure 1-15 Separation between micro-rotation and macro-rotation in 2D space and their effect in the

kinematics 42
Figure 2-1 Principle of critical-state-based nonlinear hardening model for sand 56
Figure 2-2 Subroutine interface of UEL 62
Figure 2-3 Flow chart of the UEL 63
Figure 2-4 Element of 2D micropolar continuum: (a) 8-node plane element; (b) integration points .. 64
Figure 2-5 Illustration of correction phase of cutting plane algorithm 70
Figure 2-6 Flow chart of iteration procedure of the cutting plane algorithm 72
Figure 2-7 Comparisons between IPP and UEL in simulating biaxial drained tests 75
Figure 2-8 Comparisons between IPP and UEL in simulating biaxial undrained tests 75
Figure 2-9 Comparison between experimental and simulated shear band for very dense sand under 100 kPa confining pressure at 10% axial strain: (a) experimental biaxial test; (b) simulated results with the micropolar model 78
Figure 2-10 Comparisons between the simulated solutions and experimental data for medium dense F-75 sand: (a) axial strain versus principle stress ratio; (b) axial strain versus volumetric strain 79
Figure 2-11 Comparisons between the simulated solutions and experimental data for very dense F-75 sand: (a) axial strain versus principle stress ratio; (b) axial strain versus volumetric strain 80
Figure 2-12 Shear bands of four different mesh sizes using the classical model: (a) mesh 10×20; (b) mesh 15×30; (c) mesh 20×40; (d) mesh 30×60 82
Figure 2-13 Load–displacement of four different mesh sizes using the classical model 82
Figure 2-14 Shear band orientation of different meshes (a) mesh 10×20 β_1=52.69°; (b) mesh 15×30 β_2=57.65°; (c) mesh 20×40 β_3=60.15° 83
Figure 2-15 Shear bands of four different mesh sizes using the micropolar model: (a) mesh 10×20; (b) mesh 15×30; (c) mesh 20×40; (d) mesh 30×60 84
Figure 2-16 Load–displacement of four different mesh sizes based on micropolar model 85
Figure 2-17 Shear band orientation of different mesh: (a) mesh 10×20 β_1=53.10°; (b) mesh 15×30 β_2=53.22°; (c) mesh 20×40 β_3=53.22°; (d) mesh 30×60 β_4=53.22° 86
Figure 2-18 A small scale retaining wall model in passive condition 87
Figure 2-19 The deformation of different meshes by classical model: (a) mesh 20×10; (b) mesh 28×14; (c) mesh 40×20; 88

Figure 2-20 The equivalent plastic strain for different meshes by classical model: (a) mesh 20×10; (b) mesh 28×14; (c) mesh 40×20; 89
Figure 2-21 The void ratio for different meshes by micropolar model: (a) mesh 20×10; (b) mesh 28×14; (c) mesh 40×20; 89
Figure 2-22 Passive load-displacement curves of the retaining wall from classical model 90
Figure 2-23 The deformation of different meshes by micropolar model: (a) mesh 20×10; (b) mesh 28×14; (c) mesh 40×20; 91
Figure 2-24 The equivalent plastic strain for different meshes by micropolar model: (a) mesh 20×10; (b) mesh 28×14; (c) mesh 40×20; 92
Figure 2-25 The void ratio for different meshes by micropolar model: (a) mesh 20×10; (b) mesh 28×14; (c) mesh 40×20; 92
Figure 2-26 Passive load-displacement curves of the retaining wall from micropolar model 93
Figure 3-1 Comparisons of load–displacement curves of four different mesh sizes between classical model and micropolar model 95
Figure 3-2 Volumetric strain versus shear strain 96
Figure 3-3 Identification of shear band thickness by equivalent plastic strain: (a) selected path and shear band orientation; (b) calculation of the shear band thickness 98
Figure 3-4 Shear band thickness identified by different variables 99
Figure 3-5 Normalized shear band thickness of four different mesh sizes 100
Figure 3-6 Evolution of a shear band 100
Figure 3-7 Influence of internal length scale l_c on load–displacement curves 101
Figure 3-8 Influence of internal length scale l_c on shear band orientation: (a) l_c = 1 mm, β_1 = 55.9°; (b) l_c = 1.5 mm, β_2 = 54.2°; (c) l_c = 2 mm, β_3 = 53.2° 102
Figure 3-9 Normalized shear band thickness of different l_c: (a) based on plastic strain along the selected horizontal path; (b) based on normalized plastic strain along the selected horizontal path 103
Figure 3-10 Relationship between thickness of shear band and micro structural size 105
Figure 3-11 Normalized shear band thickness versus mean grain size or internal length scale 105
Figure 3-12 Influence of a small G_c on load–displacement curves 107

Figure 3-13 Influence of micropolar shear modulus G_c on load–displacement curves 108
Figure 3-14 Influence of micropolar shear modulus G_c on shear band orientation: (a) G_c = 0.5G, β_1=53.22°; (b) G_c = 1.0G, β_2=53.22°; (c) G_c = 2.0G, β_3=53.22° 108
Figure 3-15 Influence of micropolar shear modulus G_c on shear band thickness 109
Figure 3-16 Influence of micropolar shear modulus G_c on shear strain 110
Figure 3-17 Influence of micropolar shear modulus G_c on shear stress 110
Figure 3-18 Influence of micropolar shear modulus G_c on micro-curvature 111
Figure 3-19 Influence of micropolar shear modulus G_c on micro-moment 111
Figure 3-20 Evolution of shear band based on the particles' rotations: (a) shear band onset corresponding to axial strain 2.5%; (b) corresponding to axial strain 3%; (c) fully formed shear band corresponding to axial strain 5% 112
Figure 3-21 Shear bands for different discretization obtained from the classical model for loose materials: (a) mesh 10×20; (b) mesh 15×30; (c) mesh 20×40; (d) mesh 30×60 114
Figure 3-22 Load–displacement curves for different discretization based obtained from the classical model for loose materials 114
Figure 3-23 Load–displacement curves of each element from the classical simulation: (a) elements located on the horizontal profile; (b) local–displacement curves of each element 115
Figure 3-24 Diffusion mode for different discretization obtained from the micropolar model for loose materials: (a) mesh 10×20; (b) mesh 15×30; (c) mesh 20×40; (d) mesh 30×60 116
Figure 3-25 Load–displacement curves for different discretization based on micropolar model for loose materials 116
Figure 3-26 Load–displacement curves of each element from the Cosserat simulation: (a) elements located on the horizontal profile; (b) local–displacement curves of each element 117
Figure 3-27 Shear bands for different discretization by the micropolar model with l_c = 1 mm: (a) 10×20 mesh; (b) 15×30 mesh; (c) 20×40 mesh; (d) 30×60 mesh 120
Figure 3-28 Load–displacement curves for different discretization using the micropolar model: l_c = 1 mm 121
Figure 3-29 Shear bands for different discretization by the micropolar model with l_c = 1.5mm: (a) mesh 10×20; (b) mesh 15×30; (c) mesh 20×40; (d) mesh 30×60 121

Figure 3-30 Load–displacement curves for different discretization by micropolar model: l_c=1.5mm 122
Figure 3-31 Shear bands for different discretization by the micropolar model with l_c = 2mm: (a) mesh 10×20; (b) mesh 15×30; (c) mesh 20×40; (d) mesh 30×60 122
Figure 3-32 Load–displacement curves for different discretization by micropolar model: l_c=2mm. 123
Figure 3-33 Shear bands for different discretization by the micropolar model with l_c = 2.25mm: (a) mesh 10×20; (b) mesh 15×30; (c) mesh 20×40; (d) mesh 30×60 123
Figure 3-34 Load–displacement curves for different discretization by micropolar model: l_c=2.25mm 124
Figure 3-35 Influence of confining pressure on the load-carrying capacity 126
Figure 3-36 Influence of confining pressure on shear band thickness: (a) based on plastic strain; (b) based on normalized plastic strain 126
Figure 3-37 Influence of initial density on the load carrying capacity 127
Figure 3-38 Influence of density on shear band thickness: (a) based on plastic strain; (b) based on normalized plastic strain 128
Figure 3-39 Influence of critical friction angle ϕ_u on the load carrying capacity 129
Figure 3-40 Influence of critical friction angle ϕ_u on shear band thickness: (a) based on plastic strain; (b) based on normalized plastic strain 130
Figure 3-41 Influence of strength parameter n_p on the load carrying capacity 131
Figure 3-42 Influence of strength parameter n_p on shear band thickness: (a) based on plastic strain; (b) based on normalized plastic strain 131
Figure 3-43 Influence of deformation parameter n_d on the load carrying capacity 133
Figure 3-44 Influence of deformation parameter n_d on shear band thickness: (a) based on plastic strain; (b) based on normalized plastic strain 133
Figure 4-1 Order of instability criteria during loading history for non-symmetric constitutive matrices 139
Figure 4-2 Definition of particles in contact 144
Figure 4-3 Second-order work behind the mechanical response 145
Figure 4-4 Comparisons of the results from classical SIMSAND model and the polarized model .. 146

Figure 4-5 Evolution of the second-order work in the classical continuum: (a) vertical displacement of 4 mm; (b) vertical displacement of 4.5 mm; (c) vertical displacement of 5 mm; (d) vertical displacement of 5.8 mm 147
Figure 4-6 Evolution of the second-order work in the micropolar continuum: (a) vertical displacement of 5.5 mm; (b) vertical displacement of 6 mm; (c) vertical displacement of 7 mm; (d) vertical displacement of 10mm 148
Figure 4-7 Instability regions identified by second-order work of different meshes in classical continuum: (a) mesh 10×20; (b) mesh 15×30; (c) mesh 20×40; (d) mesh 30×60 149
Figure 4-8 Comparisons of different meshes in a classical continuum: (a) mechanical responses; (b) evolutions of the second-order work 150
Figure 4-9 Instability regions identified by second-order work of different meshes in micropolar continuum: (a) mesh 15×30; (b) mesh 20×40; (c) mesh 30×60 151
Figure 4-10 Comparisons of different meshes in a micropolar continuum: (a) mechanical responses; (b) evolutions of the second-order work 152
Figure 4-11 Contribution of the grains rotations to the second-order work 153
Figure 4-12 Selecting an element for local analysis of the components of the second-order work .. 154
Figure 4-13 Components of the second-order work of a local element 154
Figure 4-14 Components of the global second-order work 155
Figure 4-15 Failure zone of the soil mass behind the wall identified by the vanishing of the second-order work of different mesh sizes in a classical continuum: (a) mesh 20×10; (b) mesh 28×14; (c) mesh 40×20 156
Figure 4-16 Failure zone identified by the vanishing of the second-order work of different mesh sizes in a micropolar continuum: (a) mesh 20×10; (b) mesh 28×14; (c) mesh 40×20 156
Figure 5-1 Forces stresses and couple stresses acting on a micro polar portion 160
Figure 5-2 Deformation of a micro polar continuum 164
Figure 5-3 Stress components acting on a 3D micro polar continuum 167
Figure 5-4 Element of 3D micro polar continuum: (a) 20-node solid element; (b) integration points 170
Figure 5-5 Comparisons between IPP and 3D UEL in simulating triaxial drained test 176

Figure 5-6 Comparisons between IPP and 3D UEL in simulating triaxial undrained test 176
Figure 5-7 Comparisons between IPP and 3D UEL in simulating biaxial drained 177
Figure 5-8 Comparisons between IPP and 3D UEL in simulating biaxial undrained 177
Figure 5-9 Shear bands of three different mesh sizes using the 3D classical model: (a) mesh 10×20×1; (b) mesh 15×30×1; (c) mesh 20×40×1 179
Figure 5-10 Load–displacement of three different mesh sizes using the 3D classical model 179
Figure 5-11 Shear bands of four different mesh sizes using the3D micropolar model: (a) mesh 10×20×1; (b) mesh 15×30×1; (c) mesh 20×40×1; (d) mesh 30×60×1 180
Figure 5-12 Load–displacement of four different mesh sizes using the3D micro polar model 181
Figure 5-13 Influence of internal length scale l_c on shear band thickness: (a) l_c = 0mm; (b) l_c = 1mm; (c) l_c = 1.5mm; (c) l_c = 2mm; 182
Figure 5-14 Influence of internal length scale l_c on load–displacement curves 182
Figure 5-15 Shear bands of three different mesh sizes using the 2D classical model: (a) mesh 10×20; (b) mesh 15×30; (c) mesh 20×40..... 183
Figure 5-16 Comparisons of load–displacement curves between 2D and 3D classical SIMSAND model..... 184
Figure 5-17 Shear bands of four different mesh sizes using the 2D micro polar model: (a) mesh 10×20; (b) mesh 15×30; (c) mesh 20×40; (d) mesh 30×60 184
Figure 5-18 Comparisons of load–displacement curves between 2D and 3D micropolar SIMSAND model..... 185
Figure 5-19 Boundary conditions and final schematic of the model 186
Figure 5-20 Shear bands in 3D foundations using classical model 186
Figure 5-21 Load-displacement of three different meshes using the classical model 187
Figure 5-22 Shear bands in 3D foundations using micropolar model 187
Figure 5-23 Load-displacement of three different meshes using the micropolar model 188
Figure 5-24 Comparisons of the mechanical property between classical and Cosserat simulations. 188
Figure B-1 Uniaxial tension test of a bar 195
Figure B-2 Softening response in stress-strain 196
Figure B-3 Solution dependency on the discretization for a bar in uniaxial test..... 197

Figure C-1 Asymmetry stress distribution in micro polar theory 199
Figure C-2 Micropolar plane element: (a) ideal stress distribution of a micro polar element; (b) considering the slight difference caused by micro size..... 201
Figure C-3 Symmetric part and the skew symmetric part of the shear stress in micro polar theory . 202
Figure C-4 Cube micro element and spin inertia 203
Figure C-5 Bending curvatures and couple stresses of a micropolar element 205
Figure C-6 Shear strains in micropolar theory 205
Figure D-1 Subroutine interface of UMAT 210
Figure D-2 Flowchart of UMAT 210
Figure D-3 Comparisons between IPP and UMAT in simulating triaxial drained test 212
Figure D-4 Comparisons between IPP and UMAT in simulating triaxial undrained test 212
Figure D-5 Comparisons between IPP and UMAT in simulating biaxial drained test 213
Figure D-6 Comparisons between IPP and UMAT in simulating biaxial undrained test 213
Figure E-1 Particle size distribution of F-75 sand 214
Figure E-2 Calibration of parameters with isotropic compression and triaxial drained tests of F-75 sand: (a) one isotropic compression test; (b) five different triaxial drained tests with different confining pressure 216

List of tables

Table 1-1 Summary of micropolar constitutive models and applications.....46

Table 2-1 Material parameters used to simulating the biaxial tests.....76

Table 3-1 shear band inclinations with different initial density 97

Table 3-2 shear band patterns for three different internal length scales.....103

Table 3-3 Shear band thickness in biaxial tests from experiments and simulations.....104

Table 3-4 Different combinations of internal length l_c and element size l_e 119

Table E-1 Optimized values of constitutive parameters 215

General introduction

The aim of this thesis is to investigate numerically the strain localization phenomena in geotechnical structures with the finite element method. In order to overcome the serious mesh dependency problems of the numerical solutions in the post-bifurcation regime and to reproduce reasonably the shear band, a sand model based on critical-state has been formulated within the framework of micropolar theory and implemented into a finite element code. The micropolar theory was selected as the regularization method, because we consider that it has more physical meaning than other regularization theories. That is to say, compared to other regularization approaches, the micropolar theory is able to take into account the independent rotations of the particles. The thesis is divided into five chapters followed by general conclusions and perspectives. The outline is as follows:

Chapter 1 presents a comprehensive review of the strain localization phenomena in natural or artificial geo-structures and laboratory tests. The, with the aim of explaining the strain localization phenomena, various research methods and theories including the finite element method were summarized. Considering the mesh dependency problems in models based on the classical continuum theory, several regularization theories, e.g. non-local theory, high-gradient theory, micropolar theory, were discussed. According to their advantages or disadvantages, the micropolar theory was selected and used at last.

In chapter 2, a detailed introduction of the micropolar theory is presented, followed by a brief description of a sand model based on critical-state. Then, the full formulations of the model within the framework of micropolar theory have been derived. Based on the polarized model, FE implementations and validations have been conducted by fitting a series of laboratory element tests. The capability of micropolar approach in dealing with mesh dependency problems has also been presented by simulating a biaxial test and a retaining wall.

In chapter 3, the shear band in biaxial tests is numerically investigated in terms of onset, thickness and orientation, etc. For the purposes of validation, shear band thickness was also compared with the experimental outcomes. Furthermore, an effective regularization ratio in the micropolar model was proposed and discussed. At last, the influences of all the conditions, such as

confining pressures, initial void ratios, internal length, model parameters, on shear band patterns and the effective ratio have been discussed.

In chapter 4, the strain localization problems were discussed from an energy point of view. Because the driving force behind failures is believed to be the instability, the second-order work proposed by Hill (1958) was newly defined according to the micropolar model and used herein to investigate the difference between the classical model and the micropolar model. The mesh-independency using the micropolar model was also revealed by comparing second-order work for different cases.

In chapter 5, with an intent for more wide application in simulating the failures in geotechnical engineering, the 2D micropolar model has been extended to a 3D one. The implementation and numerical simulations were performed in detail. Furthermore, both the 2D and 3D model have demonstrated powerful regularization ability to relieve the mesh dependency problems and reasonably reproduce the shear band in structures.

Finally the general conclusions and perspectives summarized the thesis and proposed some perspectives and open questions for future developments.

Besides of these, some mathematical derivations of the mesh dependency problems and the pathological solutions can be found in the Appendices. The parameters used in current manuscript by fitting an isotropic compression test and a series of triaxial tests were also calibrated and summarized in the Appendices.

Introduction générale

Cette thèse vise à étudier numériquement les phénomènes de localisation des déformations en géotechnique par la méthode des éléments finis. Afin de traiter les sérieux problèmes de dépendance au maillage des solutions numériques dans le régime post-bifurcation et de reproduire raisonnablement le développement des bande de cisaillement, un modèle de sable basé sur l'état critique a été formulé dans le cadre de la théorie micropolaire et implémenté dans un code aux éléments finis. Le choix de cette méthode de régularisation s'appuie sur le fait qu'elle a un sens physique plus parqué que d'autres approches de régularisation. C'est-à-dire, par rapport à d'autres approches de régularisation, la théorie micropolaire est capable de prendre en compte les rotations indépendantes des particules. La thèse est divisée en cinq chapitres suivis des conclusions générales et des perspectives et est structurée comme suit.

Dans le chapitre 1, une synthèse détaillée des phénomènes de localisation des déformations au sein de géo-structures naturelles ou artificielles et d'échantillons de laboratoire a été réalisée. Puis, dans le but d'expliquer les phénomènes de localisation des déformations, une série de méthodes de recherche et de théories incluant la méthode des éléments finis a été résumée. Etant donnés les problèmes de dépendance au maillage dans les modèles basés sur la théorie du continuum classique, plusieurs approches de régularisation, telles que la théorie non locale, la théorie du gradient élevé, la théorie micropolaire, ont été présentées. Sur la base des discussions sur les avantages et les inconvénients de ces différentes théories, l'approche micropolaire a finalement été sélectionnée.

Au chapitre 2, la théorie micropolaire a été illustrée en détail. Un modèle élastoplastic pour les sables, basé sur l'état critique a été retenu et les formulations complètes du modèle dans le cadre de la théorie micropolaire ont été dérivées. Ce modèle polarisé a été implémenté dans un code de calcul aux éléments finis et des validations ont été réalisées en s'appuyant sur une série d'essais élémentaire de laboratoire. La capacité de l'approche micropolaire dans le traitement des problèmes de dépendance au maillage a également été présentée.

Dans le chapitre 3, la bande de cisaillement dans les essais biaxiaux ont été numériquement étudiée en termes d'amorcé de la localisation, d'épaisseur et d'orientation des bandes, etc... A des fins de validation, l'épaisseur de la bande de cisaillement a également été comparée à celles obtenues

dans les expériences. De plus, un ratio de régularisation efficace dans le modèle micropolaire a été proposé et discuté. Enfin, les influences de différentes conditions d'essai, telles que la pression de confinement et l'indice des vides initial, sur les caracteristiques des bandes de cisaillement obtenues numériquement et sur la valeur du rapport de régularisation ont été discutées. De même l'influence de la longueur interne et celle des paramètres du modèle ont été examinées.

Au chapitre 4, les problèmes de localisation des déformations ont été discutés d'un point de vue énergétique. Parce que l'instabilité matérielle est considéré comme étant le moteur des défaillances structurales, le travail du second ordre proposé par Hill (1958) a été redéfini dans le cadre du modèle micropolaire et utilisé ici pour analyser et comprendre les différences entre le modèle classique et le modèle micropolaire. L'indépendance du maillage à l'aide du modèle micropolaire a également été en évidence en étudiant le travail du second ordre pour différents cas de chargement.

Dans le chapitre 5, avec comme objectif une application plus large dans la simulation des défaillances en ingénierie géotechnique, le modèle micropolaire 2D a été étendu à un modèle 3D. La mise en œuvre et les simulations numériques ont été présentées en détail pour illustrer les capacités de cette modélisation. Comme le modèle 2D et le modèle 3D a démontré une capacité de régularisation puissante pour soulager les problèmes de dépendance au maillage et reproduire raisonnablement les bandes de cisaillement dans les structures géotechnique.

Le mémoire se terminé par des conclusions générales reprenant les avancées scientifiques principales obtenues au cours de ce travail de ce thèse et des perspectives et questions ouvertes pour des développements futurs.

Certaines dérivations mathématiques des problèmes de dépendance au maillage et des solutions pathologiques sont présentées en annexe. L'étalonnage des paramètres du modèle de comportement utilisés dans le manuscrit sur la base d'une série d'essais triaxiaux est également présenté en annexe.

Chapter 1 Literature Survey

1.1 Introduction

Natural and artificial geotechnical structures play an essential role in our lives. Granular soils, whether as the main construction materials or the foundation of geotechnical structures, determine, to an extent, their failure mechanisms. Many disasters that affect our lives are linked to geotechnical failures, such as landslides, slope instability of high embankments or dams, collapse of excavated tunnel surfaces, and uneven settlement of buildings and roads. Most geotechnical hazards can be identified as examples of progressive failure caused by the occurrence and development of severe strain localization. Accordingly, this phenomenon, as it pertains to geotechnical engineering, has long been an important and extensively researched topic.

Although strain localization has long been observed at the scales of both geotechnical structures and laboratory experiments, systematic studies designed to observe and analyze shear banding in geomaterials have been undertaken only during the past decades (Desrues and Viggiani, 2004). Based on the monitoring or observation of strain localization phenomena, the mechanism underpinning strain localization has become clearer. Although a macroscopic occurrence, its origin lies in the material microstructure. A variety of theories and methods have been proposed with the aim of describing and explaining these phenomena against the backdrop of geotechnical engineering, for example, equilibrium theories, discontinuity theories, bifurcation theories, and different constitutive models. Occasionally, these models have been enhanced using a range of regularization approaches, which have chiefly been adopted for post-failure analysis. With the help of a suitable theory and constitutive model, the typical strain localization with shear band can be reproduced via numerical simulations. The shear banding invariably refers to failure surface inclination, shear banding thickness, and the global bearing capacity of structures during the overall failure process.

In this chapter, a detailed synthesis of strain localization phenomena from natural or artificial geo-structures to laboratory tests was first summarized. Then, the mechanism of strain softening of granular material or structures was discussed. As an intent of explaining the strain localization phenomena, a series of research methods and theories was reviewed. Shear band, the main specific

feature of strain localization phenomena, was focused on in terms of its onset, inclination, thickness, etc. Next, the advantages and disadvantages of numerical methods were discussed. Considering the deficiencies of FEM in modelling strain localization problem, several main regularization approaches, such as viscosity theory, non-local theory, high-gradient theory and micropolar theory, are naturally introduced. According to the properties of each regularization technique, the micropolar theory was favored in the present manuscript at last. Therefore, the applications of micropolar theory in geotechnical engineering and its internal length scale parameters have been comprehensively summarized and discussed.

1.2 Strain localization phenomena

1.2.1 Engineering scale: collapse of geotechnical structures

The collapse of natural or artificial geotechnical structures, when attributable to their excessive shear strain localization, has a number of possible factors. It has been found that accumulation of plastic strain resulted in the instability of structures.

(a) (b)

Figure 1-1 Uneven settlement and the collapse of buildings: (a) Tower of Pisa; (b) residential buildings in Shanghai

Interestingly, we start this section by the picture of Leaning Tower of Pisa in Italy in Figure 1-1 (a) and its comparison in Figure 1-1 (b). The Leaning Tower of Pisa, relating to the uneven

deformation of foundation, is a very famous example in geotechnics. The collapse of a 13-story residential building under construction in Shanghai, China, in 2009 is also an example of excessive leaning, while it is a disaster. The Leaning Tower's uneven settlement is attributable to the self-heterogeneous nature of the materials in the foundation. For the 13-story building, by contrast, temporary excavation (unloading) adjacent to the structure on one side, together with temporary spoils piles (loading) on the other, caused slightly uneven settlement of the building that then induced an excess of external unbalanced forces sufficient to shear the pile foundations, causing global slope stability failure and ultimately collapse. We can imagine that if the uneven displacement of a building constructed on a soil foundation were not monitored and controlled as soon as possible, it would no doubt transition from a state similar to that of the famous Leaning Tower to a final collapsed condition, just as this obscure residential building did. The building's state would change from the onset of inhomogeneous deformation to, ultimately, total collapse, a process that could be identified as progressive failure caused by the development of shear strain localization.

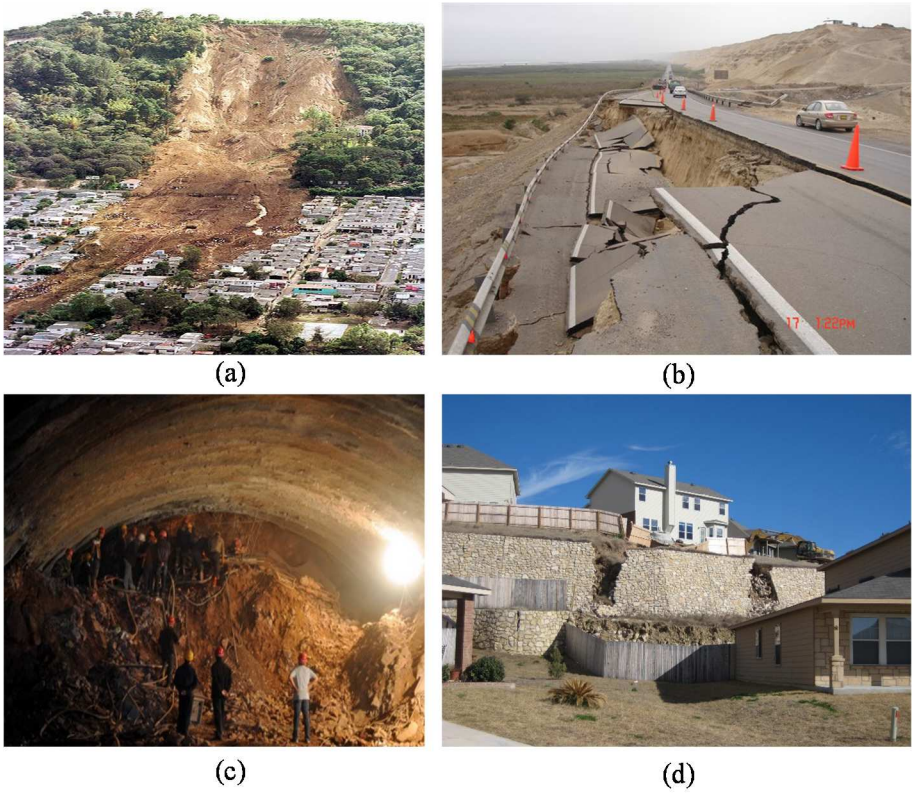

Figure 1-2 Collapse of typical geotechnical structures: (a) landslide in San Salvador; (b) slide of a high embankment; (c) collapse of the excavation surface; (d) failure of a retaining wall

Besides the uneven settlement of buildings, certain other geotechnical failures can also be identified as instances of such failure, such as landslides, erosion of high embankments or dams, the collapse of the excavated surface of a tunnel, and the failure of a retaining wall. Figure 1-2 illustrates such eventualities: (a) a landslide on a mountain slope after a 2001 earthquake in San Salvador (*http://kids.britannica.com/kids/article/landslide/433121*); (b) the break-up of a high embankment; (c) the collapse of a tunnel under construction in Inner Mongolia, China, 2010 (*http://www.chinadaily.com.cn/china/2010-03/20/content_9616414.htm*); (d) the slide of backfilled soils behind a retaining wall in the U.S. city of San Antonio (*http://www.retainingwallexpert.com/artman2/publish/Wall_Failures/Retaining_Wall_Failure_-_San_Antonio_TX.shtml*). The term *landslide* is used to refer to a wide variety of processes that result in the downward and outward movement of slope-forming materials, including rock, soil, or artificial fill or a combination of all of these. The failures of all these structures, then, can be explained by defining them as landslides. The key factor that causes a landslip to occur is instability of the slope, whether steep or shallow. Many geological factors (such as type of rock, grain size, and steepness of slope) influence a particular location's susceptibility to landslide. When the gravitational force reaches a certain threshold (which varies according to location, rock type, and so on), the slope fails and a landslide occurs. Whether this outcome is sudden or slow, it always undergoes the same progressive process. Although many possible causes may be acting independently or in tandem to cause a landslide, certain key events are likely to trigger them: volcanic or earthquake activity, heavy rain, isostatic rebound (melting of glacial ice, which causes land to rise), and human activity such as mining or construction.

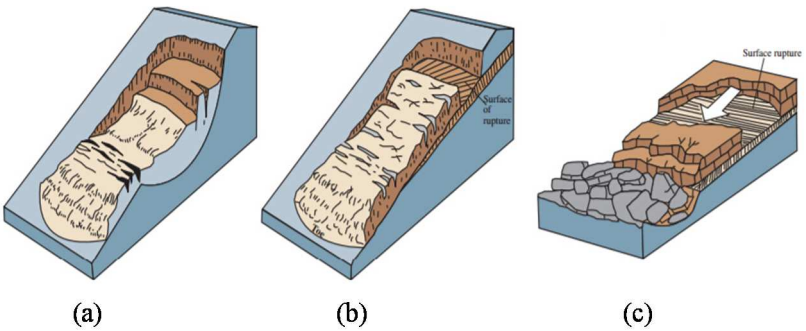

Figure 1-3 Major types of failure of slope: (a) rotational landslide; (b) translational landslide; (c) block slide

Although instability can cause a structure to fail in many ways, this section will be restricted to the phenomenon of the collapse of several typical geotechnical structures at an engineering scale. Other mechanisms will be discussed and studied in subsequent sections. According to the classification of the U.S. Geological Survey, the two most common types of slide are rotational and translational landslides, as shown in Figure 1-3. In fact, what links different geological failures is the common phenomenon of severe rotational and translational deformation of materials in the strain-localized region. The failures of structures are closely related to the grain conditions inside the strain localized regions. That is to say the rotations and rearrangements of grains located in the local failure regions affect greatly the global mechanical response, which will be discussed in detail in the following chapters.

1.2.2 Model scale: strain localization in model tests

Work on model walls began in 1954 with Roscoe, as reported by Schofield (1968). Those who have continued his work have conducted, and recorded on radiographs, many model wall tests (active or passive) (Arthur, 1962; James, 1965; Lucia, 1966; May, 1967; Adeosun, 1968; Bransby, 1968; Lord, 1969; Smith, 1972; Milligan, 1974). These follow-ups were performed at Cambridge University between 1962 and 1974. The researchers' main purpose was to obtain high-quality strain measurements inside the sand mass using the X-ray method, but not to study the shear band (Leśniewska, 2000). Their work provided subsequent researchers with abundant data concerning numerous shear bands, contributing significantly to the study of strain localization.

Later on, increasing numbers of researchers conducted model test series to investigate the failures of geotechnical structures. Considering the stress-dependent behavior of soil, centrifuge has proven to be a highly suitable and powerful technique for investigating several types of practical problems in geotechnics. Many measuring and test techniques in experimental geotechnics have been developed and applied by Allersma and his team, who designed and built a small geo-centrifuge at the geotechnical laboratory (Allersma, 1994b, a, 2002). Furthermore, several projects have been modeled correctly in the centrifuge, such as those simulating the instability of dykes and embankments, land subsidence, the instability of street pile walls, the collapse of steep cuttings, and so on.

In Figure 1-4, (a) is the centrifuge developed by TU Delft, while (b), (c), and (d) represent the modeling of the instability of a dyke and the uneven settlement and collapse of a street pile wall (*http://hgballersma.net/tudweb*). From the model tests undertaken by TU Delft, strain localization phenomena can easily be observed.

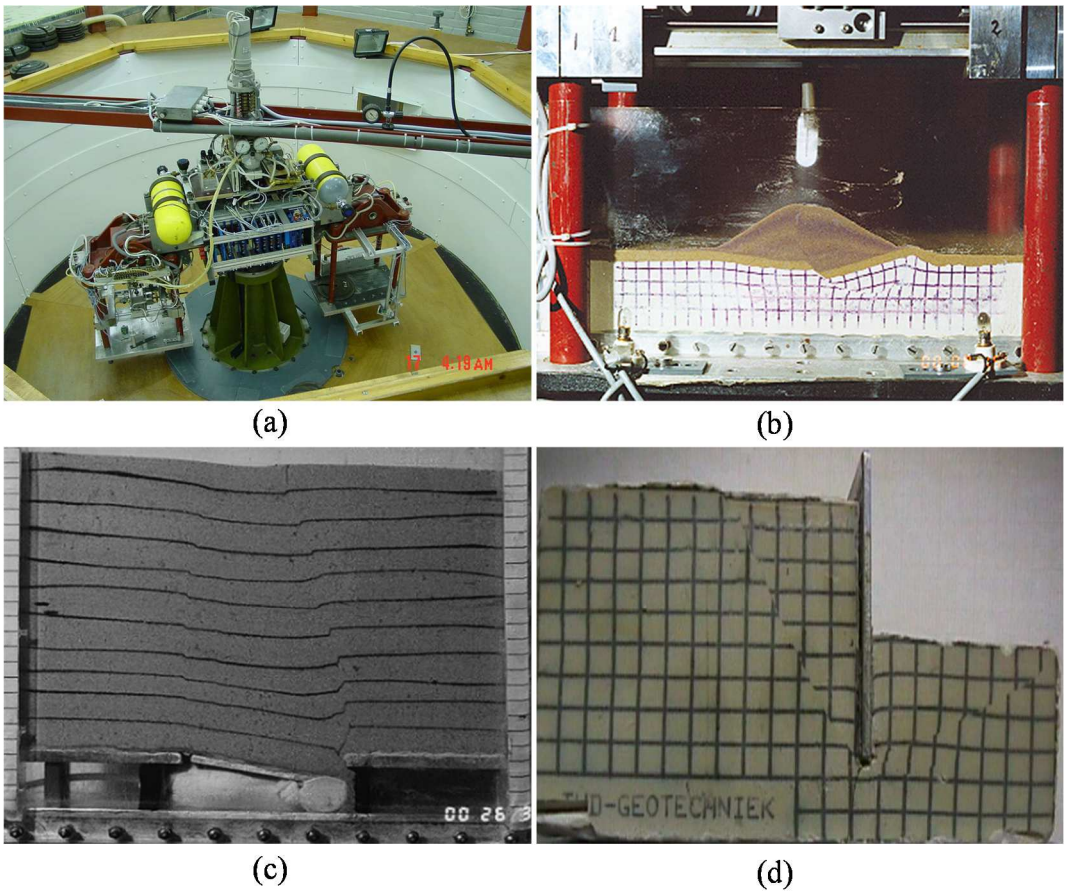

Figure 1-4 Centrifuge and typical centrifuge modellings. (a) Centrifuge machine (b) Dike model (c) Uneven settlement (d) Street pile wall

As well as centrifuge modeling, other model tests have also been performed by many researchers, such as the tank model conducted as part of the British Geological Survey. Figure 1-5 shows the reconstruction of a typical geo-hazard, retaining wall failure, using a tank model in 2013 (*https://www.youtube.com/watch?v=MS4H_u0ARpo*). A retaining wall is intended to safeguard the buildings constructed above the soil behind it. This can be observed where roads, railways, or other excavations have been built that cut into the land. The failure of such a wall can be used to explain the familiar hazard process in ground engineering. Figure 1-5 demonstrates the entire progressive failure process of a retaining wall. With the rotation of the wall around its toe, the first main shear

band appears before the right-side region of the shear band begins to slide downward and outward; then, the retaining wall moves to a certain extent and secondary shear bands form in the previous sliding region. This is followed by the collapse of the soils behind the wall as well as the construction above it.

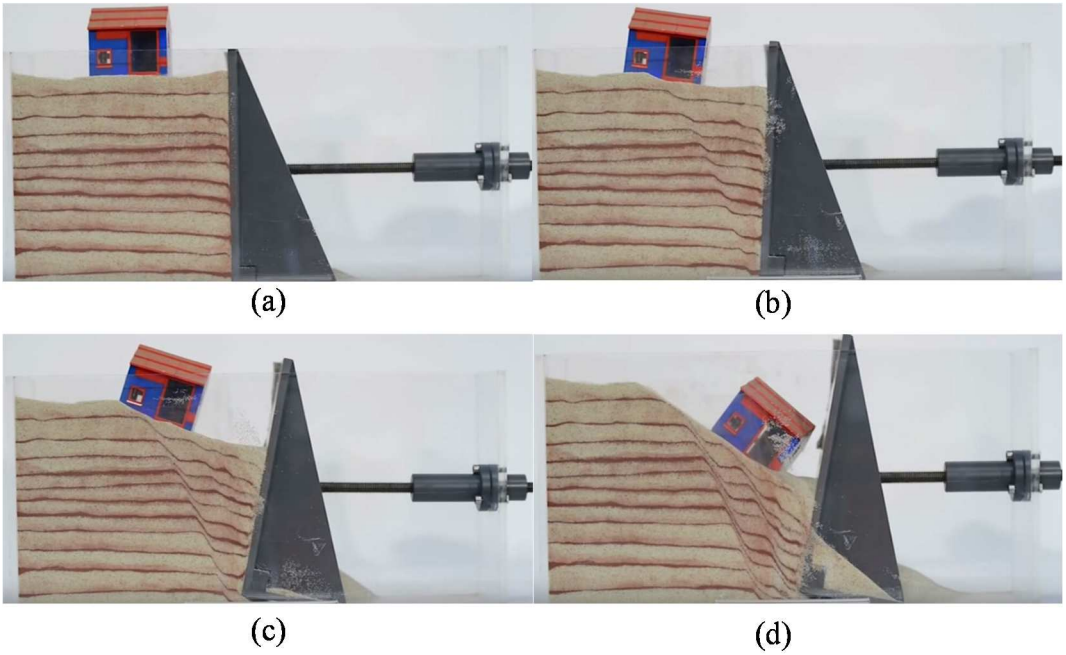

Figure 1-5 Progressive failure of retaining wall by geo-hazard tank model: (a) initial state; (b) formation of first shear band; (c) formation of several shear band; (d) collapse of soil

Recently, Lluís (2017) demonstrated for educational purposes the progressive failure process of soil under rigid footing. From his video recording, we can also observe the entire formation process of the strain localization phenomenon. Initially, only the soils immediately beneath the footing begin to sink. With the footing's increasing penetration into the soils, those beneath the footing form a triangular shape because of the frictional constraint between the rough base of the footing and the soil. At the same time, the soil around the triangular area is subjected to pressure and slide outward along an inclined surface. Finally, the soil at both sides of the footing is significantly uplifted laterally, leading to the occurrence of instability. The shapes of the failure (shear band) under ultimate loading conditions are displayed in image (d). The failure is accompanied by the appearance of failure shear bands and considerable bulging of a sheared mass of sand. This type of failure was designated as general shear failure by Terzaghi (1943). However, the surfaces are in theory sliding

surfaces rather than, as in reality, sliding shear bands of finite thickness. It should be noted that two other failure types can occur: local shear failure and punching shear failure.

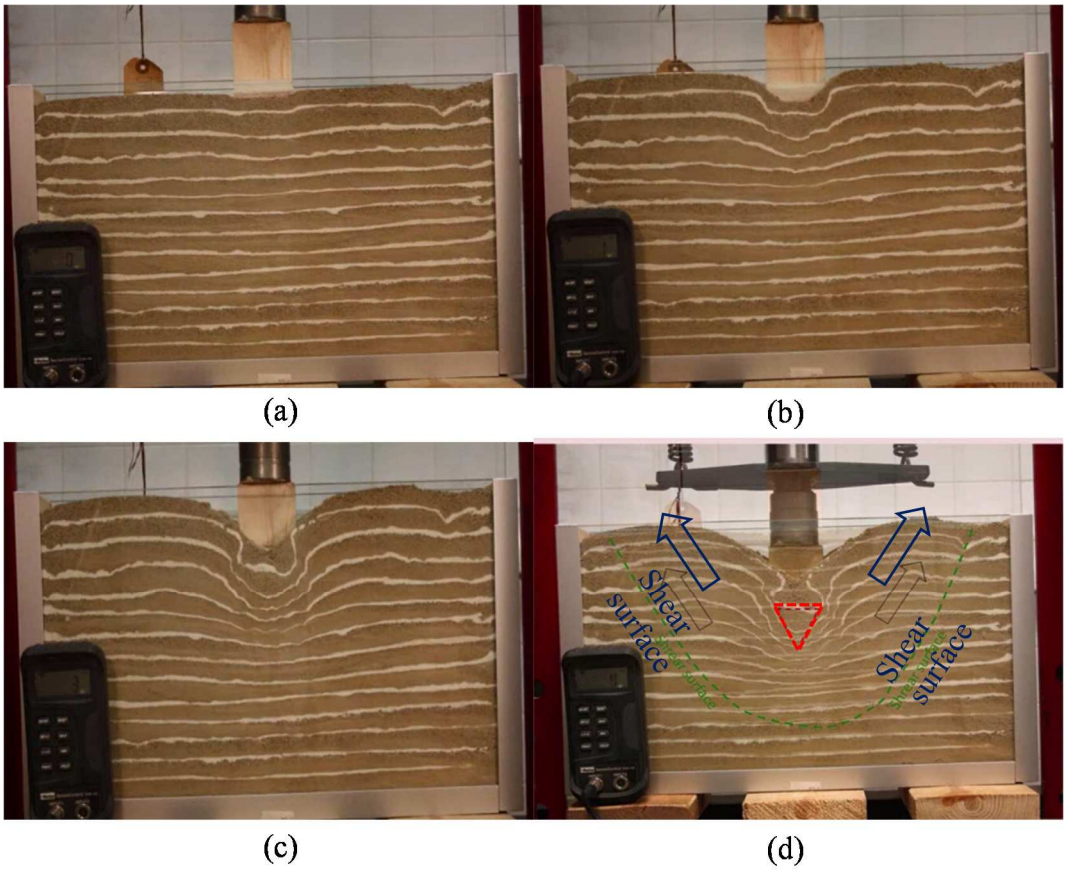

Figure 1-6 Soil failure under footing by geo-hazard tank model: (a) initial state; (b) formation of the triangle area under footing; (c) laterally uplift outward; (d) formation of slide surface

1.2.3 Laboratory sample scale: strain localization in specimens

In the laboratory, strain localization is usually reproduced using shear bands formed in specimens during loading. This is done in the direct shear test, simple shear test, hollow cylinder, triaxial test, and biaxial test, for example. It is a narrow zone of intense shearing strain, usually plastic in nature, which develops during severe deformation of ductile materials. Sample tests of shear bands have been conducted by many researchers, e.g. Vardoulakis (1980), Desrues (1990), Han and Drescher (1993), and Alshibli et al. (2002). Strain localization phenomena can be clearly observed in their studies. As examples, soil specimens (overconsolidated clay and dense sand) of triaxial and biaxial tests are shown in Figure 1-7; the pictures on the left are of triaxial and biaxial apparatuses operated

by Tang (2007) and Alshibli (1996), respectively. The next two pictures represent the deformed specimens in various states. In these tests, the specimens are usually compressed and then sheared by increasing the axial strain. For the triaxial test, after an axial–symmetric compression test, the sample was initially cylindrical in shape; because the researchers attempted to preserve symmetry during the test, the cylindrical shape was maintained for a short time and the deformation was homogeneous. But at extreme loading, two crossed shear bands formed and the subsequent deformation was strongly localized. For the biaxial test, conducted on dense Ottawa sand, we can also observe that the uniform deformation of the specimen was broken at an early stage by the first inclined shear band after only a small axial deformation. With the increasing axial strain, the second shear band appeared and formed two clear crossed (X-shaped) shear bands. In general, it is easy to discern that shear bands are narrow zones of finite thickness and a certain orientation, which have been studied by many researchers via experimental and numerical means. In addition, strain localization should be held responsible for a reduction in global bearing strength. This section is limited to a discussion of the strain localization phenomenon. Shear bands will be investigated in detail in subsequent parts.

Researchers have also found that shear bands inside dense or overconsolidated specimens in triaxial tests are highly complex. In contrast, the bands formed easily, early, and clearly in biaxial tests. As well as the macro-observation of the strain localization phenomenon in the laboratory, micro-observations have also been performed by many groups. Recently, with the latest discrete grain scale Volumetric Digital Image Correlation (V-DIC) method developed by 3S-R in Grenoble, the translations and substantial rotations of grains in shear strain–localized regions have been confirmed by Viggiani et al. (2010).

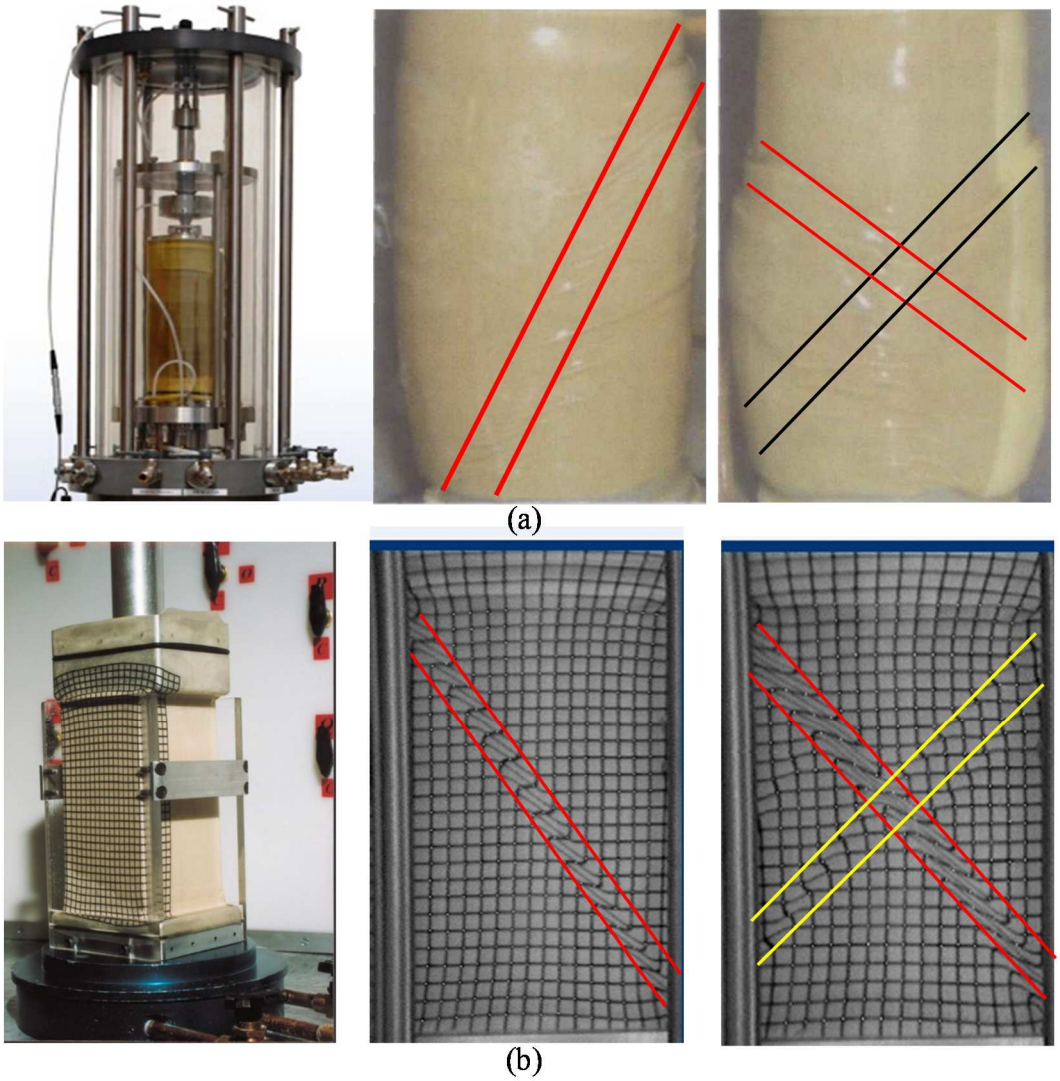

Figure 1-7 Apparatus and specimens: (a) triaxial test; (b) biaxial test

1.3 Mechanisms of strain localization

At the macroscopic level of observation, a shear band may be described as a zone of intense deformation bounded by two discontinuity planes with a finite thickness. This phenomenon may be caused by geometrical effects (shape and boundary conditions of the body can augment the bifurcation conditions of the interior (Dietsche and Willam, 1997) or by material effects (heterogeneity and local defects). Taking the sample test as an example, the mechanism of strain localization can be discussed in terms of its onset, development, and causes. Shear bands—the typical sign of strain localization—are usually found in the specimens in triaxial or biaxial tests on

overconsolidated soil or dense sand. In these tests, the specimen is usually compressed first, before being sheared to the point of failure. During the shearing stage, initially the strength increases and the total volume decreases with the growing axial strain, which corresponds to Stage 1 as shown in Figure 1-8. After a short period of homogeneous deformation, the specimen begins to dilate, accompanied by the appearance of the shear band. The dilatancy of granular materials in strain-localized regions results in an increase of global volume. At the same time, the bearing strength reaches an apex just after the onset of the shear band, then reduces gradually. This process is illustrated in Stage 2 in Figure 1-8. With the further increase of axial strain, the increased volume, caused by dilatancy, and the decreased load capacity, mainly caused by failure, stop changing and tend to a terminal steady state, respectively, which corresponds to Stage 3 in Figure 1-8.

Although many factors, such as grain size, grain shape, grain surface roughness, confining pressure, boundary condition, initial imperfections, initial density, and so on, have been proven to affect the formation of the shear band (Alsaleh, 2004), the forms (thickness and orientation) of said band and the trend of the mechanical response are generally similar. Accordingly, the influences of these different factors will not be discussed in this section.

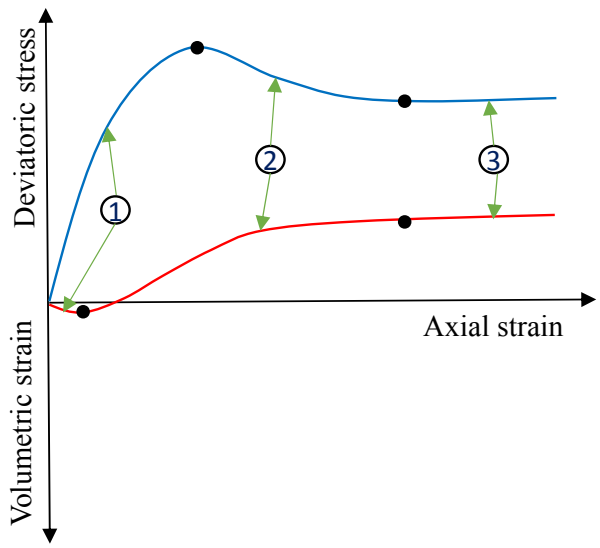

Figure 1-8 Stress and strain of the specimen in triaxial or biaxial test

As most granular materials share the same strain-softening behavior, we can be in no doubt that the softening behavior of soil or sand can result in the global softening phenomenon for a specimen, greatly influencing shear band formation. However, it is worth noting that the softening behavior is

not a necessary factor as regards the onset and development of shear bands (de Borst et al., 1993). From a physical point of view, we can explain the strain localization phenomenon, which is accompanied by a reduction of bearing strength, as follows: “Because a specimen composed of granular particles always has intrinsic heterogeneity and different boundary restraints on its borders, the stress distribution will be non-uniform and the strain distribution will also not be homogeneous. When the sample is loaded, some local regions will be first to reach their strength limit and start to rupture; and thus the local strength reduces with further deformation and is not sufficient to resist the previous loadings. At the same time, local imperfection results in a reduction of the global bearing capacity. Then, to keep the force balanced, the additional burden will be transferred and shared by the neighboring soil regions. This will continue until the internal resistance can balance the external load. If the latter does not happen, the strain-localized regions will continually spread and develop in a certain direction until the formation of complete shear bands, which will divide the sample into a certain number of independent parts before the final collapse of the structure. During this process, failure occurs in certain regions and spreads to their surroundings, which is also a progressive balancing process. With the reduction of global bearing capacity, the parts outside the strain-localized regions unload for the sake of equilibrium.”

The strain-localized and other regions have very different deformation gradients. Accordingly, we may conclude that the failure of a sample or structure is a progressive process, in the course of which the strain localization phenomenon is often accompanied by a significant reduction of the load bearing capacity. Vardoulakis (1998) also explained the softening phenomenon from a micro point of view; in his opinion, reduction of coordination number and grain column buckling produce macroscopic softening of materials inside the localized zone. For equilibrium reasons, the material outside the localized zone is unloaded. He also pointed out that the modeling of localized deformation in geomaterials is quite a challenging task, because of the mathematical difficulties that are generally encountered while dealing with the behavior of non-associated and softening materials. Finally, to accurately predict the development of failure and prevent geotechnical hazards, the study of this progressive kinematic process is of great importance and significance in the real world.

1.4 Theories and methods of describing strain localization

1.4.1 Experimental investigations

1.4.1.1 Techniques for observing the shear band

As is widely known, investigations into the shear localization phenomenon have been fruitful, thanks to the unrelenting efforts of those who have done before. The most valuable experimental contributions to the understanding of shear banding have been those that have measured, in one way or another, the full extent of deformation in a specimen, which is the only means by which test results can be adequately interpreted (Viggiani et al., 2010) .

Full-field analysis of the strain localization phenomenon in sand began in the 1960s in Cambridge, which was followed by the work of several groups, including 3S-R in Grenoble (Desrues, 1984, 1990; Bésuelle and Rudnicki, 2004; Viggiani et al., 2004; Desrues et al., 2010; Viggiani et al., 2010). In the 1960s X-ray radiography was first used to measure 2D strain fields in sand, and from the early 1980s X-ray tomography was used by a few groups working in geomechanics. Thereafter, the advent of X-ray micro-tomography, as used by Oda and his colleagues (Oda et al., 1982; Oda et al., 1997; Oda &Kazama, 1998) , allowed researchers to study the mechanics of granular media (in 3D) at the grain level, which would not have been possible with the previous standard X-ray tomography images. However, the images taken by Oda were obtained after the fact, and the evolution of the entire deformation process was ignored. Because of the deficiencies of X-ray micro-tomography, in-situ X-ray tomography was proposed, which could scan and record throughout the entire loading process. Now, highly accurate strain-filed evolution measurement techniques have been developed and used widely, including false relief stereo photogrammetry (FRS) and computed tomography (CT) as proposed by 3S-R in Grenoble, France (Desrues et al., 2007) , and the digital image processing technique developed by Shao (2006). These new techniques enable full tracking of strain localization from onset to complete formation of shear band. In recent work, the researchers in 3S-R have also applied the 3D Volumetric Digital Image Correlation (V-DIC) method to a sequence of X-ray tomography images taken during their tests. Furthermore, they proposed a grain-scale

V-DIC that permits the characterization of the full kinematics (i.e., 3D displacements and rotations) of all the individual grains in a specimen.

In terms of the study of strain localization, the focus has mainly been on the onset and propagation of the shear band, its thickness and orientation, and the influences of key factors, such as mean grain size, confining pressure, initial density, and so on, on its formation.

1.4.1.2 Onset of shear band

For many years, the received wisdom on the onset of shear bands was that they occurred and developed only in dense sand and overconsolidated soils. This was because we cannot always discern bands in loose specimens with the naked eye. Years later, Leśniewska (2000) gave two explanations for the invisible shear bands of loose sand: "First, tests performed on loose samples were often terminated before the peak friction angle had been attained. This occurred because such samples were investigated in the same range of deformation as their dense counterparts (usually about 5% of axial strain), whereas they required higher strains to achieve the peak friction angle. If the tests had been taken further, it is likely that shear bands would have been observed. The second explanation related to the technical observation. In general, no appropriate equipment existed at that time to record shear bands, which are somewhat faint in the case of loose samples."

In order to provide a better understanding of physical mechanics of shear bands, Hicher and Wahyudi (1994) conducted a series triaxial tests with normal consolidated clay. In their study, the influences of testing factors such as boundary conditions, sample dimensions, over-consolidation ratio were examined. With the use of scanning and transmission electron microscopes, they also managed to observe the failures at the particle level, which showed a strong reorientations of the particles along the sliding surfaces, indicating that large displacements and rotation took place in the strain localized regions. Desrues et al. (1996) showed the entire pattern of faint localizations within dense and loose sand using computed tomography. Then Finno et al. (1997) found shear bands in all their loose samples with the help of stereo photogrammetry. Later, they were also confirmed by Alshibli et al. (2000b, 2010) and Bésuelle et al. (2007), who used computed tomography in the 3D condition as shown in Figure 1-9. Although imperfection (as a kind of discontinuity) can be regarded as a factor in the initiation of strain localization, it has been proven not to be the most essential one.

After years of attempts to guarantee the homogeneity of the stress–strain state within the specimen (uniform deposition of sand samples; enlarged, polished, and lubricated end platens; elimination of load eccentricities), researchers came to gradually accept that at a certain load level, the uniformity of the stress–strain state was always lost. Strain localization seems to be an inevitable aspect of all kinds of granular materials, regardless of the type used in the experiment. In fact, experimental types and the initial conditions affect the onset of the shear band. Results have shown that the onset of a shear band comes earlier in biaxial than in triaxial tests, and that the denser the specimen, the more easily the band appears. Furthermore, a reduction of the specimen size or its slenderness will result in the retardation of the band's onset (Desrues, 2004).

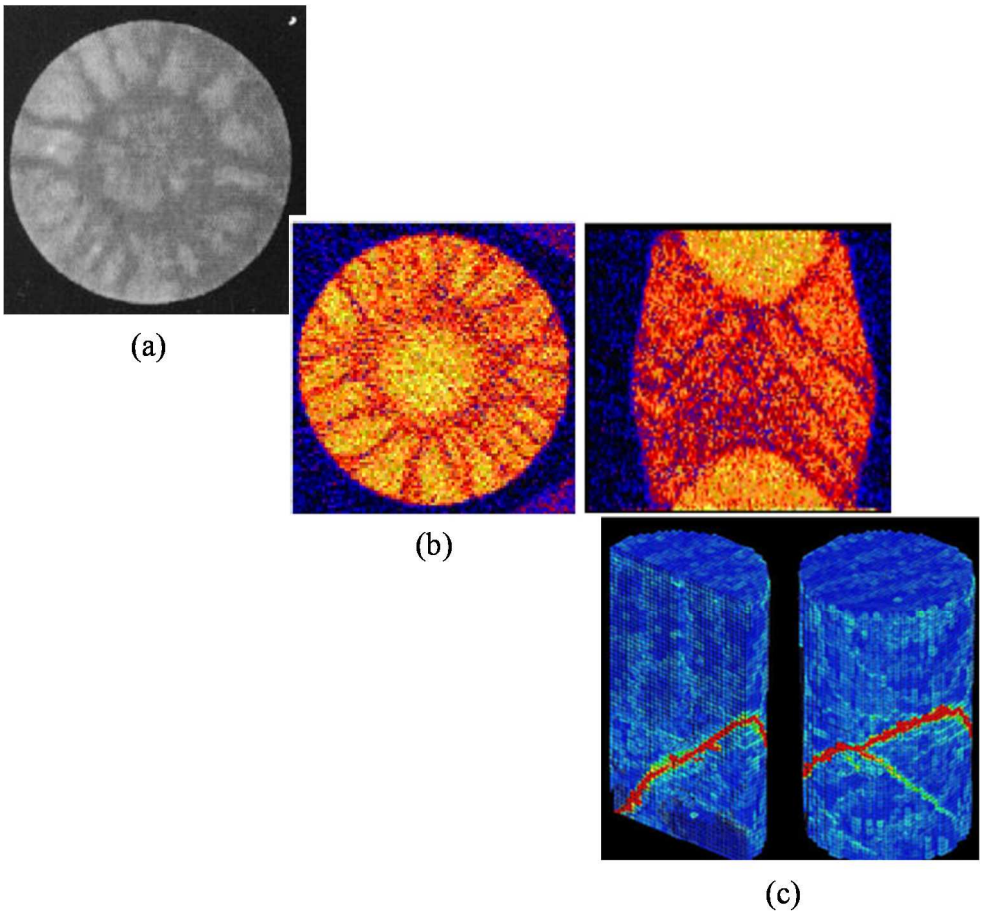

Figure 1-9 Investigations of shear band with computed tomography technique: (a) observation of Desrues; (b) observation of Alshibli; (c) observation of Bésuelle

1.4.1.3 Inclination of shear band

Turning to the orientation of the shear band, its inclined angle in relation to the principal stresses or strains is invariably considered. Three main equations are always used to predict the inclination. The

first classical solution for shear band inclination in frictional materials subjected to plane strain condition is known as the Mohr–Coulomb solution. According to the Mohr–Coulomb criterion, the inclination angle of the shear band is given by Eq. (1.1). θ_C is the angle measured from the direction of the minimum principal effective stresses, ϕ is the mobilized angle of internal friction defined by Eq. (1.4) for cohesion-free materials, and σ_1 and σ_3 are major and minor principal stresses, respectively. The second classical solution was proposed by Roscoe (1970) in the form of Eq. (1.2). θ_R is the angle between the shear band and the direction of the minor principal strain increment $d\varepsilon_3$; ψ is the dilation angle at failure, which is defined by Eq. (1.5); $d\varepsilon_1^p$ and $d\varepsilon_3^p$ are major and minor plastic principal strains, respectively. Seemingly, the solutions given by Mohr–Coulomb and Roscoe represent an upper bound and a lower limit, respectively (Vardoulakis, 1980). In the case of associated plasticity, the mobilized friction angle equals the dilatancy angle, meaning that the Mohr–Coulomb and Roscoe equations coincide. However, the non-associated plastic flow rule has been proven to be more reasonable for describing the behaviors of granular materials. Later, based on experimental observations, Arthur et al. (1977) proposed an intermediate solution for shear band inclination, as shown in Eq. (1.3). Shortly thereafter, Vardoulakis (1980) validated Arthur's solution using the bifurcation theory, whereas Vermeer (1982) used compliance methods to derive an expression for the shear band inclination angle that agreed well with the solutions suggested by Arthur et al. and Vardoulakis. As may be observed, if associated plasticity is adopted, the solution obtained by Arthur's equation will be the same as those garnered from the Mohr–Coulomb or Roscoe equations. In most articles, the shear band inclination is within a range between the Mohr–Coulomb and Roscoe solutions.

$$\theta_C = 45^\circ + \frac{\phi}{2} \tag{1.1}$$

$$\theta_R = 45^\circ + \frac{\psi}{2} \tag{1.2}$$

$$\theta_A = 45^\circ + \frac{\phi + \psi}{4} = \frac{\theta_C + \theta_R}{2} \tag{1.3}$$

$$\sin\phi = \left\{ \frac{\sigma_1 - \sigma_3}{\sigma_1 + \sigma_3} \right\}_{\max} \tag{1.4}$$

$$\sin\psi = \frac{d\varepsilon_v^p}{d\varepsilon_d^p} = \frac{d\varepsilon_1^p + d\varepsilon_3^p}{d\varepsilon_1^p - d\varepsilon_3^p} \tag{1.5}$$

In fact, for many years no agreement could be reached between the experimental inclinations published by different authors. Some were closer to Mohr–Coulomb, some were closer to Roscoe, and others lay in between. Lade et al. (1996), who studied shear band formation via triaxial extension tests, investigated three different sands and found that in all cases, the Coulomb inclination was clearly favored. Alshibli and Sture (2000), meanwhile, conducted a comprehensive experimental study to investigate the effects of specimen density, confining pressure, and sand type on the stress–strain and stability behavior of sand tested under the plane strain condition. Different from the conclusion of Lade et al. (1996), all their experimental investigations showed that the Mohr–Coulomb solution overestimated the shear band inclination, whereas Roscoe's prediction was closer to the mark. Another team, Saada et al. (1999), reported that the inclination of shear bands in sand appears to depend on the effective angle of friction and that of dilation in a combination defined by Arthur et al. (1977) and Vardoulakis (1980). Elsewhere, Finno et al. (1997) concluded that the measured shear band orientation in plane strain tests on loose, fine-grained, water-saturated sand in drained or undrained conditions, lay between the Coulomb and Arthur et al. solutions. That said, Vardoulakis et al. (1978) also found that the measured shear band inclination was extremely sensitive to boundary conditions and that loose specimens were more sensitive than dense ones. Similarly, Oda and Kazama (1998) later argued that difficulties were inherent in determining shear band inclination in their plane-strain tests, because the bands were not perfectly straight in the vertical sections of the sample; rather, they were generally curved. Thus, in their opinion, the inclination angle is not necessarily a material constant, but rather a variable sensitive to certain boundary conditions. The experimental results gained by Viggiani and Desrues (2004) also demonstrated that the shear band pattern depends on boundary conditions and the slenderness of the specimen. Various patterns of shear zones were observed, including even parallel and crossing zones. They claimed that the shear zone reflection at rigid boundaries was a typical mode of propagation in short specimens.

1.4.1.4 Thickness of shear band

Shear band thickness is another important aspect of shear banding in the research into strain localization. Based on direct experimental observations, Roscoe (1970) found that the width of shear bands is about 10 times the average grain diameter (or mean grain size) d_{50}, a figure that was verified

by Scarpelli and Wood (1982). In the experimental observations gained from biaxial tests of different sands by Mühlhaus and Vardoulakis (1987), it was concluded that the average shear band thickness is about 16 times the mean grain diameter d_{50}. The results garnered by Desrues (1984) proved that shear band thickness is augmented with increasing particle size, which specifically in the range of 7.5 to 9.6 times the mean grain size (Mokni and Desrues, 1999). Yoshida et al. (1994) found that the most important factor controlling the shear deformation was particle size and that the shear band thickness was about 8–22 times the d_{50}. Thereafter, strip foundation tests on dense SLB sand were carried out by Tatsuoka et al. (1997), who found that the thickness of the shear band was about 10 times the d_{50}. Based on the results of biaxial tests on three different sands, conducted by Alshibli (2000), the shear band thickness is in the range of 13–14 d_{50} for fine sand, 11–12 d_{50} for medium-grained sand, and 10–11 d_{50} for coarse-grained sand. In experimental tests of earth pressure performed by Nübel and Huang (2004), it was found that the thickness of the shear band was 11–15 times d_{50} for active cases and 20 times d_{50} for passive cases. As we can observe from all this, almost all researchers normalize the shear band thickness using the mean grain size, and many have also found that the normalized shear band thickness is not constant. Instead, the conclusion that shear band thickness increases along with d_{50}, and that normalized shear band thickness by d_{50} decreases as d_{50} increases, has been commonly validated and accepted.

Own-wall friction tests were carried out by Tejchman and Wu (1995) using a plane strain apparatus developed by Vardoulakis et al. (1978) for dense and loose Karlsruhe sand with different wall roughness to study the shear localization in the boundary region. In their tests, strain localization was caused by geometrical effects (boundary condition) but not by material effects (heterogeneity and local defects). It was found that the thickness of the shear zone formed along the inclined wall was approximately 1 mm ($2\times d_{50}$) for a rough wall and 3 mm ($6\times d_{50}$) for a very rough wall. Thereafter, the experimental tests on dense and loose medium Karlsruhe sand (d_{50} = 0.45 mm) in a plane strain model silo with parallel (bin) and convergent walls (hopper) and a slowly moveable bottom, by Tejchman (2008), demonstrated that the shear band thickness was approximately 5 mm ($11\times d_{50}$) at the smooth wall, 20 mm ($45\times d_{50}$) at the very rough wall with loose Karlsruhe sand, and 15–20 mm ($(33–45)\times d_{50}$) at the very rough wall with dense Karlsruhe sand. The thickness of the shear zone with coarse Karlsruhe sand (d_{50} = 1.0 mm) was 10 mm ($10\times d_{50}$) at the smooth wall, 25

mm ($25\times d_{50}$) at the very rough wall with initially loose sand, and 22–25 mm ($(22–25)\times d_{50}$) at the very rough wall with initially dense sand (Tejchman, 2008).

1.4.1.5 Influencing factors for the formation of shear band

Initial void ratio (initial density), confining pressure, particle size, boundary conditions, and the like have been proven to influence shear band inclination and thickness. Moreover, it is worth noting that different factors' sensitivity on shear band inclination or thickness may be different for different cases. Experimental observation by Alshibli (1995) indicated that shear band inclination angle increases with confining pressure for F-sand, whereas it decreases for C-sand. For the M-sand, shear band inclination decreases with confining pressure for dense specimens but increases for loose specimens. In his study, for all sands, shear band inclination angles were larger for dense specimens than for loose specimens (Alshibli and Sture, 2000). Based on the experimental results reported by Desrues (1984), shear band inclination decreased with increasing confining pressure, and shear band thickness decreased as confining pressure and initial density increased. The results also showed that specimen boundary conditions and slenderness significantly influenced shear band patterns, including even parallel and crossing shear zones. The strain localization reflection at rigid boundaries was a typical mode of propagation in short specimens. Shear bands were steeper in dense specimens than in loose ones. By reducing the specimen's size or slenderness, the onset of strain localization was retarded, and the inclination of the shear band was reduced and its thickness increased. What's more, onset of shear localization occurred slightly before the peak stress ratio. Inclination was not affected by the mean grain size and non-uniformity of sand grading. The results also demonstrated that the imperfection dictated the location of the shear strain localization and acted as a trigger for the onset of shear strain localization. Yoshida et al. (1994) found that the shear band thickness decreased with the increasing confining pressure. The shear band inclination relative to the horizontal direction decreased with increasing particle size. The plane strain compression tests conducted by Pradhan (1997) indicated that shear band thickness depended on confining pressure and mean grain size. The thickness decreased with increasing confining pressure and decreasing particle size. In turn, the shear zone inclination depended on confining pressure, anisotropy, and

mean grain size. The inclination to the horizontal plane decreased as mean grain diameter and pressure level increased.

In addition to widely accepted main factors such as initial void ratio, confining pressure, and particle size, some researchers (e.g. Rowe, Vardoulakis, Gudehus, Alshibli, and Alsakeh) believe that particles' surface roughness and shape also significantly affect shear band forms. Experimental tests conducted by Rowe (1962)found that shear strength and dilatancy depended on the surface friction and particle packed ways which supported strain localization's being affected by particle shape and surface roughness. Vardoulakis and Sulem (1995) argued that surface roughness would affect inter-particle slipping in granular materials. Alshibli and Sture (2000) found that shear band inclination decreased as grain size and angularity increased. Gudehus and Nübel (2004) found that grain angularity affected, to a certain extent, grains' rotational resistance, which in turn affected the onset and development of shear band. Based on the experimental and numerical study conducted by Alsakeh (2004), it was obvious that surface roughness significantly affects the behavior of granular materials, which in turn affects shear band thickness, and that shear band thickness increases slightly with the surface roughness of the particles. Two indices, I_R and I_{SPH}, are used to define sphericity and roughness of the particle, with the higher these two indices the larger the dilation, which then leads to a thicker localization zone (Alsaleh, 2004).

The foregoing experimental observations were mainly concentrated on a global scale. Nowadays, however, with the appearance and development of precise nondestructive detective devices, shear band observations have become possible on the micro scale, and the kinematic performance of grains in the shear band has also become increasingly clear. Grain rotations were observed by Kuhn (1999) within shear bands in the deforming of granular materials. Using an X-ray micro-tomography technique, Oda et al. (1982, 1997, 1998) thoroughly investigated the phenomenon of strain localization in granular materials and found that grain rotation significantly affected media dilatancy. Consequently, microrotations, a prominent cause of failure, must be taken into consideration with their couple stress. What's more, columns of aligned grains were also observed inside the shear band (Oda et al., 1982; Oda et al., 1997; Oda & Kazama, 1998; Oda, 1999; Takemura et al., 2004). Recently, the results obtained from advanced discrete C-DIC in 3S-R confirmed once again the significance of grain rotations for strain localization. A clear

correspondence can thus be established between the zones of a specimen experiencing localization of continuum shear strain and the zones where grain rotations are more intense. A deeper analysis of the kinematics of particles in the shear band at grain scale and of their evolution is now possible. In constitutive modeling, one must understand the physical performance of materials from the micro scale to the continuum scale. Accordingly, the rotations of grains are important and should be taken into consideration regardless of the type of model or the solving technique.

1.4.2 Constitutive models and theories

Many researchers have studied strain localization in metal, composites, and geomaterials since the early 1900s, including by proposing constitutive models based on experimental data and phenomena. At first, scientists could only predict the failure condition of small scale models using rather rough mathematical equations. At that time, Coulomb's equation for the shear strength was used to describe the shear failure of soil, but then Otto Mohr introduced the Mohr–Coulomb equation based on Coulomb's theory (Labuz and Zang, 2012). Even this, however, was too simple to accurately predict failure, being unable to reasonably describe the mechanical behavior of granular materials. Since then, more and more advanced constitutive models have been proposed to study instability and strain localization based on plasticity theory while at the same time considering bifurcation theory, non–coaxial theory, and so forth.

Shear band formation is an example of a material instability, corresponding to an abrupt loss of deformation homogeneity in a solid sample that has been subjected to a loading path compatible with continued uniform deformation. In this sense, it may be interpreted as a deformation mechanism "alternative" to a trivial one and thus as a bifurcation or loss of uniqueness of a "perfect" equilibrium path. This bifurcation is distinctive for occurring even in an infinite body or under the extreme constraint of smooth contact with a rigid constraint. When localization begins, deformations migrate from a continuous mode to both continuous and discontinuous modes, and the continuum splits into localized and continua regions. Based on triaxial tests, Sulem and Vardoulakis (1990) argued that the bifurcation might occur during the hardening regime but not just in the post–bifurcation regime, a prediction that has been widely verified by later researchers. They grouped two modes of bifurcation: localized and diffuse. These bifurcation modes provide sufficient information about failure progress

in materials. It was argued that diffuse mode might occur in the pre-peak regime, whereas localization mode had more chances to occur in the post–peak regime. The bifurcation theory was also used to explain and trace the strain localization phenomena that occurred in the post–failure regime. These work can be found in Cheng (1971), Vardoulakis and Sulem (1979, 1983, 1990, 1995), Saada (1999), Bauer (1999), Darve et al. (1987, 1995, 2000, 2004), Nova et al. (1994, 2003), Nicot et al. (2007, 2009, 2011, 2017) and Daouadji et al. (2009, 2012), among others.

Strain softening is known to be a significant accompanying characteristic even though it is not a necessary factor of strain localization. Many constitutive models that contain softening behaviors have been proposed to describe the stress–strain behavior of materials or to study strain localization phenomena. Later on, researchers have increasingly found that the non–associated flow rule was more reasonable and widely used in describing stress–strain behavior, which can also result in structural instability. According to Rudnicki and Rice (1975), strain localization might occur even in strain hardening models when non–associated flow rules have been adopted. Li et al. (2002) also proposed a critical state condition of losing stability for dynamic analysis of saturated porous media with non–associated flow rule. In other words, even without softening behavior, but only if the tangent modulus matrix becomes asymmetric, materials will become unstable, and shear strain localization phenomena will occur in the specimen or structure. Many researchers have found that when shear strain localization occurs, the direction of the principal stress no longer coincides with that of principal strain. Moreover, the inherent anisotropy of the majority of materials is believed to be the main characteristic, which is also a trigger to the strain localization. In this sense, the proposition of non-coaxial constitutive models, being able to describe the principal stress rotation and anisotropy, is of great significance. Accordingly, some researchers have proposed the non–coaxial theory, which can be related to local deformation and instability. For example, Rudnicki and Rice (1975) added non–coaxial terms into the classical Drucker–Prager model with a view of analyzing strain localization problems. Papamichos and Vardoulakis (1995) argued that the inadequacy of the ordinary flow and deformation theories of plasticity for explaining experimental results having to do with shear band formation led to the development of a consistent non–coaxial plasticity theory. Moreover, using non–coaxial theory, theoretical predictions for shear band orientation and its onset has been shown to agree well with experimental observations of biaxial tests.

Yatomi (1989) systematically extended the well-known Cam-Clay model developed for small strains to use in the model for finite strains, and then incorporated a non–coaxial term in the model to examine the effects of the non–coaxial term on shear band formation. Zhao (2000) analyzed the influence of the non–axial flow rule on shear band formation and proposed the modified method of considering the non–coaxial terms. Qian (2006) compared numerical predictions and experimental data. All results of the analysis indicated that a non–coaxial plastic flow theory needs to be incorporated into the classical constitutive model so as to describe the bifurcation, which would be able to correctly predict the state of bifurcation. Huang et al. (2009, 2017) accurately predicted the strain localization of sand sample using a non–coaxial elastoplastic model.

1.4.3 Numerical analysis

Based on the strain localization phenomena of geotechnical structures and the laboratory samples, several analytical and numerical methods have been adopted to study and describe these failure modes. The rapid progression of computing science technology has greatly increased the efficiency and precision of calculations in geotechnical engineering. To achieve more accurate solutions, numerical simulation methods (e.g., the finite element method, the discrete element method) have seen wide introduction in geotechnical engineering. The development of numerical algorithms and other computer-based numerical schemes has reached a stage at which solutions for many different geotechnical problems are obtainable. Moreover, thanks to the significant progress in numerical simulation techniques, shear band onset and propagation in relatively complex situations can be traced closely, albeit still at great computational cost.

1.4.3.1 Limit analysis

Based on laboratory tests, the numerical prediction of the failure of structures in geoengineering is always used, especially in practical engineering. For example, the conventional limit equilibrium method is a very useful stability analysis. Stability analysis using the limit equilibrium method was first performed by Hultin and Pettersson in 1916, as documented in 1955 (Janbu, 1959). A safety factor F_s should be estimated to judge the stability of slopes, as still widely used in geotechnical engineering nowadays (Michalowski, 1995). According to the model's tests results for a wall,

conducted systematically by Cambridge from 1962 to 1974, Leśniewska (2000) systematically studied shear band patterns, formations, and mechanism using the limit equilibrium method.

However, doing so requires so many assumptions that only very experienced engineers can make a reasonable prediction. In short, the limit equilibrium method is no more an accurate method than any others in analyzing structural failure (Vardoulakis et al., 1978).

1.4.3.2 DEM based analysis

Granular materials are of great importance in civil engineering or in manufacturing processes whether they are granular soils in nature or raw materials for industries. Because of their discrete nature, the behavior of such materials is complex and it is not trivial to carry out their modelling. DEM (discrete element method) (Cundall and Strack, 1979; O'Sullivan, 2011) is a very powerful numerical tool to simulate the granular materials with the significance of physics. The DEM modeling involves specifying the equations of motion for a system of discrete bodies, and solving the resulting equations. The mechanical response of granular materials in DEM is governed by the contacts between particles and also between particles and boundaries. Therefore, the physical quantities in microscale, such as particle rotations, contact orientations, contact forces, etc., can easily be measured. If the micro-mechanism of materials is of great interests to be focused on, DEM is undoubtedly a good choice.

The realistic description and accurate solution of DEM have attracted a lot of attentions for both academic research and application in civil engineering. The materials in local zones must undergo a collapse before a global failure of the structures, and the microstructure of granular materials affects a lot the macro behavior. Numerous researchers have contributed to study the strain localization phenomena in a microscale level with DEM. Bardet and Proubet (1991) investigated the structure of the persistent shear bands by DEM, linking the particle rotations with the shear band formation in granular materials. By means of DEM, Wang et al. (2007, 2010) analyzed the shear band in a direct shear test, including the onset, evolution, shape, etc. Shear band simulations with DEM were intensively investigated by Jiang et al. (2006, 2010, 2011, 2012, 2013a, 2013b, 2013, 2015) from biaxial tests to geostructures. Nearly all the factors, such as confining pressure, initial void ratio, grain rotations, rolling resistance at particle contact, affecting the formation of shear band were

analyzed. Lin and Wu (2016) simulated the biaxial test and the simple shear test with DEM, it was found that high rotations occurred inside the shear band or in the corners, and left the rotations of the grains outside shear band almost zero as shown in Figure 1-10. Almost all the above researchers highlighted the importance of particle rotations to the shear band development, which is consistent with the experimental observations.

However, the numbers of contacts between particles are limited by computational power, preventing the use of the discrete element method for modeling a real scale structure (e.g., a dam, slope, tunnel, foundation) containing very huge numbers of particles.

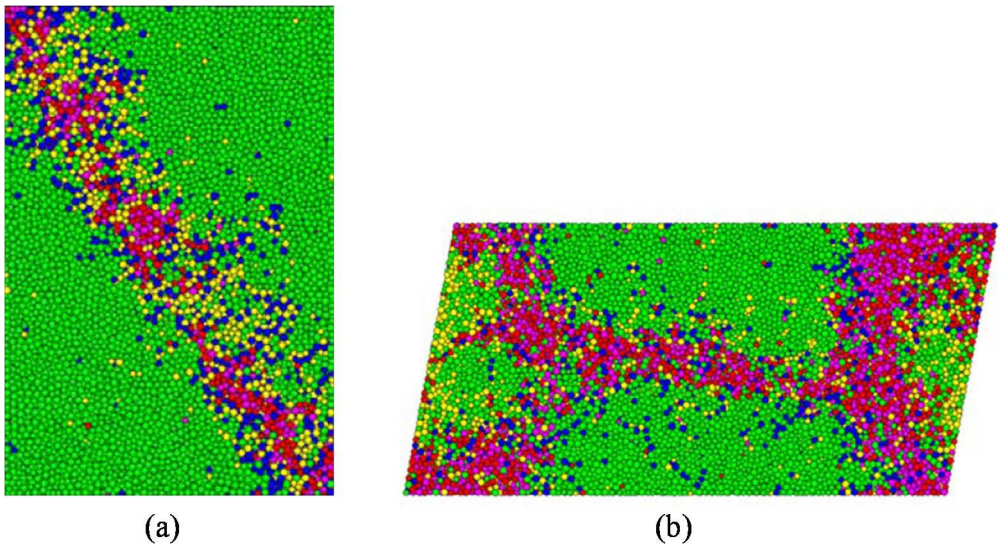

Figure 1-10 DEM simulations of shear band in: (a) biaxial test; (b) simple shear test

1.4.3.3 Finite element analysis

Compared to DEM, the finite element method is more efficient and less expensive when modeling large scale geostructures, which should be divided simply by fine or coarse mesh. Regions of particular interest should feature more elements, being finely divided so as to obtain more accurate solutions.

The finite element method offers an effective way to solve partial differential equations containing the mechanics and thermal unknowns. The standard procedure is displayed in Figure 1-11. First, structures (even those having very complex geometry) are discretized into smaller elements, creating a mesh during the preprocessing stage. During this stage, material properties are also assigned for all integration points (Gauss points) of each element. At the same time, all boundary

constraints, the initial stress state, and external loading are also set. Second, fundamental unknowns such as displacement, reaction forces, stresses, and strains, as well as state variables, will be solved during the solving–processing stage. This always features two main solvers: the explicit solver and the implicit solver. The latter is used chiefly to calculate static problems and the former chiefly to calculate dynamic problems. The third stage is that of post–processing, during which all solutions can be visualized and output. The whole progressive failure process can be dynamically reproduced and traced. In the present study, the finite element method will be adopted to simulate strain localization phenomena.

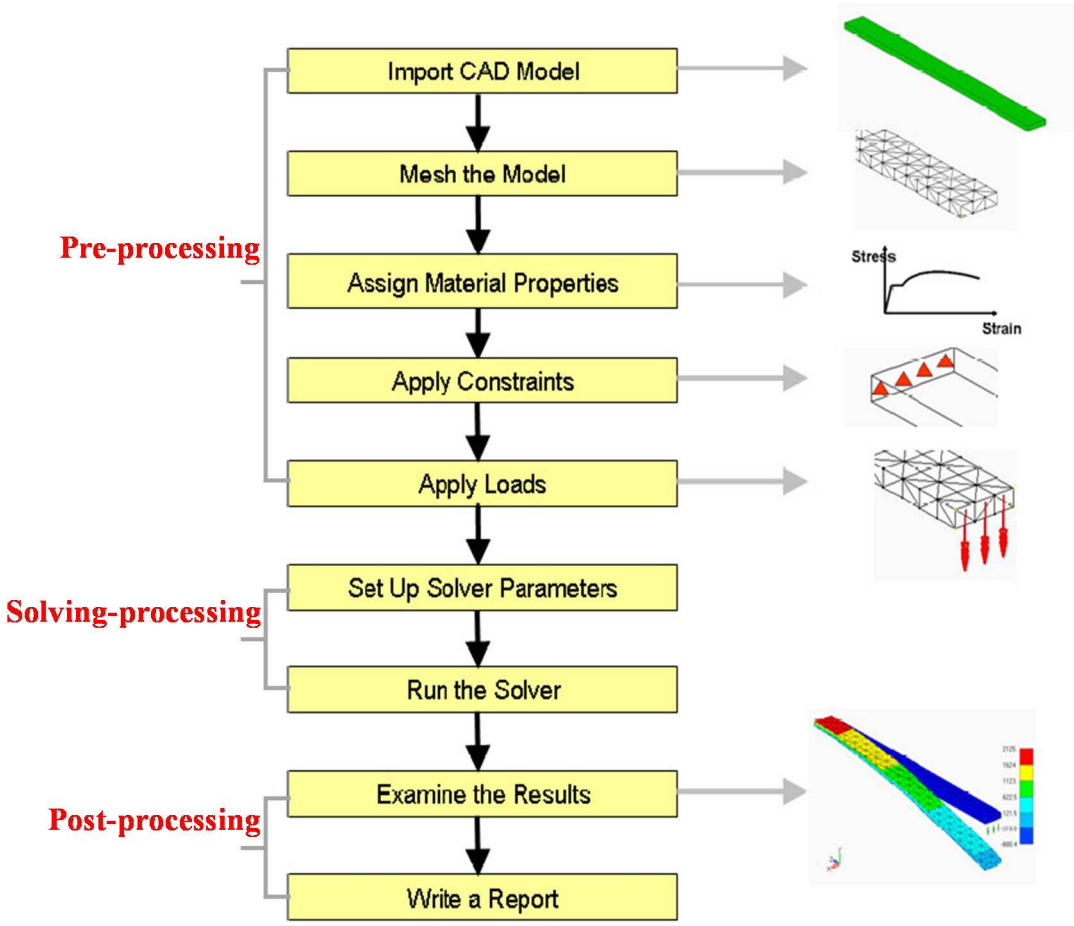

Figure 1-11 Standard procedure of Finite Element Analysis

Up to now, various finite element implemented constitutive models have widely been used to simulate the failure of specimens or geotechnical structures. In order to get more accurate solutions, two-scale approach has recently been adopted to investigate the strain localization of granular structures by combining the advantages of DEM and FEM (Nitka et al., 2009a; Nitka et al., 2009b;

Nitka et al., 2011; Guo and Zhao, 2014; Desrues et al., 2015; Guo and Zhao, 2015, 2016; Shahin et al., 2016). FEM is used to describe the global mechanical responses and DEM mainly aims at the local mechanics of granular materials. Therefore, the shear band in granular materials can be accurately and effectively predicted.

However, it should be worth noting that most FE implemented models are based on the conventional continuum mechanics. In this sense, when bifurcation occurs, the partial differential governing equations will change their properties, resulting in pathological solutions and the solutions seriously depending on the mesh sizes (the detailed derivations of the numerical pathological solutions of static and dynamic problems and a mesh dependency example can be referred in the Appendix at the end of the manuscript). That is to say, shear band thickness can vary from wide to narrow when the element mesh is divided from coarse to fine. The fundamentals behind the mesh dependency problems are due to the lack of internal scale in the constitutive models to reflect the microscale structure. Therefore, the introduction of non–localized regularization approaches, aiming at dealing with mesh dependency problems into FEM is of great significance, which will be introduced in detail in the following section.

1.4.4 Non–localized regularization approaches

Nowadays, more and more constitutive models (Jefferies, 1993; Wu & Bauer, 1993; Wu et al., 1996; Gajo & Wood, 1999; Yao et al., 2004, 2008; Yin et al., 2010a, 2010b, 2014) have been proposed to describe the behavior of granular soils. However, these models all fall within the framework of classical continuum theory. Numerical and analytical solutions for strain localization under classical continuum mechanics are known to suffer from serious mesh dependency. The pathological solutions are caused by the loss of ellipticity when using governing field equations for static problems and hyperbolicity for dynamic problems. Accordingly, non–localized methods are needed to rectify this problem. Any technique that can remove or reduce the spurious mesh dependency observed during the simulation of strain localization phenomena is called a regularization technique. In most cases, regularization techniques alleviate mesh dependency problems when simulating strain localization phenomena by incorporating at least one implicit or explicit intrinsic parameter with length scale. The length scales incorporated in the models, usually characterizing the microstructures of material,

manage to define the width of the strain-localized regions. The main regularization methods include viscosity approach, nonlocal theory, gradient theory, and micropolar theory. However, as main regularization techniques, the advantages and disadvantages of these regularization approaches are rarely symmetrically summarized and compared. Accordingly, a comprehensive review of these regularization approaches is necessary for a deep understanding of the differences between these approaches and for the selection of the appropriate regularization method in different cases.

1.4.4.1 Viscosity regularization

Soils and granular materials have important rate-dependent behaviors that are a function of their viscosity. For example, strain rate within the shear band exceeds that outside it; when the difference is obvious enough, shear bands will form. Viscosity regularization relies on high deformation rates in the localized region being reduced and distributed in the finite element mesh by means of the viscosity. Needleman (1988) argued that even without clear internal parameters for the dimension of length in the classical viscoplastic model, rate-dependent constitutive models implicitly introduce a length scale into the governing equations, at which the incremental equilibrium equations for quasistatic problems remain elliptic and wave speeds for dynamic problems remain real, even in the presence of strain softening. The pathological mesh sensitivity associated with numerical solutions of localization problems for rate-independent solids is eliminated. In this way, introducing the viscosity into the elastoplastic model with strain softening behavior is able, in some degree, to reduce the mesh dependency of finite element solutions. It is thus not surprising that the fluid in saturated media should greatly affect the degree of mesh sensitivity.

Viscoplasticity is a theory in continuum mechanics that describes the rate-dependent inelastic behaviour of solids. The elastic response of viscoplastic materials can be represented in one-dimension by Hookean spring elements. Rate-dependence can be represented by nonlinear dashpot elements in a manner similar to viscoelasticity. Plasticity can be accounted for by adding sliding frictional elements as shown in Figure 1-12.

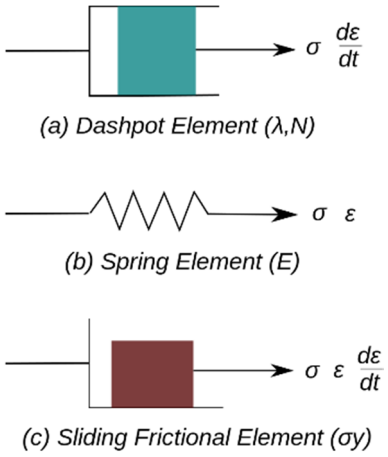

Figure 1-12 One-dimensional viscoplastic model for example

Viscoplasticity is usually modelled in three-dimensions using overstress theory of Perzyna (1963, 1966) or Duvaut and Lions (1972). In these models, the stress is allowed to increase beyond the rate-independent yield surface upon application of a load and then allowed to relax back to the yield surface over time. The yield surface is usually assumed to be rate-independent in such models. Rate-dependence was initially introduced to describe mesh sensitivity for localization problems in metal, as by Needleman (1988), Shawki and Clifton (1989), and Wu and Freund (1984). Later, it was applied to deal with the instability and localization phenomena of saturated porous media (Loret and Prevost, 1991), of concrete and rock fracture (Sluys and de Borst, 1991; Sluys, 1992; Sluys and de Borst, 1992), and of dilatant materials and clay (Higo, 2004; Karstunen and Yin, 2010; Oka et al., 1994, 1995, 2002; Yin and Hicher, 2008; Yin and Karstunen, 2011; Yin et al., 2010a, 2010b, 2011, 2015a, 2015b, 2017, 2018). Building on the work of Sluys and de Borst (1991, 1992), Wang et al. (1997) introduced a consistency viscoplastic model in which the viscosity is implemented by means of a rate-dependent yield surface. It has been proven to have a faster global convergence than the overstress viscoplastic models ((Perzyna, 1963, 1966) and (Duvaut and Lions, 1972)). Based on viscoplastic models proposed by Perzyna and Duvaut-Lions, Dias (2004) also proposed a simple model for viscous regularization of elastoplastic constitutive laws with softening. This model, when tested in a problem with slip-driven softening (von Mises material) as well as in a problem with decohesion-driven softening (Cam-Clay model), exhibited its capability to regularize the solution.

With the regularization of viscosity, mesh dependency problems have been significantly alleviated, allowing shear band thickness to be predicted and specified. For example, in Eq. (1.6) the

strain rate distribution along a one-dimensional element was implicitly expressed by the internal length scale l in the consistency model proposed by Wang et al. (1997),

$$e^{-\frac{3Gl}{2c_g m}}\left[1+\frac{4h+3G}{4c_g m}l\right]\approx\beta \tag{1.6}$$

where β is a small constant that represents the cutoff value of the relative strain rate at the edge of the shear band, G is the shear modulus and $c_g=\sqrt{G/\rho}$ is the elastic shear wave speed, m is the viscosity parameter, and h is the strain softening parameter. Wang et al. (1997) found that the smaller value of the internal length scale l and the imperfection size w determined the shear band thickness ($L = min[l, w]$). In their numerical examples, they observed that on mesh refinement, the shear band thickness converged to the material length scale l as defined in Eq. (1.6). Clearly, the thickness of shear band will decrease when the viscosity m decreases or when the absolute value of the softening parameter $|h|$ increases (h is a negative value). If the imperfection size w was taken into consideration, it was observed that the imperfection size dominated the shear band thickness when it was smaller than the material length scale ($w < l$). In contrast, if the imperfection size exceeded the material length scale, the influence of the imperfection would disappear, and the material length scale determined the shear band thickness.

The main advantage of viscosity regularization is that it does not need any additional global discretization, because it requires only supplementary operations at the local level in constitutive models, whose implementation in common nonlinear finite element packages is very simple. Furthermore, it works equally well for both the decohesion failure mechanism and the slip-driven softening failure mechanism. Its main disadvantage is the need to add an artificial feature of "viscosity" to describe the material behavior when it does not exhibit rate dependence, that its applicability is obviously limited to transient loading conditions, and that the regularizing effect rapidly decreases for slow loading rates or when approaching the rate-independent limit.

1.4.4.2 Nonlocal theory

Modern nonlocal elastic constitutive models of the integral type—that is, using weighted spatial averages—first saw use in the 1960s, motivated by homogenization of the atomic theory of Bravais lattices. By means of nonlocal approaches, researchers managed to describe the damage and

dislocation phenomena in crystals on a scale comparable to the range of interatomic forces. They found that nonlocal models could approximately reproduce the dispersion of short elastic waves and enhance descriptions of interactions between crystal defects such as voids, interstitial atoms, and dislocations (Eringen, 1966, 1972a, 1972b, 1976; Eringen and Edelen, 1972; Kroner, 2012; Kunin, 1966) . Several years later, plastic nonlocal models were first proposed as a way of describing the stress field at a fracture front (Ari and Eringen, 1980; Eringen, 1981, 1983). However, Eringen's formulation did not mean to serve as a localization limiter, and the averaging operator was applied to the total strain tensor, which could lead to spurious instabilities. Later, nonlocal plasticity theory was improved and initially introduced to describe strain localization phenomena of softening materials by Bažant and Lin (1988). After these initial developments, a comprehensive number of relevant contributions rapidly emerged (Perrin and Devaux, 1994; Strömberg and Ristinmaa, 1996; Nilsson, 1997; Jirásek, 1998; Needleman and Tvergaard, 1998; Nilsson, 1998; Fuschi and Polizzotto, 1999; Borino and Failla, 2000; Jackiewicz, 2000; Benvenuti and Tralli, 2003; Engelen et al., 2003; Jackiewicz and Kuna, 2003; Jirásek and Rolshoven, 2003; Rolshoven, 2003; Bobinski and Tejchman, 2004; De Angelis, 2007; Andrade, 2013). Nonlocal regularization has been proven to reduce mesh sensitivity when simulating the damage behavior of ductile materials with microdefects and strain localization phenomena caused by strain softening.

The derivation of any nonlocal theory starts from the choice of the variable to be enhanced by nonlocality. Typical choices are, among others, the regularization of variables related to kinematics (such as the strain tensor), regularization of internal state variables (such as scalar measurements of the amount of plastic strain or damage) or regularization of thermodynamic forces power-conjugated with internal state variables (for instance, the elastic energy release rate in damage models). Faced with this wide range of possibilities, deciding which option is more effective is difficult. Indeed, the choice of the nonlocal variable depends on the kind of material to be modeled, as well as on the nature of the problem to be solved. In the particular case of elastoplastic damaging ductile solids, internal degradation, which is closely related to the localization phenomena, is usually chosen as an internal non-localized variable. After the nonlocal variable is chosen, its nonlocal counterpart can be expressed, in an integral-type formulation, by means of the spatially weighted averaging integral. For

example, the spatial average of the magnitude of the plastic strain ε^p at location **x** has been suggested by Bazant et Lin (1988), as shown in Figure 1-13,

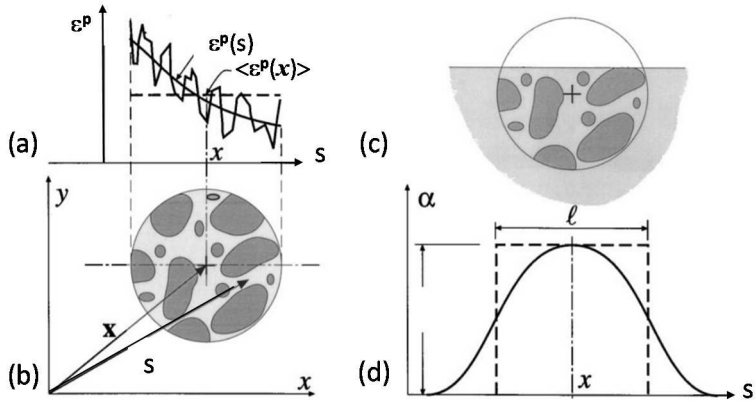

Figure 1-13 Spatial average: (a) profiles of micro strain and average strain along a segment with point x in the centre of a representative volume; (b) sketch of the representative volume with the centre point x; (c) the representative volume near the surface of the body; (d) the weighting function for non-local averaging integral and its relation to the internal length scale *l*

and the formulations are presented as follows,

$$\left\langle \varepsilon^p(\mathbf{x}) \right\rangle = \frac{1}{V_r(\mathbf{x})} \int_V \alpha(\mathbf{s}-\mathbf{x}) \varepsilon^p(\mathbf{s}) dV = \int_V \alpha'(\mathbf{x},\mathbf{s}) \varepsilon^p(\mathbf{s}) dV \tag{1.7}$$

in which

$$V_r(\mathbf{x}) = \int_V \alpha(\mathbf{s}-\mathbf{x}) dV \tag{1.8}$$

$$\alpha'(\mathbf{x},\mathbf{s}) = \alpha(\mathbf{s}-\mathbf{x}) / V_r(\mathbf{x}) \tag{1.9}$$

The brackets $\langle\ \rangle$ denote the averaging operator, with ε^p and $\left\langle \varepsilon^p \right\rangle$, the local and nonlocal internal variables, respectively. V is a finite volume of the body that is dictated by one constitutive parameter, generally called intrinsic length l with a dimension of length. V_r has approximately but not exactly the same meaning as the representative volume in the statistical theory of heterogeneous materials. $\alpha(\mathbf{x})$ is the weighting function that defines the averaging and **s** the general coordinated vector. Because numerical computations show much better convergence if the weighting function is smooth, the error density function (normal distribution function) has been suggested as the suitable form of the weighting function (Bažant and Lin, 1988),

$$\alpha(\mathbf{x}) = e^{-\left(k|(\mathbf{x})|/l\right)^2} \tag{1.10}$$

in which, for one, two, and three dimensions

$$1\mathrm{D}: \quad |\mathbf{x}|^2 = x^2, \qquad k = \sqrt{\pi} \tag{1.11}$$

$$2\mathrm{D}: \quad |\mathbf{x}|^2 = x^2 + y^2, \qquad k = 2 \tag{1.12}$$

$$3\mathrm{D}: \quad |\mathbf{x}|^2 = x^2 + y^2 + z^2, \qquad k = \left(6\sqrt{\pi}\right)^{1/3} \tag{1.13}$$

l is the characteristic length, a material property that defines the diameter of the representative volume (a line segment, circle, or sphere), and is determined pursuant to the condition that the representative volume have the same volume as the normal distribution function extending to infinity (x, y, z are the Cartesian coordinates). For numerical finite element computations, only those elements whose integration points are distributed in the domain of $2l$ around $\mathbf{x}$ need to be included in the sum using the Gauss integration method. For those elements outside the domain, the error density function α is negligible. As for the strain localization problems caused by softening, the nonlocal average should simply be applied to those variables controlling strain softening.

Nonlocal approaches work well for both types of failure mechanisms (mode I: decohesion; mode II: slip). For total stress–strain relations (without decomposition into elastic and plastic parts) the nonlocal approach is computationally more efficient than the gradient models discussed in the next section. An example is the elasticity-based nonlocal damage model proposed by Pijaudier-Cabot and Bažant (1987). A definite disadvantage of current nonlocal formulations is that they are at odds with existing numerical strategies (Simo et al., 1989). Gradient models, for their part, are much more amenable to an efficient numerical implementation by preserving their favorable property of containing an internal length scale (de Borst and Mühlhaus, 1991). Another disadvantage is the consistency condition resulting in an integral-differential equation instead of an algebraic equation that can be solved locally.

1.4.4.3 High-order gradient (grade-n) theory

Generally speaking, gradient models and nonlocal models belong to a common theoretical category, with the gradient model a particular nonlocal model. Gradient models can be derived from nonlocal models by expanding the kernel of the integral employed in the averaging procedure for the inelastic strains. The gradient theory has been widely used as a very effective tool for regularizing finite

element solutions so as to study strain localization phenomena in geotechnical engineering. Gradient dependence was first used within the theory of rigid plastic material to analyze persistent slip bands (Aifantis, 1984, 1987) and shear bands (Coleman and Hodgdon, 1985) in metals. Vardoulakis and Aifantis (1989, 1991) used the second-order gradient theory in studying the heterogeneous deformation in granular media. They modified the flow theory and the yield function by incorporating a high-order gradient, and use of an appropriate length scale allowed them to capture the shear band thickness. For more detailed formulations and to gain a better understanding of its application, the paper of Vardoulakis and Sulem (1995) should be referenced by interested readers. Ever since, many other researchers have also contributed greatly to this area. Chambon et al. (2001) proposed a local and Cosserat second-order gradient theories model for dealing with localization phenomena. Chikazawa et al. (2001) used a gradient-dependent viscoplastic constitutive model to study the strain localization of water saturated soils and found strain localization to be highly dependent on strain gradient. Borja (2002) obtained a finite element solution for the shear banding evolution using the deformation gradient to map between stress tensors. Voyiadjis and Song (2002) used the gradient theory to capture strain localization of porous media by considering micro-interactions between grains. The thermoelastic Helmholtz free energy function was dependent on those internal variables and their second-order gradients. Voyiadjis and Dorgan (2003) used the second-order gradient theory in the kinematic hardening by introducing an internal length scale. Even so, the internal length has no clear physical meaning, being merely a mathematical method.

Now, with a view to explain the procedure of gradient continuum theory (second-order generally suffices), we revisit the gradient plasticity formulations proposed by de Borst et al. (1991, 1993, 1996), in which they restricted the yield function to second-order derivatives so that the yield function was also dependent on the Laplacian of a hardening parameter in addition to the hardening parameter itself (de Borst and Mühlhaus, 1991; de Borst et al., 1993; Pamin, 1994; de Borst and Pamin, 1996):

$$f(\boldsymbol{\sigma}, \gamma^p, \nabla^2\gamma^p) = 0 \tag{1.14}$$

Compared with nonlocal theory, a distinct advantage of gradient plasticity is that the consistency condition yields a partial differential equation instead of an integral differential equation,

$$\dot{f} = \mathbf{n}^{\mathrm{T}}\dot{\boldsymbol{\sigma}} - h\dot{\lambda} + g\nabla^2\dot{\lambda} = 0 \tag{1.15}$$

where $\mathbf{n}^{\mathrm{T}}$, h, and g are given by

$$\mathbf{n}^{\mathrm{T}} = \frac{\partial f}{\partial \boldsymbol{\sigma}} \tag{1.16}$$

$$h = -\frac{\dot{\gamma}^p}{\dot{\lambda}} \frac{\partial f}{\partial \gamma^p} \tag{1.17}$$

$$g = \frac{\dot{\gamma}^p}{\dot{\lambda}} \frac{\partial f}{\partial \nabla^2 \gamma^p} \tag{1.18}$$

in which g is a positive gradient influence coefficient with the dimension of force (Pamin, 1994). For $g = 0$, the classical plastic flow theory is retrieved. The enhanced gradient theory aims at preserving the well-posedness of the governing equations for materials that do not comply with the material stability requirement. When a softening relation between stresses and strains ($h < 0$) is assumed or when non–associated plastic flow is postulated as reproducing an experimental response of soil, the tangential stiffness matrix $\mathbf{D}^{ep}$ becomes non–symmetric, leading to an inclination of instability. For strain softening materials ($h < 0$), the gradient term seen in Eq. (1.18) can act as a stabilizer and guarantee ellipticity of the governing partial differential equation Eq. (1.15) after the onset of plastic deformation. For example, in a one-dimensional problem (de Borst et al., 1993), the gradient influence coefficient g is expressed by a strain softening parameter and an internal length parameter l:

$$g = -hl^2 > 0 \tag{1.19}$$

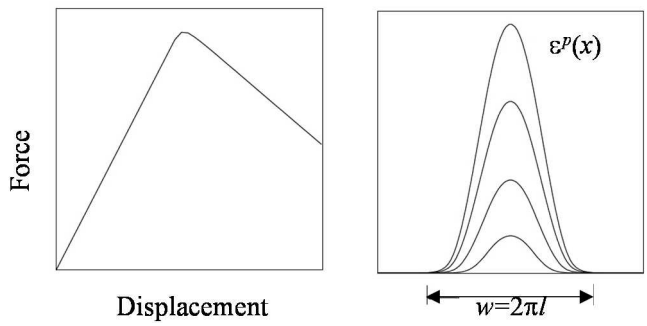

Figure 1-14 Typical evolution of plastic strain distribution in strain localization of softening materials

For strain hardening materials, the Laplacian term with $g > 0$ is also demonstrably able to smooth the solution. Similar observations can also be obtained for the general cases of three-dimensional continua (Mühlhaus and Alfantis, 1991; de Borst and Mühlhaus, 1992). The width of localized zones in strain localization problems, as measured by the evolution of plastic strain, has been estimated

analytically by a constant $w = 2\pi l$ in a one-dimensional localization problem (pure tension of a bar with length L) (de Borst and Mühlhaus, 1992; Pamin, 1994).

Gradient plasticity theory has proven to be highly versatile for describing localization of deformation in a continuum medium while also being computationally much more efficient. The regularization of the gradient approach is effective for both mode I (decohesion) and mode II (frictional slip) failures. A disadvantage of the approach is the introduction of an additional variable at the global level in addition to the conventional displacement degrees of freedom. Moreover, the parameter determination of is not an easy task. Importantly, the gradient terms disappear from the constitutive equations if a homogeneous state of strain and stress is analyzed, and although the gradient terms are negligible if strains vary slowly in the pre–peak regime of softening problems, they exert a significant influence in the presence of strain localization (in the post–peak regime). Because higher-order continuum models have no effect for homogeneous deformations, additional parameters of high-order continuum models cannot be measured directly from elementary tests such as uniaxial or triaxial tension or compression tests; rather, a semi-inverse method is required whereby the experimental results of different types of tests are fitted in the post–peak regime.

1.4.4.4 Micropolar theory

Micropolar theory is one of the most important regularization approaches, which has a more physical meaning than a wholly mathematical technique when compared with other regularization approaches (e.g. nonlocal and high-gradient). Many researchers (Mühlhaus and Vardoulakis, 1987; Mühlhaus, 1989; de Borst, 1991; de Borst and Sluys, 1991; de Borst, 1993; Tejchman and Wu, 1993, 1996; Tejchman et al., 1999; Pasternak and Mühlhaus, 2001; Huang and Bauer, 2003; Nübel and Huang, 2004; Huang et al., 2005; Li and Tang, 2005; Alshibli et al., 2006; Arslan and Sture, 2008b; Tang et al., 2013; Tang and Hu, 2017) have used micropolar theory as a regularization approach for analyzing strain localization problems, and it has proven to be effective enough to alleviate or even solve mesh dependency problems by preserving the ellipticity of the governing partial differential equations for boundary value problems.

Cosserat theory (micropolar theory) is a generalized classical continuum theory that includes couple stress. Couple stress theory (constrained Cosserat theory) considers the possibility of body

couples existing in the interior of the body and of surface couples existing on the surface of the body. According to Ristinmaa (1996), one of the oldest theories belonging to this class of models is the centennial couple stress theory originally proposed by Voigt (1887) and later developed by the Cosserat brothers (1909), who removed the connection between the rotational field and the displacement gradients. Because of its relative complexity, however, it received little attention. Investigations into Cosserat theory saw an uptick in the early 1960s with the work of, notably, Mindlin (1962) and Koiter (1969). Ever since then, Cosserat theory has also been called micropolar theory, a terminology in vogue at that time that has also been adopted in the present study. Interest in the applications of Cosserat theory began to increase in the mid-1970s when specialists in geotechnical engineering began to link Cosserat kinematics and strain localization phenomenon. Finite element calculations using micropolar theory with independent rotations began with Mülhaus (1989) and de Borst and Sluys (1991, 1991). After that, more and more micropolar constitutive models were implemented and adopted to analyze the shear localization problems of other microstructural problems by means of the finite element method.

In classical continuum mechanics, the Cauchy strain tensor can be decomposed into a symmetric part (the stretch tensor) and an antisymmetric part (the spin tensor) regardless of whether it is the Green–Lagrangian strain tensor or the Eulerian strain tensor. The classical spin tensor generally corresponds to the macro-rotation caused by differences in displacement gradients. However, in practical cases, the onset and evolution of shear bands is closely related to grain rotation as well as non-uniform displacements (global rotation) or translational deformations that have also been confirmed by experimental results (Desrues et al., 2007) . Unlike in classical continuum mechanics theory, which accounts for only macro-rotations, micropolar theory takes into account the independent micro-rotations of material points, as seen in Figure 1-15 (an element having four material points):

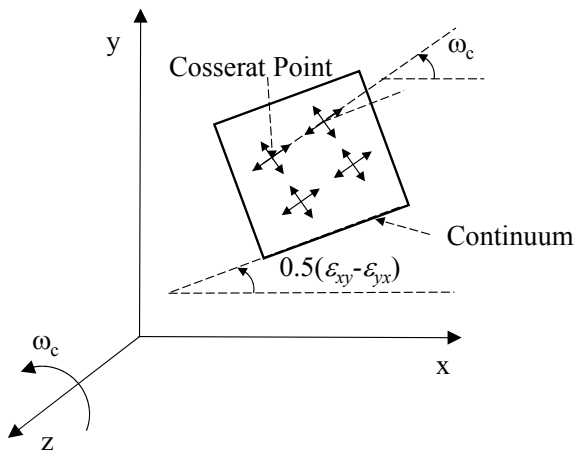

Figure 1-15 Separation between micro-rotation and macro-rotation in 2D space and their effect in the kinematics

Rotational degrees of freedoms are independent of the displacement field and are linked only at the constitutive level and by balance equations. From a material point of view, these rotations can be considered as the rotations of grains or aggregates. Accordingly, each grain or aggregate has additional rotational degrees of freedom beyond just translational degrees of freedom. Thus there are six degrees of freedom (three translational and three rotational) in three-dimensional problems and three (two translational and one rotational) in two-dimensional problems for each point:

$$\begin{aligned} &3\,\mathrm{D}: \quad \mathbf{u} = \left[u_x \; u_y \; u_z \; \omega_x \; \omega_y \; \omega_z \right] \\ &2\,\mathrm{D}: \quad \mathbf{u} = \left[u_x \; u_y \; \omega_z \right] \end{aligned} \tag{1.20}$$

where ω_x, ω_y, and ω_z are the micro-rotations in the x, y, and z directions. These micro-rotations will cause the micro-curvatures and the corresponding energy-conjugated couple stresses in the micro-element surfaces. Moreover, the normal stresses are no more homogeneous, for the theorem of conjugate shearing stress is no better satisfied. For 3D problems, the generalized stress and strain components in micropolar theory are augmented:

$$\boldsymbol{\sigma} = \left[\sigma_{xx} \; \sigma_{yy} \; \sigma_{zz} \; \sigma_{xy} \; \sigma_{yx} \; \sigma_{yz} \; \sigma_{zy} \; \sigma_{zx} \; \sigma_{xz} \; \frac{m_{xx}}{l_t} \; \frac{m_{yy}}{l_t} \; \frac{m_{zz}}{l_t} \; \frac{m_{xy}}{l_c} \; \frac{m_{xz}}{l_c} \; \frac{m_{yx}}{l_c} \; \frac{m_{yz}}{l_c} \; \frac{m_{zx}}{l_c} \; \frac{m_{zy}}{l_c} \right]^T \tag{1.21}$$

$$\boldsymbol{\varepsilon} = \left[\varepsilon_{xx} \; \varepsilon_{yy} \; \varepsilon_{zz} \; \varepsilon_{xy} \; \varepsilon_{yx} \; \varepsilon_{yz} \; \varepsilon_{zy} \; \varepsilon_{zx} \; \varepsilon_{xz} \; \kappa_{xx} l_t \; \kappa_{yy} l_t \; \kappa_{zz} l_t \; \kappa_{xy} l_c \; \kappa_{xz} l_c \; \kappa_{yx} l_c \; \kappa_{yz} l_c \; \kappa_{zx} l_c \; \kappa_{zy} l_c \right]^T \tag{1.22}$$

For 2D problems, the generalized stress and strain components are simplified:

$$\boldsymbol{\sigma} = \left[\sigma_{xx} \; \sigma_{yy} \; \sigma_{zz} \; \sigma_{xy} \; \sigma_{yx} \; m_{zx}/l_c \; m_{zy}/l_c \right]^T \tag{1.23}$$

$$\boldsymbol{\varepsilon} = \left[\varepsilon_{xx} \; \varepsilon_{yy} \; \varepsilon_{zz} \; \varepsilon_{xy} \; \varepsilon_{yx} \; \kappa_{zx} l_c \; \kappa_{zy} l_c \right]^T \tag{1.24}$$

where $\sigma_{xy} \neq \sigma_{yx}, \sigma_{xz} \neq \sigma_{zx}, \sigma_{zy} \neq \sigma_{yz}$, and m_{ij} are the coupled stress components (m_{ii} are the torsion ones and m_{ij} are the bending moments). κ_{ij} are the gradients of micro-rotations ω_j in direction i.

Of the two new added micro–length scale parameters l_c and l_t, l_c is the length scale parameter related to bending couple stress, and l_t is related to torsion couple stress. When the microstructure is considered, a typical strain localization problem such as the relation of shear band to microstructure can be reasonably predicted to give the thickness of the specified shear band. At the same time, the high-order terms guarantee the ellipticity of the governing partial differential equations, especially in the post-peak regime—and the mesh dependency problems have, obviously, been removed.

Micropolar theory can yield efficient and fully mesh-independent solutions for static problems as well as for dynamic problems. In analyzing the problems of the frictional slip failure mode (mode II failure type) involving a high localized shear band, the micropolar approach seems to be a particularly natural framework, being easily implemented and physically meaningful. However, a disadvantage of the micropolar continuum theory is that the rotational degrees of freedom are activated only under shear loading. Numerical results suggest that for failure problems in which decohesion plays a prevailing role (mode I failure type), the rotational degrees of freedom become inactive and the microcurvatures remain zero, as do the work-conjugated couple stresses. That is to say, when decohesion rather than frictional slip is the predominant failure mode, the regularization effect of micropolar theory is generally too weak to preserve the ellipticity of the boundary value problems. Instead, for tensile loadings in which decohesion is the main cause of structure failure, nonlocal models (Bažant et al., 1984) are very effective at keeping the boundary value problem elliptic. It is worth noting that strain localization in dry and saturated specimens has been studied experimentally by many researchers on loose sand as well as dense sand, demonstrating that strain localization is the dominant failure phenomenon. It is also the main failure mechanism for geostructures in reality. There is no doubt, then, that micropolar theory can be used to analyze strain localization problems in geomaterials. For anyone who is deeply interested in micropolar theory, the full formulations of micropolar theory can be found in the Appendix at the end of the manuscript.

1.4.4.5 Discussions of regularization methods

Inevitably, every regularization method has limitations, and in some cases in which a single regularization method does not work well, a regularization method combining at least two regularization approaches might be efficient. In general, the combination of viscosity with another regularization technique has seen wide adoption. For instance, Wang et al. (1997, 1998) proposed a model regularized by both rate dependency (viscoplasticity) and plastic gradient that was effective for both quasistatic and dynamic problems when dealing with mesh dependency problems. Moreover, interactions between these two methods in controlling shear band thickness have also been discussed. Oka et al. (2000, 2002) proposed a gradient-dependent elastoviscoplastic model for clay to study the strain localization problems and deformation mode. Based on a typical plastic constitutive model proposed by de Borst et al. (1997) that featured both rate and gradient dependence for strain localization analysis, Zhang et al. (2003, 2004) predicted the internal length scale of the combined model for general cases and illustrated the interactions between different length scale parameters for rate dependency models and gradient plastic models from a mathematical point of view using a one-dimensional example. Tang and Li (2007) proposed a coupled Biot-Cosserat model by combining both Biot's theory (rate-dependency) and Cosserat continuum theory with a view to simulate strain localization phenomena caused by strain softening in saturated porous media. Numerical results demonstrated the developed model's ability to maintain the well-posedness of boundary value problems while incorporating strain softening behavior, as well as the capacity to model strain localization phenomena in saturated media.

From the above descriptions of the four main regularization techniques, it can be seen that the domain of the strain localized region is closely related to the internal length scale, however, the meanings of different length scales and their relations to the thickness of shear band are not identical. For viscoplastic model, take the consistency model proposed by Wang et al. (1997), the shear modulus, shear wave speed, viscosity parameter as well as the softening parameter, etc. are believed to decide the thickness of shear band, and these factors can be related to the cut off value of the strain rate at the edge of the shear band by an implicit parameter with length scale. What's more, under the approximate form of the relation, the implicit length scale is able to denote the thickness of shear band. For non-local theory, certain internal variables closely related to the strain localization are

averaged in a non-local finite volume to reach the regularization effectiveness, and the finite representative volume decided by the parameter with length scale is believed to be the damaged region and strain localized region. In this way, the size of the strain localized region is controlled by the internal length scale and the chosen weighting function. For gradient theory, a special case of the non-local theory, the gradient term can be denoted by the softening parameter and the internal length scale, then it can be thought to reflect the fact that below the certain size scale the interaction between the microstructural carriers of the deformation is non-local, resulting in the thickness of shear band decided by the internal length scale. For a micropolar model, the independent grains' rotations result in the couple stresses, therefore, in 2D problems the internal length scale is naturally regarded as the bending length between grains or aggregates for granular materials. Thus, the thickness of shear band can be predicted by the value of the internal length parameter as the relation between the grain size and the shear band thickness in experimental tests.

In conclusion, a single or combined regularization approach has always been adopted for reproducing strain localization phenomena in geotechnical engineering using finite element method. No matter which regularization method is adopted, at least one explicit or implicit internal length scale parameter must generally be incorporated into the constitutive model. In the research of various scientists, internal length scale parameters have also been hypothetically related to the microstructure, with random constants distributed within a certain range of the ratio of a structure's typical dimension, internal defection, or even interactions, indicating that the physical meanings of internal length scales values have not been obtained a common sense until now. Accordingly, further investigation of the physical meanings of all internal length scales in each regularization approach is still a matter of great urgency and significance. At last, the argument of Tejchman (1999) is favored in the present manuscript: " the micropolar approach is more suitable, from a physical sense, for the modeling of shear zones in granular materials than other models that seek to capture strain localization in a proper manner (e.g., the nonlocal, high-order gradient, and viscous models), because it takes into account grains' rotations and couple stresses during shearing (even though these remain negligible during homogeneous deformation)", which has been experimentally validated.

1.5 Application of micropolar theory in geotechnical engineering

1.5.1 Different polarized constitutive models and the applications

Since the Cosserat brothers proposed their own theory in 1909, Cosserat theory has been widely adopted as a way to explain and solve various phenomena and problems related to microstructures. It has performed professional efficiency to reflect the micro size effect and great capability to reproduce strain localization phenomena. In this part, the applications of the Cosserat theory (micropolar theory) are summarized in Table 1-1 with particular emphasis on geotechnical engineering.

Table 1-1 Summary of micropolar constitutive models and applications

Publications	Applications	Constitutive models
Cosserat elasticities (Mindlin, 1963, 1964; Sternberg and Muki, 1967; Cowin, 1969; Kulesh et al., 2006; Randow et al., 2006)	Studying various stress concentration problems including those around a hole, a crack tip, and near a concentrated force and dispersion of Rayleigh wave in wave propagation and the size effect in thin film	Cosserat continuum elasticity
Muhlhaus et al. (Mühlhaus and Vardoulakis, 1987; Mühlhaus, 1989; Pasternak and Mühlhaus, 2001)	Analyzing theoretically the thickness of shear band under plane strain condition; the influence of finite rotations of the blocks on the limit load was investigated	Simple Von-Mises elastoplastic model developed by Vardoulakis; continuum model for regular block structures
De Borst et al. (de Borst, 1990, 1991; de Borst and Sluys, 1991; de Borst, 1993)	Mesh independency: infinite long shear layer; plane strain biaxial tests	Von-Mises elastoplastic model; pressure dependent J_2 flow model
Ehlers et Volk (Ehlers et al., 1997; Ehlers and Volk, 1997a, b, 1998)	Shear band localization phenomena of footing acted on fluid-saturated elastoplastic porous solid materials and slope failure induced by an excavation process	Hookean elasticity model for elastic domain and the single surface plastic yield criterion by Ehlers (1993a,1995) for ideal inelastic domain
Adhikary et al. (Adhikary and Dyskin, 1997; Adhikary et al., 1999)	Providing an accurate prediction of the load-deflection behavior of layered materials: flexural toppling failures of foliated rock slopes; bulking problem in a stratified rock mass; critical Euler buckling load for a package of non-interacting layers	A model for layered geomaterials: state of slip (layer interface) is defined by a simple Coulomb slip model

Tejchman et al. (Tejchman and Wu, 1993; Tejchman and Bauer, 1996; Tejchman et al., 1999; Tejchman and Gudehus, 2001; Tejchman, 2002; Tejchman and Niemunis, 2006; Tejchman, 2008)	Capturing the shear band in plane strain compression tests; monotonic shearing of an infinite layer; stripe foundation; earth pressure; direct and simple shear; advanced applications including sandpiles, direct symmetric cyclic shearing under constant normal stiffness condition, wall boundary conditions, deterministic and statistical size effects, non-coaxiality and stress-dilatancy rule and textural anisotropy.	A polarized hypoplastic constitutive model; elastoplastic model proposed by Muhlhaus
Huang et al. (Huang et al., 2002; Huang and Bauer, 2003; Nübel and Huang, 2004; Huang et al., 2005; Huang et al., 2014; Huang and Xu, 2015)	Simulating plane coquette shear and biaxial tests; reproducing the strain localization in sand behind the retaining wall and under strip footing	A polarized hypoplastic constitutive model
Alsaleh et al. (Alsaleh, 2004; Voyiadjis et al., 2005; Alsaleh et al., 2006; Alshibli et al., 2006)	Reproduce the strain localization phenomena on F-75 silica sand, coarse silica sand and two sizes of glass beads compressed under plane strain conditions (biaxial tests)	The single hardening Lade's constitutive model proposed by Lade et Nelson
Li et al. (Li and Tang, 2005; TANG and LI, 2007; Tang and Li, 2008; Tang et al., 2013; Tang and Hu, 2017)	Predicting the shear band and proving the mesh independency capabilities in the plane strain and 3D conditions: shear layer with infinite length; uniaxial compression of a square panel; progressive failure of slope, footing, excavation and retaining wall. In 3D condition: studying the size effect by a micro cantilever beam and a micro rod (elastic)	2D and 3D Pressure dependent Drucker-Prager type elastoplastic model
Liu et al. (Liu et al., 2007)	Mesh independency: infinite long shear layer; strain localization in 3D specimen	3D two phase Desai hierarchical model
Arslan et al. (Arslan and Sture, 2008b, a)	Predicting the load behavior of a shallow footing and failure behavior of a slope as well as the size effect by footing tests	Drucker–Prager type elastoplastic model
Riahi et al. (Riahi and Curran, 2009; Riahi and Curran, 2010)	Predicting the deformation of layered structures: plate structures with various geometry (Cantilever, Rectangular, Circular) and boundary condition; excavation in layered rock	3D layered model based on plate theory
Manzari et al. (Manzari, 2004; Manzari and Dafalias, 2005; Manzari and Yonten, 2011)	Several examples of failure analysis, such as a deep excavation, shallow foundation, and a retaining wall, were presented showing the regularization abilities of micropolar technique in overcoming the numerical difficulties in boundary value problems	A critical state two-surface micropolar plasticity model for sands

As shown in Table 1-1, Cosserat theory demonstrates extensive applicability, being introduced first into elastic continuum materials and then into elastoplastic ones. In micropolar elastic materials, rather than mimicking classical continuum theory, it is able to reflect the micro size effect shown in experiment tests such as stress concentration problems, dispersion of Rayleigh wave-in-wave propagation, and the size effect in thin film. For elastoplastic materials, it is mainly used as a regularization technique to alleviate mesh sensitivity problems when modeling strain localization using finite element method, especially in the post-failure regime. To reproduce and study the strain localization phenomena in laboratory tests or of geostructures' failures in reality, where the material response is essentially inelastic, various elastoplastic micropolar models as well as hypoplastic micropolar models have been proposed and widely used as presented in the table above. Moreover, micropolar theory is also adopted to describe the strain localization phenomena in multiphase media. It is inevitable that the table cannot encompass all the micropolar constitutive models, but the majority of constitutive models being able to inspire readers have been listed.

1.5.2 Internal length scale and micropolar shear modulus

In elastic micropolar continuum approaches, analytical solutions that predict the size effect have been used to determine material constants in experiments. Huang et al. (2014) have illustrated the determination of micro–deformation-related parameters in inelastic micropolar theory. However, the determination of the additional parameters of micropolar constitutive models is still an open topic.

Two additional key parameters are incorporated into micropolar continuum models for 2D problems in static loading analysis: internal characteristic length scale l_c and micropolar shear modulus G_c. For the choice of G_c, it is widely accepted as proven that G_c can be set to about half the conventional shear modulus G (de Borst and Mühlhaus, 1991; de Borst and Sluys, 1991; de Borst, 1993; Arslan and Sture, 2008b, a; Tang and Li, 2008; Kondo, 2010). Taking into account that the micropolar shear modulus influences the final results only very slightly, such as in the thickness of shear bands and the load-bearing capacity in biaxial tests, emphasis is laid on the effect of the internal length scale l_c.

Indeed, l_c, reflecting the microstructure, significantly influences the effectiveness of regularization, as well as the final numerical results. The choice of the internal length scale is still an

open question and has been argued by de Borst (1993). In his article, he set l_c as a random value, but l_c depends on the shape and the size of the micro-element, as was also pointed out. Tang and Li (2008) proposed a range within which to consider l_c reasonably. In their opinion, the internal length scale l_c must be no less than $1/100H$, generally $1/100H < l_c < 1/10H$, where H is the concerned dimension of the structure (e.g., the height of a slope or width of a footing). Only in this condition the regularization role of the micropolar continuum model, as well as the accuracy of the attendant numerical results, can be guaranteed. In most cases, l_c is regarded as the mean grain size d_{50} (Tejchman et al., 1999; Alshibli et al., 2006; Arslan and Sture, 2008b). Alternatively, l_c can also be identified as an equivalent radius of assembly of grains (Papanastasiou and Vardoulakis, 1989) or as being proportional to the microstructure length – the mean grain diameter d_{50} (Huang and Xu, 2015).

It is questionable whether or not a fixed value of the material length scale is used to model strain localization phenomena through the whole process. With dilatancy and rearrangement of particles, a significant change in length scales is expected owing to the effect of the shape indices and the surface roughness of the particles. Accordingly, in contrast to the foregoing assumptions that l_c is a random value or merely related to microstructure length, some also believe that internal length scale is affected by surface roughness index, sphericity index, and the like.

Two simple formulations have been proposed to calculate the contact surface between two adjacent particles and the rotation arm length in the micropolar continuum model (Alsaleh, 2004; Voyiadjis et al., 2005),

$$\begin{cases} l_s = \dfrac{I_{SPH}}{I_R} d_{50} \\ l_a = \dfrac{I_R}{I_{SPH}} d_{50} + R_a \end{cases} \tag{1.25}$$

where l_s and l_a are the length of surface contact and arm of rotation, respectively. I_{SPH}, I_R, and R_a are sphericity index, roughness index, and mean surface roughness.

Rub and Voyiadjis (2004) suggested an evolving equation of the average internal length that starts with an initial value and then decreases exponentially as a function of the total accumulated effective plastic strain ξ,

$$l_{Ave} = l_0 e^{-k_0 \xi} \tag{1.26}$$

where k_0 is a constant and l_0 is the initial length scale, which can be defined as

$$l_0 = \frac{l_s + l_a}{2} = \frac{1}{2}\left[\frac{I_{SPH}}{I_R} d_{50} + \frac{I_R}{I_{SPH}} d_{50} + R_a\right] \tag{1.27}$$

Based on the formulation in the previous equation, two other length scale evolving formulations have been suggested by Liu et al. (2011). One assumes that the evolution of the internal length scale depends on both the deviatoric and the rotational effective plastic strain,

$$l_{Ave} = l_0 e^{-k_0(\xi_D + \xi_R)} \tag{1.28}$$

and others consider a coupling of the deviatoric and the rotational components,

$$l_{Ave} = \eta l_D + (1-\eta) l_R \tag{1.29}$$

where η is the ratio between the deviatoric strains and the total strains,

$$\eta = \frac{\xi_D}{\xi_D + \xi_R} \tag{1.30}$$

and

$$\begin{cases} l_D = l_0 e^{-k_0 \xi_D} \\ l_R = l_0 \left[1 - \left(\dfrac{\xi_R}{\delta + \xi_R}\right)^2\right] \end{cases} \tag{1.31}$$

in which k_0 and δ are parameters that control the evolution rate of the length scale components.

Then, Arslan and Sture (2008a) proposed a length scale equation intended to include the effects of micro-rotation, normal stress, and contact area,

$$l^2 = \frac{1}{G}\left(K\Delta\theta + \frac{2}{3}\sigma_N(\pi A^2)\tan\phi^c\right) \tag{1.32}$$

in which G and K are the conventional shear modulus and the rotational stiffness modulus, respectively. $\Delta\theta$ is the relative rotation at contact, A denotes the contact area, and σ_N is the normal stress.

Considering the crushing of grains within granular materials, an evolving formulation of the internal length scale regarded as the current mean grain size has been proposed by Tejchman (2010) in a micropolar hypoplastic constitutive model,

$$d_{50} = (1-B) d_{50}^o + B d_{50}^u \tag{1.33}$$

in which d_{50}^{u} is the ultimate mean grain diameter, calculated under the assumption that the grain size distribution tends to be fractal (Hardin, 1985), d_{50}^{o} denotes the initial mean grain diameter, and B is the current relative breakage index.

From the preceding summary, the common sense of researchers is that the internal length scale depends on the mean grain diameter for particle materials and that the value may differ slightly for different problems (Aifantis, 1999). However, it must be noted that obtaining accurate values for the new parameters in these formulations is a difficult task.

1.6 Conclusions

This chapter summarized strain localization phenomena in large-scale structures as well as in tank models and specimens in laboratory tests, and then illustrated mechanisms of strain localization in detail. After that, it summarized theories and methods relating to the study of strain localization and reviewed the influences of various factors on shear band onset, thickness, and inclination.

Various investigations on the strain localization phenomena by numerical methods were reviewed, such as DEM, FEM, among others. Their advantages and disadvantages were discussed. Considering the mesh dependency problems in modelling strain localization phenomena using the finite element method within the framework of classical continuum theory, several typical regularization approaches, like viscosity theory, nonlocal theory, gradient theory, and micropolar theory, were introduced naturally. The advantages and disadvantages of each regularization approach was symmetrically summarized and compared, helping us to gain a deep understanding of the differences between these approaches and to select an appropriate regularization method in different cases. Furthermore, emphases were laid on the micro polar theory, whose applications and the internal length scale parameter were summarized and discussed in detail. According to the review, the present thesis aims at investigating the progressive failure of granular material made structures. And the micropolar approach is used to overcome the convergence difficulties and mesh dependency problems when simulating strain localization phenomena by FEM.

Chapter 2 Finite Element Implementation of the Micropolar SIMSAND Model

2.1 Introduction

When subjected to high levels of stress, particles of granular materials inside strain localization zones will be forced to rearrange and deform with great intensity. The grains or aggregates of such materials will undergo extreme and irreversible rotational and translational deformations. Many researchers have supported the idea that particles' rotations are most dominant at the failure or bifurcation point (Oda et al., 1997, 1998, 2002; Vardoulakis & Sulem, 1995). Accordingly, apart from the translations of grains, it is of great importance that grain rotations be brought into the formulations so to describe the realistic behavior of granular materials. Many constitutive models have been developed in the literature to describe the mechanical behavior of granular materials. However, most of the formulations of these models fit within the framework of classical continuum theory, and the finite element solutions suffer from serious mesh dependency problems when the strain localization phenomena are simulated. The main reason for mesh dependency is the lack of length scale parameter to reflect the internal micro-structure, and the partial differential governing equations will lose ellipticity in the post-bifurcation regime. As mentioned by Vardoulakis and Sulem (1995), the Cosserat theory (micropolar theory), proposed by the Cosserat brothers (1909), can be used to describe the strain localization phenomenon. Micropolar theory takes into account the micro rotations of grains and is able to relieve the mesh dependency problems in finite element analysis.

In this chapter, the recently developed critical state–based elastoplastic sand model (SIMSAND) has been formulated under the framework of micropolar theory. Then, the numerical implementations and validations have been performed. At last, the regularization ability in dealing with the mesh dependency problems in finite element analysis of the micropolar SIMSAND model was demonstrated by simulating a biaxial test and a passive retaining wall.

2.2 Introduction of micropolar SIMSAND model

2.2.1 Description of SIMSAND model

Over the past few decades, many constitutive models have been developed for sand from linear elastic models and ideal plastic models to nonlinear models and even advanced critical state–based models (such as the NorSand model by Jefferies (1993), the Severn–Trent model by Gajo and Muir Wood (1999), the SANISAND model by Taiebat and Dafalias (2008), and micromechanical models by Chang and Hicher (2005) and Yin et al. (2010, 2014)). These advanced sand models have described the behavior of sand accurately. In this section, a different simple critical state–based nonlinear model (the SIMSAND model) would be introduced briefly. For more detailed information of SIMSAND model, the publication of Jin et al. (2016) and Wu et al. (2017) should be referred to.

The constitutive relations are introduced as follows, with the total strain rate conventionally decomposed into the elastic part and the plastic part:

$$\dot{\varepsilon}_{ij} = \dot{\varepsilon}_{ij}^{e} + \dot{\varepsilon}_{ij}^{p} \tag{2.1}$$

The hypoelastic behavior is assumed to be isotropic with bulk modulus K or shear modulus G. The forms of these two moduli proposed by Richart et al. (1970) have been adopted,

$$\dot{\varepsilon}_{ij}^{e} = \frac{1+\upsilon}{3K\left(1-2\upsilon\right)}\dot{\sigma}'_{ij} - \frac{\upsilon}{3K\left(1-2\upsilon\right)}\dot{\sigma}'_{kk}\delta_{ij} \tag{2.2}$$

which, if defined in the p'–q plane, produces

$$\dot{\varepsilon}_{v}^{e} = \frac{\dot{p}'}{K},\ \dot{\varepsilon}_{d}^{e} = \frac{\dot{q}}{3G} \tag{2.3}$$

in which

$$K = K_0 \cdot p_{at}\frac{\left(2.97-\mathrm{e}\right)^2}{1+e}\left(\frac{p'}{p_{at}}\right)^{\zeta} \tag{2.4}$$

$$G = G_0 \cdot p_{at}\frac{\left(2.97-\mathrm{e}\right)^2}{1+e}\left(\frac{p'}{p_{at}}\right)^{\zeta} \tag{2.5}$$

where K_0, G_0 are reference values of bulk modulus and shear modulus, respectively. ζ is an input parameter controlling the nonlinearity of the confining stress effect; e is the void ratio; υ is Poisson's

ratio; p' is the mean effective stress; and p_{at} is the atmospheric pressure used as reference pressure (p_{at} = 101.3 kPa). Shear modulus and bulk modulus can be related by Poisson's ratio,

$$\frac{K}{G} = \frac{2(1+\upsilon)}{3(1-2\upsilon)} \tag{2.6}$$

Thus the reference value of bulk modulus K and Poisson's ratio υ can be taken as the input parameters.

The plastic strain is based on the shear sliding,

$$\dot{\varepsilon}_{ij}^{p} = d\lambda \frac{\partial g}{\partial \sigma'_{ij}} \tag{2.7}$$

where g is the plastic potential function and $d\lambda$ is the plastic multiplier. The yield surface for shear sliding can be expressed in a similar way to those proposed by many previous researchers (Vermeer, 1978; Jefferies, 1993; Gajo and Wood, 1999; Yin et al., 2010),

$$f = \frac{q}{p'} - \frac{M_p \varepsilon_d^p}{k_p + \varepsilon_d^p} \tag{2.8}$$

in which f is the yield function, q is the deviatoric stress ($q = \sqrt{3J_2}$), k_p relates to the plastic shear modulus, M_p is the stress ratio corresponding to the peak strength and determined by the peak friction angle ϕ_p (M_p = 6sin(ϕ_p)/(3–sin(ϕ_p))), and ε_d^p is the deviatoric plastic strain ($\varepsilon_d^p = \sqrt{2e_{ij}e_{ij}/3}$). The potential surface, accounting for contraction or dilation, which is also similar to those proposed by the aforementioned researchers, can be expressed as

$$\begin{aligned} &\frac{\partial g}{\partial \sigma'_{ij}} = \frac{\partial g}{\partial p'}\frac{\partial p'}{\partial \sigma'_{ij}} + \frac{\partial g}{\partial q}\frac{\partial q}{\partial \sigma'_{ij}} \\ &with\ \frac{\partial g}{\partial p'} = A_d\left(M_{pt} - \frac{q}{p'}\right); \frac{\partial g}{\partial q} = 1 \end{aligned} \tag{2.9}$$

where A_d is the stress–dilatancy parameter; M_{pt} = 6sin(ϕ_{pt})/(3–sin(ϕ_{pt})) can be calculated from the phase transformation friction angle ϕ_{pt}.

M, the slope of the critical state line in the p'–q plane, is expressed as M = 6sin(ϕ_u)/(3–sin(ϕ_u)). The peak friction angle ϕ_p and the phase transformation friction angle ϕ_{pt} are associated with the critical friction angle ϕ_u (corresponding to the critical state line CSL in the p'–q plane in Figure 2-1)

and the critical void ratio e_c (obtained from the critical state line *CSL* in the e–log p' plane in Figure 2-1) as follows (Jin et al., 2016; Wu et al., 2017):

$$\tan\phi_p = \left(\frac{e_c}{e}\right)^{n_p} \tan\phi_u,\ \tan\phi_{pt} = \left(\frac{e_c}{e}\right)^{-n_d} \tan\phi_u \tag{2.10}$$

According to the critical state concept and experimental observations, a simple critical state line (Li and Wang, 1998) has been used to calculate the critical state void ratio e_c,

$$e_c = e_{ref} - \lambda \ln\left(\frac{p'}{p_{at}}\right) \tag{2.11}$$

where n_p and n_d are model parameters, e_{ref} is the reference critical void ratio corresponding to p_{at}, and λ is the slope of the *CSL* in the e–log p' plane. The simple form of the critical state line given by Eq. (2.11) is suitable for sand under a mean effective stress of no more than 1 MPa with very few particle breakages.

From Eq. (2.10) and Figure 2-1, we can find that for loose sand with $e > e_c$, the phase transformation stress ratio M_{pt} is bigger than M and the peak stress ratio M_p is smaller than M, which allows the loose sand to contract during deviatoric loading with a strain-hardening behavior; for dense sand with $e < e_c$, the phase transformation stress ratio M_{pt} is smaller than M, and the peak stress ratio M_p is bigger than M, which allows the dense sand first to contract and then to dilate during deviatoric loading, with the peak strength followed by a softening behavior. For both loose and dense granular assemblies, when the stress state reaches the critical state line, the void ratio e becomes equal to the critical void ratio e_c, after which zero dilation or contraction takes place. Thus the constitutive equations guarantee that stresses and void ratio simultaneously reach the critical state in the p'–q–e space.

The plastic multiplier $d\lambda$ can be calculated in a conventional way according to plasticity:

$$d\lambda = \frac{\left[\dfrac{\partial f}{\partial \sigma_{ij}}\right]^T D_{ijkl} d\varepsilon_{kl}}{\left[\dfrac{\partial f}{\partial \sigma_{ij}}\right]^T D_{ijkl} \dfrac{\partial g}{\partial \sigma_{kl}} - \dfrac{\partial f}{\partial \varepsilon_d^p}\dfrac{\partial g}{\partial q}} \tag{2.12}$$

Based on the foregoing constitutive equations, the stress–strain relationship can be solved.

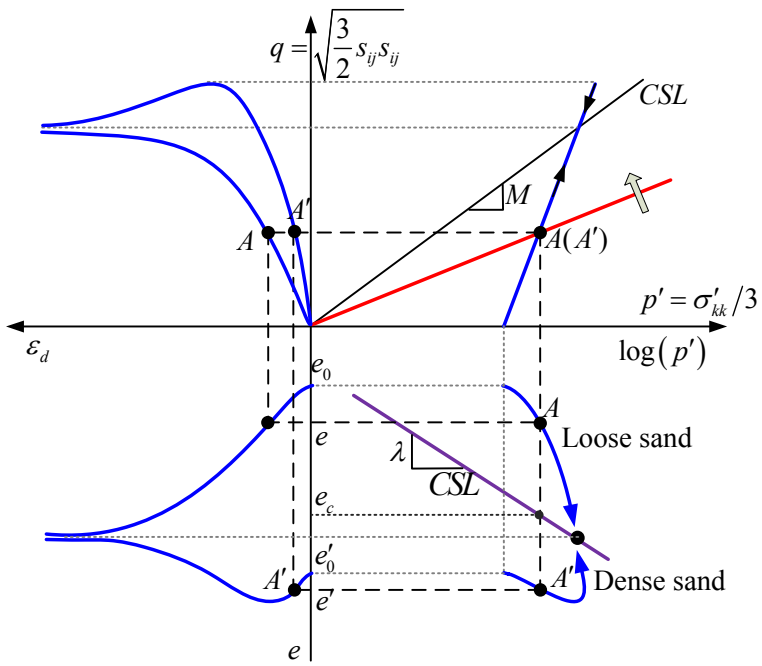

Figure 2-1 Principle of critical-state-based nonlinear hardening model for sand

2.2.2 Extension to the micropolar SIMSAND model

Classical constitutive models feature six components in stress and strain vectors for three-dimensional problems and four components for two-dimensional problems (e.g., plane strain problems) if not repeatedly counting mutual–equal shear stress components:

$$3\mathrm{D}:\begin{cases}\boldsymbol{\varepsilon}=\left[\varepsilon_{xx}\ \varepsilon_{yy}\ \varepsilon_{zz}\ \varepsilon_{xy}\ \varepsilon_{yz}\ \varepsilon_{zx}\right]^T\\ \boldsymbol{\sigma}=\left[\sigma_{xx}\ \sigma_{yy}\ \sigma_{zz}\ \sigma_{xy}\ \sigma_{yz}\ \sigma_{zx}\right]^T\end{cases}\tag{2.13}$$

$$2\mathrm{D}:\begin{cases}\boldsymbol{\varepsilon}=\left[\varepsilon_{xx}\ \varepsilon_{yy}\ \varepsilon_{zz}\ \varepsilon_{xy}\right]^T\\ \boldsymbol{\sigma}=\left[\sigma_{xx}\ \sigma_{yy}\ \sigma_{zz}\ \sigma_{xy}\right]^T\end{cases}\tag{2.14}$$

The simple critical state–based elastoplastic model just illustrated has been polarized to account for couple stresses and rotations of grains under plane strain condition by the augmentation of the strain and stress vectors. Herein, we revisit strain and stress vectors, as well as the elastic stiffness matrix $\mathbf{D}^e$ under plane strain condition, in the enhanced micropolar model:

$$\boldsymbol{\varepsilon}=\left[\varepsilon_{xx}\ \varepsilon_{yy}\ \varepsilon_{zz}\ \varepsilon_{xy}\ \varepsilon_{yx}\ \kappa_{zx}l_c\ \kappa_{zy}l_c\right]^T\tag{2.15}$$

$$\boldsymbol{\sigma}=\left[\sigma_{xx}\ \sigma_{yy}\ \sigma_{zz}\ \sigma_{xy}\ \sigma_{yx}\ m_{zx}/l_c\ m_{zy}/l_c\right]^T\tag{2.16}$$

$$\mathbf{D}^e = \begin{bmatrix} \lambda+2G & \lambda & \lambda & 0 & 0 & 0 & 0 \\ \lambda & \lambda+2G & \lambda & 0 & 0 & 0 & 0 \\ \lambda & \lambda & \lambda+2G & 0 & 0 & 0 & 0 \\ 0 & 0 & 0 & G+G_c & G-G_c & 0 & 0 \\ 0 & 0 & 0 & G-G_c & G+G_c & 0 & 0 \\ 0 & 0 & 0 & 0 & 0 & 2G & 0 \\ 0 & 0 & 0 & 0 & 0 & 0 & 2G \end{bmatrix} \tag{2.17}$$

where l_c is the incorporated internal length scale parameter in the micropolar model, and G_c denotes the micropolar shear modulus.

Compared with the initial SIMSAND model, the stress and strain invariants in the micropolar SIMSAND model have been modified to consider the couple curvatures and corresponding energetically conjugated couple stresses. According to de Borst et al. (1987, 1991, 1991), the strain and stress invariants can be formulated as

$$\dot{\varepsilon}_d^p = \left[b_1 \dot{e}_{ij}^p \dot{e}_{ij}^p + b_2 \dot{e}_{ij}^p \dot{e}_{ji}^p + b_3 \dot{\kappa}_{ij}^p \dot{\kappa}_{ij}^p l_c^2 \right]^{\frac{1}{2}} \tag{2.18}$$

$$J_2 = a_1 s_{ij} s_{ij} + a_2 s_{ij} s_{ji} + a_3 m_{ij} m_{ji} / l_c^2 \tag{2.19}$$

where $\dot{e}_{ij}^p$ is the plastic deviatoric strain rate tensor, $\dot{\kappa}_{ij}^p$ is the plastic micro-curvature rate tensor, s_{ij} is the deviatoric stress tensor, and m_{ij} is the micro-moment tensor. The summation convention with respect to repeated indices has been adopted. Furthermore, the deviatoric stress q is updated by new stress invariant $\sqrt{3J_2}$. For numerical convenience, the choice $a_1 = a_2 = 1/4$, $a_3 = 1/2$ and $b_1 = b_2 = 1/3$, $b_3 = 2/3$ has been used in majority cases (de Borst, 1990, 1991; de Borst and Sluys, 1991). To arrive at a compact matrix–vector notation, the formulation of q is expressed as

$$q = \sqrt{\frac{1}{2} \boldsymbol{\sigma}^{\mathrm{T}} \mathbf{P} \boldsymbol{\sigma}} \tag{2.20}$$

where **P** is called the plastic potential matrix (Li and Tang, 2005):

$$\mathbf{P}=\begin{bmatrix} 2 & -1 & -1 & 0 & 0 & 0 & 0 \\ -1 & 2 & -1 & 0 & 0 & 0 & 0 \\ -1 & -1 & 2 & 0 & 0 & 0 & 0 \\ 0 & 0 & 0 & 3/2 & 3/2 & 0 & 0 \\ 0 & 0 & 0 & 3/2 & 3/2 & 0 & 0 \\ 0 & 0 & 0 & 0 & 0 & 3 & 0 \\ 0 & 0 & 0 & 0 & 0 & 0 & 3 \end{bmatrix} \tag{2.21}$$

Similarly, if the equivalent plastic strain ε_d^p is expressed directly by the seven generalized strain components as the manner for calculating the second invariant of deviatoric stress q, then the equivalent plastic strain can be expressed in compact matrix–vector notation,

$$\varepsilon_d^p=\sqrt{\frac{2}{3}\left(\boldsymbol{\varepsilon}^{\mathbf{p}}\right)^{\mathbf{T}}\mathbf{Q}\,\boldsymbol{\varepsilon}^{\mathbf{p}}} \tag{2.22}$$

with the matrix **Q** defined as follows:

$$\mathbf{Q}=\begin{bmatrix} 2/3 & -1/3 & -1/3 & 0 & 0 & 0 & 0 \\ -1/3 & 2/3 & -1/3 & 0 & 0 & 0 & 0 \\ -1/3 & -1/3 & 2/3 & 0 & 0 & 0 & 0 \\ 0 & 0 & 0 & 1/2 & 1/2 & 0 & 0 \\ 0 & 0 & 0 & 1/2 & 1/2 & 0 & 0 \\ 0 & 0 & 0 & 0 & 0 & 1 & 0 \\ 0 & 0 & 0 & 0 & 0 & 0 & 1 \end{bmatrix} \tag{2.23}$$

Notably, however, Muhlhaus and Vardoulakis (1987) have suggested that other combinations of the coefficients a_1, a_2, a_3 and b_1, b_2, b_3 in Eq. (2.18) and Eq. (2.19) might have more representative meanings for granular assemblies based on micromechanical considerations.

As can be seen, augmenting a classical constitutive model to produce a micropolar model in a stress–strain level is not a complex task. The stress and strain vectors must simply be extended to consider the micromoments and microcurvatures, which also requires that stress and strain invariants be newly defined based on the foregoing equations. Note, however, that when the independent microrotation is constrained, all micro qualities are null values and the micropolar model is retrieved to a classical one.

2.2.3 Summary of model parameters

The micropolar constitutive model features 12 parameters in total. Besides those parameters that can straightforwardly be given a meaningful value before fitting the experimental curves, such as Poisson's ratio υ, the parameters in the constitutive model can be divided into four groups: (1) elasticity-related parameters: K_0, υ, and ζ; (2) critical state–related parameters: ϕ_u, e_{ref}, and λ; (3) plasticity interlocking parameters: k_p, A_d, n_p, and n_d; and (4) the newly incorporated parameters in a micropolar constitutive model for 2D problems: l_c and G_c.

A typical value for Poisson's ratio of υ=0.2 is usually assumed. The values of K_0 and ζ chiefly control the isotropic compression curve, and the values of ϕ_u, e_{ref}, λ, k_p, A_d, n_p, and n_d chiefly control the triaxial shearing curves. Accordingly, the elasticity-related parameters K_0, ζ can be obtained based on an isotropic compression curve; to identify the critical state–related parameters ϕ_u, e_{ref}, and λ, at least three set of triaxial tests with different confining pressures and different initial void ratios should be required; the plastic interlocking parameters k_p, A_d, n_p, and n_d can be determined by one triaxial drained test. The micropolar parameters l_c and G_c chiefly control the thickness strain localization zones and the bearing capacity in specimens' or structures' post-failure regime. Consequently, the micropolar parameters may be determined by analyzing the thickness of shear bands such that results match the real experimental width. Unlike macro-scale material parameters, however, the micro-scale material parameter cannot be easily determined through experiment. Lakes (1995) proposed some experimental methods for elastic micropolar continuum. These experiments are quite complicated and work only for materials such as metal. For granular materials, no standard experiment exists that is suited to micropolar theory, nor any recognized definition of the length scale.

In terms of the influence on the material behavior of these parameters, k_p and n_p control the peak strength, A_d and n_d control the dilatancy behavior, and ϕ_u, e_{ref}, and λ control the position of the critical state line in the q–p' plane and the e–log p' plane. Specifically, k_p controls the initial slope of the curve $q/p' - \varepsilon_d^p$; in addition, the degradation rate of the stiffness at small strain levels is determined by the plastic shear modulus k_p: a smaller value of k_p gives a slower degradation of the global shear modulus; A_d is the stress dilatancy multiplier, which controls the magnitude of dilatancy;

n_d controls the slope of the transformation line; ϕ_u controls the slope of the critical state line in the q–p' plane; and e_{ref} and λ control the specific position and slope of the said line in the e–log p' plane.

There are two ways of identifying the interlocking effect-related parameters k_p, A_d, n_p, and n_d: one is the conventional curve-fitting method, the success of which depends greatly on experience; the other is by means of an optimization method. Sometimes, optimization methods allow parameters to be found more quickly and effectively (Jin et al., 2016).

In terms of the two additional incorporated parameters, which are identified as the internal length scale parameter l_c and the micropolar shear modulus G_c in the model within the framework of micropolar theory for plane strain problems, the thickness of the shear band is commonly recognized as being decided primarily by the internal length scale; thus l_c, reflecting the microstructure, is generally related to microstructures such as the mean grain size d_{50} or is linearly proportional to the same. The influence of micro-properties, such as the shape and surface roughness of the particles on the value of the internal length scale parameter l_c, will not be considered in the present research. It has been widely accepted that G_c can be set to about half the conventional shear modulus G (de Borst and Mühlhaus, 1991; de Borst and Sluys, 1991; de Borst, 1993; Arslan and Sture, 2008b, a; Tang and Li, 2008). Taking into account that the micropolar shear modulus (when $G_c \geqslant 0.5G$) has only a very slight influence on the final results, such as for shear band thickness and load carrying capacity in biaxial tests, the emphasis is put on the effect of the internal length scale l_c. The value of l_c has a considerable influence on the load–displacement curve, as well as the distribution of strain localization. A larger l_c will result in more toughness in the post-peak regime as well as in a wider shear zone. The influence of l_c can finally be observed and analyzed by simulating the strain localization phenomena using the finite element method when the rotational degree of freedom is taken into account.

2.3 Finite element implementation

2.3.1 Formulations of UEL

2.3.1.1 Introduction of UEL

When using micropolar theory, an additional rotational degree of freedom, apart from the translational degrees of freedom for a 2D element, is activated in finite element analysis. For all the 2D element types in ABAQUS, there are only two translational degrees of freedom, meaning that the user-defined element (UEL) subroutine, which provides the platform for advanced development, should be used to define a new element that satisfies the various requirements of different users. The advantages of implementing UEL in ABAQUS, instead of writing a complete analysis code, are obvious. Additionally, we can use the pre-processing and post-processing platforms of ABAQUS, maintaining and porting subroutines is much easier than doing the same for a complete finite element program. The programming language used for the user subroutines of ABAQUS can be FORTRAN, C, or C++. A UEL subroutine is just one of the various user subroutines, and a specific format of interface, as shown in Figure 2-2, exists in each subroutine to realize the data transferring and sharing between subroutines and the solvers of ABAQUS. Certain necessary and indispensable arrays must be defined. *RHS* contains the contributions of this element to the right-hand-side vectors of the overall system of equations—for most nonlinear analysis procedures, *NRHS* = 1 and *RHS* should contain the residual vector; *AMATRX* contains the contribution of this element to the Jacobian (stiffness) or other matrix of the overall system of equations; *SVARS* contains the values of the solution-dependent state variables associated with this element, and the number of such variables is *NSVARS*. At the end of the subroutine UEL, *AMATRX* and *RHS* must be updated and saved for further calculation.

```
C-------------User defined ELement subroutine--------------------C

      SUBROUTINE UEL(RHS,AMATRX,SVARS,ENERGY,NDOFEL,NRHS,NSVARS,
     1 PROPS,NPROPS,COORDS,MCRD,NNODE,U,DU,V,A,JTYPE,TIME,DTIME,
     2 KSTEP,KINC,JELEM,PARAMS,NDLOAD,JDLTYP,ADLMAG,PREDEF,NPREDF,
     3 LFLAGS,MLVARX,DDLMAG,MDLOAD,PNEWDT,JPROPS,NJPROP,PERIOD)
C
      INCLUDE 'ABA_PARAM.INC'
C
      DIMENSION RHS(MLVARX,*),AMATRX(NDOFEL,NDOFEL),PROPS(*),
     1 SVARS(*),ENERGY(8),COORDS(MCRD,NNODE),U(NDOFEL),
     2 DU(MLVARX,*),V(NDOFEL),A(NDOFEL),TIME(2),PARAMS(*),
     3 JDLTYP(MDLOAD,*),ADLMAG(MDLOAD,*),DDLMAG(MDLOAD,*),
     4 PREDEF(2,NPREDF,NNODE),LFLAGS(*),JPROPS(*)


      user coding to define RHS, AMATRX, SVARS, ENERGY, and PNEWDT


      RETURN
      END

C-------------------------------------------------------------C
```

Figure 2-2 Subroutine interface of UEL

The programming of a UEL is more difficult and complex than that of a UMAT, which simply requires the description of the strain–stress relationship. Accordingly, this feature of ABAQUS is intended for advanced users only. Before programming a UEL subroutine, certain key characteristics of a user element must be defined, such as the number of nodes on the element, the number of coordinates at each node, the degrees of freedom active at each node, the number of element properties, and the number of solution-dependent state variables to be stored per element.

Figure 2-3 presents a flowchart of a UEL, which illustrates the entire process of a UEL in detail. We can find that the process is completely the same with the finite element analysis within the framework of classical continuum mechanics theory. However, the element type, represented by shape functions, is defined by the user rather than the ones in ABAQUS. The cutting plane method to update stresses will be illustrated in the next section. Because the additional degree of freedom—rotational can be regarded as a specific and particular translational one, the micropolar theory is also referred to as the generalized continuum mechanics theory.

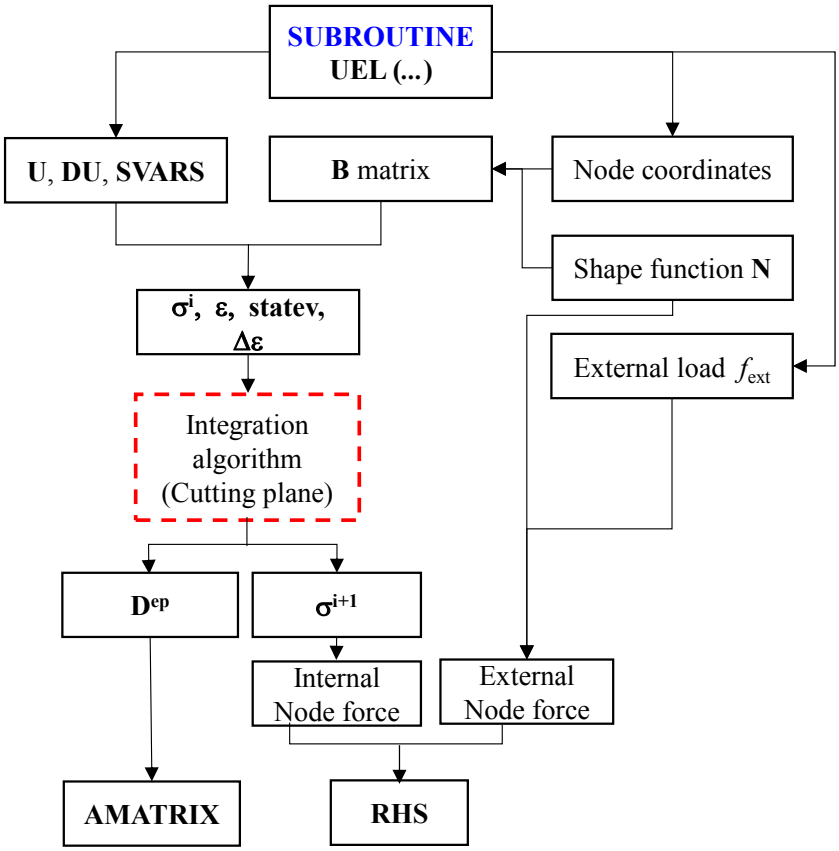

Figure 2-3 Flow chart of the UEL

2.3.1.2 Derivations of a user defined element

The finite element formulations, conducted in the updated Lagrangian frame, have been implemented into the commercial finite element tool ABAQUS via the UEL function.

As with the introduction of micropolar theory aforementioned, there are three degrees of freedom for each node for the plane-strain element. To address the issue of full integration causing shear volumetric locking and reduced integration leading to hourglass of a four-node bilinear quadrilateral element, as shown in Figure 2-4, an eight-node biquadratic quadrilateral element was defined. And, reduced integration was used in the present study, which is suitable for nearly all plane strain conditions without any problem.

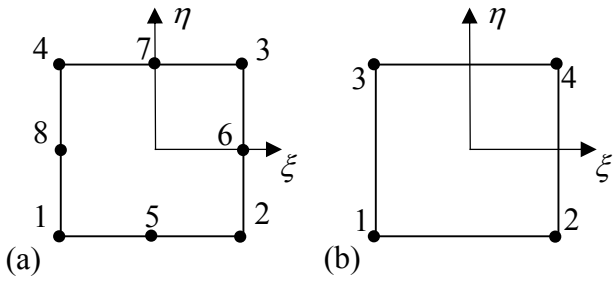

Figure 2-4 Element of 2D micropolar continuum: (a) 8-node plane element; (b) integration points

Based on the interpolation approximation method, the displacements and rotations of an element can be calculated by the counterparts of each node, as demonstrated by

$$\mathbf{u} = \mathbf{N}\boldsymbol{\delta}^{\mathbf{e}} \tag{2.24}$$

where **u** is the displacement (rotation) of the element, **N** is the interpolation function matrix, and $\boldsymbol{\delta}^{\mathbf{e}}$ is the displacement vector of all nodes of the element. For the current 2D element

$$\mathbf{u} = \begin{Bmatrix} u \\ v \\ \omega_z \end{Bmatrix}, \boldsymbol{\delta}^{\mathbf{e}} = \begin{Bmatrix} \delta_1 \\ \delta_2 \\ \delta_3 \\ \delta_4 \\ \delta_5 \\ \delta_6 \\ \delta_7 \\ \delta_8 \end{Bmatrix}, \delta_i = \begin{Bmatrix} u_i \\ v_i \\ \omega_{zi} \end{Bmatrix} \left(\mathrm{i} = 1,2,...,8\right) \tag{2.25}$$

$$\mathbf{N} = \left[\mathbf{I}N_1\ \mathbf{I}N_2\ \mathbf{I}N_3\ \mathbf{I}N_4\ \mathbf{I}N_5\ \mathbf{I}N_6\ \mathbf{I}N_7\ \mathbf{I}N_8\right], \mathbf{I} = \begin{bmatrix} 1 & 0 & 0 \\ 0 & 1 & 0 \\ 0 & 0 & 1 \end{bmatrix} \tag{2.26}$$

The shape functions of the plane-strain eight-node isoparametric element were displayed as follows:

$$
\begin{cases}
N_1 = \frac{1}{4}(1-\xi)(1-\eta) - \frac{1}{2}(N_5 + N_8) \\
N_2 = \frac{1}{4}(1+\xi)(1-\eta) - \frac{1}{2}(N_5 + N_6) \\
N_3 = \frac{1}{4}(1+\xi)(1+\eta) - \frac{1}{2}(N_6 + N_7) \\
N_4 = \frac{1}{4}(1-\xi)(1+\eta) - \frac{1}{2}(N_7 + N_8) \\
N_5 = \frac{1}{2}(1-\xi^2)(1-\eta) \\
N_6 = \frac{1}{2}(1+\xi)(1-\eta^2) \\
N_7 = \frac{1}{2}(1-\xi^2)(1+\eta) \\
N_8 = \frac{1}{2}(1-\xi)(1-\eta^2)
\end{cases}
\tag{2.27}
$$

Then, the strain can be derived from the displacement, as in the classical continuum mechanics theory. The **L** matrix (defined in Appendix C) is used as a bridge of strain and displacement:

$$
\boldsymbol{\varepsilon} = \mathbf{Lu} = \mathbf{LN}\boldsymbol{\delta}^{\mathbf{e}} = \mathbf{B}\boldsymbol{\delta}^{\mathbf{e}} \tag{2.28}
$$

B is named the strain matrix and written in blocked form by node number:

$$
\mathbf{B} = \mathbf{LN} = \left[B_1 \; B_2 \; B_3 \; B_4 \; B_5 \; B_6 \; B_7 \; B_8 \right] \tag{2.29}
$$

Thus, **B** is formulated as

$$
B_i = \begin{bmatrix}
\frac{\partial N_i}{\partial x} & 0 & 0 \\
0 & \frac{\partial N_i}{\partial y} & 0 \\
0 & 0 & 0 \\
0 & \frac{\partial N_i}{\partial x} & -N_i \\
\frac{\partial N_i}{\partial y} & 0 & N_i \\
0 & 0 & \frac{\partial N_i}{\partial x} \\
0 & 0 & \frac{\partial N_i}{\partial y}
\end{bmatrix} \quad (\mathrm{i} = 1, 2 \ldots 8) \tag{2.30}
$$

When the strain has been obtained, the stress can be calculated based on the constitutive law; this will be discussed in detail in the next section.

$$\boldsymbol{\sigma} = \mathbf{D}^{ep}\boldsymbol{\varepsilon} = \mathbf{D}^{ep}\mathbf{B}\boldsymbol{\delta}^{e} \tag{2.31}$$

From this formula, we may discern that to calculate stress and strain vectors, the shape function **N**, as expressed in the natural coordinate system, must be transferred to the Cartesian coordinate system. The Jacobian matrix is introduced to realize the map between the current and previous configurations. The isoparametric element is used in this paper, which means that the nodes used to decide the element's shape and displacement are the same, as are the shape functions. The element's global coordinate in the plane can also be obtained from the shape functions and global coordinate of each node:

$$\begin{cases} x = \sum_{i=1}^{8} N_i x_i = N_1 x_1 + N_2 x_2 + \ldots + N_8 x_8 \\ y = \sum_{i=1}^{8} N_i y_i = N_1 y_1 + N_2 y_2 + \ldots + N_8 y_8 \end{cases} \tag{2.32}$$

According to the partial differential rule, we know that

$$\begin{cases} \dfrac{\partial N_i}{\partial \xi} = \dfrac{\partial N_i}{\partial x}\dfrac{\partial x}{\partial \xi} + \dfrac{\partial N_i}{\partial y}\dfrac{\partial y}{\partial \xi} \\ \dfrac{\partial N_i}{\partial \eta} = \dfrac{\partial N_i}{\partial x}\dfrac{\partial x}{\partial \eta} + \dfrac{\partial N_i}{\partial y}\dfrac{\partial y}{\partial \eta} \end{cases} \tag{2.33}$$

Eq. (2.33) can be also expressed as

$$\begin{Bmatrix} \dfrac{\partial N_i}{\partial \xi} \\ \dfrac{\partial N_i}{\partial \eta} \end{Bmatrix} = \begin{bmatrix} \dfrac{\partial x}{\partial \xi} & \dfrac{\partial y}{\partial \xi} \\ \dfrac{\partial x}{\partial \eta} & \dfrac{\partial y}{\partial \eta} \end{bmatrix} \begin{Bmatrix} \dfrac{\partial N_i}{\partial x} \\ \dfrac{\partial N_i}{\partial y} \end{Bmatrix} = [\mathbf{J}] \begin{Bmatrix} \dfrac{\partial N_i}{\partial x} \\ \dfrac{\partial N_i}{\partial y} \end{Bmatrix} \tag{2.34}$$

after which the partial difference in Eq. (2.30) can be obtained,

$$\begin{Bmatrix} \dfrac{\partial N_i}{\partial x} \\ \dfrac{\partial N_i}{\partial y} \end{Bmatrix} = [\mathbf{J}]^{-1} \begin{Bmatrix} \dfrac{\partial N_i}{\partial \xi} \\ \dfrac{\partial N_i}{\partial \eta} \end{Bmatrix} \tag{2.35}$$

where [**J**] is named the Jacobian matrix and formulated as

$$[\mathbf{J}]=\begin{bmatrix}\frac{\partial x}{\partial \xi} & \frac{\partial y}{\partial \xi}\\ \frac{\partial x}{\partial \eta} & \frac{\partial y}{\partial \eta}\end{bmatrix}=\begin{bmatrix}\frac{\partial \sum N_i x_i}{\partial \xi} & \frac{\partial \sum N_i y_i}{\partial \xi}\\ \frac{\partial \sum N_i x_i}{\partial \eta} & \frac{\partial \sum N_i y_i}{\partial \eta}\end{bmatrix}=\begin{bmatrix}\frac{\partial N_1}{\partial \xi} & \frac{\partial N_2}{\partial \xi} & \cdots & \frac{\partial N_8}{\partial \xi}\\ \frac{\partial N_1}{\partial \eta} & \frac{\partial N_2}{\partial \eta} & \cdots & \frac{\partial N_8}{\partial \eta}\end{bmatrix}\begin{bmatrix}x_1 & y_1\\ x_2 & y_2\\ \cdots & \cdots\\ x_8 & y_8\end{bmatrix} \tag{2.36}$$

2.3.1.3 Discretization of the governing field equations

According to the mechanics theory, the total potential energy of the structure, based on the virtual displacement principle in the two-dimensional plane strain problem, is expressed as

$$\prod_p = \int_\Omega \frac{1}{2}\boldsymbol{\varepsilon}^{\mathrm{T}}\mathbf{D}^{\mathbf{ep}}\boldsymbol{\varepsilon} t dxdy - \int_\Omega \mathbf{u}^T \mathbf{f} t dxdy - \int_S \mathbf{u}^T \mathbf{T} dS \tag{2.37}$$

where t is the thickness of the 2D elastic element, $\mathbf{f}$ is the body force vector in the interior of the element, and $\mathbf{T}$ is the surface force vector exerted on the boundary.

Combing Eq. (2.28) and Eq. (2.37), the total potential energy of the system is equal to the sum of the potential energy of each element. The total potential energy of the discrete model is expressed as

$$\begin{aligned}\prod_p = \sum_e \prod_p^e = \sum_e \left((\boldsymbol{\delta}^{\mathbf{e}})^{\mathrm{T}} \int_{\Omega_e} \frac{1}{2}\mathbf{B}^T \mathbf{D}^{\mathbf{ep}} \mathbf{B} t dxdy \boldsymbol{\delta}^{\mathbf{e}} \right)\\ - \sum_e \left(\int_{\Omega_e} (\boldsymbol{\delta}^{\mathbf{e}})^{\mathrm{T}} \mathbf{u}^T \mathbf{f} t dxdy \right) - \sum_e \left(\int_{S_e} (\boldsymbol{\delta}^{\mathbf{e}})^{\mathrm{T}} \mathbf{N}^T \mathbf{T} ds \right)\end{aligned} \tag{2.38}$$

Based on the minimum potential energy principle and the randomness of the virtual displacement, the partial differential $\frac{\partial \prod_p}{\partial \boldsymbol{\delta}^{\mathbf{e}}} = 0$ must be satisfied. Then the discretized governing field equations of finite element analysis are derived as

$$\mathbf{K}^e \boldsymbol{\delta}^{\mathbf{e}} = \mathbf{P}^e \tag{2.39}$$

where $\mathbf{K}^{\mathrm{e}}$ is the element stiffness matrix and $\mathbf{P}^{\mathrm{e}}$ is the element equivalent node load vector:

$$\mathbf{K}^e = \int_{\Omega_e} \frac{1}{2}\mathbf{B}^T \mathbf{D}^{\mathbf{ep}} \mathbf{B} t dxdy \tag{2.40}$$

$$\mathbf{P}^e = \int_{\Omega_e} \mathbf{u}^T \mathbf{f} t dxdy + \int_{S_e} \mathbf{N}^T \mathbf{T} ds \tag{2.41}$$

For the total system, the discretized equation is formulated as

$$\mathbf{K}\boldsymbol{a} = \mathbf{P} \tag{2.42}$$

where **K** is the global stiffness matrix of the structure, ***a*** is the global node displacement array, and **P** is the global equivalent node force array of the total system. The derivations above are also suitable for the elastoplastic continuum. Here, **K** and **P** correspond to *AMATRX* and *RHS* in the interface of the user element subroutine, respectively, and ***a*** is *U* or *DU*. In ABAQUS, the Newton–Raphson technique is used to fulfill the static equilibrium equations of the nonlinear problems. Via the transition of the Jacobian matrix, the integration zones are changed from irregular to regular under natural coordinates. Because the integrations are too complex to be solved easily while attaining an accurate analytical solution, a numerical method, such as Gauss integration, is invariably adopted. Take the element stiffness matrix, for example:

$$\mathbf{K}^e = \int_{\Omega_e} \mathbf{B}^T \mathbf{D}^{\mathbf{ep}} \mathbf{B} t dxdy = \int_{-1}^{1}\int_{-1}^{1} \mathbf{B}^T \mathbf{D}^{\mathbf{ep}} \mathbf{B} \,|\, \mathbf{J} \,| d\xi d\eta = \sum_{i=1}^{m}\sum_{j=1}^{n} H_i H_j \mathbf{B}^T \mathbf{D}^{\mathbf{ep}} \mathbf{B} t \,|\, \mathbf{J} \,| \qquad (2.43)$$

In this case, $m = n = 2$, H_i, and H_j are the corresponding weight factors of each integration point.

2.3.2 Integration algorithm-cutting plane method

During the numerical implementation of micropolar SIMSAND model, the cutting plane algorithm (Ortiz and Simo, 1986) was adopted to update the stresses. All the internal state variables (such as void ratio, plastic work, and plastic strain) were also updated within the UEL using the explicit forward Euler integration scheme. According to the flow rule, the key factor for obtaining the plastic strains is the plastic multiplier dλ. The direct means of calculating dλ is explicit, which requires a very small loading step and much computing time. The algorithm presented here is semi-implicit, which can allow a more accurate solution with a larger loading step compared to the direct approach. The efficiency and effectiveness of calculation can therefore be improved using this algorithm.

The cutting plane algorithm uses explicit elastic predictions that follow an iterative plastic correction loop. The framework of the algorithm is sufficiently general to be used with a wide variety of constitutive models with rate-independent plasticity, or viscoplasticity models. The formulation of the cutting plane algorithm considers strain-controlled loading, meaning that incremental strains are input quantities in this algorithm and incremental stresses are calculated from the incremental strains using the constitutive model.

In general, the total strain $\boldsymbol{\varepsilon}$ can be decomposed into elastic and plastic parts $\boldsymbol{\varepsilon}^{\mathbf{e}}$ and $\boldsymbol{\varepsilon}^{\mathbf{p}}$, so that

$$\boldsymbol{\varepsilon} = \boldsymbol{\varepsilon}^{\mathbf{e}} + \boldsymbol{\varepsilon}^{\mathbf{p}} \tag{2.44}$$

First, the stresses are considered the function of the elastic strain vector $\boldsymbol{\varepsilon}^{\mathbf{e}}$ and the internal plastic variables H_k, where k is the number of the internal plastic state variables:

$$\sigma_{ij} = \sigma_{ij}\left(\varepsilon_{ij}^{\ e}, H_k\right) \tag{2.45}$$

Then, based on the flow rule, the evolution of the plastic strain and state variables will be calculated per the formulations

$$d\varepsilon_{ij}^{p} = d\lambda \frac{\partial g}{\partial \sigma_{ij}} \tag{2.46}$$

$$dH_i = d\lambda h_i\left(\sigma, \mathbf{H}\right) \tag{2.47}$$

where g is the plastic potential function, $h_i(\boldsymbol{\sigma}, \mathbf{H})$ represents the incremental direction of the state variable H_i, and $\mathbf{H}$ contains all the internal plastic state variables.

Turning to the procedure of the cutting plane algorithm, the total incremental strain is first assumed to be completely elastic; thus the incremental plastic strains and the internal plastic state variables equal zero:

$$d\boldsymbol{\varepsilon} = d\boldsymbol{\varepsilon}^{\mathbf{e}} \tag{2.48}$$

$$d\sigma_{ij} = D_{ijkl} d\varepsilon_{kl} \tag{2.49}$$

$$d\boldsymbol{\varepsilon}^{\mathbf{p}} = 0 \tag{2.50}$$

$$dH_i = 0 \tag{2.51}$$

After the elastic prediction, stresses, strains, and other state variables (such as the void ratio) should be updated:

$$\sigma_{ij} = \sigma_{ij} + d\sigma_{ij} \tag{2.52}$$

$$\varepsilon_{ij} = \varepsilon_{ij} + d\varepsilon_{ij} \tag{2.53}$$

Furthermore, the position of the new stress state, relative to the initial yield surface, is checked by calculating the yield function f. The value of the function is checked against the yield surface error tolerance *FTOL*, where *FTOL* is a small positive number (e.g., 1E-7). If the stress state is within the yield surface, or sufficiently close to it that the yield function is less than or equal to *FTOL*, then the

increment is accepted as totally elastic and the algorithm is complete. However, if the new stress state exceeds the boundary of the yield surface, the algorithm enters into an iterative plastic correction loop as shown in Figure 2-5. The process by which plastic correction is made when plasticity occurs is clearly displayed in Figure 2-5. As in the figure, the elastic prediction is first done to obtain a new stress state $\sigma^{i=0}$, which exceeds the initial yield surface, where the superscript i counts for the iteration of the loop. The yield function $f^{i=0}$, which gives the distance between the stress state and the previous yield surface, is greater than $FTOL$, causing the algorithm to enter the plastic correction loop. After one iteration of the correction loop, the stress is decreased to $\sigma^{i=1}$ and the plastic variables $H^{i=0}$ are adjusted, causing the yield surface to kinematically harden and move toward the current stress state. These adjustments work in harmony to decrease the value of the yield function. If the yield function $f^{i=1} \geqslant FTOL$, the next iteration should be made. After the second iteration in this illustration, $f^{i=2}$ is less than FTOL and the iteration is complete.

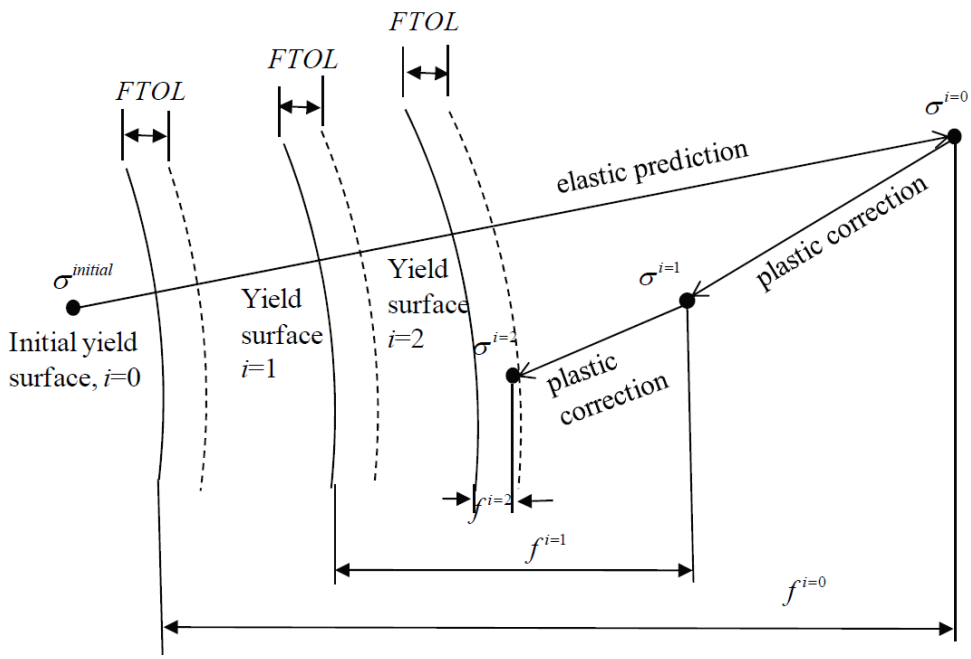

Figure 2-5 Illustration of correction phase of cutting plane algorithm

During the plastic phase, the equations governing the plastic correction loop are as follows:

$$d\sigma_{ij} = -D_{ijkl} d\varepsilon_{kl}^{p} \tag{2.54}$$

$$d\boldsymbol{\varepsilon} = d\boldsymbol{\varepsilon}^{\mathbf{e}} + d\boldsymbol{\varepsilon}^{\mathbf{p}} = 0 \tag{2.55}$$

$$d\varepsilon_{ij}^{p} = d\lambda \frac{\partial g}{\sigma_{ij}} \tag{2.56}$$

$$dH_i = d\lambda \cdot h_i \tag{2.57}$$

The target outcome is that the stress state must be corrected to return into the domain of the yield surface based on current σ^i and f^i, so that the value of the new yield function satisfies $f^{i+1} = 0$. If the yield function is expanded to a Taylor series, in terms of the current stress and internal plastic state variables, ignoring the high-order items:

$$f^{i+1} = f^i + \left(\frac{\partial f^i}{\partial \sigma_{ij}}\right)\left(\sigma_{ij}^{i+1} - \sigma_{ij}^i\right) + \left(\frac{\partial f^i}{\partial H_k}\right)\left(\mathrm{H}_k^{i+1} - \mathrm{H}_k^i\right) \tag{2.58}$$

This equation can be also written as follows:

$$f^{i+1} = f^i + \left(\frac{\partial f^i}{\partial \sigma_{ij}}\right) d\sigma_{ij} + \left(\frac{\partial f^i}{\partial H_k}\right) dH_k = 0 \tag{2.59}$$

Combining Eq. (2.59), Eq. (2.54), Eq. (2.56), and Eq. (2.57), $d\lambda$ can be calculated as follows:

$$d\lambda = \frac{f^i}{\left[\frac{\partial f^i}{\partial \sigma_{ij}}\right]^T D_{ijkl} \frac{\partial g^i}{\partial \sigma_{kl}} - \frac{\partial f}{\partial H^i} h_i} \tag{2.60}$$

Finally, the stresses and internal plastic state variables are corrected based on the following equations:

$$\sigma_{ij}^{i+1} = \sigma_{ij}^i - D_{ijkl} d\lambda \frac{\partial g^i}{\sigma_{kl}} \tag{2.61}$$

$$H^{i+1} = H^i + d\lambda \cdot h_i \tag{2.62}$$

Then the updated stresses are used to check the yield function once more, and the plastic correction loop stops until the value of the yield function satisfies $f^{i=1} \leqslant FTOL$.

The procedure of the algorithm is summarized in Figure 2-6:

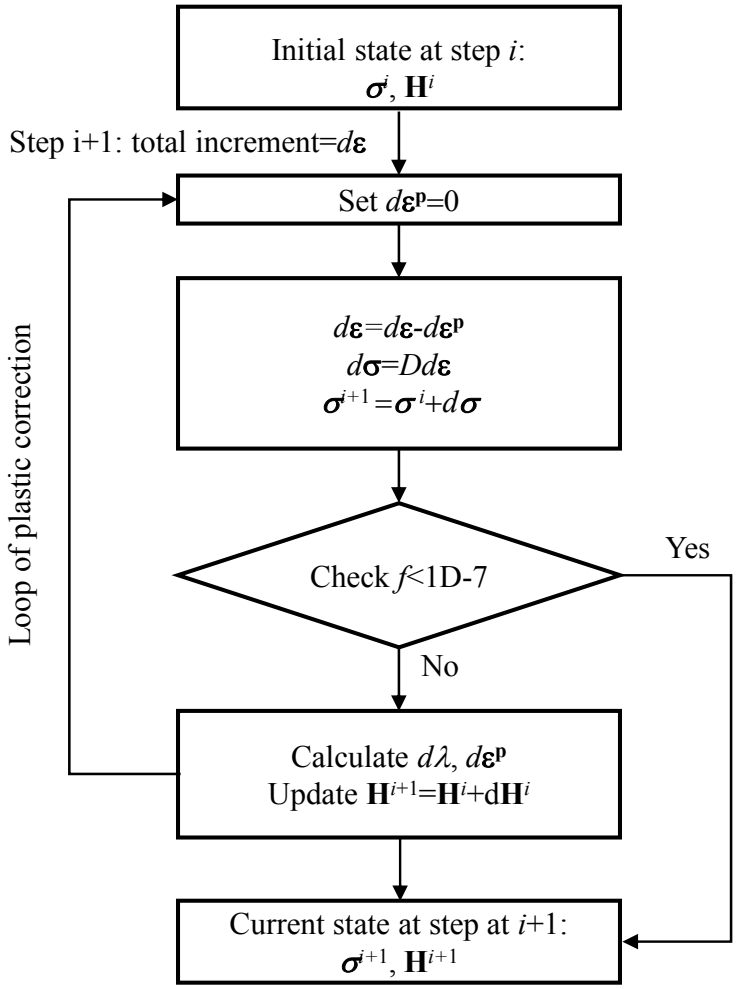

Figure 2-6 Flow chart of iteration procedure of the cutting plane algorithm

For SIMSAND model, the original constitutive model has been described in Section 2.2.1, and its extended model within the framework of micropolar theory has also been introduced in Section 2.2.2. The following derivations are simply used to calculate the plastic multiplier of the micropolar SIMSAND model, per Eq. (2.60), within the framework of micropolar theory. The plastic multiplier of the micropolar critical state–based model is expressed as

$$d\lambda = \frac{f}{\left[\frac{\partial f}{\partial \sigma_{ij}}\right]^T D_{ijkl} \frac{\partial g}{\partial \sigma_{kl}} - \frac{\partial f}{\partial \varepsilon_d^p}\frac{\partial g}{\partial q}} \tag{2.63}$$

where f is the yield function expressed in Eq. (2.8), and D_{ijkl} is the elastic stiffness matrix expressed in Eq. (2.63). Other partial derivatives are derived as follows:

$$\frac{\partial f}{\partial \sigma} = \frac{\partial f}{\partial q}\frac{\partial q}{\partial \sigma} + \frac{\partial f}{\partial p'}\frac{\partial p'}{\partial \sigma} \tag{2.64}$$

$$\frac{\partial g}{\partial \sigma}=\frac{\partial g}{\partial q}\frac{\partial q}{\partial \sigma}+\frac{\partial g}{\partial p'}\frac{\partial p'}{\partial \sigma} \tag{2.65}$$

$$\frac{\partial f}{\partial \varepsilon_d^p}=-\frac{M_p}{k_p+\varepsilon_d^p}+\frac{M_p\varepsilon_d^p}{\left(k_p+\varepsilon_d^p\right)^2} \tag{2.66}$$

$$\frac{\partial f}{\partial p}=-\frac{q}{\left(p'\right)^2},\ \frac{\partial f}{\partial q}=\frac{1}{p'} \tag{2.67}$$

$$\frac{\partial g}{\partial p}=A_d\left(M_{pt}-\frac{q}{p'}\right),\ \frac{\partial g}{\partial q}=1 \tag{2.68}$$

$$\frac{\partial p'}{\partial \sigma}=\left\{\frac{1}{3}\ \frac{1}{3}\ \frac{1}{3}\ 0\ 0\ 0\ 0\right\} \tag{2.69}$$

$$\frac{\partial q}{\partial \sigma}=\frac{1}{2q}\mathbf{P}\sigma \tag{2.70}$$

Based on all the foregoing expressions, the micropolar critical state–based model can be solved via the cutting plane algorithm with high efficiency.

2.3.3 Numerical validations

The numerical element test is a necessary process for ensuring the correctness of the implemented user subroutine. Therefore, the simulated results from a UEL should be verified by those counterparts obtained from the original integration point program (IPP), whose constitutive law is defined at the stress–strain level. The results from the stress–strain level IPP are assumed to be correct and considered as the objective ones by default. In fact, before validating the UEL program, the correctness of UMAT (less advanced than UEL) has been validated, which can be found in Appendix C. Bearing in mind that the UEL is a two-dimensional type, element tests are confined to a domain of plane strain condition. At the strain-stress level, the specimen is ideally maintained in a state of homogeneity (with no strain localization). In this condition, the micropolar approach will have no specific influence on the simulated results from the UEL, compared with those results from the IPP that are under the framework of classical continuum theory. That is to say, the micropolar theory

does not offer any advantages in the homogeneous field, in which there is no rotation of individual grains.

For validation, biaxial drained and undrained tests for both dense and loose Toyoura sand were simulated by an IPP and a UEL, with model parameters referred to (Jin et al., 2016) and (Wu et al., 2017). There are two steps for biaxial tests, the first step is isotropic compression, and the second one is the shear loading. For drained test, shear loading is applied by controlling the displacement of the top side of the specimen, while keeping the confining pressure constant. Differently, for undrained tests, the specimen volume is kept constant by controlling the axial and lateral strain at the same time in the second shear loading step. The comparisons of the simulations between IPP and UEL are shown in Figure 2-7 and Figure 2-8, from which it can be found that the simulated results produced by UEL are absolutely consistent with those from IPP, thus amply verifying the correctness of the UEL implementation. In all the figures below, each subfigure denotes different relations: (a) axial strain versus deviatoric stress, (b) mean effective stress versus deviatoric stress, (c) axial strain versus void ratio, (d) mean effective stress versus deviatoric stress. It should be noted that the step size greatly affects the final results, which is to say that a smaller step size will yield a more accurate solution.

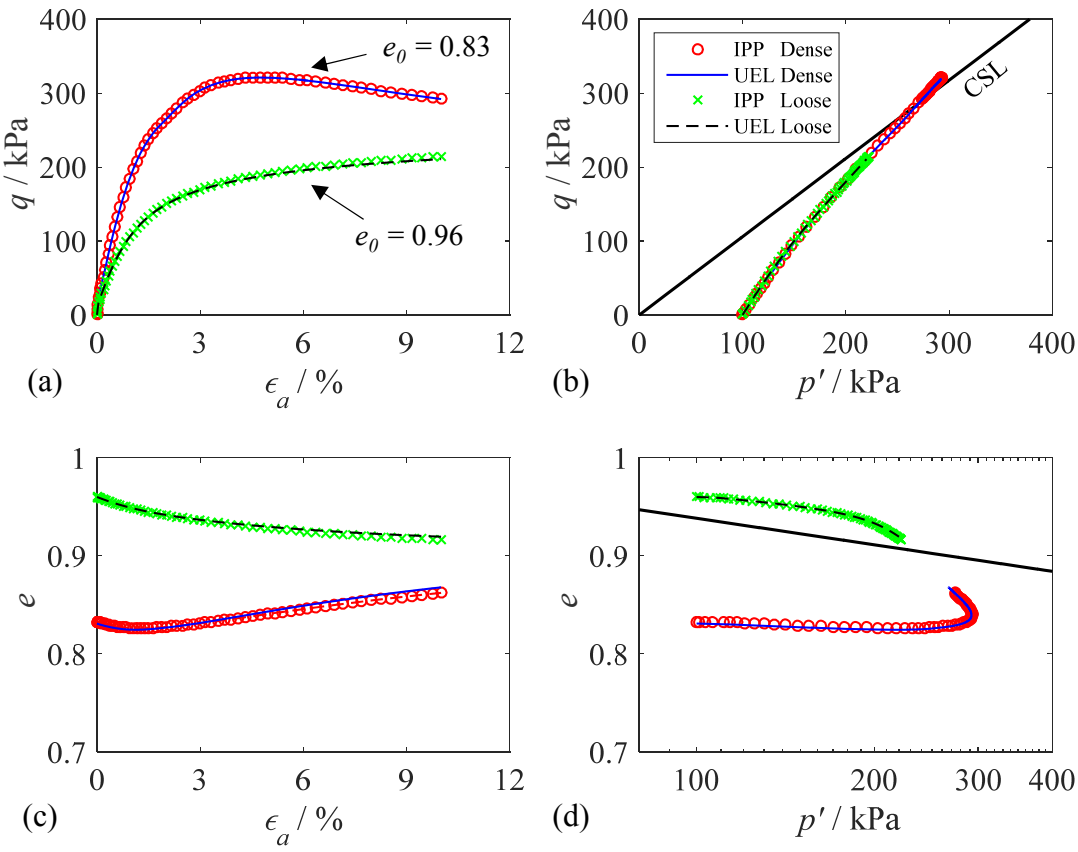

Figure 2-7 Comparisons between IPP and UEL in simulating biaxial drained tests

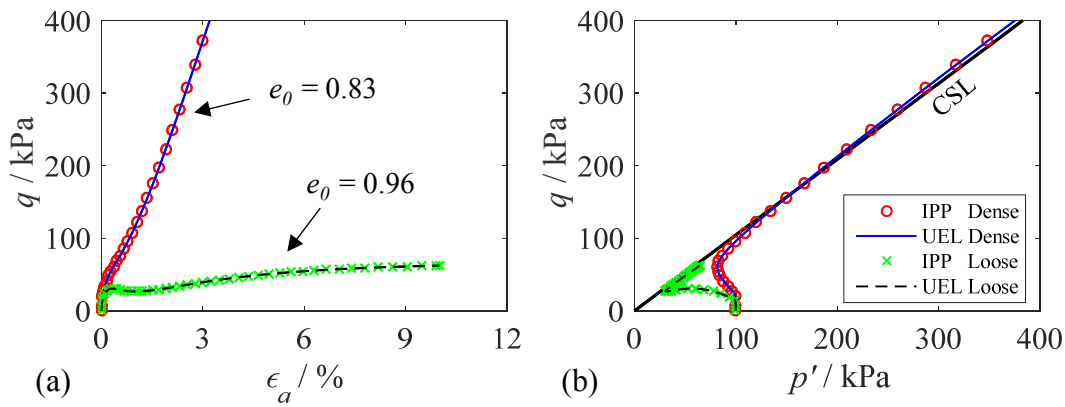

Figure 2-8 Comparisons between IPP and UEL in simulating biaxial undrained tests

2.4 Verification of the micropolar model with plane strain tests results

A series of biaxial tests have been conducted on medium dense and dense F-75 Ottawa sand (see Appendix E) under low and high confining pressure conditions to investigate the effects of specimen density, confining pressure, and sand grain size and shape on the constitutive and stability behavior of granular materials (Alshibli and Sture, 2000). The micropolar model was used to predict the stress-strain relationship of F-75 silica sand under plane strain condition. Material parameters, which are listed in Appendix E at the end of the manuscript, have been calibrated with an optimization technique by fitting the experimental data of an isotropic compression test as well as a series of triaxial tests under different confining pressures. It must be noted that on the basis of the calibrated parameters in Appendix E, the parameters used in simulating the biaxial tests have been slightly modified a little as may be found a larger critical friction angle ϕ_u listed in Table 2-1 compared to Table E-1. Some evidences could support this difference in the findings of Alshibli et al. (2003), in which the comparisons between principal stress ratio versus axial strain of conventional triaxial compression and plane strain experiments indicate that the peak stress value and the residual stress of plane strain experiments are slightly higher than those of the conventional triaxial compression experiments. From a mathematical point of view, the slightly higher value of the peak and residual stress can be explained by the fact that for different loading conditions with different Lode angles can result in the differences in the critical friction angle in the constitutive law. What's more, the restrained platen end of the specimens in the biaxial tests can also lead to a higher residual strength (Alshibli et al., 2003). For the two incorporated micropolar parameters, the internal length scale parameter l_c was set to be identical to the mean grain size d_{50} (0.22 mm) of F-75 sand and the micropolar shear modulus G_c was set to be half of the classical shear modulus G.

Table 2-1 Material parameters used to simulating the biaxial tests

Parameters	K_0	ζ	ϕ_u	e_{ref}	λ	k_p	A_d	n_p	n_d
Values	60	0.63	38.5	0.776	0.015	0.004	0.4	1	2

Referring to the publication of Alshibli and Sture (2000), experiments on dry specimens with dimensions of 150 mm in height and 80 mm in width under drained plane strain conditions were conducted. In the present study, the F-75 sand was chosen as the objective experimental data, i.e.

medium dense with initial void ratio of 0.629 (D_r = 55%) under low confining pressure (15 kPa), medium dense with initial void ratio of 0.655 (D_r = 47%) under high confining pressure (100 kPa), very dense with initial void ratio of 0.495 (D_r = 97%) under low confining pressure (15 kPa), and very dense with initial void ratio of 0.527 (D_r = 87%) under high confining pressure (100 kPa). With a constant confining pressure applied to the specimens using a cell pressure reservoir, a constant axial displacement rate was applied on the specimens. The bottom end platen was restrained from movement and the top end platen was rigidly connected to the loading ram. During the testing process, the specimen's deformation was monitored by noting the displacements of the grid imprinted on the membrane surface covering the specimen. In finite element simulations, in order to develop a single shear band which was the case in most of the experimental tests, the bottom of the specimen was allowed to slide in the lateral direction, and an imperfect element with a relative larger initial void ratio was set at the left top of the specimen to trigger the onset of strain localization.

As we know that significant grain rotations occur inside the shear band, consequently, the shear bands represented by the independent micro rotations or rearrangements of the simulated results from the micropolar model were compared with those represented by deformation from the experimental tests. Figure 2-9 shows a shear band example of the experimental test and numerical simulation for very dense sand under high confining pressure at axial strain of 10%, which illustrates that the finite element result is in good agreement with the laboratory test, and the micropolar model is able to capture the realistic shear band pattern no matter the shear band thickness or the orientation of localization. Figure 2-10 and Figure 2-11 present the comparisons between the predicted and experimental data in biaxial tests for F-75 sand, which shows that the predicted curves of the principal stress ratio versus axial strain agree fairly well with the experimental data while the volumetric strains are poorly predicted.

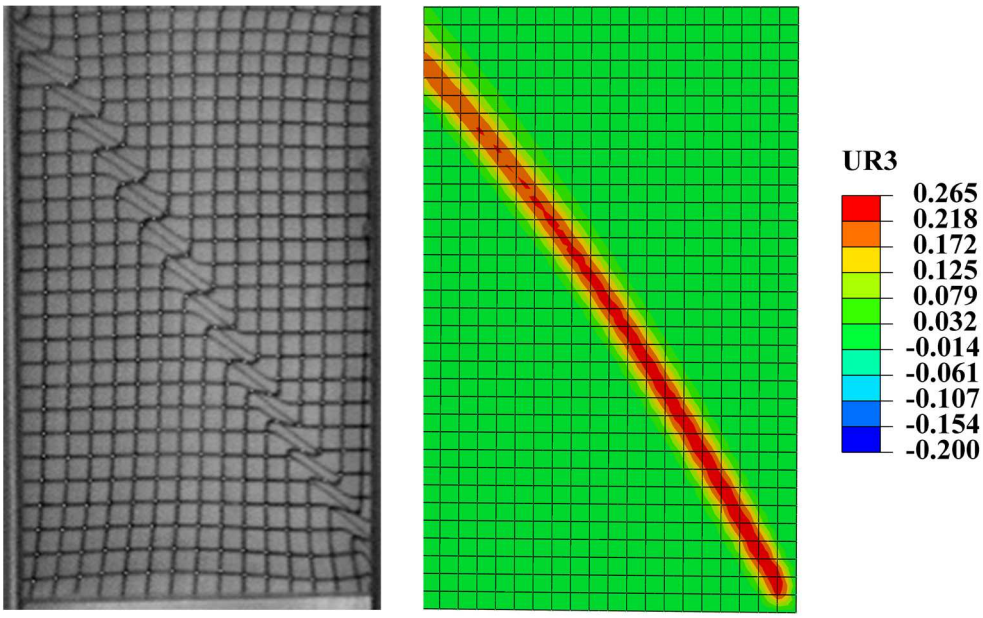

(a) (b)

Figure 2-9 Comparison between experimental and simulated shear band for very dense sand under 100 kPa confining pressure at 10% axial strain: (a) deformation in experimental biaxial test; (b) grain rotations by the micropolar model

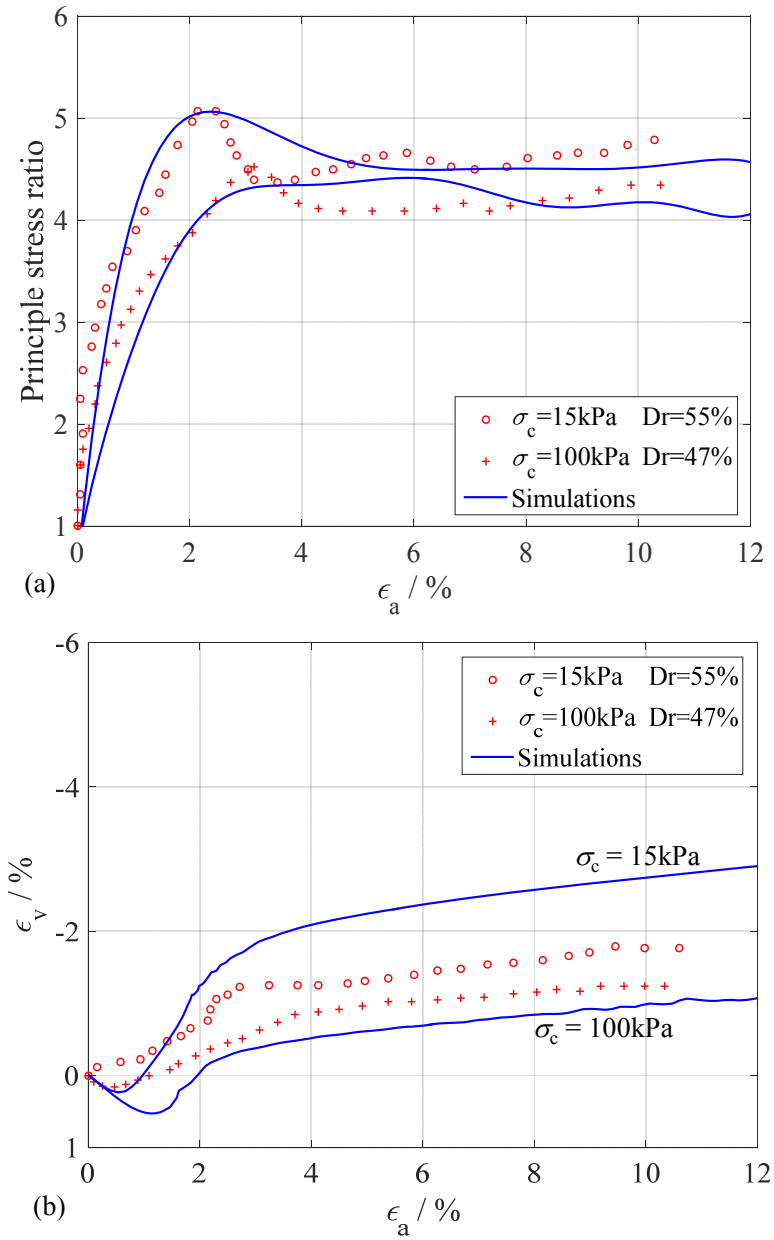

Figure 2-10 Comparisons between the simulated solutions and experimental data for medium dense F-75 sand: (a) axial strain versus principle stress ratio; (b) axial strain versus volumetric strain;

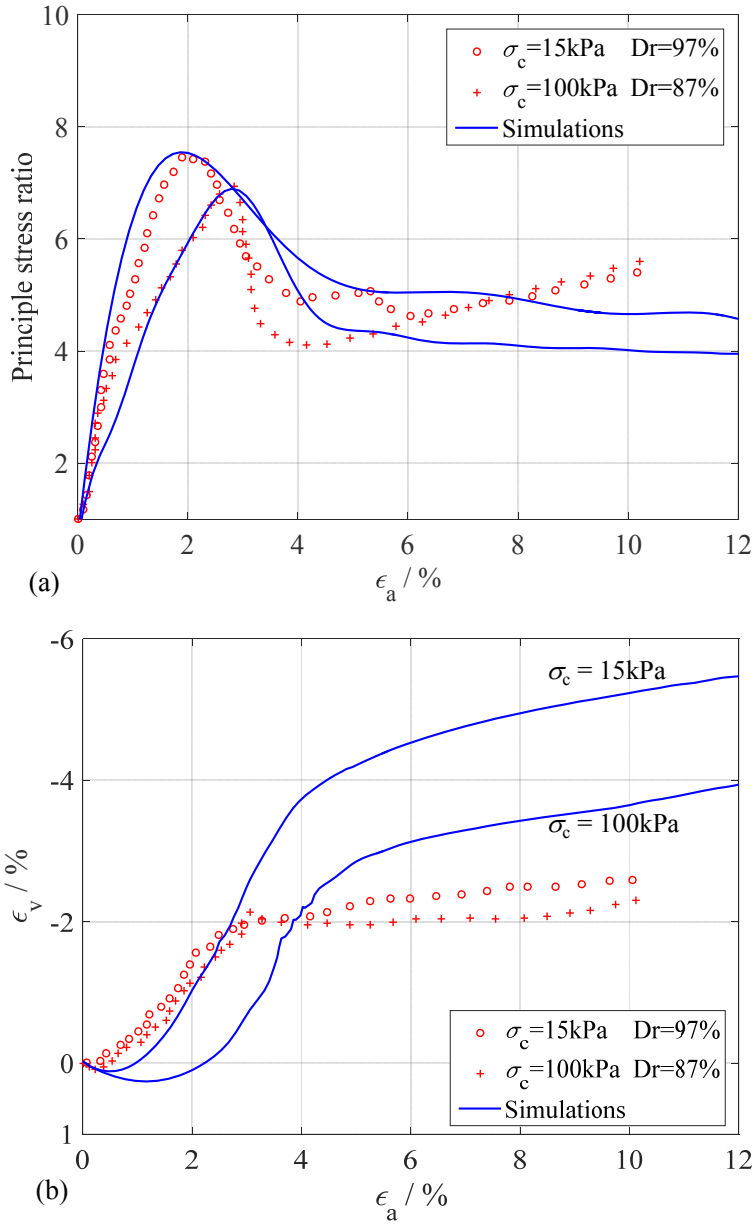

Figure 2-11 Comparisons between the simulated solutions and experimental data for very dense F-75 sand: (a) axial strain versus principle stress ratio; (b) axial strain versus volumetric strain;

2.5 Numerical simulations of shear bands in biaxial tests

Admittedly, the solutions to strain localization caused by softening based on classical continuum mechanics may have congenital numerical or analytical technical problems and suffer from ill-posed mathematics. As we know the incorporated micropolar approach is mainly used to overcome convergence difficulties and deal with the mesh dependency problems in finite element analysis

when the strain localization phenomena occur, the regularization efficiency of the polarized SIMSAND model will be analyzed in this section.

The FE simulations of the biaxial test using the micropolar SIMSAND model have been compared with those from the classical SIMSAND model. Constitutive parameters referred to the ones of Ottawa sand, which have been calibrated in the Appendix E at the end of the manuscript. We considered a dry, dense specimen with a width of 10 cm, a height of 20 cm, and a unit thickness (in 2D condition, it is 1m by default). In the test, which featured two steps, mixed control was adopted. The first step was isotropic compression with a confining pressure of 100 kPa, and the second was shear loading by controlling the displacement of the top surface (up to a total axial strain of 5%). To ease the triggering of the strain localization, the lateral deformations of the top and bottom surfaces of the specimen were constrained. Four different mesh sizes, mesh 10×20, mesh 15×30, mesh 20×40 and mesh 30×60, were used to investigate the mesh sensitivity. The expression mesh 10×20 indicates that the width and height of the specimen were uniformly divided by 10 and 20 elements, respectively. And the other expressions represent the corresponding discretizations.

2.5.1 Mesh dependency of the simulated results by classical SIMSAND model

2.5.1.1 Shear bands and mechanical response

First the simulations were conducted using the classical SIMSAND model. Shear bands in current configuration, identified by the equivalent plastic strain distribution of four different discretizations, are shown in Figure 2-12, and the load versus displacement curves of four different mesh sizes are plotted in Figure 2-13. From the shear band contours and the load–displacement curves, it can be observed that the calculations for the mesh 10×20 and mesh 15×30 are completely finished. However, for the mesh 20×40, the calculation stops just after the peak loading, and—more seriously—it does not become convergent at the peak loading for the mesh 30×60. The reason is that the occurrence of strain-softening leads to a localization of strain into a single finite element no matter how small the element is. Thus, the width of the strain-localization region and the energy consumed by failure due to strain softening converge to zero as the element size is decreased to zero, which is an unrealistic feature of local continuum and not representative of real materials(Bažant et al., 1984). For refined

meshes, the localized deformation is relative large, in which the acoustic tensors of many gauss points become singular resulting in the difficulty of convergent or pathological solutions. For the fully formed shear bands in mesh 10×20 and mesh 15×30 in Figure 2-12, we can see that the shear band thickness is dependent on the mesh size, that the coarser the element size, the thicker the shear band will be. In Figure 2-13, the load peak of the mesh 10×20 (coarse mesh) is slightly higher and more delayed than the others' (fine mesh). Additionally, the specimen displays more stiff behaviors in the softening regime of a coarse mesh than in a fine mesh. From the plastic strain contour of mesh 30×60 and the green curve in the load–displacement plane, it can be seen that the strain localization occurs just before the peak loading, which coincides with the experimental observations of Desrues and Viggiani (2004).

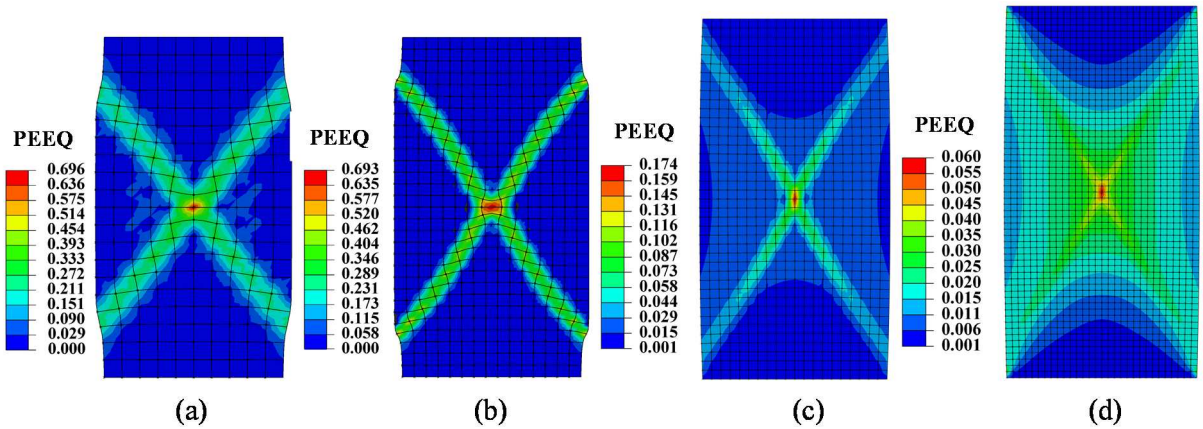

Figure 2-12 Shear bands of four different mesh sizes using the classical model: (a) mesh 10×20; (b) mesh 15×30; (c) mesh 20×40; (d) mesh 30×60

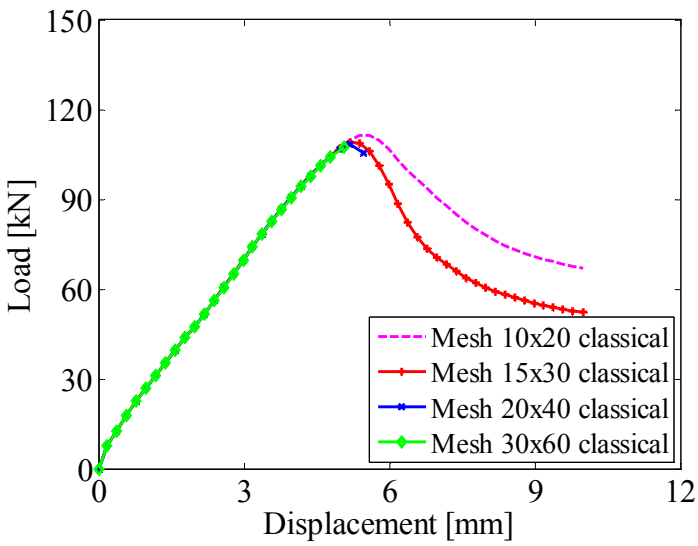

Figure 2-13 Load–displacement of four different mesh sizes using the classical model

2.5.1.2 Shear band inclination

According to the studies in the past, when it came to the investigations of the mesh dependency problems, many of the discussions were concentrated solely on shear band thickness and strength capacity in the post-peak regime, whereas shear band orientations have been rarely studied. In terms of shear band patterns, the present study considers not only the thickness of the band but also its orientation. Shear band orientation is obtained by measuring the angle between the centerline of the intense strain-localized region and the horizontal principal stress (under original configuration). The centerline can be explained as a sliding surface in experiments; the shear band orientations of three different mesh sizes are shown in Figure 2-14 (i.e., β_1, β_2, and β_3). Considering that the calculation of Mesh 30×60 did not converge in the early stage, the other three shear band orientations were measured, respectively, as β_1 = 52.69°, β_2 = 57.65°, and β_3 = 60.15°. Thus it may be discerned that the finer the mesh, the larger the shear band inclination angle.

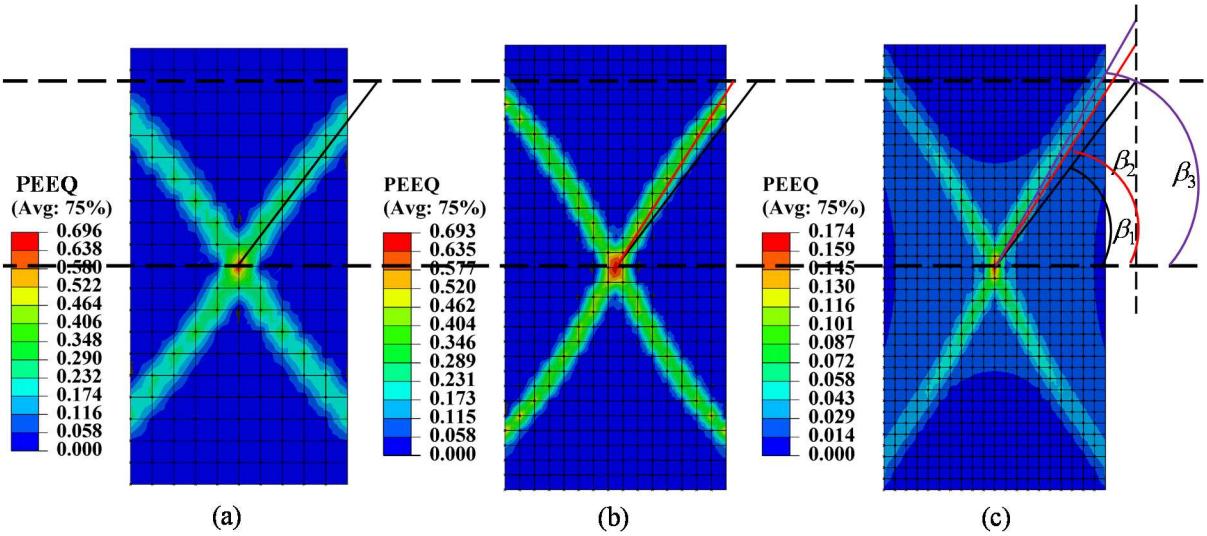

Figure 2-14 Shear band orientation of different meshes (a) mesh 10×20 β_1=52.69°; (b) mesh 15×30 β_2=57.65°; (c) mesh 20×40 β_3=60.15°

From the contours in Figure 2-12 and Figure 2-14, it can be seen that not only shear band thickness but also shear band orientation is dependent on the mesh size. As a result, some conclusions about the mesh dependency within the framework of classical continuum theory can be obtained from the simulated results. First, when the specimen is refined, the acoustic tensors of some localized elements will become singular upon the occurrence of strain localization, resulting in the

difficulty of convergence. Second, the patterns of the shear band, including thickness and orientation, are significantly dependent on the mesh size. Third, load carrying capacity relies on the mesh size, especially in the post-peak regime.

2.5.2 Mesh independency of the simulated results by micropolar SIMSAND model

2.5.2.1 Shear bands and mechanical response

To demonstrate the regularization capability of the micropolar technique, the same simulations of biaxial tests were conducted again with the micropolar SIMSAND model. The shear bands, identified by the plastic strain, of four different mesh sizes are displayed in Figure 2-15. In a departure from the calculations within the framework of classical continuum theory, all four simulations could be completely finished without any numerical convergence problem. And, the mesh independency of shear band thickness for the four different mesh sizes can be easily observed. Load versus displacement curves of the four discretizations are presented in Figure 2-16, showing that the mesh dependency problems have been significantly relieved. Although the pink curve of Mesh 10×20 is a little stiffer than the other three curves in the softening regime, the load–displacement curves of the other three fine meshes coincide with each other absolutely. It is worth noting that the difference of the curves in the load–displacement plane can be used to precisely evaluate the degree of mesh dependency.

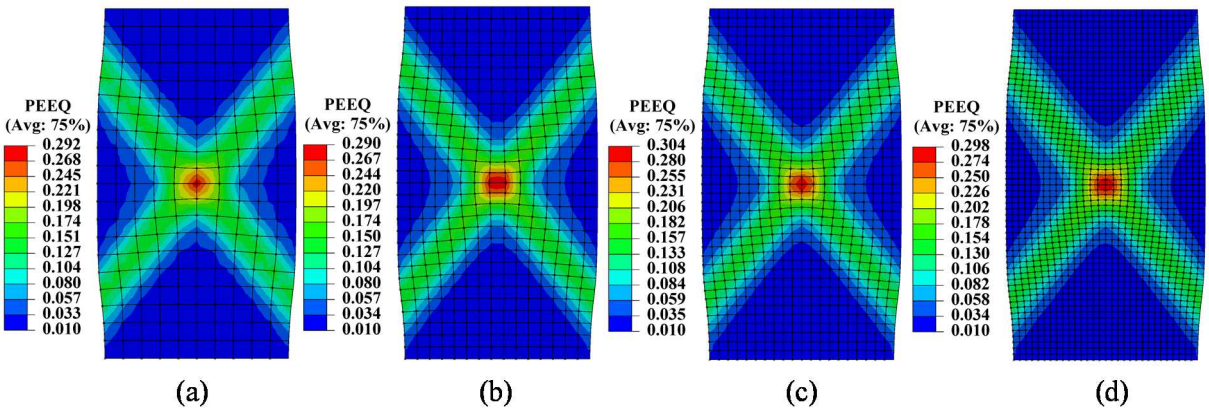

Figure 2-15 Shear bands of four different mesh sizes using the micropolar model: (a) mesh 10×20; (b) mesh 15×30; (c) mesh 20×40; (d) mesh 30×60

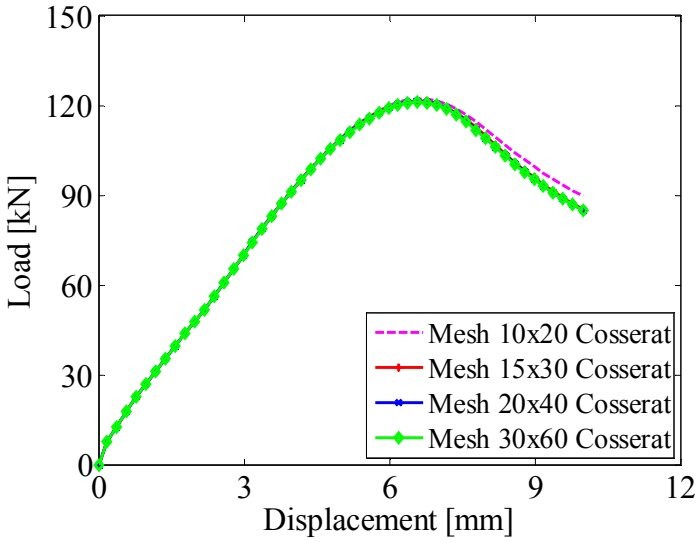

Figure 2-16 Load–displacement of four different mesh sizes based on micropolar model

2.5.2.2 Shear band orientation

Figure 2-17 measures the shear band–inclined angle of the four different meshes, with the shear band inclination of mesh 10×20 at β_1 = 53.10°—only slightly smaller than the orientations of the other three meshes. The shear band orientations of the three fine meshes have been proven to be the same: $\beta_2 = \beta_3 = \beta_4$ = 53.22°. Therefore, the micropolar SIMSAND model has succeeded in significantly relieving the mesh dependency of shear band orientation.

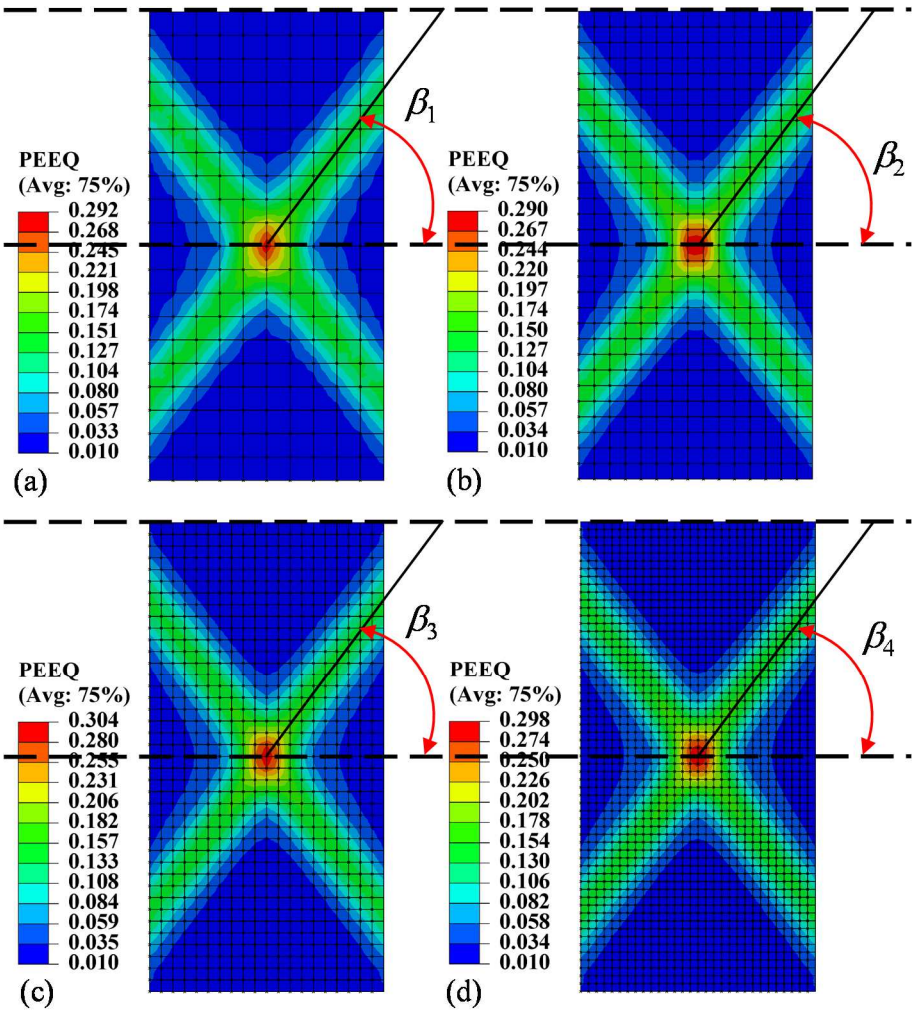

Figure 2-17 Shear band orientation of different mesh: (a) mesh 10×20 β_1=53.10°; (b) mesh 15×30 β_2=53.22°; (c) mesh 20×40 β_3=53.22°; (d) mesh 30×60 β_4=53.22°

To conclude, being more advanced than the classical constitutive model, the micropolar SIMSAND model shows a good convergence property and significantly alleviates the mesh dependency problems.

2.6 Application of the micropolar model in simulating retaining wall

Earth pressure on retaining walls is one of the soil mechanics classical problems. In this section, a small scale rigid retaining wall under passive condition was considered. As shown in Figure 2-18, a two dimensional sand block in a rectangular rigid box with the dimension of 200×100 mm is selected to be the model, and the interaction between the sand and the box is smooth, from which the boundary conditions can be clearly illustrated. The height of the wall is of 50 mm which moves

horizontally towards the soil mass, and the contact between the wall and the soil behind the wall is assumed to be perfectly adhesive.

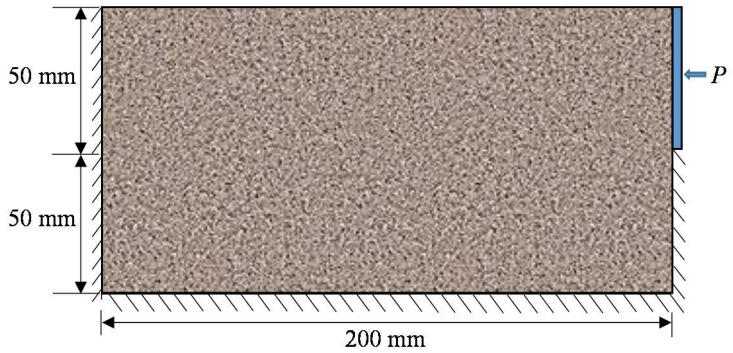

Figure 2-18 A small scale retaining wall model in passive condition

In order to illustrate the regularization effectiveness of the micropolar model to contribute to the mesh independency in simulating strain localization problems in numerical analysis with finite element method, three different element sizes, i.e. mesh 20×10, mesh 28×14, and mesh 40×20, were used to represent the model. The parameters were referred to those calibrated in Appendix E. The sand behind the wall was very dense with a relative density of 97%, and a unit density of 20 kg/m^3, moreover, a downward centrifugal acceleration 10*g* has been also considered.

2.6.1 Mesh dependency of the simulated results by classical SIMSAND model

First, the simulations were conducted by the classical SIMSAND model, the simulated results are presented in Figure 2-19 to Figure 2-22. From the deformed configurations in Figure 2-19, it can be seen that the shear band thickness is significantly affected by the element size, the larger the element sizes is, the narrower the shear band thickness will be. As a result, a great distortion occurs for the fine mesh 40×20. The shear bands identified by the equivalent plastic strain and the void ratio in Figure 2-20 and Figure 2-21 are also found to be mesh dependent. Figure 2-22 shows the mesh dependency of the load-displacement curves for different mesh sizes, which illustrates that, with a finer mesh, the loading peak is reached with a smaller horizontal displacement, while the coarser mesh has a higher residual bearing strength.

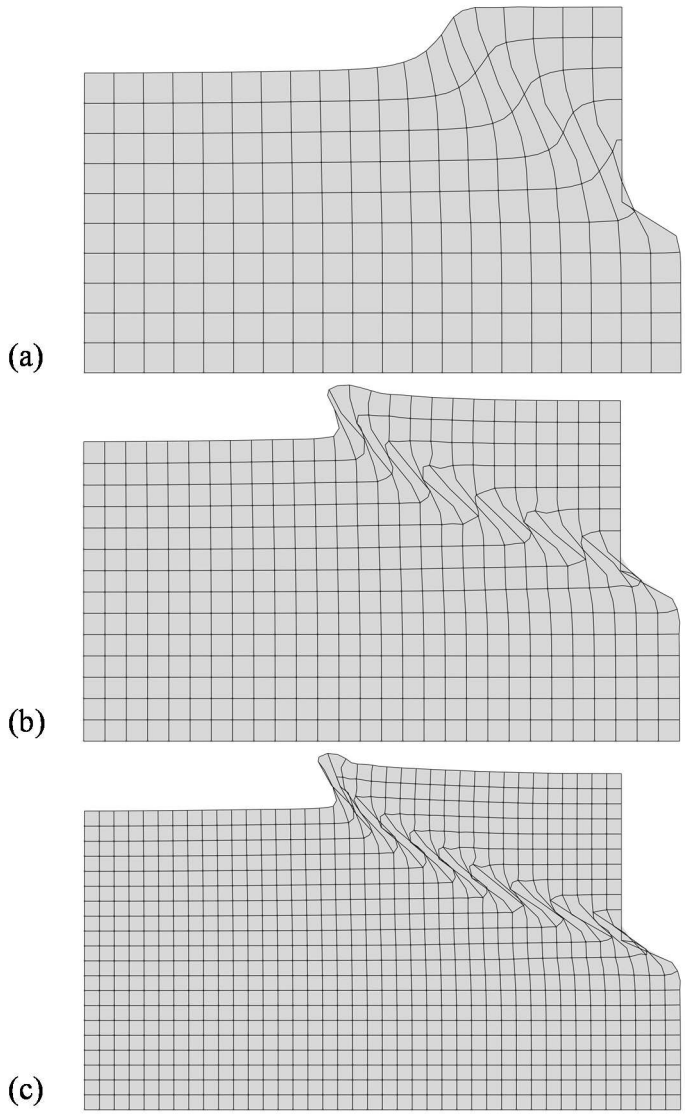

Figure 2-19 The deformation of different meshes by classical model: (a) mesh 20×10; (b) mesh 28×14; (c) mesh 40×20;

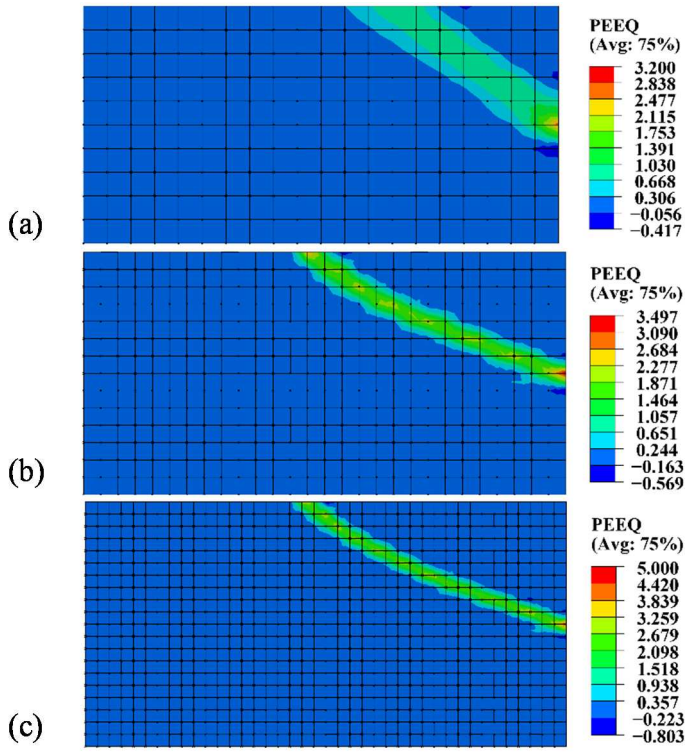

Figure 2-20 The equivalent plastic strain for different meshes by classical model: (a) mesh 20×10; (b) mesh 28×14; (c) mesh 40×20;

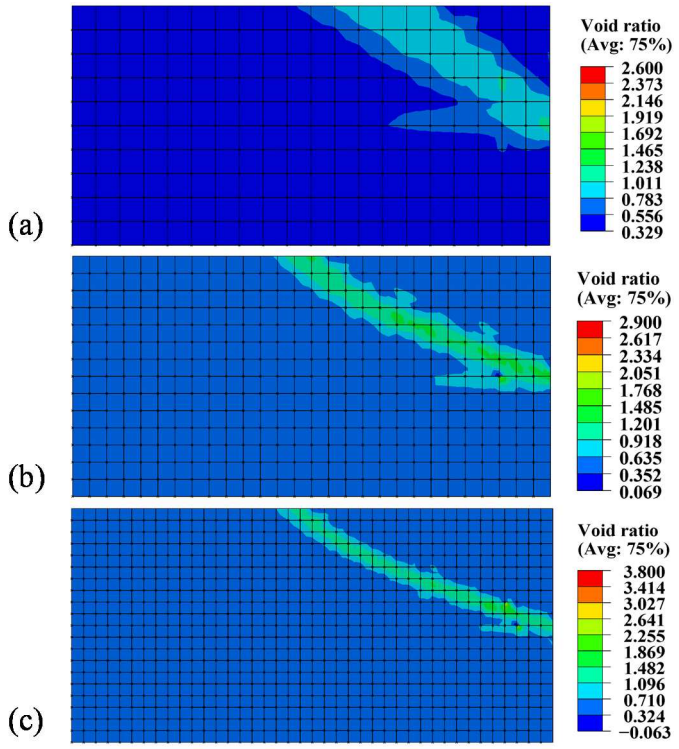

Figure 2-21 The void ratio for different meshes by micropolar model: (a) mesh 20×10; (b) mesh 28×14; (c) mesh 40×20;

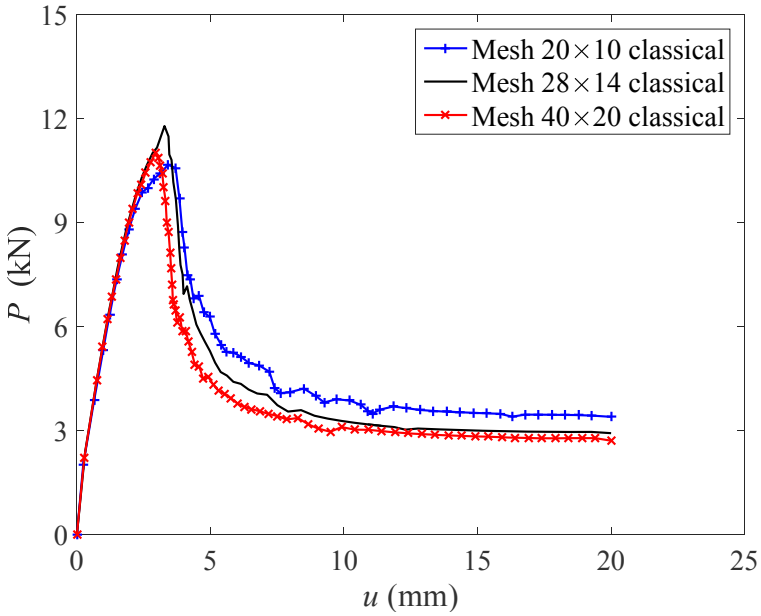

Figure 2-22 Passive load-displacement curves of the retaining wall from classical model

2.6.2 Mesh independency of the simulated results by micropolar SIMSAND model

Then, the simulations were conducted by the micropolar SIMSAND model. The numerical results are presented in Figure 2-23 to Figure 2-26. Different from the results with the classical model, the deformations obtained by the micropolar model in Figure 2-23 are very uniform and smooth regardless of the element size, because the shear band thickness is controlled by the internal length scale and not by the element size. Similarly, the shear bands obtained with different mesh sizes and identified by the equivalent plastic strain in Figure 2-24 and the void ratio in Figure 2-25 are almost the same. Consequently, the mesh dependency problems of the load-displacement curves have been significantly reduced by the micropolar model as shown in Figure 2-26.

By comparing the numerical results obtained by the classical SIMSAND model with those by the polarized SIMSAND model, the regularization effectiveness of the micropolar theory in alleviating the mesh dependency problems are again verified.

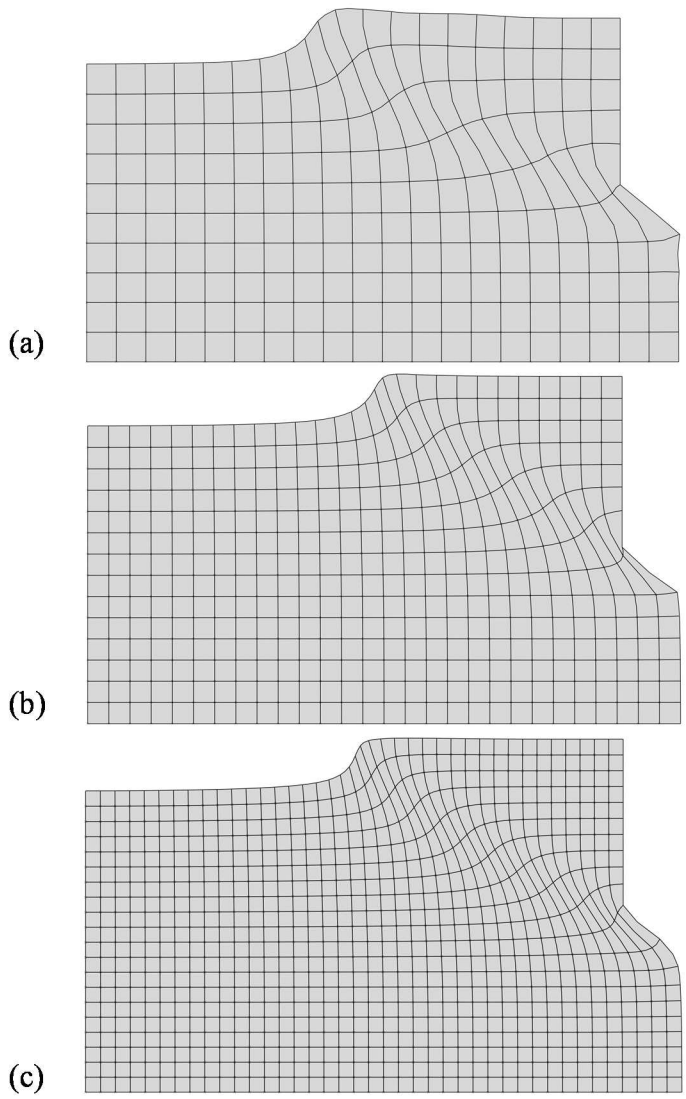

Figure 2-23 The deformation of different meshes by micropolar model: (a) mesh 20×10; (b) mesh 28×14; (c) mesh 40×20;

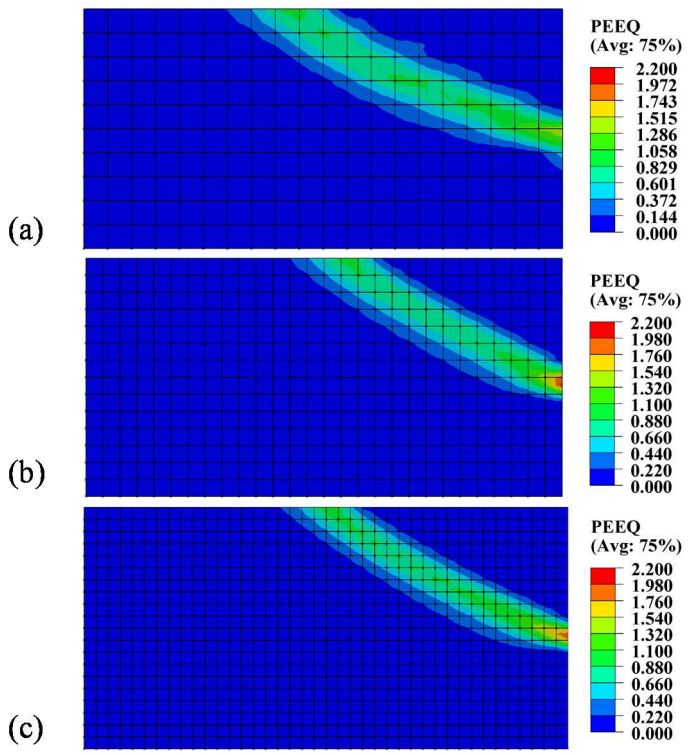

Figure 2-24 The equivalent plastic strain for different meshes by micropolar model: (a) mesh 20×10; (b) mesh 28×14; (c) mesh 40×20;

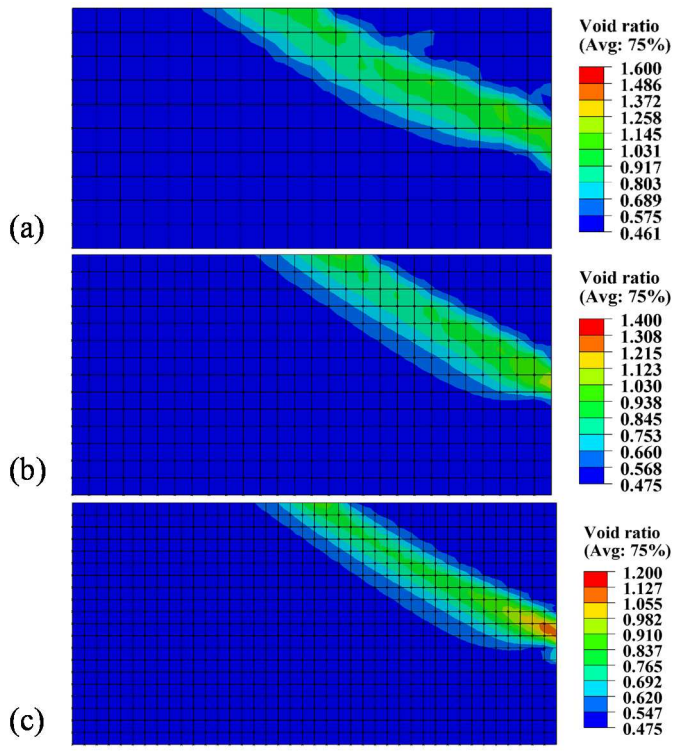

Figure 2-25 The void ratio for different meshes by micropolar model: (a) mesh 20×10; (b) mesh 28×14; (c) mesh 40×20;

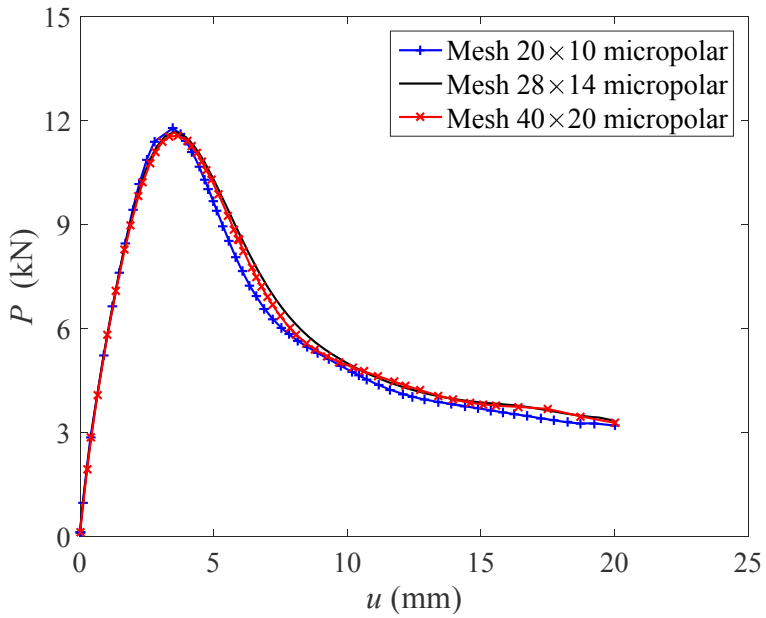

Figure 2-26 Passive load-displacement curves of the retaining wall from micropolar model

2.7 Conclusions

In this chapter, the critical state–based elastoplastic model for sand (SIMSAND model) has been enhanced within the framework of micropolar theory. The FE implementation process of the micropolar SIMSAND model via the user-defined interface of ABAQUS was illustrated in detail. Moreover, the efficiency of the cutting plane method to update stress was also clearly demonstrated. Then, the validation at the single element level was performed with both loose and dense Toyoura sand. Moreover, the micropolar model was used to fit the experimental data in biaxial tests conducted by Alshibli and Sture (2000) with loose and dense F-75 sand. At last, by simulating the shear bands in a biaxial test as well as in a passive retaining wall with Ottawa sand, the regularization effectiveness of the micropolar approach has been proven, showing that not only the bearing capacity but also the shear band patterns were independent of the element mesh size.

Chapter 3 Numerical Analysis of Shear Band

3.1 Introduction

In this chapter, the shear band in a micropolar continuum is further discussed in terms of the onset, thickness and inclination, etc. For the purposes of validation, shear band thickness was also compared with the experimental outcomes. As a regularization approach, an effective regularization ratio of the internal length scale to element size in FE analysis was proposed and discussed, with which the mesh dependency problems could be removed absolutely. In the past, a micropolar Lade's single hardening constitutive model (Alshibli et al., 2006), as well as a hypoplastic model within the framework of micropolar theory (Tejchman et al., 1999), have been used to discuss the influence of initial void ratio, pressure level, and mean grain size on shear band. However, the critical state–based type models for granular materials have rarely been enhanced by the micropolar model for the analysis of shear band.

Therefore, the polarized critical state–based model—micropolar SIMSAND model—was adopted herein to conduct the influence analysis of different factors on shear band. Based on the numerical simulations of strain localization in biaxial tests, the effects of several factors, e.g. internal length, confining pressure, initial void ratio, etc., on the onset and patterns of shear bands have been discussed. In addition, for the specific micropolar SIMSAND model, the influences of three key model parameters, i.e. the critical friction angle ϕ_u, the strength parameter n_p, and the deformation parameter n_d, on the shear band have also been analyzed. Besides the influences on the shear band thickness and the bearing capacity, the focus was also on the effect to the regularization effectiveness ratio proposed in this chapter.

3.2 Numerical investigation of shear band by micropolar approach

3.2.1 Mechanical response

In the last chapter we have shown that the mesh dependency problems could be overcome by the micropolar SIMSAND model. However, the comparisons between the mechanical response of

classical SIMSAND model and micropolar SIMSAND model have not been discussed. Therefore, to clearly identify the differences, the load–displacement curves from the classical and micropolar models are plotted in the same plane as shown in Figure 3-1. Being more advanced than the classical constitutive model, its micropolar counterpart shows a good convergence property and significantly alleviates the mesh dependency. Moreover, the simulations from the polarized model have a higher and more delayed peak load than those from the classical model, showing stiffer characteristics after being polarized in the softening regime. Certainly, the slight difference of Mesh 10×20 is caused by its mesh being too coarse. Thus, it is believed that element size may affect the regularization efficiency. Consequently, the regularization effectiveness related to the internal length scale and mesh size will be discussed in detail in the following section.

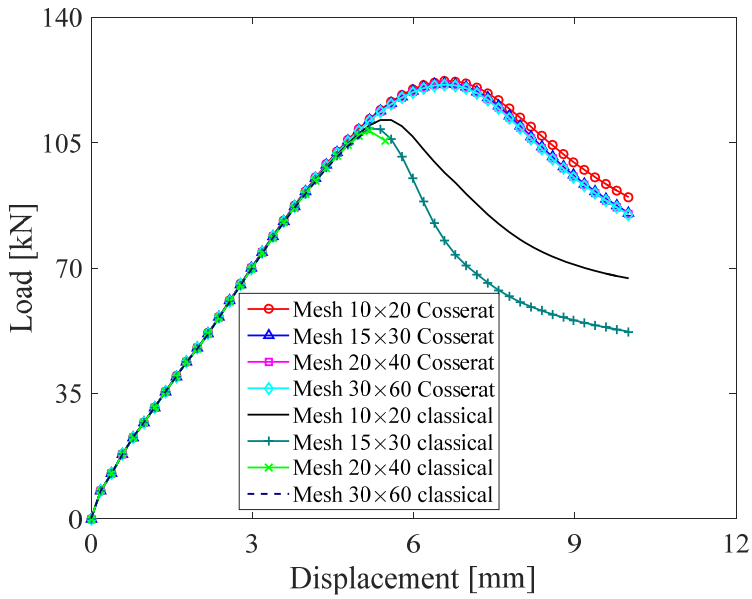

Figure 3-1 Comparisons of load–displacement curves of four different mesh sizes between classical model and micropolar model

3.2.2 Shear band inclination

The micropolar SIMSAND model has succeeded in significantly relieving the mesh dependency of shear band orientation, with the shear band inclination of mesh 10×20 at β_1 = 53.10°, other three fine meshes have been proven to be the same: β_2 = β_3 = β_4 = 53.22°. Furthermore, the shear band orientation was quantitatively studied in this section.

As shown in Figure 3-2, the mobilized dilatancy angle ψ was defined by Muhlhaus and Vardoulakis (1987) based on biaxial tests. In the plane strain condition, $\varepsilon_v = \varepsilon_1 + \varepsilon_2$ and $\gamma = \varepsilon_1 - \varepsilon_2$. Thus, the mobilized dilatancy angle can be expressed as

$$\psi = \arcsin(\alpha) \tag{3.1}$$

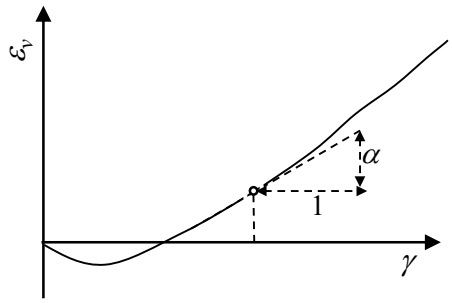

Figure 3-2 Volumetric strain versus shear strain

Based on this definition, the dilatancy angle inside the shear band in the present simulations has been approximately calculated: ψ = 16.7°. In Chapter 1, Mohr–Coulomb, Roscoe, and Arthur's estimations for shear band inclination were defined:

$$\theta_C = 45^\circ + \frac{\phi}{2} = 71^\circ \tag{3.2}$$

$$\theta_R = 45^\circ + \frac{\psi}{2} = 53.4^\circ \tag{3.3}$$

$$\theta_A = 45^\circ + \frac{\phi + \psi}{2} = 57.9^\circ \tag{3.4}$$

It may be observed that the average measured shear band orientation β = 53.2°, with an initial relative density of 100% in the simulations by the micropolar SIMSAND model, is very close to Roscoe's estimation: 45°+ψ / 2 = 53.4°, rather than Mohr–Coulomb's estimation of 71° and Arthur's estimation of 62.2°.

Because the peak frictional angle and dilatancy angle are closely related to the initial density, some other simulations, with a different initial density, should be performed to confirm the finding. The specimen has also been set to the initial void ratios of 0.52, 0.55, 0.58, and 0.65, which correspond to initial relative densities of 87%, 78%, 68%, and 46%, respectively. The measured shear band angles and predicted angles from different simulations were listed in Table 3-1.

Table 3-1 shear band inclinations with different initial density

D_r [%]	β [°]	ϕ [°]	ψ [°]	θ_C [°]	θ_A [°]	θ_R [°]
100	53.2	52	16.7	71	62.2	53.4
87	51.4	50	12.4	70	60.6	51.2
78	50.5	48	9.1	69	59.3	49.5
68	48.2	47	6.8	68.5	58.5	48.4
46	/	44	0	67	56	45

For the material having a relatively low density, no clear shear band can be found by the micropolar continuum. Based on the table, it may be discerned that for the dense material, all the shear bands by the micropolar continuum are close to Roscoe's estimation, as well as that the denser the material, the steeper the shear band inclination—consistent with the experimental conclusion of Alshibli et al. (2000). However, it should also be noted that the measured shear band inclination is extremely sensitive to boundary conditions (Vardoulakis, 1978).

3.2.3 Shear band thickness and shear band identifications

To measure an accurate shear band thickness, the equivalent plastic strain (a measure of the amount of permanent strain in an engineering body, which is calculated from the component plastic strain as defined as the equivalent stress/strain. In current study, the term plastic strain always means the equivalent plastic strain) along a path perpendicular to the shear band orientation should be extracted and recorded. For simplification, the horizontal red line through the specimen center in Figure 3-3 was selected as the reference direction for all the simulations. According to Figure 3-3 (a), the reference direction and the shear band orientation are marked, and in Figure 3-3 (b), the thickness of shear band can be calculated: TSB=$l\cdot\sin(\beta)$. In this way, the shear band thickness of different simulations can easily be compared.

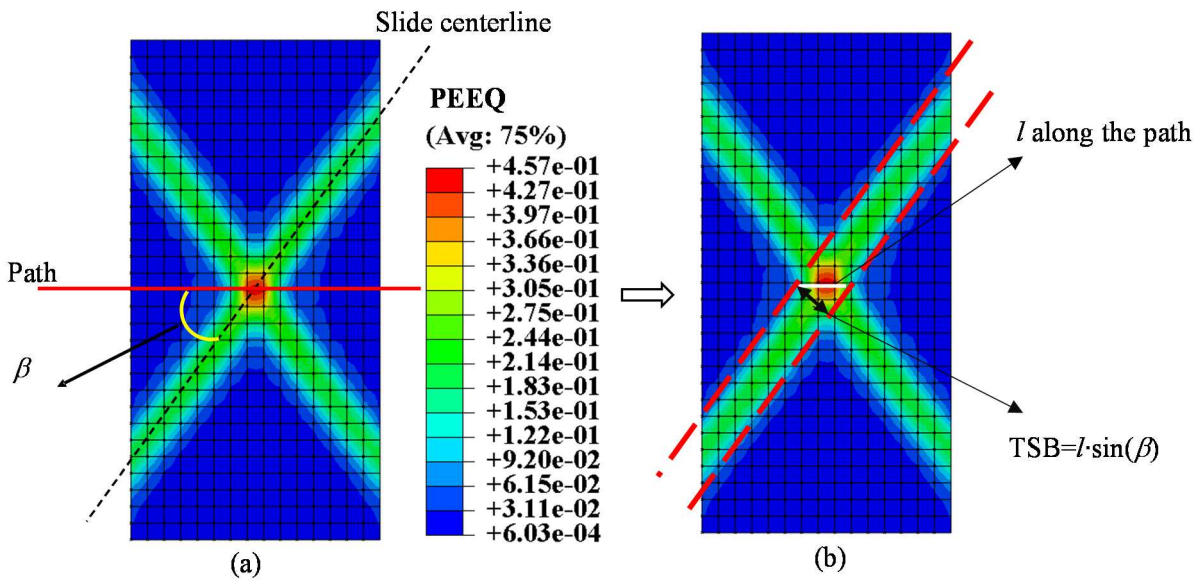

Figure 3-3 Identification of shear band thickness by equivalent plastic strain: (a) selected path and shear band orientation; (b) calculation of the shear band thickness

As has been demonstrated, in addition to equivalent plastic strain, other state variables, such as void ratio, axial strain, microrotations, and microcurvatures, can be also extracted and recorded to represent shear band. To verify this finding, these related variables have been recorded from the same simulated result (mesh 30×60, l_c = 2 mm). For purposes of comparison at the same scale, all variables have been normalized by their maximum as shown in Figure 3-4, which indicates that these variables tend to be constants outside the shear band, with the shear bands measured by these five variables being approximately the same. Accordingly, it is certain that these variables can be used to identify shear band distribution. The distributions of void ratio, equivalent plastic strain, and axial strain are bell-shaped. The peak values of plastic strain and axial strain located in the middle of shear band are caused because the largest deformation gradients occur in the middle of the shear band and gradually decrease outward. Excessive strain localization is caused chiefly by significant rearrangement and rotations of particles, which results in dilatancy inside the shear band. As a result, the void ratio in the middle of shear band is the largest. Considering that microcurvatures are entirely caused by microrotations, the distribution of curvatures is consistent with the distribution of particles' rotations, and the rotations transform from clockwise to counterclockwise at the centerline, which can thus be explained as a slide line.

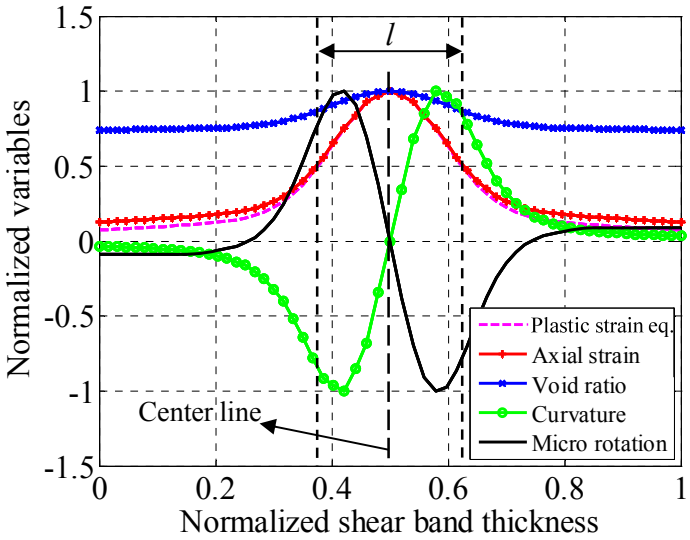

Figure 3-4 Shear band thickness identified by different variables

The equivalent plastic strain has been adopted to identify the shear band orientation and thickness. Nübel and Huang (2004) defined the shear band domain by using a criterion that the normalized plastic strain $\varepsilon^p/\varepsilon^p{}_{max}$ should exceed 0.6. However, the criterion has been redefined in the present study by comparing the shear band contours and the values of equivalent plastic strain along the selected path. Through the benchmark, it was suggested that the normalized plastic strain $\varepsilon^p/\varepsilon^p{}_{max}$ being larger than 0.5 be more appropriate to identify shear band as in Figure 3-5.

From the four normalized shear bands identified by plastic strain shown in Figure 3-5, it can be found that the four curves coincide with each other absolutely, confirming the regularization ability of micropolar theory in dealing with the mesh dependency problems. With the plastic strain distribution and shear band orientation, shear band thickness can be calculated. Accordingly, the shear band thickness in the foregoing simulations is TSB = $10l\cdot\sin(\beta)$ = 2.33·sin(53.22°) = 1.8 cm.

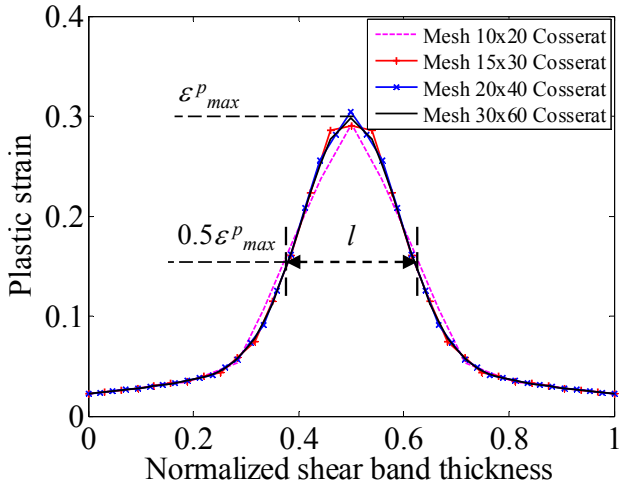

Figure 3-5 Normalized shear band thickness of four different mesh sizes

3.2.4 Shear band evolution

The evolution process of a shear band is shown in Figure 3-6. With the development of axial strain from 4% to 5%, the shear band becomes more and more obvious. However, it should be noticed that even though the plastic strain inside shear band increases with the development of axial strain, the thickness of shear band has remained constant during the whole evolution process. This indicates that once the shear band fully forms, its thickness remains constant from beginning to end.

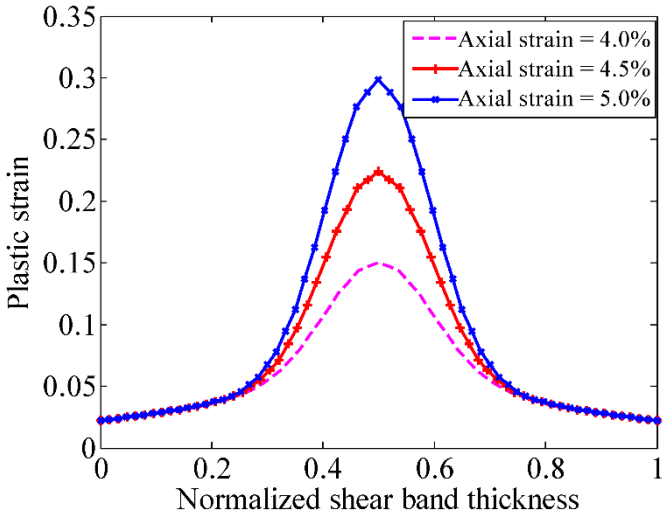

Figure 3-6 Evolution of a shear band

3.2.5 Influence of internal length on the simulated results

As has been illustrated in chapter one, no matter which regularization method is adopted, at least one explicit or implicit internal length scale parameters must be incorporated into the constitutive model. The incorporation of the internal length scale in the micropolar SIMSAND model indeed relieves the mesh dependency problems. Therefore, the discussions about the internal length scale are of significant importance. As a result, four different values of l_c were used in a fixed mesh (mesh 20×40), from which the influences of the internal length scale on biaxial tests results could be investigated.

The load–displacement curves with four different l_c are plotted in Figure 3-7. When l_c equals zero, the micropolar model reverts to a classical one, and the numerical difficulties still exist in softening regime. The load–displacement curves show that the load peak depends on the internal length scale and increases with l_c. In addition, for a larger value of l_c, it requires a larger axial strain to arrive at the peak load, indicating that the increased l_c is able to delay the bifurcation point of a structure. In the softening stage, the material having a larger l_c also demonstrates a stiffer behavior. From a physical point of view, the value of l_c controls the domain of the strain localized region, consequently, a larger l_c can drive more particles located inside the shear band to bear the loading together. In this sense, a larger l_c makes the bifurcation point more delayed and the strength stiffer.

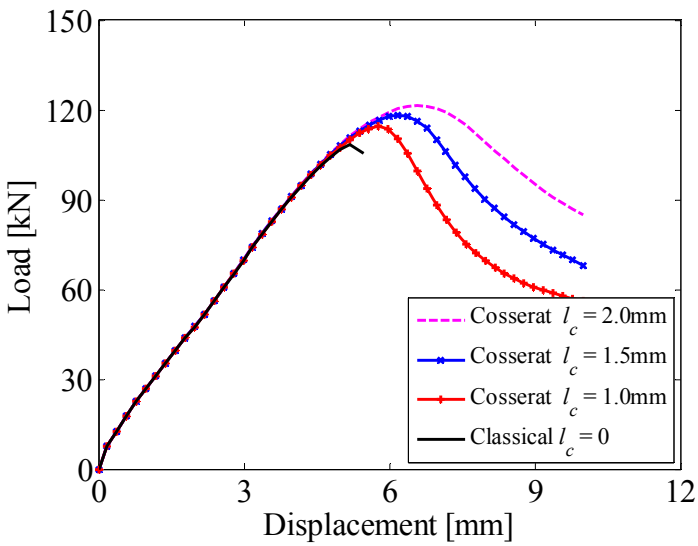

Figure 3-7 Influence of internal length scale l_c on load–displacement curves

Figure 3-8 displays shear band contours for three different values of the internal length scale. A relatively thin shear band is observed for a small internal length and two thicker shear bands for the larger internal lengths. With careful measurement of the shear band inclination of these three results, a steeper orientation can be found for the smaller internal length scale, and shear band inclination decreases with an increase in l_c, even though the difference is not substantial—consistent with the findings of Alshibli et al. (2000). The plastic strain distributions along the selected path for the three different l_c have been presented in Figure 3-9, with values of different l obtained. Based on Figure 3-8 and Figure 3-9, the thickness of three shear bands having different l_c can be calculated, as shown in Table 3-2.

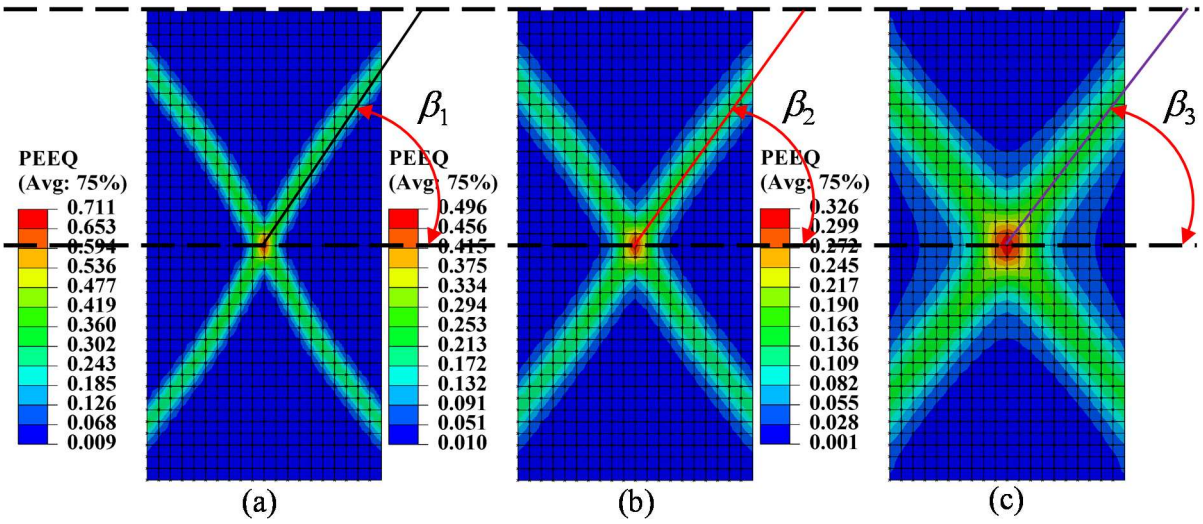

Figure 3-8 Influence of internal length scale l_c on shear band orientation: (a) l_c = 1 mm, β_1 = 55.9°; (b) l_c = 1.5 mm, β_2 = 54.2°; (c) l_c = 2 mm, β_3 = 53.2°

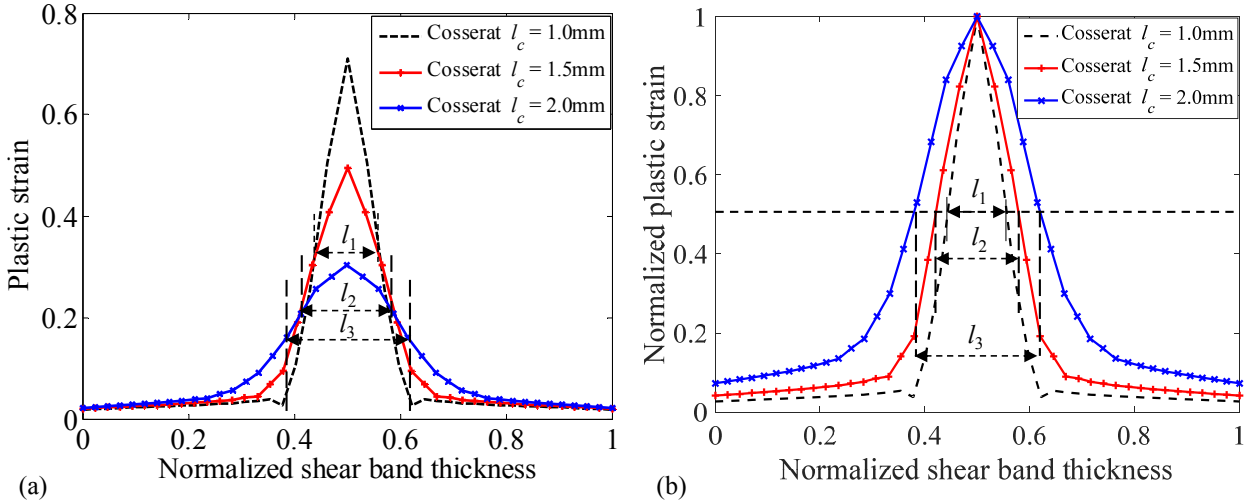

Figure 3-9 Normalized shear band thickness of different l_c: (a) based on plastic strain along the selected horizontal path; (b) based on normalized plastic strain along the selected horizontal path

Table 3-2 shear band patterns for three different internal length scales

l_c [mm]	l [mm]	β [°]	TSB = $l \cdot \sin(\beta)$ [mm]
1.0	15	55.9	12.4
1.5	18	54.2	14.6
2.0	23.3	53.2	18

Shear band thickness in laboratory tests has been measured by a number of researchers, beginning with Roscoe (1970). It has been concluded that shear band thicknesses in biaxial tests are confined within 5–20 times of the mean grain size based on the laboratory tests (Nübel and Huang, 2004; Arslan and Sture, 2008b). To discuss the relation between shear band thickness and internal length scale or mean grain size, several publications (Vardoulakis et al., 1978; Mühlhaus and Vardoulakis, 1987; Desrues, 1990; Alshibli and Sture, 1999, 2000; Viggiani et al., 2001; Alshibli et al., 2002; Alsaleh, 2004; Desrues and Viggiani, 2004) on biaxial tests are referred to, in which researchers quantitatively studied the influences of mean grain size on shear band thickness. Similarly, the relation between shear band thickness and internal length scale has been quantitatively defined via a series of numerical simulations in the present study. The experimental results by other researchers as well as the simulated results with the micropolar SIMSAND model are summarized in Table 3-3. It should be pointed out that the normalized thickness of shear band in simulations is obtained by dividing shear band thickness by the internal length scale l_c. Subsequently, the relations

between shear band thickness and mean grain size or internal length scale are alternatively presented in Figure 3-10 and Figure 3-11.

In Figure 3-10 and Figure 3-11, the abbreviations Exp. and Sim. denote the experimental and simulated results, respectively. Figure 3-10 indicates that the simulated results are very consistent with the experimental results, which are also located within the two dashed lines: $5l_c < \text{TSB} < 20l_c$. Additionally, shear band thickness in simulations increases with the internal length scale as the relation between shear band thickness and mean grain size in experiments. Figure 3-11 shows that the normalized value of shear band thickness decreases with increased mean grain size or internal length scale. Thus, the assumption that l_c equals d_{50} in the micropolar model is a reasonable one—or at least appropriate for the dimensions of a laboratory specimen.

Table 3-3 Shear band thickness in biaxial tests from experiments and simulations

Technique	Reference	d_{50} (l_c) [mm]	TSB [mm]	TSB/d_{50} (TSB/l_c)
Experiments	Muhlhaus and Vardoulakis (1987)	0.2	3.7	18.5
		0.33	4.3	13.0
	Desrues et al. (2004)	0.35	7.5	21.4
		1.2	13.5	11.3
		2.4	17.0	7.1
		3.2	22.0	6.9
	Alshibli et al. (1999)	0.22	3.0	13.6
		0.55	6.2	11.3
		1.6	17.3	10.8
Numerical simulations	Simulations with micropolar SIMSAND model	1.0	12.4	12.4
		1.5	14.6	9.7
		2.0	18.0	9.0

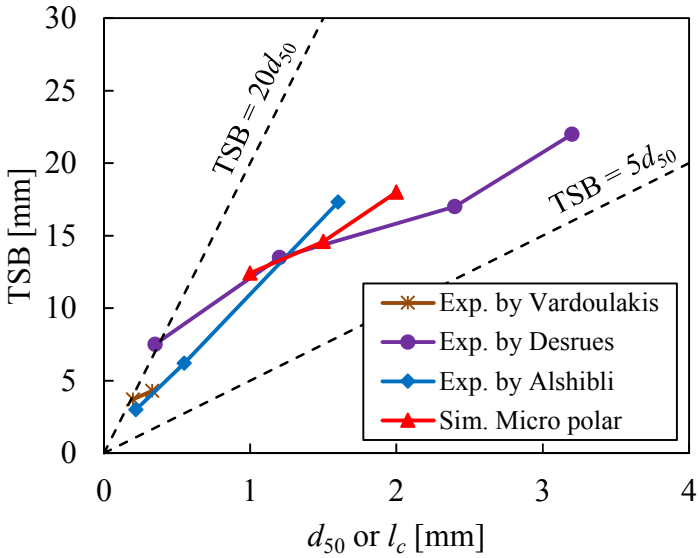

Figure 3-10 Relationship between thickness of shear band and micro structural size

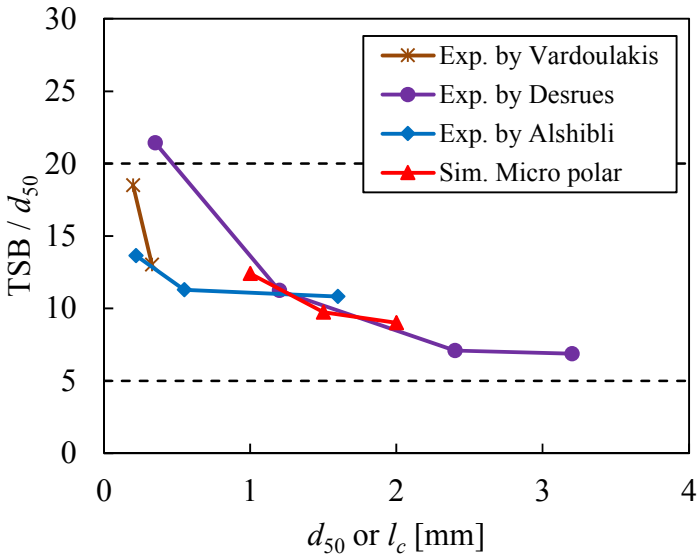

Figure 3-11 Normalized shear band thickness versus mean grain size or internal length scale

Based on the foregoing, the internal length scale l_c can be taken to significantly influence the material's strength and the shear band patterns. The larger l_c is, the larger and later the peak loading will be, and also the stiffer the load–displacement curve in the softening regime for a larger l_c. Shear band inclination will decrease slightly as l_c increases. Shear band thickness increases with the internal length scale l_c, whereas normalized shear band thickness decreases with an increase in l_c. Finally, in the case of a structure's dimensions at a laboratory scale, the mean grain size can reasonably be regarded as the internal length scale of a micropolar model.

3.2.6 Influences of the micropolar shear modulus

According to the findings of other researchers (de Borst and Mühlhaus, 1991; de Borst and Sluys, 1991; de Borst, 1993; Arslan and Sture, 2008b, a; Tang and Li, 2008), it has been widely accepted that G_c can be set to about half the conventional shear modulus G. In the opinion of these authors, when the micropolar shear modulus is set to $G_c \geqslant 0.5G$, it has a very slight influence on the final results, such as shear band thickness and load carrying capacity. Consequently, emphasis has always been laid on researching the internal length scale l_c in the past. However, the influences of micropolar modulus on shear band patterns and load carrying capacity have never been verified, and discussions of G_c have been infrequent.

In this section, the influences of the micropolar shear modulus G_c on shear band patterns and load carrying capacity were investigated. As has already been illustrated, the theorem of conjugate shearing stress is no longer satisfied in micropolar theory because of microrotation. Thus, the influence of G_c on shear stress and shear strain as well as the newly produced curvature and moment were also discussed.

When the micropolar shear modulus G_c equals zero, the micropolar model reverts to a classical one, and the simulations suffer from numerical difficulties and mesh dependency problems. Thus, by increasing the value of G_c gradually, it is possible to find a value of G_c that is able to entirely overcome the mesh dependency problems. Several relatively small micropolar shear moduli, such as $G_c = 0.01G$, $G_c = 0.05G$, and $G_c = 0.1G$, were tested initially. The load–displacement curves are shown in Figure 3-12, from which it can be found that once the micropolar model reverts to a classical one (with G_c being set to null), the convergence property is worse, especially in the post-failure regime, and with increased G_c, the convergence property becomes better than before. Moreover, G_c can affect peak load and stiffness in the softening regime: the larger the G_c, the stiffer the material.

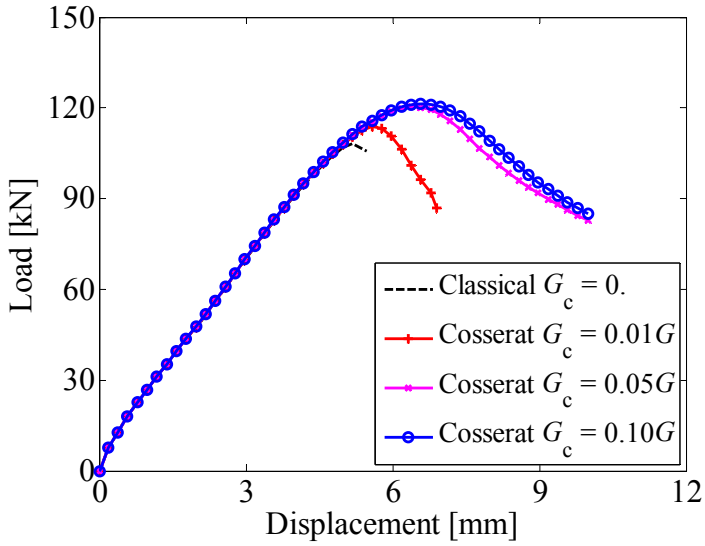

Figure 3-12 Influence of a small G_c on load–displacement curves

In further researching the influences of G_c on load carrying capacity, other values of G_c must also be discussed, such as $G_c = 0.25G$, $G_c = 0.5G$, $G_c = 1.0G$, and $G_c = 2.0G$. The load–displacement curves are shown in Figure 3-13, from which it can be found that when $G_c \geqslant 0.1G$, the numerical calculations become very stable, and the differences between these curves are slight. Furthermore, after the condition $G_c \geqslant 0.5G$ is satisfied, the micropolar shear modulus has no influence on the mechanical response, as argued by other researchers. For the values of $G_c = 0.5G$, $G_c = G$, and $G_c = 2G$, the three shear bands identified by the plastic strain are shown in Figure 3-14, letting us remark on not only the shear band thickness but also the orientation as being consistent for the three different G_c. A more precise measurement with which to compare shear band thickness is shown in Figure 3-15 for which the three curves are also wholly consistent with one another—which means that shear band thickness is not influenced by the value of G_c.

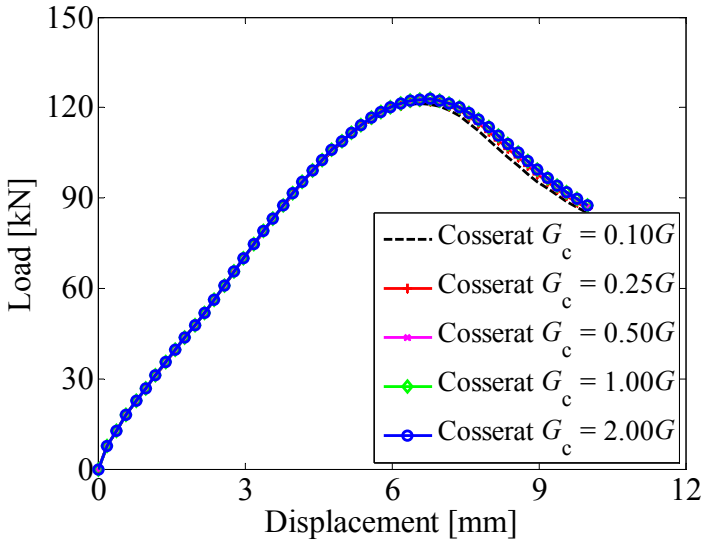

Figure 3-13 Influence of micropolar shear modulus G_c on load–displacement curves

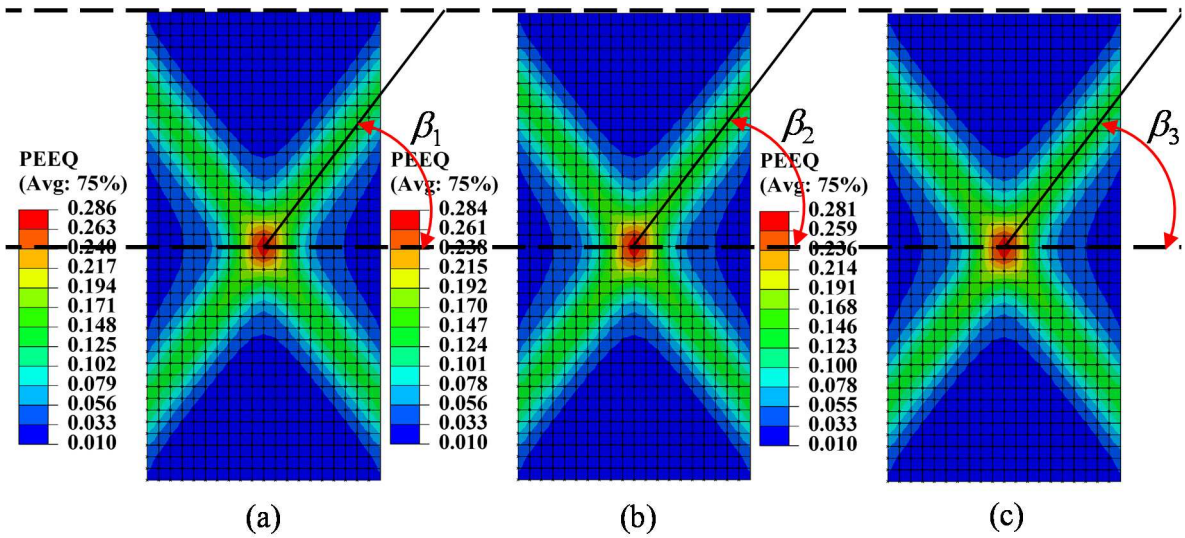

Figure 3-14 Influence of micropolar shear modulus G_c on shear band orientation: (a) G_c = 0.5G, β_1=53.22°; (b) G_c = 1.0G, β_2=53.22°; (c) G_c = 2.0G, β_3=53.22°

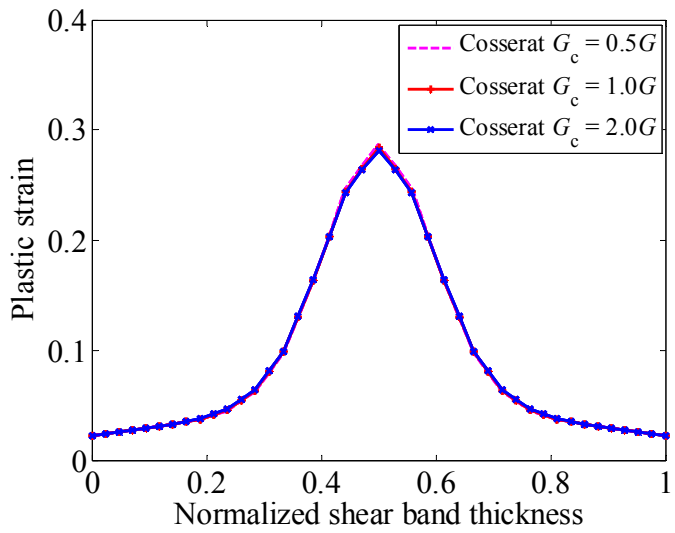

Figure 3-15 Influence of micropolar shear modulus G_c on shear band thickness

Influences of the micropolar shear modulus G_c on shear strain and shear stress are shown in Figure 3-16 and Figure 3-17, from which it can be found that the directions of shear strain and shear stress change from clockwise to counterclockwise at the center of the shear band and that peak values of shear strain and shear stress are closely related to the choice of G_c. However, it should be noted that the differences are not overly large, and the peak values of shear strain and shear stress do not grow monotonically with the increase in G_c.

For two-dimensional problems in micropolar theory, two additional parameters (i.e., internal length scale l_c and micropolar shear modulus G_c) are newly incorporated. Consequently, microcurvatures and micro-bending moments are produced between the particles. Accordingly, the influences of the micropolar shear modulus on microcurvatures and micro-bending moments have been discussed. The distribution of microcurvatures and micro-bending moments inside the shear band is shown in Figure 3-18 and Figure 3-19, and, similar to shear strain and shear stress, the directions of curvatures and bending moments are found to change from clockwise to counterclockwise at the center of shear band. Furthermore, the coincided curves in these two figures amply demonstrate that the value of the micropolar shear modulus affects the microcurvatures and micro-bending moments only slightly.

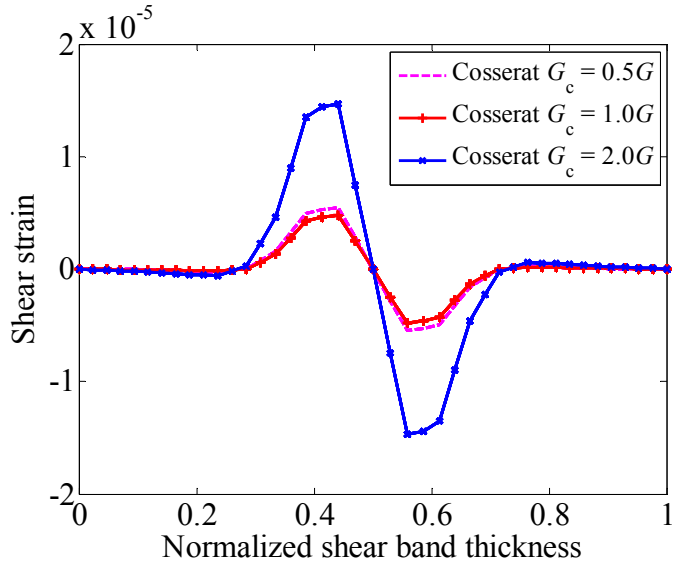

Figure 3-16 Influence of micropolar shear modulus G_c on shear strain

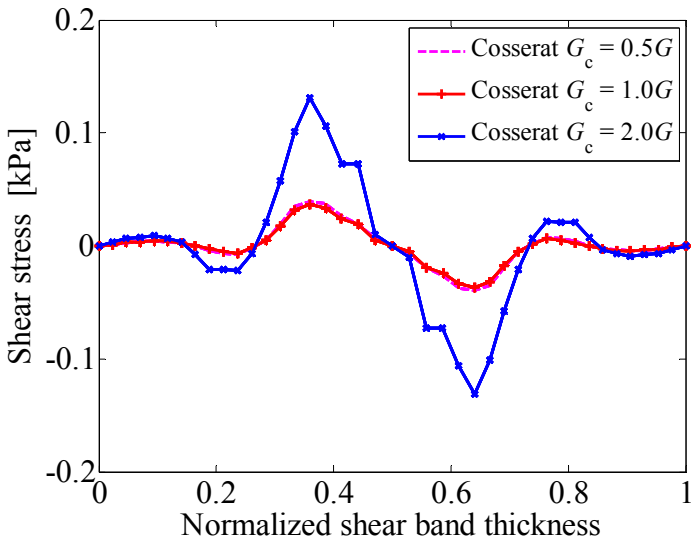

Figure 3-17 Influence of micropolar shear modulus G_c on shear stress

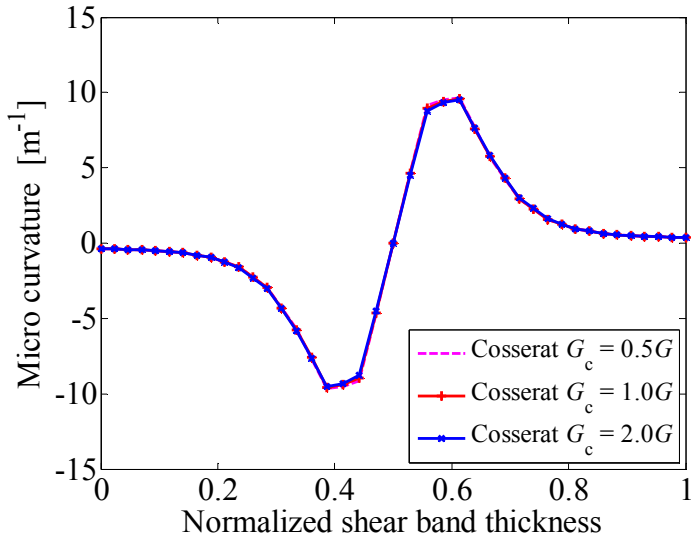

Figure 3-18 Influence of micropolar shear modulus G_c on micro-curvature

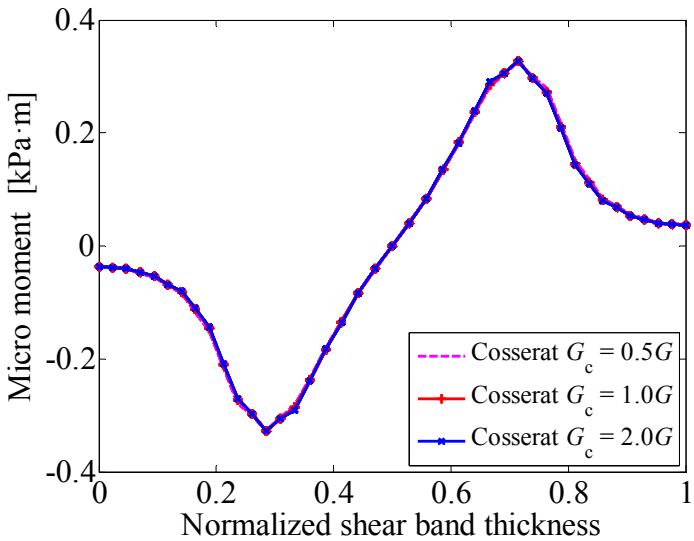

Figure 3-19 Influence of micropolar shear modulus G_c on micro-moment

From the foregoing discussions, it can be concluded that for a very small micropolar shear modulus G_c, the value of G_c can affect the convergence property and the mechanical response, and when $G_c \geqslant 0.5G$ is satisfied, it has almost no influence on shear band patterns and load carrying capacity. Accordingly, when we aim at the research of shear band patterns or the strength of specimens, there is no need to identify the value of the micropolar shear modulus. These verifications support past research, and the value $G_c = 0.5G$ can be adopted in the present study, as other researchers have done before. Moreover, the microcurvatures and micro-bending moments

inside the shear band are also found to be unrelated to the choice of G_c. Shear strain and shear stress are affected slightly by the value of G_c, but their peak does not monotonically increase with G_c.

3.3 Some other advantages of the micropolar approach

From the foregoing discussion, we see that the micropolar technique offers great promise for overcoming numerical difficulties while dealing with the mesh dependency problems in finite element analysis. Moreover, it can reflect the kinematic behaviors of microstructures of materials. Thus a micropolar model can monitor the onset and evolution of shear bands by tracing the particles' rotations. For dense materials, strain localization can be explained by the great dilatancy inside the strain-localized region, which is caused by particles' rotations and rearrangements. Because the conventional constitutive models within the framework of classical continuum theory have not considered the independent rotations of micro particles, they cannot reflect the real kinematics of the shear band evolution. Conversely, the evolution process can be recorded in the simulated results by the micropolar model, as in Figure 3-20. Subfigures (a), (b) and (c) denote the onset, developing and fully formed shear band, respectively. We can find that the microrotations start from the corners due to the constraints on the boundaries, then propagate to the center of the specimen until the complete formation of two conjugated shear bands.

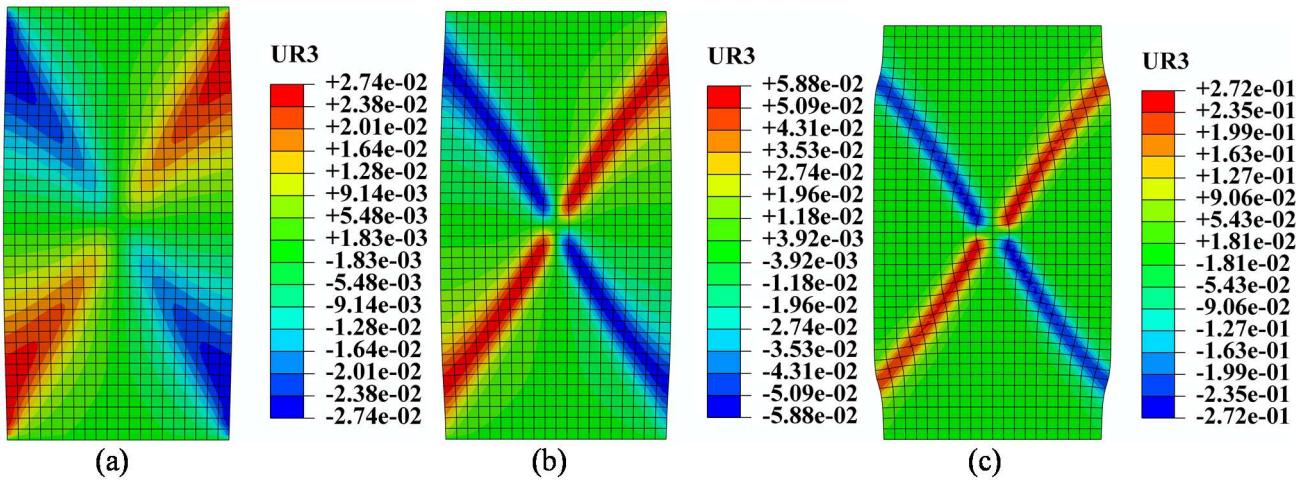

Figure 3-20 Evolution of shear band based on the particles' rotations: (a) shear band onset corresponding to axial strain 2.5%; (b) corresponding to axial strain 3%; (c) fully formed shear band corresponding to axial strain 5%

For dense materials, strain localization phenomena are often accompanied by a reduction in load-carrying capacity. However, experiments have demonstrated an absence of strain softening behavior for loose materials when loaded. Considering this, the micropolar approach is always adopted when describing dense materials' behaviors, whereas loose materials have been never studied by a micropolar model. In fact, the micropolar model has also significantly influenced the final results for loose materials by incorporating the internal length scale.

In this section, the simulated results from a classical continuum model and its polarized model were compared and discussed in terms of shear bands and mechanical response. Shear bands are identified by axial strain. For simulated results within the framework of the classical continuum theory laid out in Figure 3-21, it may be observed that several shear bands divide the specimen into many distributed sections and that the smaller the mesh size, the more divided the sections produced. Even the thickness of a single shear band is not the same in local region (the finer the mesh size, the thinner the shear band), but different quantities of shear band for different discretization produce a similar global mechanical response, see Figure 3-22. From the load–displacement curves, it can be seen that there is no softening behavior for loose materials in biaxial tests. However, the strong oscillations of the load versus displacement curves can be found just after the onset of shear bands because of the numerical instabilities within the classical continuum theory. Furthermore, the oscillations of the global load–displacement curves of the specimens can be explained by the accumulation of local numerical instabilities, as indicated in Figure 3-23 with elements located on the horizontal bearing profile given in subfigure (a) and their bearing capacities in subfigure (b).

Generally speaking, mesh dependency phenomena for loose materials are not as serious a matter as in dense materials, but numerical instabilities exist in the post-failure regime.

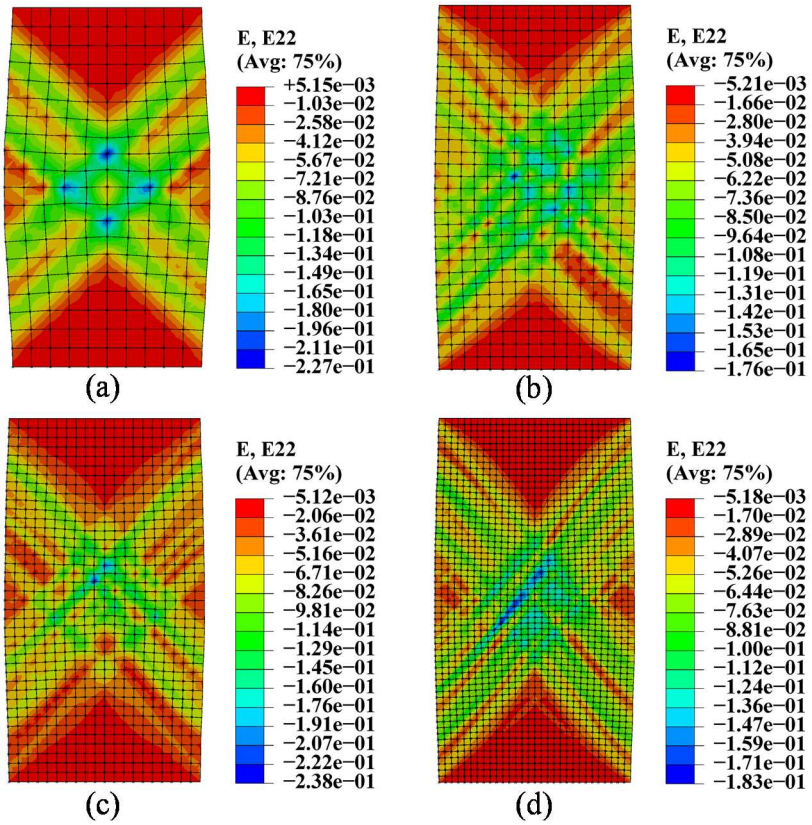

Figure 3-21 Shear bands for different discretization obtained from the classical model for loose materials: (a) mesh 10×20; (b) mesh 15×30; (c) mesh 20×40; (d) mesh 30×60

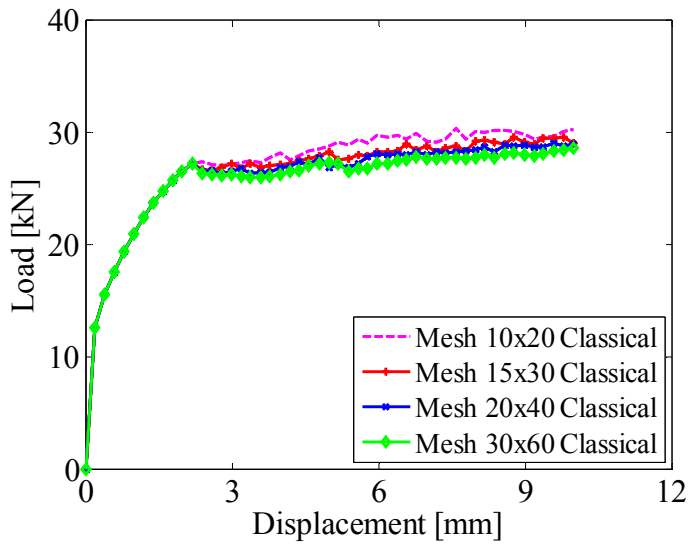

Figure 3-22 Load–displacement curves for different discretization based obtained from the classical model for loose materials

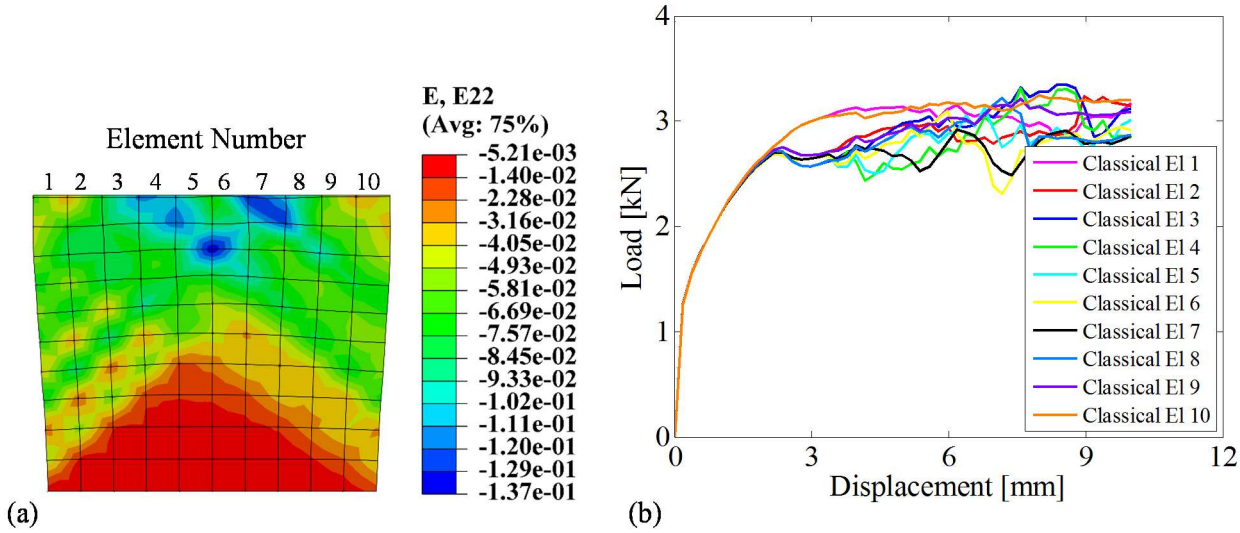

Figure 3-23 Load–displacement curves of each element from the classical simulation: (a) elements located on the horizontal profile; (b) local–displacement curves of each element

After the governing field equations were regularized using the micropolar approach, the failure mode is very different from that associated with classical continuum theory, and a consistent diffusion mode is found in the loose specimen for the four different mesh sizes rather than shear strain–localized mode, as in Figure 3-24, which has been experimentally verified by many researchers in the past. When numerical simulations are conducted within the framework of the micropolar continuum theory, not only the displacements of particles but also those particles' rotations originating from the boundary constraints play a main role, together, in forming the failure mode. The load–displacement curves obtained from the micropolar model in Figure 3-25 are seen to be smoother and more stable than classical ones. Moreover, the four curves for different discretization in Figure 3-25 coincide with each other absolutely, thereby also demonstrating the regularization ability of the micropolar technique when overcoming numerical difficulties and dealing with mesh dependency problems. Similarly, the smooth curves can be also explained by the accumulations of local bearing curves of each element located on the horizontal profile, as in Figure 3-26. Compared to the local curves from classical simulations, it is obvious that the load–displacement curves of each bearing element from micropolar simulations become more stable. Because the incorporated internal length scale can drive more particles in its surroundings to bear the loading, the load carrying capacity achieved by the micropolar model is a little higher than that given by the classical constitutive model, increasing gradually to reach a stable stage.

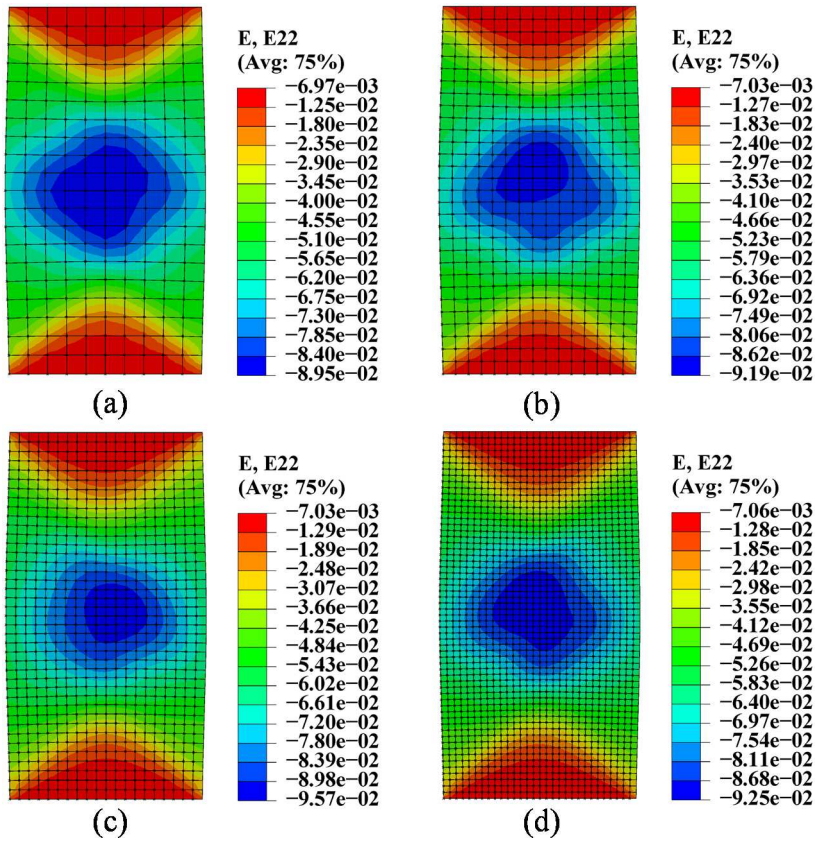

Figure 3-24 Diffusion mode for different discretization obtained from the micropolar model for loose materials: (a) mesh 10×20; (b) mesh 15×30; (c) mesh 20×40; (d) mesh 30×60

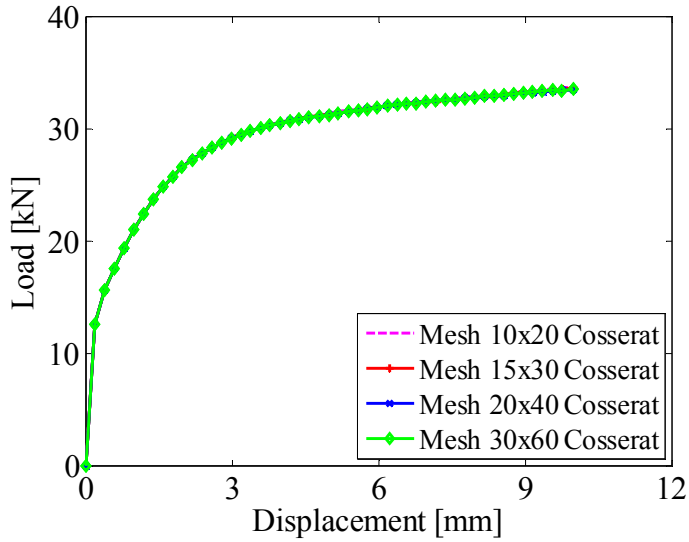

Figure 3-25 Load–displacement curves for different discretization based on micropolar model for loose materials

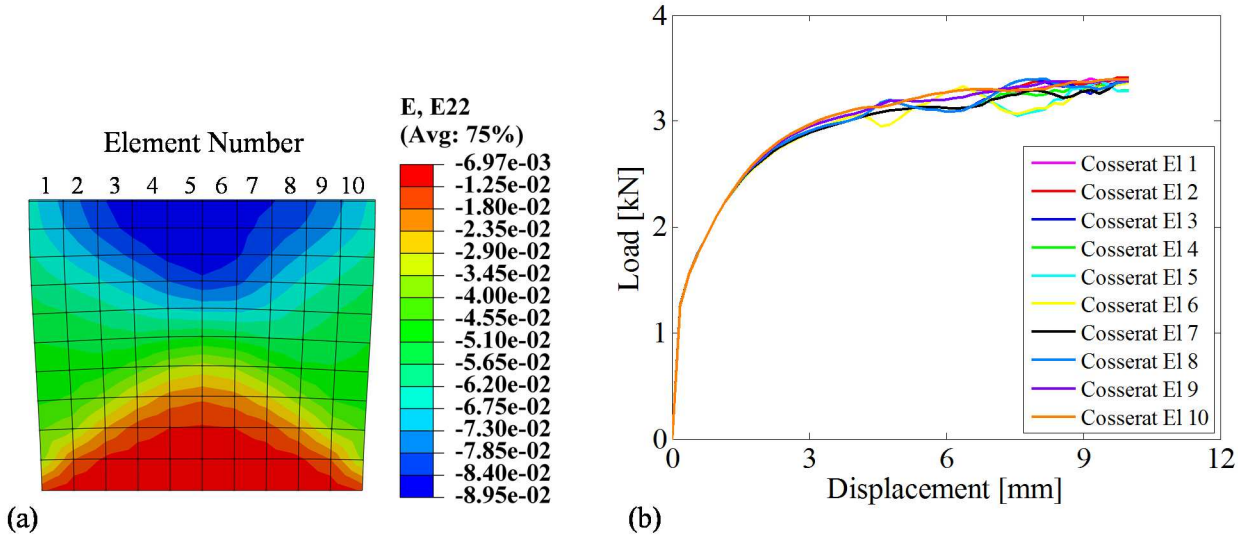

Figure 3-26 Load–displacement curves of each element from the Cosserat simulation: (a) elements located on the horizontal profile; (b) local–displacement curves of each element

From the simulated results of loose materials and dense materials in the previous sections, we can find that the density of materials greatly influences the behavior of granular materials. Indeed, density significantly affects not only failure mode but also peak strength. Dense materials always have obvious intense located shear bands, whereas the loose specimens will undergo a diffuse failure mode. Regarding load carrying capacity, dense materials have a higher strength than loose ones.

Based on these simulations—although the differences are very slight—mesh dependency problems still exist in loose materials. Although the micropolar approach has been used chiefly to describe materials having softening behavior, and only rarely to describe loose material, the additional internal length scale and rotational degree of freedom in the micropolar formulations can maintain the ellipticity of the partial differential equations during finite element analysis. As a result, numerical instabilities are well overcome and physically meaningful solutions finally obtained.

3.4 Proposition of the regularization effectiveness ratio—l_c / l_e

The simulations in the previous section showed that even though mesh dependency problems have significantly improved, the load–displacement curve of mesh 10×20 still could not coincide with the other three relatively finer meshes. Thus, it is believed that for a fixed internal length scale, the element size may affect the regularization effect. If the element size is too large compared to the

internal length scale parameter, then the element size l_e controls the thickness of shear bands instead of the internal length parameter l_c. Purely from the perspective of regularization effectiveness, then, the internal length scale parameter l_c incorporated in the micropolar model and the element size l_e should be considered simultaneously via a series of simulations of biaxial tests. Several researchers (Ristinmaa and Vecchi, 1996; Sharbati and Naghdabadi, 2006; Tejchman and Niemunis, 2006) have suggested that only if the ratio of the internal length to the discretized element size (l_c / l_e) is larger than a certain value, effective the micropolar approach will be to overcome mesh dependency problems. Ristinmaa and Vecchi (1996) found that mesh dependency problems could be wholly alleviated when the ratio condition l_c / l_e > 0.2 was satisfied. According to Tejchman (1998, 2006), all simulations were based on the premise l_c / l_e > 0.2; Sharbati and Naghdabadi (2006) proposed a new criterion l_c / l_e > 0.15 with which to overcome mesh dependency problems. Accordingly, in this section, the effective value of the internal length scale parameter l_c compared to the element size l_e will be discussed.

To study the regularization effectiveness of the micropolar model, four different values of the internal length scale l_c have been attempted for each fixed element size, with four meshes ranging from coarse to fine. Thus, four groups corresponding to 16 cases are listed in Table 3-4 for analysis.

Detailed information about the simulations is described hereafter. The width and height of the specimen was 10×20 cm, with 10×20, 15×30, 20×40, and 30×60 meshes denoting four different divided meshes. The element type adopted was the user-defined eight-node biquadratic quadrilateral element considering the rotational degree of freedom introduced in Chapter 2. Dry dense material is known to exhibit softening behavior when sheared excessively, and shear band rather than diffusion is the main failure mode in biaxial tests. Accordingly, dense material was used in the simulations based on the critical state–based micropolar model. Regularization effectiveness can be judged by two criteria: thickness of shear band and mechanical response. In this section, shear band contour is identified by the distribution of axial strain. Based on the precede results laid out, it was found that the load–displacement curve is a more precise criterion for judging regularization effectiveness. In this sense, then, a criterion - load–displacement curves coincide with each other or not for the four different meshes for a fixed internal length scale - is adopted to judge the degree of mesh dependency. As already mentioned, only if the ratio of l_c to l_e reaches a certain value is the micropolar theory able

to overcome the mesh dependency problems. We aim at finding the ratio through use of the following simulated results.

Table 3-4 Different combinations of internal length l_c and element size l_e

l_c[mm]	1.0				1.5				2.0				2.25			
l_e[mm]	10	6.67	5	3.33	10	6.67	5	3.33	10	6.67	5	3.33	10	6.67	5	3.33
l_c/l_e	0.1	0.15	0.2	0.3	0.15	0.225	0.3	0.45	0.2	0.3	0.4	0.6	0.225	0.338	0.5	0.675

First, the simulations of group 1 were made as shown in Table 3-4, using a fixed internal length scale l_c = 1 mm for four different discretization meshes of 10×20, 15×30, 20×40, and 30×60, corresponding to the four different element sizes l_e shown in Figure 3-27; the mechanical response curves are plotted in Figure 3-28. Obviously, not only shear band thickness but also load–displacement curves are mesh-dependent. The shear bands are concentrated only in a thickness of about two element sizes. As a result, the coarse mesh produces a thick shear band, whereas the fine mesh produces a narrow shear band. That is to say, the element size controls the shear band thickness but not the mean grain size or the internal length scale. For load–displacement curves, even though the peak strength is the same, the load carrying capacity is higher for the coarse mesh than for the fine mesh in the post-failure regime (softening regime). That the load–displacement curve for a ratio of 0.2 does not coincide with that for a ratio of 0.3 signifies that the ratio 0.2 does not satisfy the mesh independency criterion in the present study.

In group 2 with l_c = 1.5 mm, the shear band contours in Figure 3-29 are found to be significantly mesh-independent. However, from the load–displacement curves in Figure 3-30, we see that the curve of the relatively coarse mesh 10×20 is not consistent with the other three curves, although the other three cases are believed to be mesh-independent. Thus the ratio 0.225 satisfies the criterion for overcoming the mesh dependency problems.

For group 3 with l_c = 2 mm, the simulated results are shown in Figure 3-31 and Figure 3-32—similar to those produced by the second group in that the mesh dependency problems of the three relatively fine meshes are entirely alleviated. Certainly, the ratio 0.3 is a satisfied criterion, then, because it satisfies the criterion 0.225.

From these first three groups, we can assume that the ratio l_c / l_e should be larger than 0.225, making this a criterion for regularization effectiveness in the critical state–based micropolar model. To check the reasonability of this suggested criterion, we perform simulations for group 4 with l_c = 2.25 mm. In this group, the smallest ratio is 0.225. The simulated results are shown in Figure 3-33 and Figure 3-34, and we find not only the shear band thickness but also load–displacement curves, to some extent, to be mesh-independent. We can thus conclude that the criterion for regularization effectiveness for the micropolar model as regards mesh dependency problems is met, requiring that the ratio l_c / l_e exceed 0.225 in the present study. However, it must be noted that this ratio could be affected by other factors, such as the scale of the model, material density, confining pressure, and the parameters of the constitutive model.

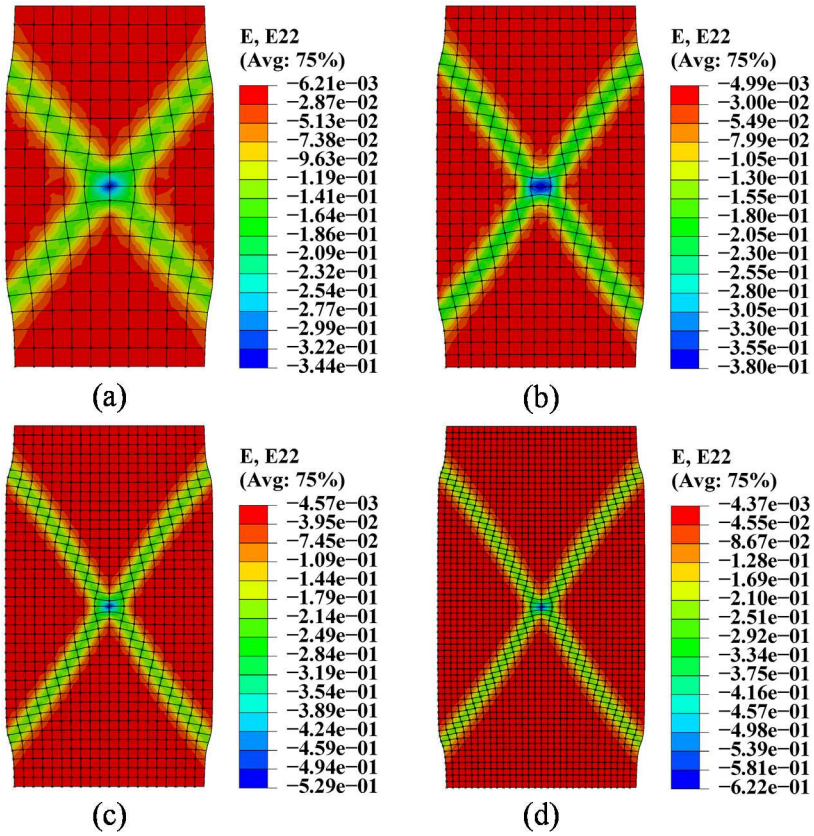

Figure 3-27 Shear bands for different discretization by the micropolar model with l_c = 1 mm: (a) 10×20 mesh; (b) 15×30 mesh; (c) 20×40 mesh; (d) 30×60 mesh

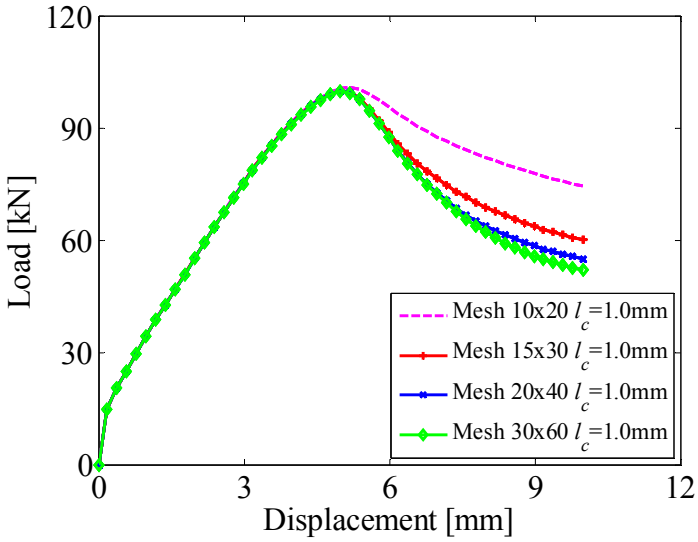

Figure 3-28 Load–displacement curves for different discretization using the micropolar model: l_c = 1 mm

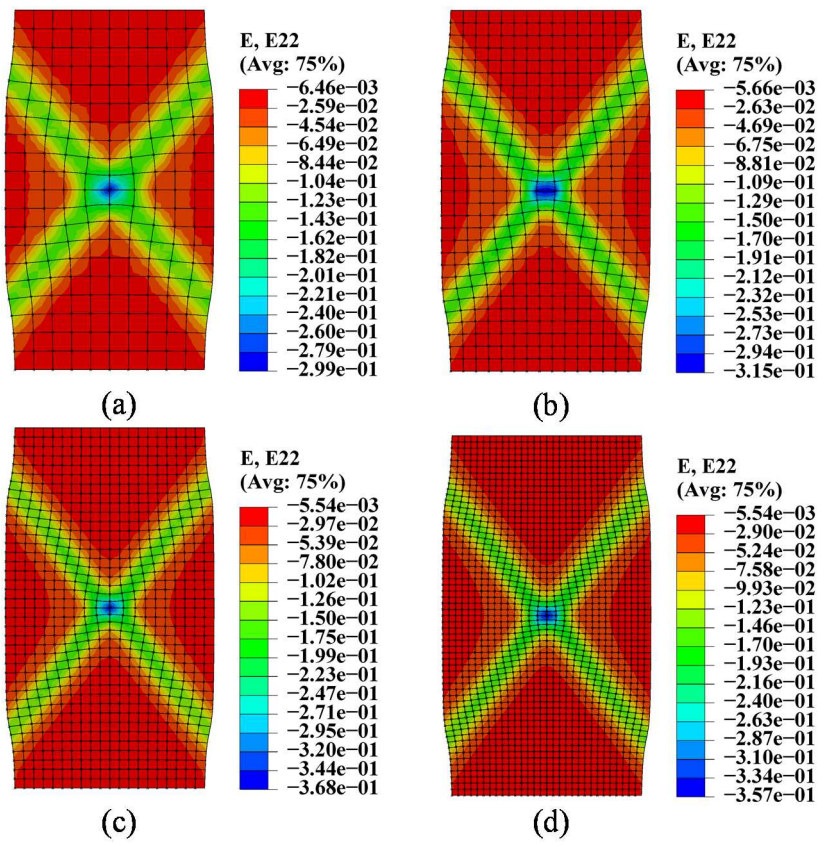

Figure 3-29 Shear bands for different discretization by the micropolar model with l_c = 1.5mm: (a) mesh 10×20; (b) mesh 15×30; (c) mesh 20×40; (d) mesh 30×60

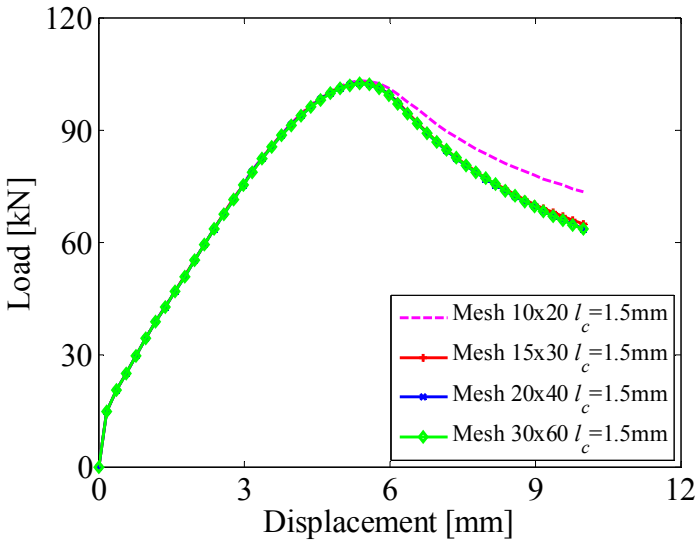

Figure 3-30 Load–displacement curves for different discretization by micropolar model: l_c=1.5mm

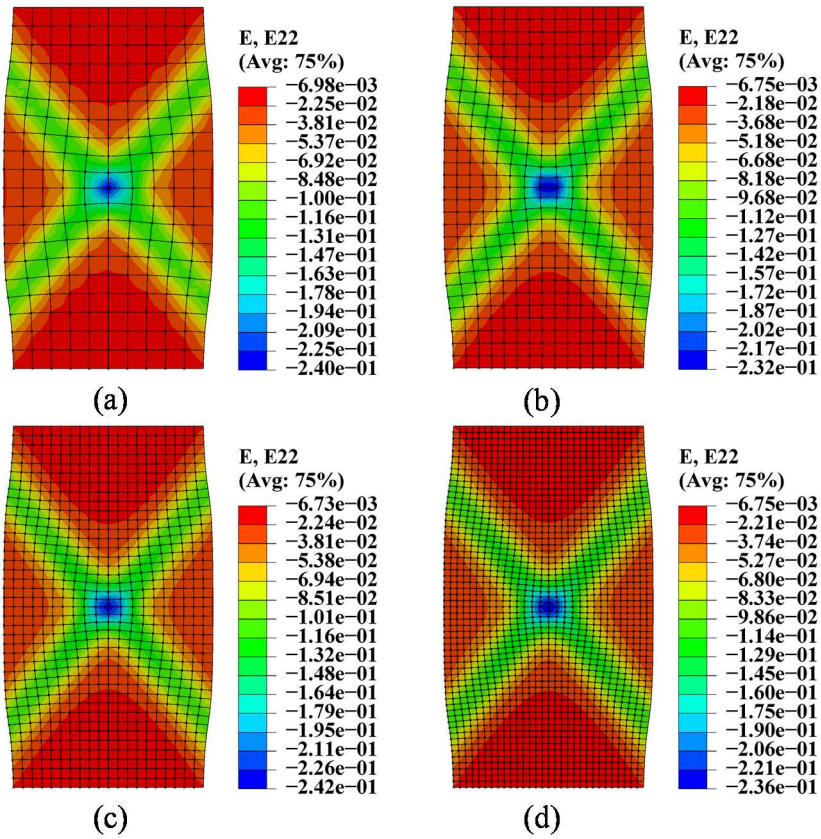

Figure 3-31 Shear bands for different discretization by the micropolar model with l_c = 2mm: (a) mesh 10×20; (b) mesh 15×30; (c) mesh 20×40; (d) mesh 30×60

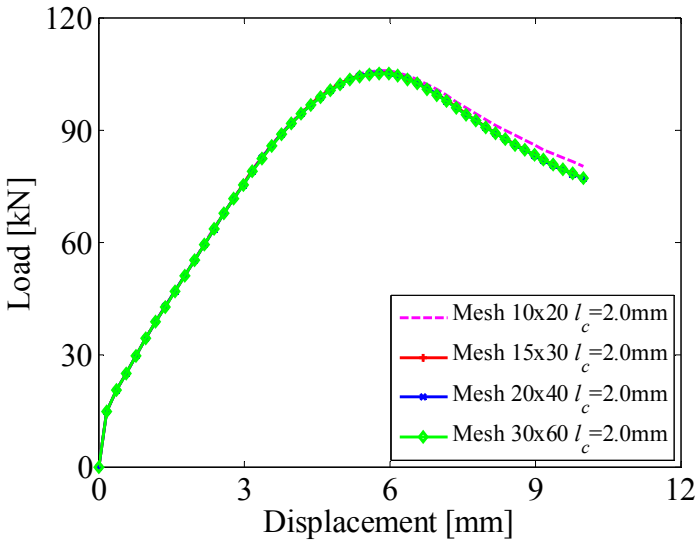

Figure 3-32 Load–displacement curves for different discretization by micropolar model: l_c=2mm

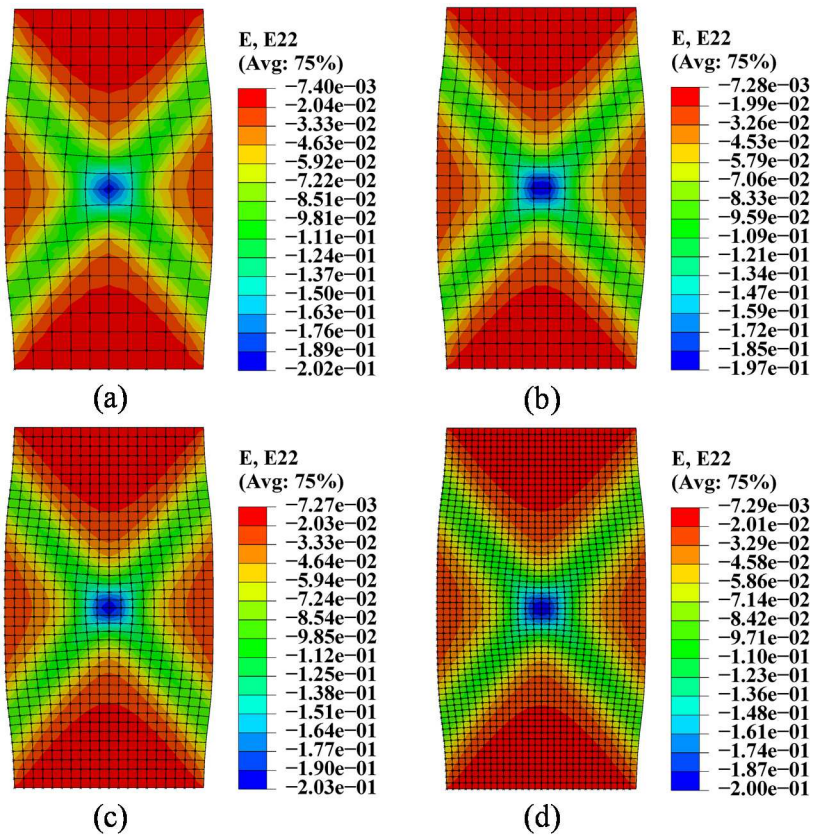

Figure 3-33 Shear bands for different discretization by the micropolar model with l_c = 2.25mm: (a) mesh 10×20; (b) mesh 15×30; (c) mesh 20×40; (d) mesh 30×60

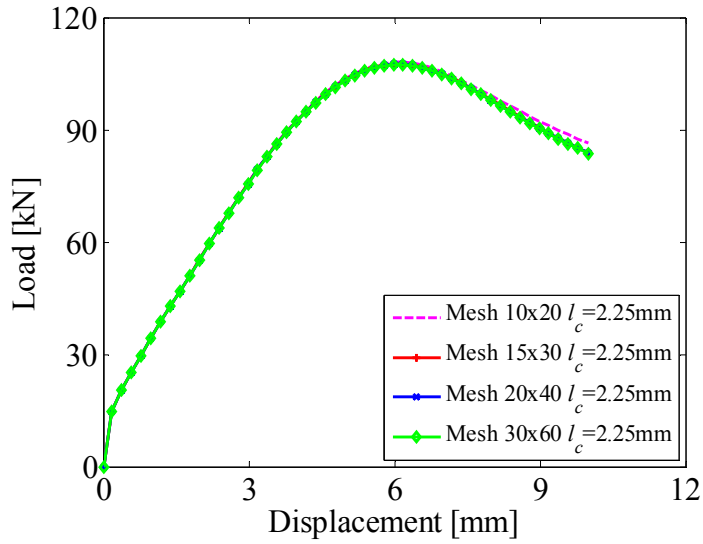

Figure 3-34 Load–displacement curves for different discretization by micropolar model: l_c=2.25mm

3.5 Influencing factors on shear band and regularization effectiveness ratio

As was pointed out, the effective ratio l_c / l_e for the micropolar approach is 0.225—even as it had been also argued that this ratio might not be a constant but rather might be affected by many factors, such as confining pressure, initial density, and constitutive parameters. Therefore, the influences of these factors on the regularization effectiveness ratio were investigated in this section.

3.5.1 Influence of confining pressure

The softening behavior following the peak-point results from bifurcation instability in the neighborhood, which causes localization of deformations into narrow shear zones and enables development of the kinematics of a failure mechanism. In short, global softening behavior has been used to describe the slip mechanism after the onset of the shear band. Based on earlier discussions, shear bands in biaxial tests have been proven to be affected by several factors, including grain size, specimen density, and confining pressure, which can be reflected by shear band thickness and a more accurate criterion: the mechanical response.

It can be easily understood from a physical point of view that loose sand might be dilatant under low confining pressure, whereas dense sand might contract under high confining pressure. There is thus no doubt that the confining pressure and the specimen density greatly influence the failure mode

(shear band) and strength of the specimen in biaxial tests. Consequently, for the micropolar approach, the confining pressure may affect the regularization effectiveness, which may be explained by the changing of the effective ratio l_c/l_e. Considering that the differences of shear band inclined angle β compared to the initial configuration for different cases are so slight when the simulations are within the framework of micropolar theory, different shear bands comparisons can be made with reference to shear band thickness.

In this section, the influence of the confining pressure on load carrying capacity and shear band thickness was observed to evaluate the regularization effectiveness ratio. Three confining pressures 50 kPa, 100 kPa, and 200 kPa were adopted, and for each confining pressure, three different meshes from coarse to fine were used for the discretization. Moreover, the ratio l_c/l_e in this section was set greater than or equal to 0.225, thus satisfying the criterion obtained from section 3.4. From Figure 3-35, it can be found that the confining pressure greatly influences the load–displacement curves. First, the stiffness decreases with a decrease in confining pressure during the hardening regime, and the softening behavior becomes more significant when the confining pressure is smaller in the post-failure regime. Second, the axial strain at peak-load (near the onset of shear band) increases with increase in the confining pressure; it seems that the bifurcation point is delayed for specimens subjected to high confining pressure. Third, load carrying capacity increases with increased confining pressure. These findings entirely agree with the findings of Han and Drescher (1993), of Alshibli and Sture (2000), and of Desrues and Viggiani (2004), who performed a series of biaxial tests to investigate the effects of the confining pressure on the onset and formation of shear bands. Closer scrutiny of the three sets of curves in Figure 3-35 reveals that the mesh dependency problems occurs at the end of the softening regime, especially for the low confining pressure. To some extent, then, it requires that the micropolar approach play additional roles in fully alleviating mesh dependency problems when the confining pressure is relatively low. In short, a smaller element size l_e (larger ratio l_c/l_e) is needed in order to regularize the solutions when the confining pressure is relatively low.

The thickness of the shear band can be found in Figure 3-36, in which sub-figure (a) signs the values of equivalent plastic strain, and sub-figure (b) can be used to judge the shear band thickness. It indicates that confining pressure's influence on shear band thickness is very slight. However, the

peak value of the equivalent plastic strain inside the shear band is obviously affected by the confining pressure. Smaller the confining pressure, greater is the peak value of the equivalent plastic strain.

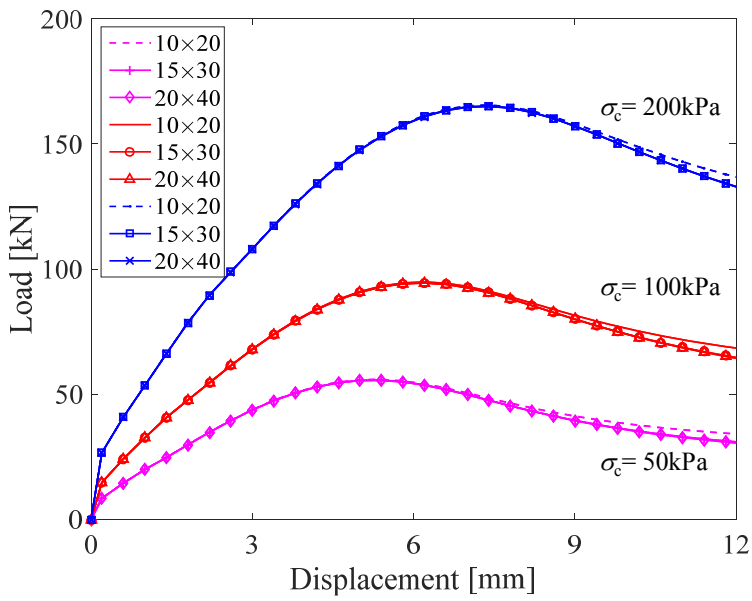

Figure 3-35 Influence of confining pressure on the load-carrying capacity

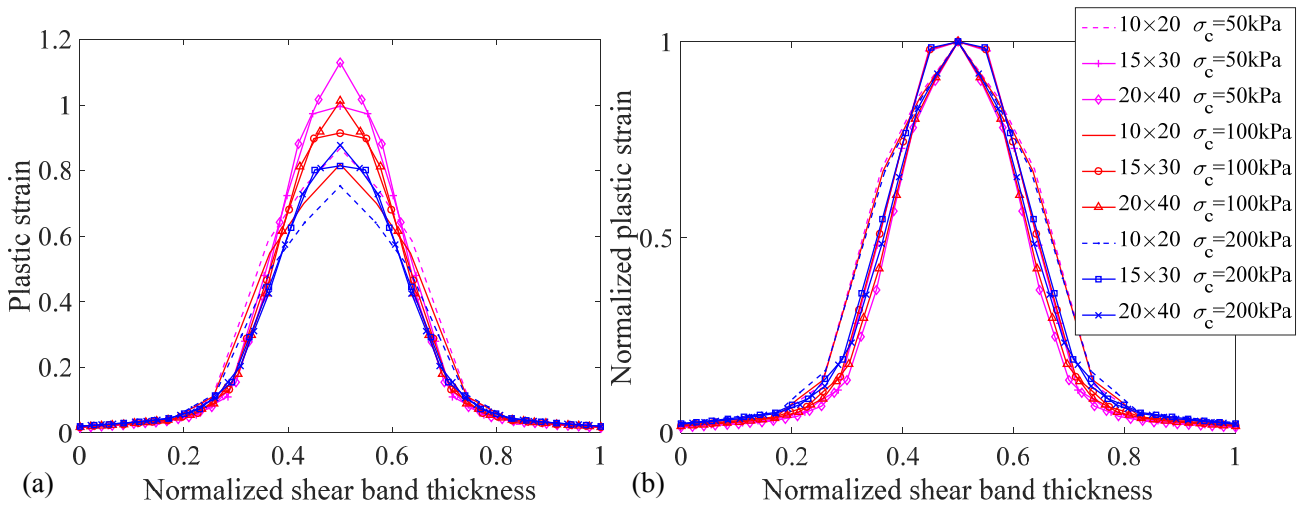

Figure 3-36 Influence of confining pressure on shear band thickness: (a) based on plastic strain; (b) based on normalized plastic strain

3.5.2 Influence of initial density

Lee (1970) and Marachi et al. (1981) concluded that as specimen density increases, specimens tend to fail at a smaller axial strain, which pointed out the influence of the initial density on strain localization. Later on, however, Han and Drescher (1993) and Alshibli and Sture (2000) argued that rather than initial density, confining pressure was the main factor affecting the onset of shear band. Three different initial void ratios were used alternatively, and for each void ratio, three different meshes were discretized. According to Figure 3-37, we can see that both the hardening and the softening behavior are more obvious when the material is denser, the initiation of the bifurcation point for specimens with different initial densities is very close, and the peak load carrying capacity increases with the initial density. Most of all, the regularization effectiveness of the micropolar approach for denser materials (blue curves) is worse than for the other two sets of simulations, especially at the end of the softening regime: it requires the micropolar approach to play a stronger role in overcoming the mesh dependency problems for denser materials. In short, a smaller element size l_e (larger ratio l_c/l_e) is required for regularizing solutions when the initial density is larger.

Figure 3-38 displays shear band thickness, allowing us to find that shear band thickness is almost identical for different initial densities. Accordingly, initial density has little influence on the thickness of shear bands in biaxial tests. The differences of peak values for plastic strain inside the shear band are also slight.

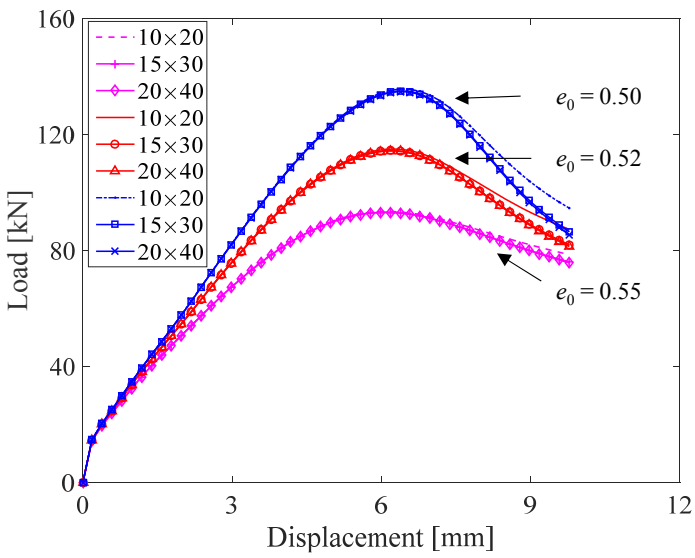

Figure 3-37 Influence of initial density on the load carrying capacity

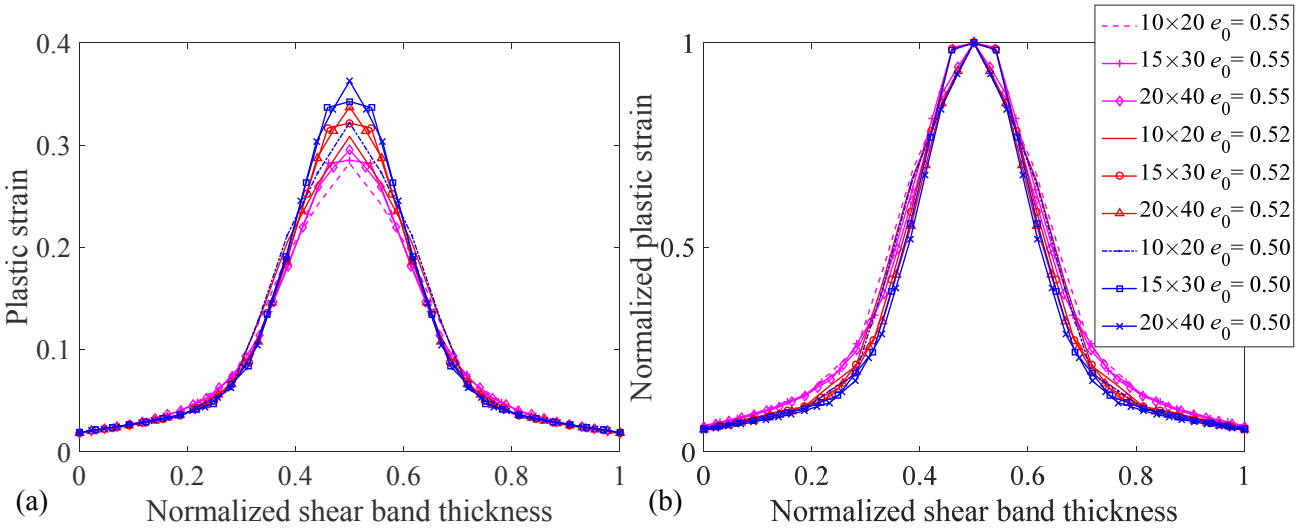

Figure 3-38 Influence of density on shear band thickness: (a) based on plastic strain; (b) based on normalized plastic strain

3.5.3 Influence of several key parameters

In this section, several important constitutive parameters, such as the critical friction angle ϕ_u (controlling the position of the critical state line), the strength parameter n_p (controlling the peak stress), and the deformation parameter n_d (controlling dilatancy) were discussed in terms of how they affect global strength as well as shear band thickness. Moreover, for each fixed parameter, the model was also discretized into three different meshes ranging from coarse to fine as had been done in previous sections. Thus, by comparing different meshes, the influence of these parameters on the regularization effectiveness ratio was observed.

3.5.3.1 Influence of the critical friction angle ϕ_u

Three different critical friction angles ϕ_u were used, and for each critical friction angle three different meshes were considered. The load carrying capacity curves for different cases are given in Figure 3-39, and from them certain phenomena can be observed: First, stiffness increases with critical friction angle during the hardening regime while at the same time softening behavior in the post-peak regime becomes significant when the critical friction angle increases during softening regime, as for the blue curves in Figure 3-39. Second, axial strain at the initiation of shear band increases significantly with critical friction angle; seemingly, the bifurcation point is delayed if the material

has a larger critical friction angle. Third, load carrying capacity increases with critical friction angle. Finally, it can be shown that the value of the critical friction angle greatly affects the effectiveness of regularization—that is to say, for material having a larger critical friction angle ϕ_u, the micropolar approach is required to play a stronger role in overcoming the mesh dependency problems during finite element analysis. Thus, a smaller element size l_e (larger ratio of l_c to l_e) is needed to regularize solutions if a larger critical friction angle ϕ_u has been adopted.

Considering the shear band thickness shown in Figure 3-40, we can find that differences of equivalent plastic strain distributions among the three groups having a different value of critical friction angle are less than obvious. Thus the critical friction angle ϕ_u has little influence on the thickness of shear bands in biaxial tests, but the critical friction angle ϕ_u significantly affects the peak value of equivalent plastic strain inside the shear band—and the less ϕ_u is, the greater the plastic strain peak inside the shear band.

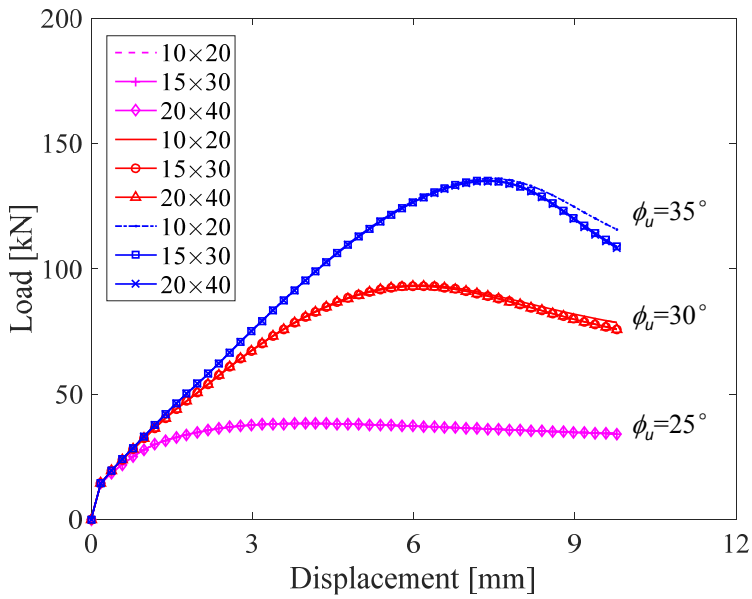

Figure 3-39 Influence of critical friction angle ϕ_u on the load carrying capacity

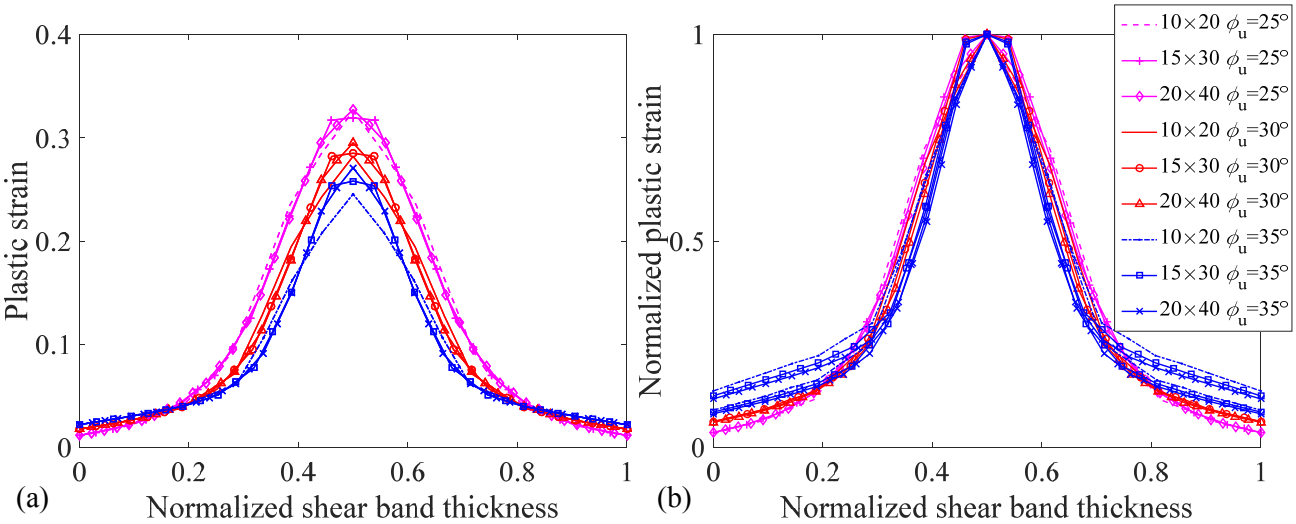

Figure 3-40 Influence of critical friction angle ϕ_u on shear band thickness: (a) based on plastic strain; (b) based on normalized plastic strain

3.5.3.2 Influence of the interlocking parameter n_p

The influence of the interlocking parameter n_p on strength and shear band was discussed in this section. Three different values of n_p have been adopted, with three different meshes performed for each fixed n_p. The load–displacement curves of the different cases are shown in Figure 3-41, allowing certain conclusions to be drawn. First, stiffness increases with the parameter n_p during the hardening regime, while at the same time the softening behavior in the post-peak regime becomes more significant when the parameter n_p increases as for the blue curves in Figure 3-41 and the strength of the largest n_p at the end of the softening regime is even less than for the other two groups (red and pink curves). Second, the axial strain at the onset of shear band increases slightly with the increase of the parameter n_p, which is to say that a large parameter n_p is able to delay the bifurcation point. Third, the parameter n_p greatly influences the specimen strength, with peak load carrying capacity increasing significantly with the value of the parameter n_p. Finally, it was also found that parameter n_p significantly affects the effectiveness of regularization, requiring the micropolar approach to play more roles in overcoming the mesh dependency problems for material having a larger parameter n_p. In other words, for materials having a larger parameter n_p, a smaller element size l_e (larger ratio l_c/l_e) is always needed to regularize the solutions.

Comparisons of shear band thickness for different cases are shown in Figure 3-42, which indicates that the larger the parameter n_p, the narrower the shear band will be. Nevertheless, the

influence of parameter n_p on shear band thickness is not very significant. Moreover, the peak value of plastic strain can be found to be also affected by the value of n_p, and the larger n_p is, the greater the maximum plastic strain inside the shear band.

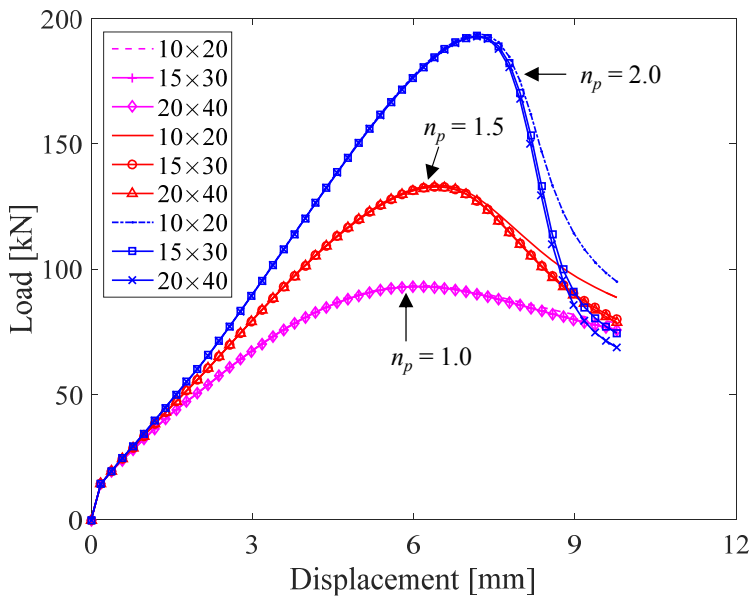

Figure 3-41 Influence of strength parameter n_p on the load carrying capacity

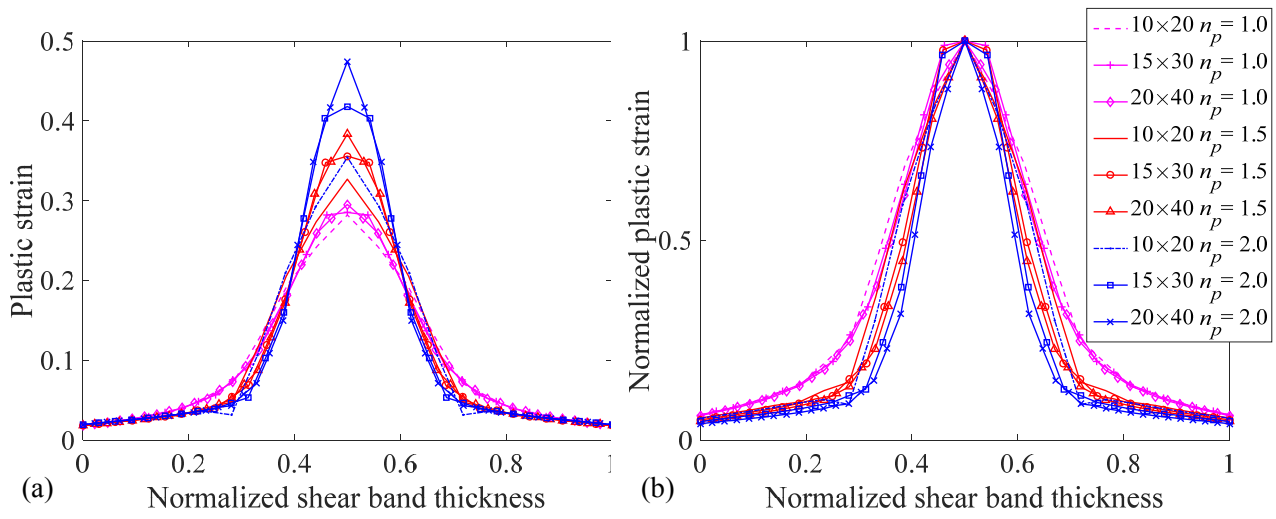

Figure 3-42 Influence of strength parameter n_p on shear band thickness: (a) based on plastic strain; (b) based on normalized plastic strain

3.5.3.3 Influence of the interlocking parameter n_d

The deformation parameter n_d, which controls the dilatancy behavior, is very important. It influences the specimen strength, the shear band thickness, and the effectiveness of regularization, as discussed in this section. The load carrying capacity of the specimen in different cases is shown in Figure 3-43, allowing certain observations. First, stiffness increases with deformation parameter n_d during the hardening regime, while at the same time the softening behavior in the post-peak regime becomes more significant when the deformation parameter n_d increases as for the blue curves in Figure 3-43. Second, the most obvious influence of deformation parameter n_d on the load–displacement curve is that the axial strain at the initiation of the shear band increases significantly with n_d. That is to say, the bifurcation point occurs earlier if the material has a larger deformation parameter n_d, which also demonstrates that the strain localization is closely related to the local dilatancy. Third, the influence of the deformation parameter n_d on the peak load carrying capacity can be found very slight. Finally, it can also be observed that deformation parameter n_d affects the effectiveness of regularization significantly, requiring the micropolar approach to play more roles in overcoming the mesh dependency problems for materials having a larger deformation parameter n_d. In short, a material having a larger deformation parameter n_d needs a smaller element size l_e (larger ratio of l_c to l_e) to regularize the solutions during finite element analysis.

Shear band thickness for different cases is shown in Figure 3-44, showing that differences among cases are not very obvious: the deformation parameter n_d has little influence on the thickness of shear bands in biaxial tests. However, the peak value of the equivalent plastic strain inside the shear band is seriously affected by the value of n_d—and the larger n_d is, the higher the maximum equivalent plastic strain.

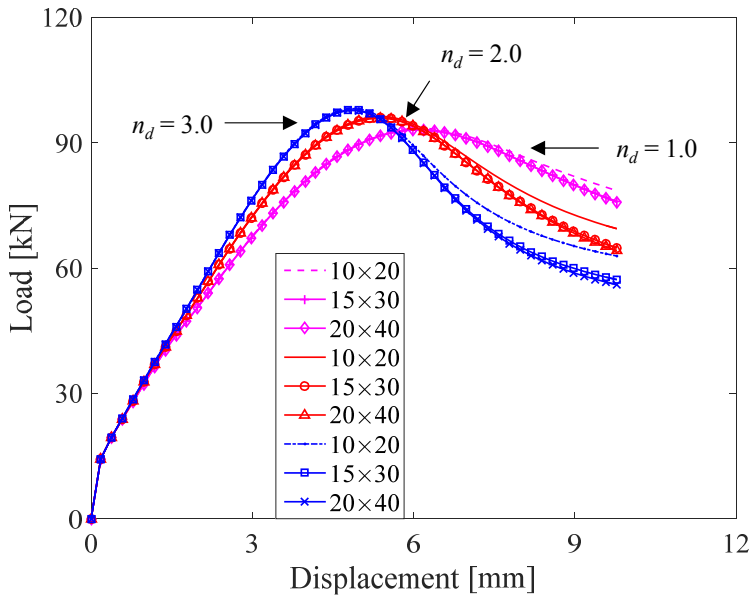

Figure 3-43 Influence of deformation parameter n_d on the load carrying capacity

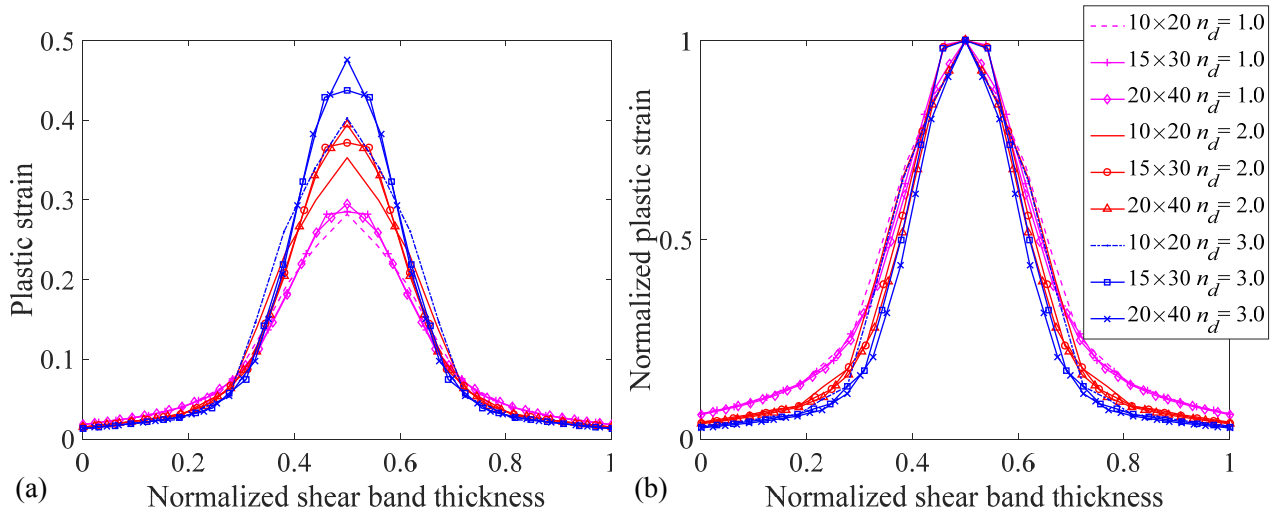

Figure 3-44 Influence of deformation parameter n_d on shear band thickness: (a) based on plastic strain; (b) based on normalized plastic strain

3.6 Conclusions

A series of simulations of biaxial tests using the polarized SIMSAND model was conducted in this chapter. Based on these simulated results, the shear band was deeply investigated, and some conclusions have been obtained as follows.

Through comparison with simulated results from the classical continuum theory–based model, the micropolar technique can be seen to have great capacity for overcoming numerical difficulties and is capable of dealing with mesh dependency problems during finite element analysis. Two-dimensional problems call for two newly incorporated parameters, among which the internal length scale l_c has particularly great influence on the shear band patterns and the load carrying capacity of a specimen, whereas the influence of the micropolar shear modulus G_c is negligible. The larger l_c is, the larger and later the peak load carrying capacity will be—and a larger l_c corresponds to more ductile material in the softening regime. Shear band inclination decreases slightly with the increase in l_c. Shear band thickness increases with internal length scale l_c, whereas normalized shear band thickness decreases with the increase of l_c. All these findings also validate the physical assumption that l_c can be regarded as the mean grain size d_{50}—at least during simulations of small structures during biaxial tests in the laboratory.

Unlike in the articles already referenced, which merely suggested a ratio for l_c in terms of l_e, the regularization effective ratio l_c/l_e was first proposed in the present study, along with the suggestion that for simulations having different meshes one certain ratio exists that can entirely alleviate mesh dependency problems. Moreover, discussions of the regularization effectiveness ratio of the micropolar technique have been featured in details. However, it must be noted that this ratio can be affected by other factors, such as material density, confining pressure, and the parameters of the constitutive model.

The influence on load carrying capacity and the thickness of shear bands of some other factors has been discussed, with simulated results demonstrating that peak load carrying capacity increases with initial density, confining pressure, critical friction angle ϕ_u, strength parameter n_p, and deformation parameter n_d. However, the impact of each factor varies—for example, the deformation parameter n_d has only slight, indeed ignorable, effect on the peak load carrying capacity, whereas the strength parameter n_p greatly influences the peak load carrying capacity. The influence on shear band thickness of these factors is negligible. Based on these influence analyses, a consistent conclusion has been obtained: if the softening behavior is more significant during the softening regime, then a smaller l_e (larger effective ratio l_c/l_e) is needed to entirely alleviate mesh dependency problems.

Chapter 4 Second-Order Work Criterion in Micropolar Theory

4.1 Introduction

It is well known that the failures of geostructures are due to the loss of stability. The definition of stability was initially introduced by Lyapunov (1907). Half a century later, some theories associated to the stability were put forward one after another, including the stability criteria of Drucker (1957) and of Hill (1958), among others. The stability criterion proposed by Hill (1958) was the one favored by numerous researchers in decades. The form of Hill's criterion can be expressed as the second-order work of materials in a Lagrangian formalism. Stability is related to the sign of the second-order work. For the small deformation cases, the second-order work can be expressed by the Cauchy stress tensor and strain tensor instead of the first Piola-Kirchoff stress tensor and the general term of deformation gradient in the original form (Nicot et al. 2007).

The second-order work in the numerical simulations with DEM (discrete element method) and FEM (finite element method) has been used to judge the instability of homogenous material problems (Hossain et al., 2007; Nicot and Darve, 2007; Nicot et al., 2007; Nicot et al., 2009; Nicot et al., 2011; Daouadji et al., 2012; Nicot et al., 2012a; Nicot et al., 2013; Wan et al., 2013; Nicot and Darve, 2015; Hadda et al., 2016; Nicot et al., 2017). Moreover, the second-order work criterion was recently extended from the homogeneous problems to judge also the instability of boundary value problems (Nicot, 2007).

In this chapter, the second-order work in micropolar theory has first been formulized. Then, based on the simulations of a biaxial test, the differences in the expression of the second-order work by classical continuum theory and micropolar theory based models were discussed and compared, from which the contributions of the couple stresses and curvatures in micropolar model to the second-order work have been analyzed. What's more, the mesh independency in simulating the shear bands in biaxial tests of the micropolar approach was demonstrated by the evolution of the second-order work during loading. At last, the envelope of the vanishing of the second-order work within the framework micropolar theory was also applied to an analysis of the failure a retaining wall.

4.2 Mathematical implications of instability

4.2.1 Material instability

The definition of stability was initially introduced by Lyapunov (1907) for elastic materials only. Since then, many researchers have contributed much to the domain of the instability of materials (Hill, 1958, 1961; Rudnicki and Rice, 1975; de Borst et al., 1993; Nova, 1994, 2003; Daouadji et al., 2009; Nicot et al., 2009; Nicot et al., 2011; Nicot and Darve, 2011; Daouadji et al., 2012; Nicot et al., 2012a; Hadda et al., 2013; Nicot et al., 2013; Wan et al., 2013; Nicot and Darve, 2015; Hadda et al., 2016; Nicot et al., 2017).

The classical stable postulate proposed by Drucker (1957) requires a linear incremental stress–strain relation and an associated flow rule. The criterion of stability is more restrictive, because it requires that the plastic component of the second-order work density remains positive:

$$d^2\boldsymbol{W}_{pl} = d^2\boldsymbol{W} - d^2\boldsymbol{W}_{el} = \dot{\varepsilon}_{ij}^{p}\dot{\sigma}_{ij} > 0 \tag{4.1}$$

Thus, the consequence is that an instable state for Drucker's criterion might be stable for Hill's criterion hereafter explained.

In Hill's (1958, 1961), a slight wave perturbation acted on an infinite material with a homogenous state of stress and strain, after which the stability was checked by analyzing the response to the wave. If the perturbation increased, the material was in a state of instability; otherwise, the material was stable. According to Hill (1958), the second-order work must be positive for the constitutive relationship of stable material (expressed by the Cauchy stress and strain herein).

$$d^2\boldsymbol{W} = \dot{\varepsilon}_{ij}\dot{\sigma}_{ij} > 0 \tag{4.2}$$

We can find for the perfect elastic plastic materials that Drucker's criterion is the same as Hill's criterion. If we limit our interest to incrementally linear constitutive equations,

$$\dot{\sigma}_{ij} = D_{ijkl}\dot{\varepsilon}_{kl} \tag{4.3}$$

then Eq. (4.2) can be expressed as

$$\dot{\varepsilon}_{ij}D_{ijkl}\dot{\varepsilon}_{kl} > 0 \tag{4.4}$$

where $\dot{\varepsilon}_{ij}$ and $\dot{\sigma}_{ij}$ are strain rate and stress rate tensors, respectively, D_{ijkl} is the material tangential matrix (in general non-symmetric), and the summation convention is adopted. Conversely, if the value of the equation $\dot{\varepsilon}_{ij} D_{ijkl} \dot{\varepsilon}_{kl} < 0$, it satisfies a necessary condition for material instability. If we consider the vectorial instead of the tensorial form, it can be expressed as follows

$$\dot{\boldsymbol{\varepsilon}}^T \dot{\boldsymbol{\sigma}} = \dot{\boldsymbol{\varepsilon}}^T \mathbf{D} \dot{\boldsymbol{\varepsilon}} = 0 \tag{4.5}$$

Similarly, the equality of Eq. (4.5) marks the onset of material bifurcation. Mathematically, this condition coincides with the loss of the positive-definiteness of the material tangential stiffness matrix **D** or the singularity of the symmetric part of **D**

$$\det(\mathbf{D} + \mathbf{D}^{\mathbf{T}}) = 0 \tag{4.6}$$

The loss of the uniqueness of the incremental solution in theoretical continuum mechanics was first studied by Darve and Chau (1987). Then, the non-uniqueness of the solutions was theoretically demonstrated by the loss of controllability (Nova, 1994, 2003; Wan et al., 2013). Based on the stress-strain curve, the limit point condition has the form

$$\dot{\boldsymbol{\sigma}} = \mathbf{D} \dot{\boldsymbol{\varepsilon}} = 0 \tag{4.7}$$

The condition det(**D**) = 0 can mark the plastic limit and the existence of a non-unique solution of the differential Eq. (4.7). For a symmetric tangential stiffness matrix **D**, the loss of positive-definiteness of **D** coincides with the limit point or the loss of controllability (non-uniqueness).

Obviously, the softening behavior can lead to the violation of the stability criterion that the inner product of the stress rate and the strain rate is positive. There is also a class of material instabilities that can cause the inner product of stress rate and strain rate to become negative even without the occurrence of strain softening (de Borst et al., 1993). For a non-symmetric tangential stiffness matrix, the non-symmetry is in itself sufficient to cause the loss of material stability, even if the slope of the vertical stress–strain curve is still rising (Rudnicki and Rice, 1975). For the material with the non-symmetric tangential stiffness matrix, the loss of material stability may be encountered prior to the limit point or loss of uniqueness. The reason is that the real-valued Eigen-spectrum of **D** is bounded by the minimum and maximum eigenvalues of 1/2(**D**+**D**^{T}). Thus det(**D**+**D**^{T}) = 0 always precedes the condition of det(**D**) = 0 (de Borst et al., 1993; Etse and Willam, 1994).

According to the suggestions of de Borst (1993), material instabilities can be classified into two major categories. In category one, the prevailing failure mechanism is decohesion, which may be denoted as mode I fracture, like fracture in masonry concrete and rocks under low confining pressure levels. The second category of failure is governed by the frictional slip, which may be identified as mode II failure, like frictional slip failures in metals, in soils, and in concrete and rocks under high confining pressure levels. In the same article, de Borst (1993) also argued that this distinction had deep implications for the effectiveness of various regularization approaches used to restore the well-posedness of the boundary value problems.

The formation of discontinuity in the deformation gradient has traditionally been identified with strain localization. In the research of Rudnicki and Rice (1975), strain localization has been considered as a bifurcation in the macroscopic constitutive description of the material. A shear band means a zone of intense deformation bounded by two discontinuity planes. It can be detected by the vanishing of the determinant of the acoustic tensor in the expression

$$\det(\mathbf{nDn}) = 0 \tag{4.8}$$

where **n** is the normal vector of the discontinuity (Rudnicki and Rice, 1975). The singularity of the acoustic tensor and the formation of the discontinuity correspond to the local loss of ellipticity of the rate equilibrium equations. It should be noted that this criterion allows us to detect only certain particular failures related to strain localization mode, but not failure in diffuse mode. Fortunately, it has been confirmed that the non-positiveness of the second-order work illustrated in the previous section can generally be used to detect both diffuse and localized failure (Etse and Willam, 1994).

To summarize the knowledge of material instability, Wan et al. (2013) clearly defined the hierarchy of material instabilities with the sign of each indicator as shown in Figure 4-1 (for a non-symmetric constitutive matrix **D**). For a symmetric constitutive matrix, all indicators tend to coincide at the peak response during loading history, with the possibility of det(**nDn**) occurring later in the softening regime.

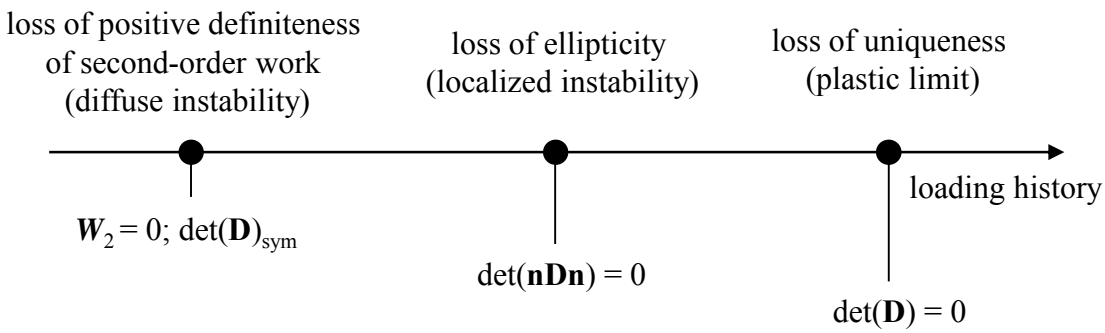

Figure 4-1 Order of instability criteria during loading history for non-symmetric constitutive matrices

4.2.2 Structural instability

Based on the material instability aforementioned, the structural instability will be analyzed. According to Hill's definition, the stability of a body (structural stability) that occupies the volume V can be guaranteed for all kinematically admissible $\dot{\boldsymbol{\varepsilon}}$ only if Eq. (4.9) is satisfied. If the inequality in Eq. (4.9) is replaced by equality, it also means the onset of potential structural instability. Therefore, the material instability may lead to structure instability.

$$\int_V \dot{\boldsymbol{\varepsilon}}^T \dot{\boldsymbol{\sigma}}\, dV > 0 \tag{4.9}$$

For a discrete mechanical system, we can introduce the structural tangential stiffness matrix **K**,

$$\mathbf{K} = \int_V \mathbf{B}^{\mathrm{T}}\mathbf{D}\mathbf{B}dV \tag{4.10}$$

where the superscript T is the transpose symbol and the matrix **B** relates the strain rate vector $\dot{\boldsymbol{\varepsilon}}$ to the nodal displacement rate vector $\dot{\mathbf{a}}$,

$$\dot{\boldsymbol{\varepsilon}} = \mathbf{B}\dot{\mathbf{a}} \tag{4.11}$$

and the onset of structural bifurcation may be denoted by the loss of positive-definiteness for the structural stiffness matrix **K**

$$\det(\mathbf{K} + \mathbf{K}^{\mathrm{T}}) = 0 \tag{4.12}$$

From Eq. (4.10), we can see that if the local material tangential stiffness matrix **D** loses positive-definiteness, the structural stiffness matrix **K** may lose positive-definiteness as well. In short, material instabilities may lead to structural instability, even in the absence of geometric destabilizing terms. However, the loss of positive-definiteness for material stiffness matrix **D** is not a necessary triggered for structural instabilities. But it can result in local loss of ellipticity for the equilibrium rate

equations. It is worth noting that the ellipticity of the governing equations is one of the three necessary conditions for well-posedness of the rate boundary value problems in static analysis, since the ellipticity must be preserved in the static case to obtain physically meaningful solutions. The other two conditions for well-posedness are the satisfaction of the boundary complementing condition and the satisfaction of the interfacial complementing condition (de Borst et al., 1993). More details can be found in Needleman (1991).

When considering structural instability, it must be noted whether the solution in the post-peak equilibrium path is the critical one at a lowest energy level or whether other equilibrium states exist at the same energy level. For this reason, the solution uniqueness is discussed hereafter. It is assumed that there are two different stress field rates $\dot{\boldsymbol{\sigma}}_1$ and $\dot{\boldsymbol{\sigma}}_2$, both of which satisfy the incremental equilibrium equation

$$\int_V \delta\boldsymbol{\varepsilon}^{\mathrm{T}}\dot{\boldsymbol{\sigma}}dV = \delta\mathbf{a}^{\mathrm{T}}\dot{\mathbf{f}} \tag{4.13}$$

where δ denotes the variation of a quantity and $\mathbf{f}$ assembles the external forces. Subtracting the two preceding equilibrium equations produces

$$\int_V \delta\boldsymbol{\varepsilon}^{\mathrm{T}}\Delta\dot{\boldsymbol{\sigma}}dV = 0 \tag{4.14}$$

where Δ denotes the difference between two different stress quantities corresponding to the same energy level. Substituting Eq. (4.3) and Eq. (4.11) into the foregoing Eq. (4.14), we can find for any visual displacement field $\delta\mathbf{a}$, with Eq. (4.14) able to be obtained only if

$$\mathbf{K}\Delta\dot{\mathbf{a}} = 0 \tag{4.15}$$

Multi-solutions of Eq. (4.15) exist only when

$$\det(\mathbf{K}) = 0 \tag{4.16}$$

This also means structural plastic limit point. From the foregoing discussion, we can conclude again that for a symmetric structural tangential stiffness matrix $\mathbf{K}$, the loss of structural stability coincides with the loss of uniqueness of the solution. For a non-symmetric tangential stiffness matrix $\mathbf{K}$, the structural instability ($\det(\mathbf{K}+\mathbf{K}^{\mathrm{T}}) = 0$) may occur before the loss of uniqueness ($\det(\mathbf{K}) = 0$) (Maier and Hueckel, 1979; de Borst et al., 1993).

4.2.3 Second-order work framework

The Hill's stability criterion has been favored in decades (Nova, 1994, 2003; Daouadji et al., 2009; Nicot et al., 2009; Nicot et al., 2011; Nicot and Darve, 2011; Daouadji et al., 2012; Nicot et al., 2012a; Hadda et al., 2013; Nicot et al., 2013; Wan et al., 2013; Nicot and Darve, 2015; Hadda et al., 2016; Nicot et al., 2017), because the authors found that the loss of uniqueness or controllability coincided with the vanishing of Hill's second-order work. Nicot et al. (2007, 2009) succeeded in mathematically explaining the physical meaning of Hill's criterion, and built a framework to study the instability based on the second-order work theory. Moreover, the second-order work theory was recently applied from homogenous problems to boundary value problems by Nicot et al. (2017).

As a proposition to understand the second-order work physically, Nicot et al. (2007) introduced the concept of sustainability, which refers to the stability of mechanical states in the sense that any external perturbation at constant control variables will cause an outburst in kinetic energy growth and, hence, sudden collapse. Thereafter, Nicot et al. (2007, 2009) worked out from energy equations that there could be a loss of sustainability of equilibrium states without any incremental input in the external work for a certain kinematical velocity field. Based on energy conservation, this condition would manifest itself through a sudden outburst of kinetic energy with a transition from a quasi-static phase to a dynamical regime in Eq. (4.17).

$$\ddot{E}_c = I_2 + W_2^{ext} - W_2^{\text{int}} \tag{4.17}$$

The term on the left-hand side $\ddot{E}_c$ is the second-order time derivative of the kinetic energy; the first term on the right-hand side $I_2 = \int_{V_0} \rho_0 \ddot{\mathbf{u}} dV_0$ is an internal term. As a quadratic average of the acceleration, this term is always positive. The second term in the right-hand side W_2^{ext} denotes the external second-order work, and the third terms W_2^{int} is the internal second-order work. The increase in kinetic energy from an equilibrium state, under incremental loading, was shown to be equal to the difference between the external second-order work, involving the external loading parameters, and the internal second-order work, involving the constitutive properties of the material (Nicot and Darve, 2015). When the system is quasi-static, the inertial term I_2 and the kinetic energy $\ddot{E}_c$ are nil, the internal second-order work is equal to the external second-order work. It turned out

that this transition could also be mathematically expressed by the vanishing of the second-order work. The failure mechanism of the material was initiated at the same time as the internal second-order work vanishes (Wan et al., 2013).

As a new interpretation of the second-order work, they indeed provided the relations between the loss of positive definiteness, loss of control, and loss of sustainability of equilibrium states because of incompatibility between imposed loading and material response. In this sense, the missing links in Hill's pioneering publications on second-order work and its physical interpretations were successfully explained by Nova (1994, 2003) and Nicot et al. (2009). Following that, a synthesis on the second-order work from several collaborating research teams was done by Daouadji et al. (2012). Furthermore, Wan et al. (2013) reinterpreted the basic theory of the second-order work in a rather concise but clear manner by comparing high-quality laboratory experimental results with finite element simulations.

4.3 Formulations of second-order work in micropolar theory

4.3.1 General equation of second-order work

The vanishing of the second-order work is fundamental and necessary for the collapse of the system to occur. Starting from an equilibrium state, and restricting problems in small deformations, the second-order work in local and global senses are defined as follows

$$W_2^{loc} = d\boldsymbol{\sigma} : d\boldsymbol{\varepsilon} \tag{4.18}$$

$$W_2^{glo} = \int_V d\boldsymbol{\sigma} : d\boldsymbol{\varepsilon}\, dV \tag{4.19}$$

, respectively. According to Hill (1958), whenever the second-order work vanishes or becomes negative, there is potential for material instability. At the global scale, if the negative second-order work pervades enough throughout the structure, it is anticipated that collapse will eventually occur (Wan et al., 2013).

4.3.2 Second-order work in classical continuum theory based FE analysis

In finite element analysis, the system is discretized into numerous elements connected to each other by common nodes. Therefore, the local second-order work in FEM can be calculated in a single element i

$$W_2^i = \dot{\boldsymbol{\sigma}}\dot{\boldsymbol{\varepsilon}}V_i \tag{4.20}$$

While the global second-order work can be obtained by summing all the local ones

$$W_2^{glo} = \sum_{i=1}^{n} W_2^i = \sum_{i=1}^{n} (\dot{\boldsymbol{\sigma}}\dot{\boldsymbol{\varepsilon}})_i V_i \tag{4.21}$$

where i is the element indicator, n is the total number of elements, and V_i is the volume of element i. $\dot{\boldsymbol{\sigma}}$ and $\dot{\boldsymbol{\varepsilon}}$ are the stress and strain rate vectors, respectively. It is worth noting that in all the cases of instability analysis with FEM in past studies, the contributions of the micro moments and the corresponding curvatures to the second-order work have not been considered.

4.3.3 Second-order work in micropolar theory based FE analysis

Since particles' rotations and rearrangements play significant roles in the failure of geotechnical structures, the micro moments and the energetically conjugated curvatures should be indispensable parts to the contribution of the second-order work.

Before the introduction of the second-order work in micropolar theory, it is useful to analyze the contribution of the grains' rotations to the second-order work, as it has already been examined in DEM. Based on the definition of particles in contact in DEM, as the contact (p-q) shown in Figure 4-2, Nicot et al. (2012b) wrote the second-order work expression as a function of microscopic variables describing the granular material microstructure

$$W_2 = \sum_{p,q} \delta f_i^c \delta l_i^c + \sum_{p \in V} \delta f_i^p \delta x_i^p \tag{4.22}$$

where l^c is the branch connecting the two centers of a contacting pair of particles in contact (p-q), f^c is the inter-particulate contact force, f^p is the resultant contact force applying on the particle p and x^p denotes the position of the mass center of p. The first term in the right-hand side implies the contact force and the branch vector between the particles in contact, which can be linked to the part of the

second-order work associated to the relative displacement of particle p to particle q. The second term in the right-hand side denotes the contribution to the second-order work of micro-structural rearrangements, which should not be neglected in strain localization analysis with significant rotations inside the shear band. Eq. (4.22) introduces the micro-mechanical expression of the second-order work, which allows us to investigate, at the microscopic scale, the origin of the vanishing of the macroscopic second-order work.

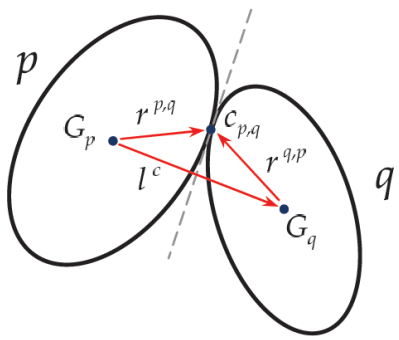

Figure 4-2 Definition of particles in contact

Besides the DEM, the micropolar theory is also able to consider the particles' independent rotations; consequently, the produced moments and micro curvatures can be taken into account. For two-dimensional problems, the stress and strain vectors in micropolar theory, enhanced by the micro moments and curvatures, have been generalized as

$$\boldsymbol{\varepsilon} = \left[\varepsilon_{xx}\ \varepsilon_{yy}\ \varepsilon_{zz}\ \varepsilon_{xy}\ \varepsilon_{yx}\ \kappa_{zx} l_c\ \kappa_{zy} l_c \right]^T \tag{4.23}$$

$$\boldsymbol{\sigma} = \left[\sigma_{xx}\ \sigma_{yy}\ \sigma_{zz}\ \sigma_{xy}\ \sigma_{yx}\ m_{zx}/l_c\ m_{zy}/l_c \right]^T \tag{4.24}$$

Thus, in FE analysis with the implemented micropolar SIMSAND model, the second-order work in one element should be defined as follows

$$W_2^i = \left(\dot{\sigma}_{xx}\dot{\varepsilon}_{xx} + \dot{\sigma}_{yy}\dot{\varepsilon}_{yy} + \dot{\sigma}_{xy}\dot{\varepsilon}_{xy} + \dot{\sigma}_{yx}\dot{\varepsilon}_{yx} + \dot{m}_{zx}\dot{\kappa}_{zx} + \dot{m}_{zy}\dot{\kappa}_{zy} \right) V_i \tag{4.25}$$

Similarly, the second-order work of the global system W_2^{glo} can be obtained according to Eq. (4.21).

4.4 Discussions of second-order work in FE analysis by simulating a biaxial test

In this section, failure in granular media was analyzed by the second-order work from a fundamentally energy viewpoint. Based on the simulations of a biaxial test by the classical

SIMSAND model and the polarized one, the differences of second-order work in the classical continuum theory and micropolar theory were discussed and compared. Constitutive parameters referred to the calibrated ones for Ottawa sand in Appendix E-Table E-1, and the specimen size, the boundary conditions and the test process referred to the description in Chapter 2-section 2.4. Similarly, four different mesh sizes, mesh 10×20, mesh 15×30, mesh 20×40 and mesh 30×60, were used as before.

4.4.1 Second-order work behind the mechanical response

Given an equilibrium state of the system, the mechanical response is the external performance, while the second-order work is the intrinsic reason responding to the outward behavior. We considered a failure analysis in a biaxial test simulation (e.g. the classical model with mesh 10×20), and plotted the mechanical response and the second-order work in the same plane as shown in Figure 4-3. It can be observed that the vanishing of the second-order work corresponds to the peak point of the bearing force, and the values of the second-order work are negative in the softening regime. The degree of softening is also reflected by the rate of the negative second-order work.

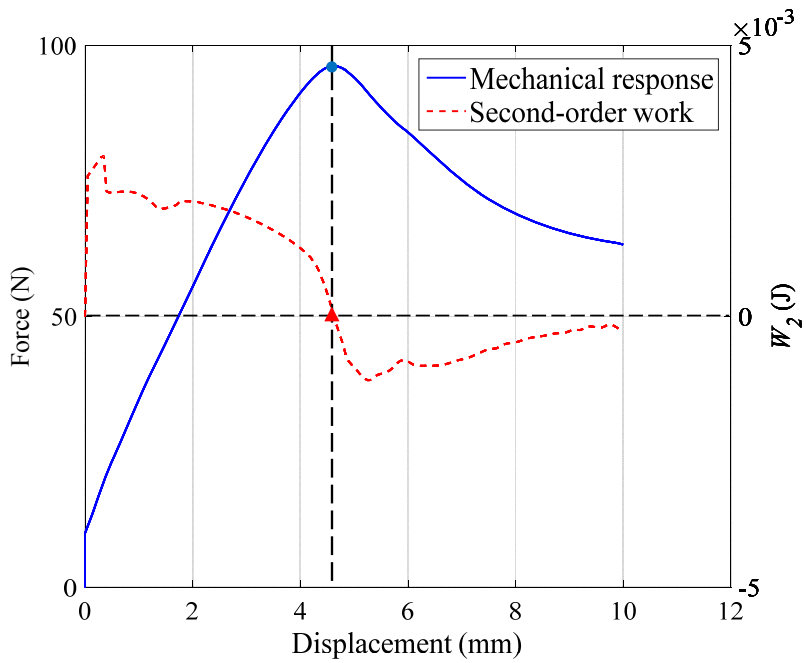

Figure 4-3 Second-order work behind the mechanical response

4.4.2 Comparisons of second-order work from classical model and polarized model

The comparison between the second-order work calculated from the classical SIMSAND model and from the micropolar SIMSAND model are the subject in hand. For the same specimen (with the same mesh: mesh 15×30), the simulated results by the two models are presented in Figure 4-4. It can be observed that by considering the contribution of coupled stresses and curvatures, the vanishing of the second-order work in micropolar theory occurs obviously later than that from the classical continuum theory. As an instability criterion, the vanishing of the second-order work in both the classical continuum theory and the micropolar theory can predict the bifurcation point which is a necessary condition for a potential failure. However, for the analysis in classical continuum theory, the negative values of second-order work calculated from the current stress-strain state in the post-bifurcation regime are influenced by pathological mesh dependency solutions. After the regularization of the micropolar approach, the numerical solutions become corrected in the post-bifurcation region; consequently, the negative values of the second-order work calculated from the micropolar SIMSAND model are meaningful.

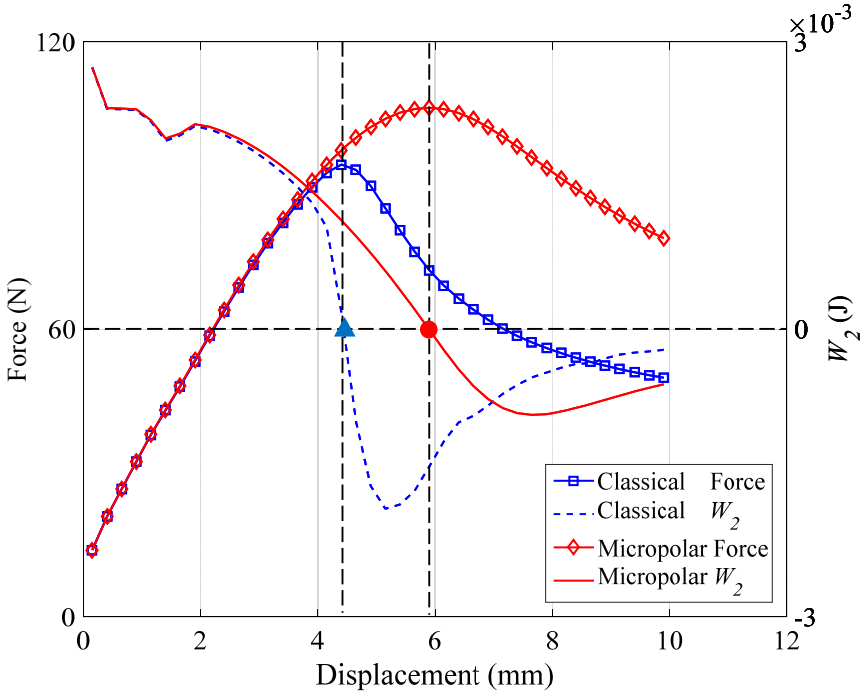

Figure 4-4 Comparisons of the results from classical SIMSAND model and the polarized model

It is well known that the failure can be triggered from local regions as a local instability inside the specimen and then be amplified to the whole sample. Therefore, the evolution of local

second-order work of the classical continuum and the micropolar continuum are presented in Figure 4-5 and Figure 4-6. From the evolution of the second-order work of the classical continuum in Figure 4-5, it can be observed that the local instability starts from the center of the specimen at a vertical displacement of 4mm, and then propagates to the corners. At a vertical displacement of 4.5 mm, the vanishing of the local second-order work results in the vanishing of the global second-order work as shown in Figure 4-4, which means the potential instability of the specimen. The complete failure can be found at the displacement of 5mm, showing that the vanishing of the local second-order work penetrates within the specimen. Moreover, the failure regions in the classical continuum are relatively narrow with a thickness of one element size. Figure 4-6 shows the similar evolution of the vanishing of the second-order work of the micropolar continuum. However, some obvious differences can be easily found. The failure regions of the micropolar continuum are larger than those of classical continuum. The reason is that in the micropolar continuum, the thickness of the shear band is controlled by the internal length rather than the element size. Besides the delay of the vanishing of the global second-order work compared to the classical continuum (see Figure 4-4), the complete penetration of the vanishing of the local second-order work is also delayed at a vertical displacement of about 7 mm. Afterwards, the shear bands with a finite thickness can be identified by the vanishing of the local second-order work. To some sense, the localized regions can be also defined by the domains of the vanished local second-order work, which affects significantly the global mechanical response.

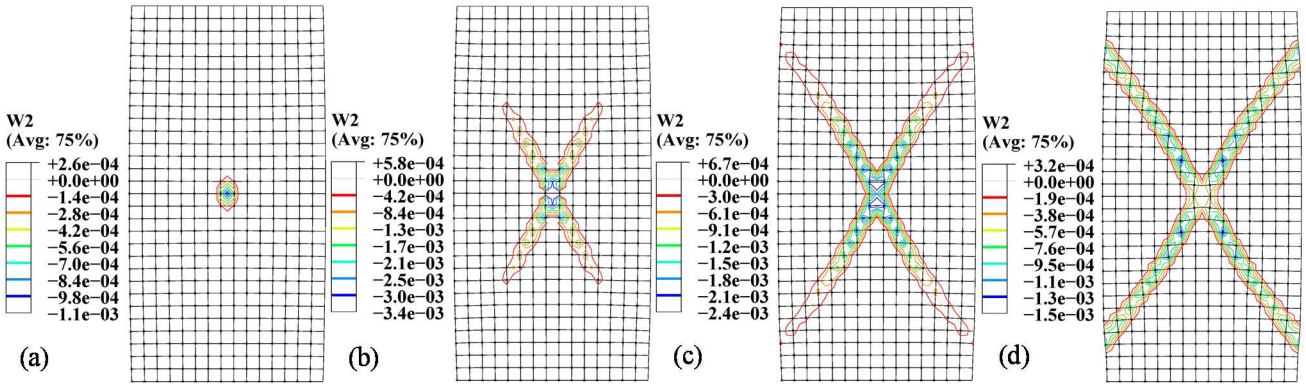

Figure 4-5 Evolution of the second-order work in the classical continuum: (a) vertical displacement of 4 mm; (b) vertical displacement of 4.5 mm; (c) vertical displacement of 5 mm; (d) vertical displacement of 5.8 mm

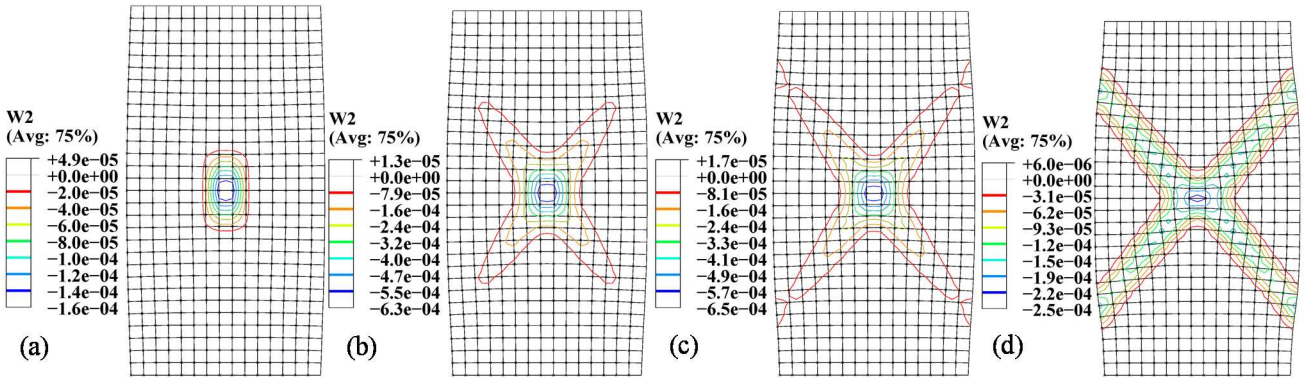

Figure 4-6 Evolution of the second-order work in the micropolar continuum: (a) vertical displacement of 5.5 mm; (b) vertical displacement of 6 mm; (c) vertical displacement of 7 mm; (d) vertical displacement of 10mm

4.4.3 Mesh dependency analysis of classical model by the second-order work

First, for the investigation of the second-order work in the classical continuum, we consider the four different meshes, mesh 10×20, mesh 15×30, mesh 20×40 and mesh 30×60.

The envelope diagrams of the vanishing of the second-order work at the end of the calculation for different meshes are shown in Figure 4-7, which can be used to denote the failure regions. We can find that the failure regions identified by the vanishing of the second-order work are dependent on the discretization. For mesh 10×20 and mesh 15×30, the calculations could be finished; however, the shear band of mesh 10×20 is obviously thicker than that of mesh 15×30. For the relatively fine meshes, mesh 20×40 and mesh 30×60, the envelope diagrams of the vanishing of second-order work just appeared at the center of the specimen, and could not propagate to the corners due to the difficulty of convergence in the vicinity of the bifurcation in classical continuum theory based FE analysis.

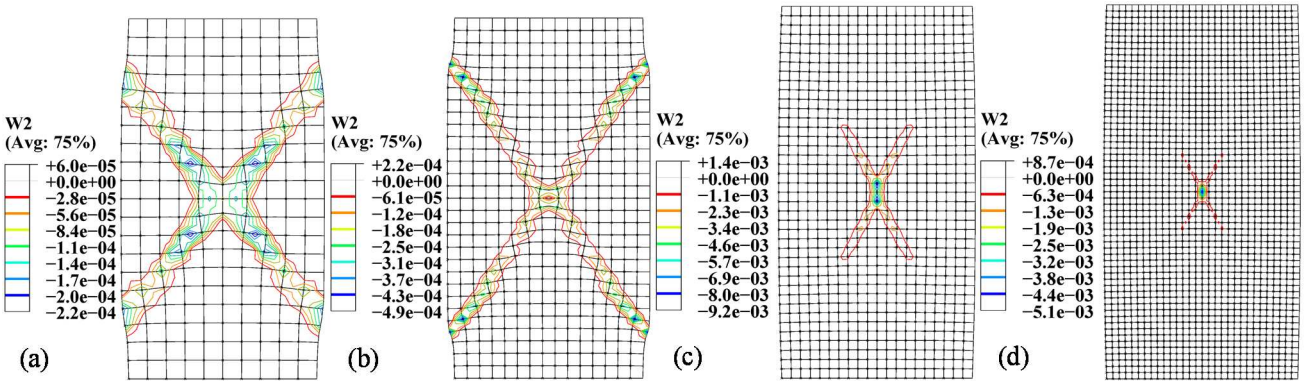

Figure 4-7 Instability regions identified by second-order work of different meshes in classical continuum: (a) mesh 10×20; (b) mesh 15×30; (c) mesh 20×40; (d) mesh 30×60

Figure 4-8 presents the evolutions of the mechanical response and the global second-order work for different meshes, showing also obvious mesh dependency. For mesh 30×60, the vanishing of the global second-order work is not reached because of numerical difficulties, which can also be found from the force-displacement curve. For mesh 20×40, the calculation becomes not convergent just after the vanishing of the second-order work. According to the figure, we can see that the second-order work vanishes at different vertical displacement for different mesh sizes, a coarse mesh having a later vanishing of the global second-order work; consequently, the mechanical responses for different meshes are also different.

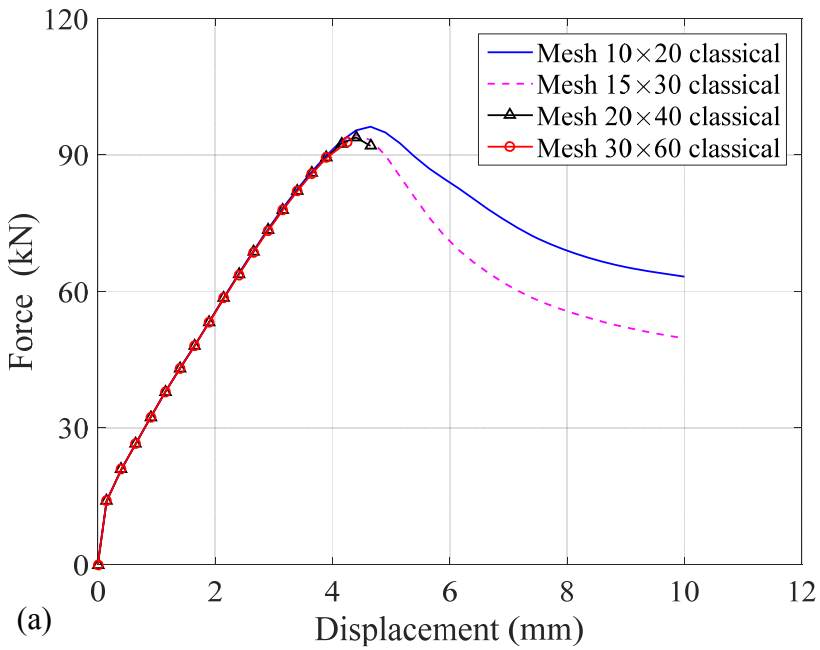

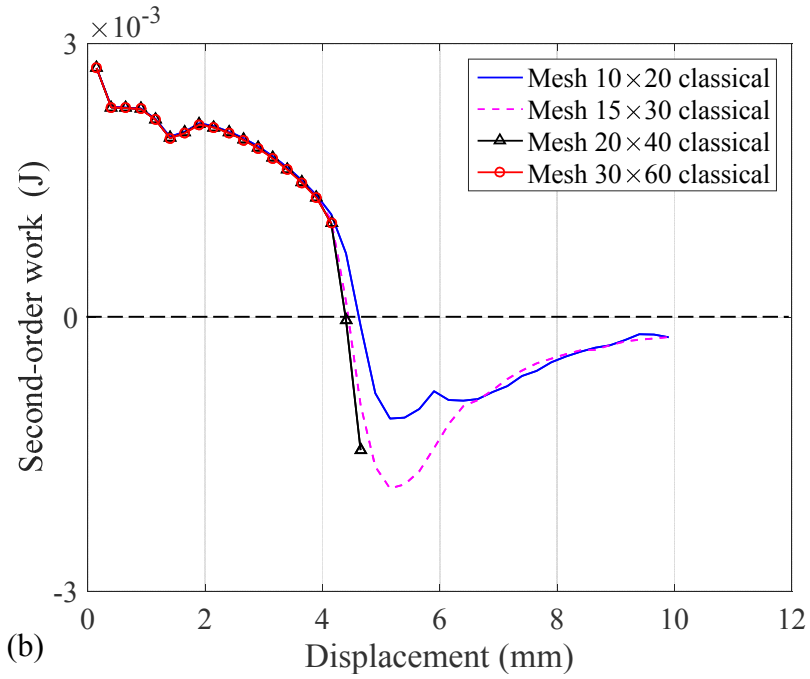

Figure 4-8 Comparisons of different meshes in a classical continuum: (a) mechanical responses; (b) evolutions of the second-order work

In conclusion, in the failure analysis using a classical theory based model, either the numerical calculation has to be stopped caused by convergence problems or the numerical solutions are pathologically dependent on the discretized element size. Thus, the negative values of the second-order work from the classical model are also mesh dependent; consequently, the instable envelope diagrams by the vanishing of second-order work are not objective.

4.4.4 Mesh independency analysis of micropolar model by the second-order work

Then, the second-order work in the micropolar continuum is investigated. According to the regularization effective ratio defined in Chapter 3-section 3.4, the three relative fine meshes, mesh 15×30, mesh 20×40 and mesh 30×60, which satisfy the effective ratio, are used for simulation by the micropolar SIMSAND model. Compared to the results from the classical model, significant improvements can be observed in Figure 4-9 and Figure 4-10.

With the regularization of micropolar approach, no convergence difficulty was encountered for all the different meshes, and all the calculations proceeded from beginning to end. From Figure 4-9, it can be observed that the failure regions identified by the envelope diagrams of the vanishing of

second-order work in the micropolar continuum are nearly the same. So the mesh dependency problems have been efficiently relieved.

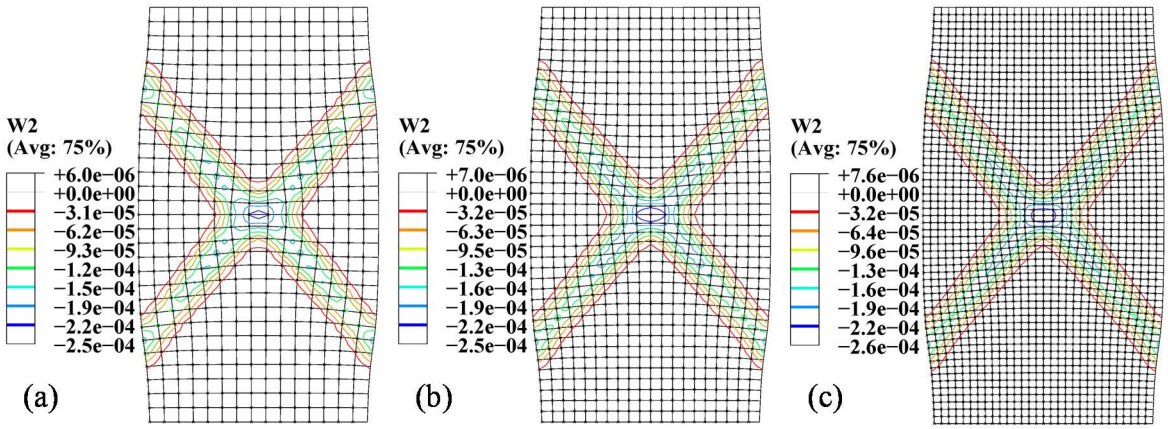

Figure 4-9 Instability regions identified by second-order work of different meshes in micropolar continuum: (a) mesh 15×30; (b) mesh 20×40; (c) mesh 30×60

Furthermore, the mesh independency of the mechanical responses and the global second-order work evolution for the three different meshes can also be found in Figure 4-10, indicating that the vanishing of the second-order work occurs at the same vertical displacement regardless of the discretization. Moreover, the three curves coincide with each other even after the vanishing of the second-order work corresponding to ~~the~~ consistent force–displacement curves after the bifurcation point. Considering that the micropolar theory can preserve the ellipticity (for static problems) of the partial differential governing equations after the onset of bifurcation, consequently, the second-order work in the post-failure regime of the micropolar continuum is still meaningful and can be used not only to detect the bifurcation point but also to reflect the tendency of the mechanical response after the bifurcation point.

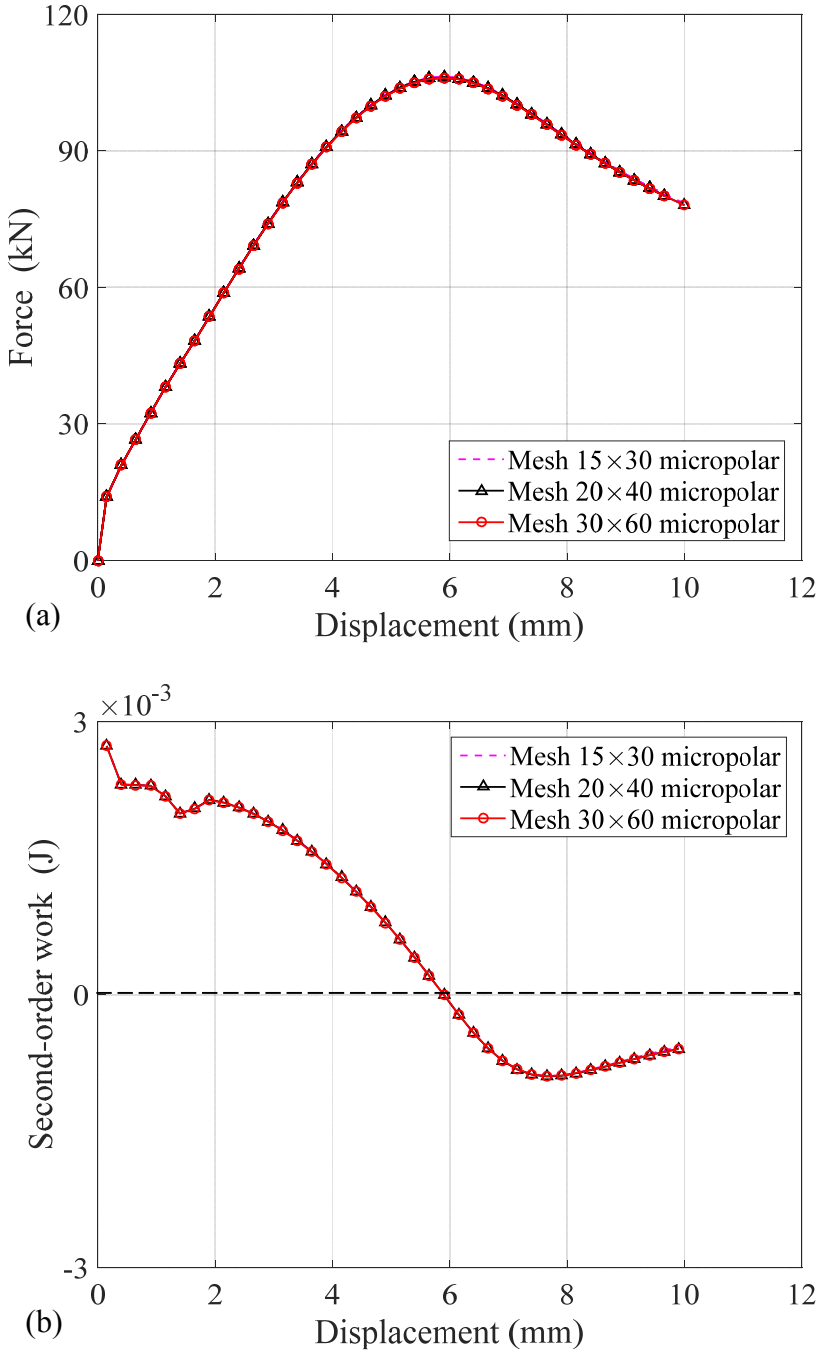

Figure 4-10 Comparisons of different meshes in a micropolar continuum: (a) mechanical responses; (b) evolutions of the second-order work

If the vanishing of the second-order work from classical and micropolar results are compared based on Figure 4-8 and Figure 4-10, we can see that the bifurcation points in the micropolar continuum are significantly delayed. Owning to the incorporation of the rotational degree of freedom and the internal parameter with a microstructural length scale, the conventional definition of the

second-order work has been generalized to consider the contribution of couple stresses and the conjugated curvatures, which leads to the delay of the vanishing of the second-order work.

4.4.5 Discussions of the contribution of micro rotations to the second-order work

As has been illustrated in the previous section, the contribution of the couple stresses and the micro curvatures should be responsible for the delay of the vanishing of the second-order work. Therefore, in order to investigate the role that the micro rotations played on the second-order work, the second-order work of a micropolar continuum is divided into two parts, the part calculated from the conventional Cauchy stresses and strains and another part calculated from the couple stresses and micro curvatures.

Significant grain rotations have been observed to occur inside the shear band, and it has been found that the rotations of grains changed from clockwise to anticlockwise in the centerline of the shear band. In this sense, the highest rotations are located at the edge of the strain localization regions. Consequently, it is believed that larger contributions of the couple stresses and micro curvatures to the second-order work should also be located at the edge of the shear band, which can be obviously verified by the contour of the rotational part of the second-order work in the sample as shown in Figure 4-11. Therefore, for the local analysis of the components of the second-order work, an element at the edge of a shear band (based on micropolar model: mesh 15×30) is chosen as shown in Figure 4-12.

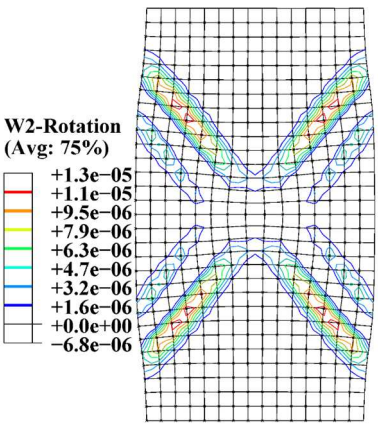

Figure 4-11 Contribution of the grains rotations to the second-order work

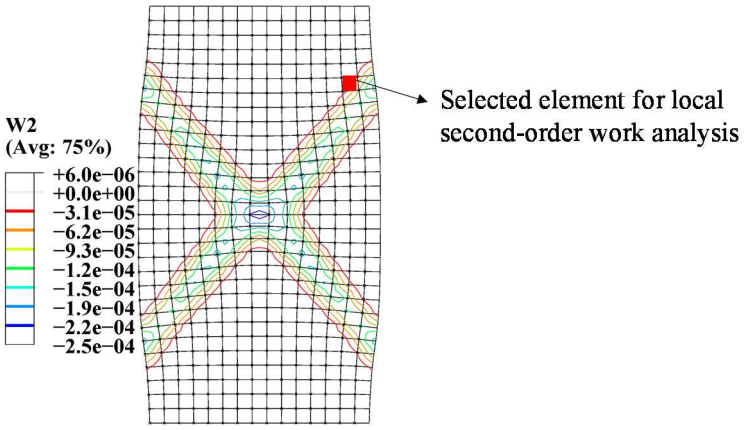

Figure 4-12 Selecting an element for local analysis of the components of the second-order work

The second-order work of the element and its two parts, the conventional part based on Cauchy stresses and strains and the rotational part based on couple stresses and micro curvatures, are plotted in Figure 4-13. In Figure 4-13, W_2 micropolar denotes the total second-order work of the micropolar continuum, W_2 Cauchy stress and W_2 Couple stress represent the conventional part and the rotational part of the total second-order work, respectively. We can see that the rotational part contributes significantly to the second-order work and, because of its positive value, the vanishing of the local second-order work is obviously delayed.

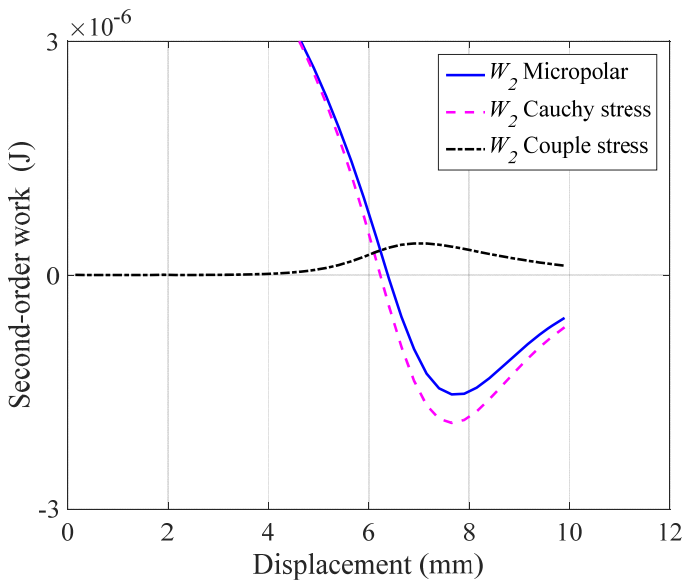

Figure 4-13 Components of the second-order work of a local element

Similarly, in Figure 4-14 the global second-order work of the specimen (based on micropolar model: mesh 15×30) is also divided into two parts, corresponding to the conventional part and rotational part, respectively. It is also found that the contribution of the couple stresses and curvatures in the micropolar continuum delays slightly the vanishing of the global second-order work.

It is worth noting that at the global scale the contributions from micro moments and curvatures are relatively small compared to classical Cauchy stresses and strains, because the rotations of the grains in most regions outside the shear bands are very small; consequently, the global rotational part does not contribute much to the global total second-order work. However, the rotational degree of freedom and the internal length scale in the micropolar theory based models have great influence within the strain localized domains. Thus, the mechanical response or the evolution of the second-order work of the micropolar continuum is very different from that of a classical continuum.

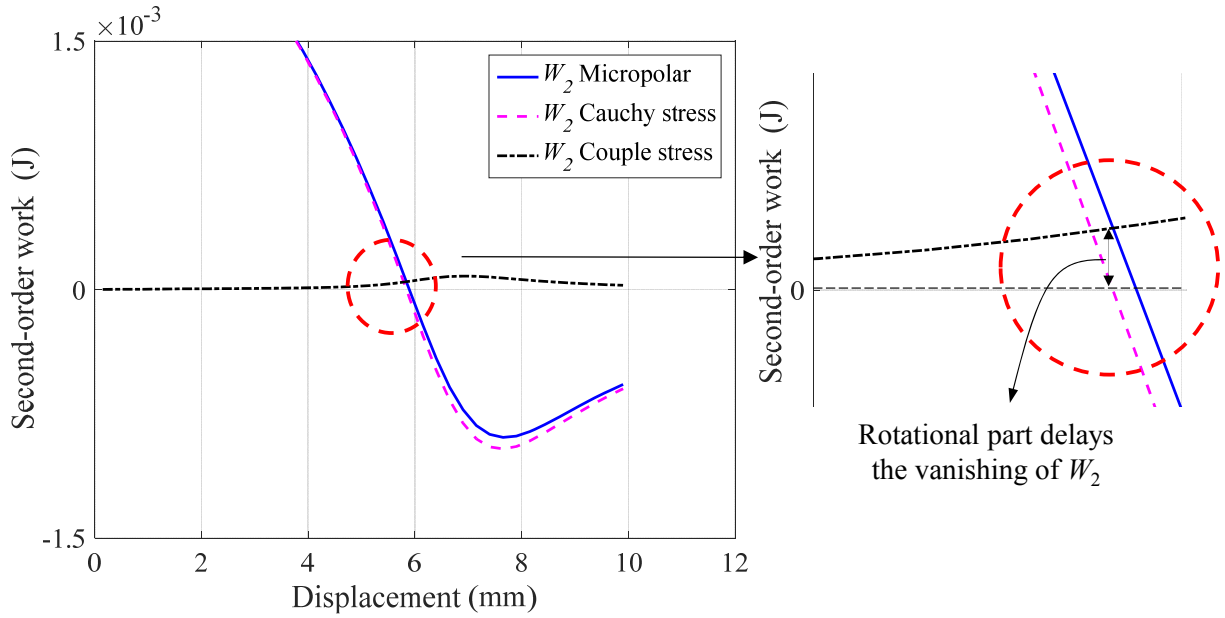

Figure 4-14 Components of the global second-order work

4.5 Application of the second-order work in the analysis of a retaining wall

The numerical analyses of a retaining wall under passive condition with the finite element method by both the classical SIMSAND model and the micropolar SIMSAND model have been conducted in chapter 2, which illustrated well the regularization ability of the micropolar approach in relieving the mesh dependency problems faced with the classical continuum theory based model. In this section, the vanishing of the second-order work for different mesh sizes within the framework of the classical continuum theory and of the micropolar theory was used to investigate the failure of the soil mass behind a retaining wall, which are presented, respectively, in Figure 4-15 and Figure 4-16.

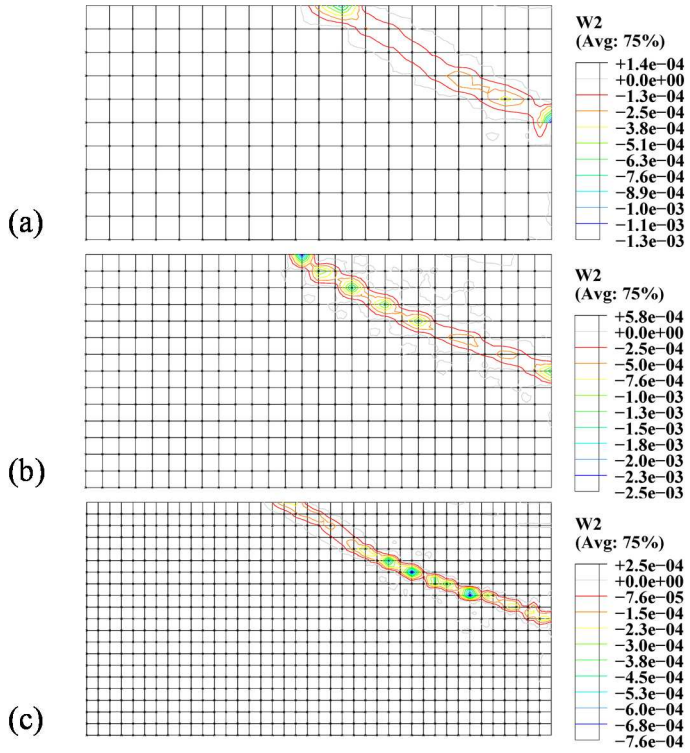

Figure 4-15 Failure zone of the soil mass behind the wall identified by the vanishing of the second-order work of different mesh sizes in a classical continuum: (a) mesh 20×10; (b) mesh 28×14; (c) mesh 40×20

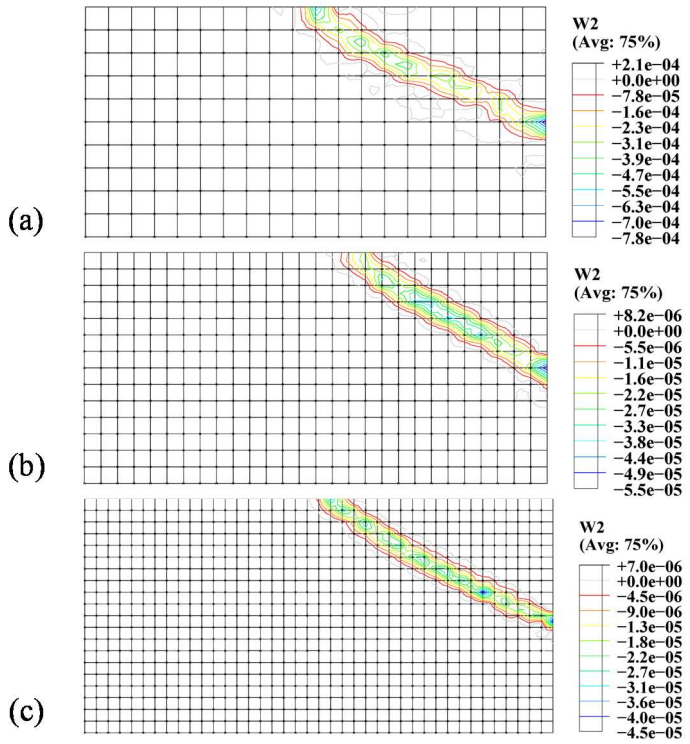

Figure 4-16 Failure zone identified by the vanishing of the second-order work of different mesh sizes in a micropolar continuum: (a) mesh 20×10; (b) mesh 28×14; (c) mesh 40×20

From Figure 4-15, it can be seen that the regions of the vanishing second-order work are seriously dependent on the element size, the finer the element size is, the narrower the thickness of the region of the vanishing second-order work will be. Moreover, the envelopes of the vanishing of the second-order work for the three mesh sizes based on the classical continuum theory are rough and fluctuant, which means the instability of the calculation by the classical model. In contrast, the envelops of the vanishing of the second-order work for the three different mesh sizes based on the micropolar theory are showed in Figure 4-16, from which it can be seen that the thicknesses of the three failure regions identified by the vanishing of the second-order work are nearly the same, and the envelopes of these regions are smoother and regular. Accordingly, the generalized second-order work can not only reflect the regularization effectiveness of the micropolar theory but also characterize the potential instable regions regardless of the element size.

4.6 Conclusions

In this chapter, the instability criteria closely related to material and structure failures were reviewed. Focuses have been laid on the second-order work proposed by Hill (1958), based on which Nicot et al. (2007, 2009) have succeeded in building a framework to study the instability. Then, the formulations of the second-order work criterion in micropolar theory has been derived and its applications have been investigated by simulating the failure of the specimen in biaxial test and a retaining wall.

It is well known that the second-order work is the intrinsic factor responding to the external mechanical response, therefore, the regularization role of the micropolar theory was illustrated from an energy point of view by the second-order work criterion. According to the simulated results, it can be concluded that the vanishing of the second-order work in both the classical continuum and the micropolar continuum can predict the bifurcation point. However, the bifurcation point in classical continuum is dependent on the discretized mesh size. In the post-bifurcation regime, the negative values of the second-order work based on the classical model become meaningless because of the pathological numerical solutions. In contrast, the mesh dependency problems can be effectively overcome by the regularization in micropolar theory. Because of the incorporation of a rotational

degree of freedom and an internal length scale, the bifurcation point in the micropolar continuum is significantly delayed. Moreover, in the shear band zones with great rotations of grains, the couple stresses and curvatures contribute a lot to the second-order work and delay significantly the vanishing of the second-order work. Global failure is the developed result of the local failure, therefore, the envelope diagrams of the vanishing of the second-order work are very physically meaningful to represent the failure regions, and thus to obtain the correct failure domains in the micropolar continuum regardless of the mesh size.

Chapter 5 Extension of the micropolar model from 2D to 3D

5.1 Introduction

The aforementioned research based on micropolar theory focuses chiefly on two-dimensional plane strain problems. However, most actual engineering structures belong to the three-dimensional domain. Accordingly, extension of the current two-dimensional micropolar model to make it three-dimensional is needed. Recently, some researchers have formulated a framework for the three-dimensional micro polar model, and several numerical simulations have also been conducted with it (Khoei et al., 2010; Riahi et al., 2009; Riahi and Curran, 2009; Tang and Hu, 2017) , but a more advanced constitutive model for sand with the notion of critical state has never been generalized from 2D to 3D.

In this chapter, a three-dimensional finite element formulation of a micropolar continuum was first presented. After that, the user-defined element within the framework of the micropolar theory was derived and developed via the interface of the commercial finite element software ABAQUS. Finally, the finite element implementation of the 3D critical state–based micropolar model for granular soils was demonstrated. To validate the correctness of the 3D micropolar SIMSAND model, a series of test simulations, including triaxial and biaxial drained and undrained tests for dense and loose sand, was conducted and compared in terms of the results obtained through use of the integrated point program (IPP) and the 3D micropolar model. Furthermore, numerical simulations of boundary value problems have been conducted using the 3D micropolar model and validated through comparison of results from the 2D model. Finally, the regularization effectiveness of the 3D model when dealing with mesh dependency problems was discussed.

5.2 Framework of the 3D micropolar theory

5.2.1 Equilibrium formulations

According to Mindlin and Tiersten (1962), the conservation of mass, balance of momentum, moment of momentum, and conservation of mechanical energy for a micropolar continuum must be satisfied.

Figure 5-1 depicts the motion of a portion V of a material volume, bounded by a surface S with outward normal n. S separates the portion of a material volume V from the remainder. Across S act force stress and couple stress vectors $\mathbf{t}_n$ and $\mathbf{m}_n$, respectively, and within V act body–force and body–couple vectors $\mathbf{f}$ and $\mathbf{c}$, respectively. Force stress vector $\mathbf{t}_n$ and body–force vector $\mathbf{f}$ are polar vectors, whereas the couple stress vector $\mathbf{m}$ and the body–couple vector $\mathbf{c}$ are axial vectors. Axial vectors are taken to be positive in the direction of advance of a right-handed screw.

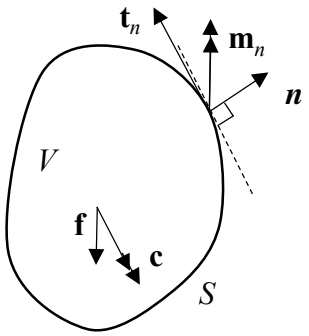

Figure 5-1 Forces stresses and couple stresses acting on a micro polar portion

Then the equilibrium equations, including conservation of mass, balance of momentum, moment of momentum, and conservation of mechanical energy are formulated, respectively, as

$$\frac{d}{dt}\int_V \rho dV = 0 \tag{5.1}$$

$$\frac{d}{dt}\int_V \mathbf{v}\rho dV = \int_S \mathbf{t}_n dS + \int_V \mathbf{f} dV \tag{5.2}$$

$$\frac{d}{dt}\int_V \mathbf{r}\times\mathbf{v}\rho dV = \int_S (\mathbf{r}\times\mathbf{t}_n + \mathbf{m}_n) dS + \int_V (\mathbf{r}\times\mathbf{f} + \mathbf{c}) dV \tag{5.3}$$

$$\frac{d}{dt}\int_V \left(\frac{1}{2}\mathbf{v}\cdot\mathbf{v} + U\right)\rho dV = \int_S \left(\mathbf{t}_n\cdot\mathbf{v} + \frac{1}{2}\mathbf{m}_n\cdot\nabla\times\mathbf{v}\right) dS + \int_V \left(\mathbf{f}\cdot\mathbf{v} + \frac{1}{2}\mathbf{c}\cdot\nabla\times\mathbf{v}\right) dV \tag{5.4}$$

where $\frac{d}{dt}$ is the material time-derivative, ρ is the mass density, $\mathbf{r}$ is the spatial position vector from a fixed origin, $\mathbf{v}$ is the material velocity $\frac{d\mathbf{r}}{dt}$, U is the internal energy per unit mass, ∇ is the special gradient $\frac{\partial}{\partial\mathbf{r}}$, and $\frac{1}{2}\nabla\times\mathbf{v}$ is the vorticity.

Consideration of the equilibrium of forces acting on the elementary tetrahedron, as the volume of the tetrahedron shrinks to zero, leads to the definition of the usual force stress dyadic $\boldsymbol{\sigma}$:

$$\mathbf{t}_n = \mathbf{n} \cdot \boldsymbol{\sigma} \tag{5.5}$$

An analogous treatment of the equilibrium of moments acting on the tetrahedron yields the definition of the couple stress dyadic $\mathbf{m}$:

$$\mathbf{m}_n = \mathbf{n} \cdot \mathbf{m} \tag{5.6}$$

From Eq. (5.2), we have

$$\int_S \mathbf{t}_n dS = \int_S \mathbf{n} \cdot \boldsymbol{\sigma} dS = \int_V \nabla \cdot \boldsymbol{\sigma} dV \tag{5.7}$$

According to the divergence theorem, combining Eq. (6.1), Eq. (6.2), and Eq. (6.7) gives

$$\int_V \left(\nabla \cdot \boldsymbol{\sigma} + \mathbf{f} - \rho \dot{\mathbf{v}} \right) dV = 0 \tag{5.8}$$

This allows the usual force stress equation of motion to be obtained:

$$\nabla \cdot \boldsymbol{\sigma} + \mathbf{f} = \rho \dot{\mathbf{v}} \tag{5.9}$$

The left and right side of Eq. (5.3) can be also formulated:

$$\frac{d}{dt} \int_V \mathbf{r} \times \mathbf{v} \rho dV = \int_V \frac{d\left(\mathbf{r} \times \mathbf{v}\right)}{dt} \rho dV = \int_V \left(\mathbf{v} \times \mathbf{v} + \mathbf{r} \times \dot{\mathbf{v}} \right) \rho dV = \int_V \mathbf{r} \times \dot{\mathbf{v}} \rho dV \tag{5.10}$$

$$\begin{aligned} \int_S \mathbf{r} \times \mathbf{t}_n dS &= \int_S \mathbf{r} \times \left(\mathbf{n} \cdot \boldsymbol{\sigma} \right) dS = -\int_S \mathbf{n} \cdot \boldsymbol{\sigma} \times \mathbf{r} dS \\ &= -\int_S \nabla \cdot \left(\boldsymbol{\sigma} \times \mathbf{r} \right) dV = \int_V \left[\mathbf{r} \times \left(\nabla \cdot \boldsymbol{\sigma} \right) + \boldsymbol{\sigma} \times \mathbf{I} \right] dV \end{aligned} \tag{5.11}$$

$$\int_S \mathbf{m}_n dS = \int_S \mathbf{n} \cdot \mathbf{m} dS = \int_V \nabla \cdot \mathbf{m} dV \tag{5.12}$$

where $\mathbf{I}$ is the unit spatial dyadic. Hence Eq. (5.3) becomes

$$\int_V \mathbf{r} \times \left(\nabla \cdot \boldsymbol{\sigma} + \mathbf{f} - \rho \dot{\mathbf{v}} \right) dV + \int_V \left(\nabla \cdot \mathbf{m} + \mathbf{c} - \boldsymbol{\sigma} \times \mathbf{I} \right) dV = 0 \tag{5.13}$$

From Eq. (6.9) and Eq. (6.13), we can get the couple stress equation of motion:

$$\nabla \cdot \mathbf{m} + \mathbf{c} - \boldsymbol{\sigma} \times \mathbf{I} \tag{5.14}$$

The force stress $\boldsymbol{\sigma}$ can be divided into a symmetric part and an antisymmetric part:

$$\boldsymbol{\sigma} = \boldsymbol{\sigma}^A + \boldsymbol{\sigma}^S \tag{5.15}$$

The antisymmetric part of $\boldsymbol{\sigma}$ is $\boldsymbol{\sigma}^A = -\frac{1}{2}\mathbf{I}\times(\boldsymbol{\sigma}\times\mathbf{I})$. Hence

$$\boldsymbol{\sigma}^A = \frac{1}{2}\mathbf{I}\times(\nabla\cdot\mathbf{m}+\mathbf{c}) \tag{5.16}$$

Substituting Eq. (5.15) and Eq. (5.16) into Eq. (5.9), we find an alternative form of the equation of motion:

$$\nabla\cdot\boldsymbol{\sigma}^S + \frac{1}{2}\nabla\times\nabla\cdot\mathbf{m}+\mathbf{f}+\frac{1}{2}\nabla\times\mathbf{c} = \rho\dot{\mathbf{v}} \tag{5.17}$$

For the equation of conservation of mechanical energy, the left and right side can be also formulated:

$$\frac{d}{dt}\int_V\left(\frac{1}{2}\mathbf{v}\cdot\mathbf{v}+U\right)\rho dV = \int_V\left(\mathbf{v}\cdot\dot{\mathbf{v}}+\dot{U}\right)\rho dV \tag{5.18}$$

$$\int_S \mathbf{t}_n\cdot\mathbf{v}dS = \int_S \mathbf{n}\cdot\boldsymbol{\sigma}\cdot\mathbf{v}dS = \int_V \nabla\cdot(\boldsymbol{\sigma}\cdot\mathbf{v})dV = \int_V\left[\boldsymbol{\sigma}:\nabla\mathbf{v}+(\nabla\cdot\boldsymbol{\sigma})\cdot\mathbf{v}\right]dV \tag{5.19}$$

$$\begin{aligned}\int_S \mathbf{m}_n\cdot\nabla\times\mathbf{v}dS &= \int_S \mathbf{n}\cdot\mathbf{m}\cdot\nabla\times\mathbf{v}dS = \int_V \nabla\cdot(\mathbf{m}\cdot\nabla\times\mathbf{v})dV \\ &= \int_V\left[\mathbf{m}:\nabla\nabla\times\mathbf{v}+(\nabla\cdot\mathbf{m})\cdot\nabla\times\mathbf{v}\right]dV\end{aligned} \tag{5.20}$$

Thus Eq. (5.4) can be written as

$$\int_V \rho\dot{U}dV = \int_V\left[(\nabla\cdot\boldsymbol{\sigma}+\mathbf{f}-\rho\dot{\mathbf{v}})\cdot\mathbf{v}+\frac{1}{2}(\nabla\cdot\mathbf{m}+\mathbf{c})\cdot\nabla\times\mathbf{v}+\boldsymbol{\sigma}:\nabla\mathbf{v}+\frac{1}{2}\mathbf{m}:\nabla\nabla\times\mathbf{v}\right]dV \tag{5.21}$$

Combining Eqs. (5.9), (5.14), (5.16), and Eq. (5.21) produces

$$\rho\dot{U} = \boldsymbol{\sigma}^S:\nabla\mathbf{v}+\frac{1}{2}\mathbf{m}:\nabla\nabla\times\mathbf{v} \tag{5.22}$$

Because the scalar of $\nabla\nabla\times\mathbf{v}$ also equals zero, the right-hand side of the preceding equation can be written as

$$\rho\dot{U} = \boldsymbol{\sigma}^S:\nabla\mathbf{v}+\frac{1}{2}\mathbf{m}^D:\nabla\nabla\times\mathbf{v} \tag{5.23}$$

where $\mathbf{m}^D$ is the deviator of $\mathbf{m}$:

$$\mathbf{m}^D = \mathbf{m} - \frac{1}{3}\mathbf{m}:\mathbf{II} \tag{5.24}$$

Furthermore, because $\nabla \times \nabla \cdot (\mathbf{II} : \mathbf{m}) = 0$, Eq. (5.17) can be also written as

$$\nabla \cdot \boldsymbol{\sigma}^S + \frac{1}{2}\nabla \times \nabla \cdot \mathbf{m}^D + \mathbf{f} + \frac{1}{2}\nabla \times \mathbf{c} = \rho \dot{\mathbf{v}} \tag{5.25}$$

From the foregoing formulations of balance of momentum, moment of momentum, and conservation of mechanical energy for a micropolar continuum, we find that the antisymmetric part of the force stress and the scalar of the couple stress do not contribute to the internal energy and the equation of motion and are instead indeterminate—a peculiarity of the micropolar equation.

5.2.2 Kinematics formulations

5.2.2.1 Deformation of a micropolar continuum

In this section, a brief introduction of the kinematical relations of a micropolar continuum is presented with reference to the publications of Eringen (1999) and Altenbach (2012). To describe the motion of a micropolar particle, this particle is assumed to be endowed with six degrees of freedom. Three of the degrees of freedom are translational as in classical elasticity, and other three degrees are orientational or rotational:

$$\mathbf{u} = \left[u_x \; u_y \; u_z \; \omega_x \; \omega_y \; \omega_z \right]^T \tag{5.26}$$

In the actual configuration χ at instant t, the position of a particle on the micropolar continuum is given by the position of vector $\mathbf{r}$. The particle orientation is defined by an orthonormal trihedron $\mathbf{d}_k$ (k = 1, 2, 3) whose vectors are called directors. The two vectors $\mathbf{r}$ and $\mathbf{d}_k$ define the translational and rotational motions of a particle, respectively.

To describe the relative deformation, a fixed position of the body, which may be taken at t = 0 or another fixed instant, should be referred to as the reference configuration. Herein, the referred state of a particle is defined by the position vector $\mathbf{R}$ and its orientation directors $\mathbf{D}_k$ (see Figure 5-2). It should be noted that the reference configuration need not be chosen at the initial state; any time will suffice.

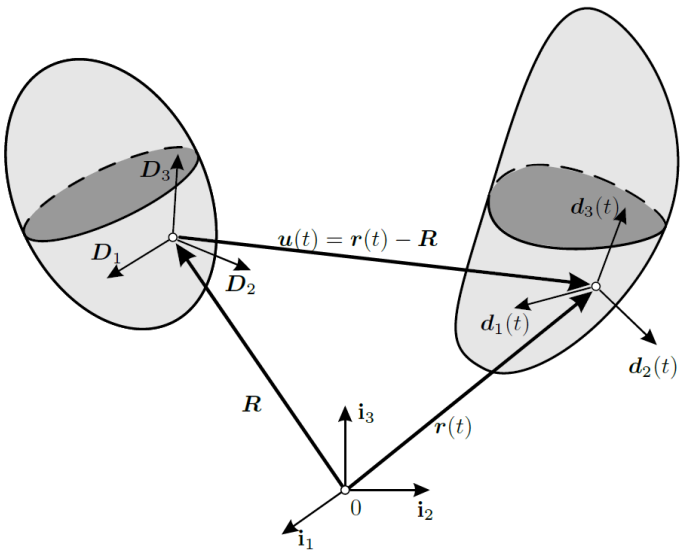

Figure 5-2 Deformation of a micro polar continuum

The motion of a micropolar continuum can be described by the following vectorial fields:

$$\mathbf{r} = \mathbf{r}(\mathbf{R}, t)\,,\ \ \mathbf{d}_k = \mathbf{d}_k(\mathbf{R}, t) \tag{5.27}$$

During the deformation, the trihedron $\mathbf{d}_k$ stays orthonormal at $\mathbf{d}_k \cdot \mathbf{d}_m = \delta_{km}$. The change of the directors can thus be described by an orthogonal tensor:

$$\mathbf{H} = \mathbf{d}_k \otimes \mathbf{D}_k \tag{5.28}$$

H is called the microrotation tensor. Thus **r** describes the position of the particle of the continuum at time t, whereas **H** defines its orientation. The orientations of $\mathbf{D}_k$ and $\mathbf{d}_k$ can be selected identically so that **H** is properly orthogonal. Hence the micropolar continuum deformation can be described by the following relations:

$$\mathbf{r} = \mathbf{r}(\mathbf{R}, t)\,,\ \ \mathbf{H} = \mathbf{H}(\mathbf{R}, t) \tag{5.29}$$

The linear velocity is given by the relation

$$\mathbf{v} = \dot{\mathbf{r}} \tag{5.30}$$

The angular velocity vector, also called the micro-gyration vector, is given by

$$\boldsymbol{\omega} = -\frac{1}{2}\left(\mathbf{H}^T \cdot \mathbf{H}\right)_\times \tag{5.31}$$

Eq. (5.31) means that $\boldsymbol{\omega}$ is the axial vector associated with the skew symmetric tensor $\mathbf{H}^T \cdot \mathbf{H}$.

5.2.2.2 Microrotation of a micropolar continuum

The most general form representing micropolar rotation has been proposed as

$$\mathbf{R}^c = \exp\left(\operatorname{spn}\left(\boldsymbol{\omega}\right)\right) \tag{5.32}$$

$\boldsymbol{\omega}$ can be also expressed by

$$\boldsymbol{\omega} = \omega_i e_i \tag{5.33}$$

where e_i is the ith component of the base vector and rotation angle ω is defined as

$$\omega = \|\boldsymbol{\omega}\| \tag{5.34}$$

The skew symmetric tensor associated with the axial vector is expressed by

$$\operatorname{spn}\left(\boldsymbol{\omega}\right) = \mathbf{e}\cdot\boldsymbol{\omega} = \begin{bmatrix} 0 & -\omega_3 & \omega_2 \\ \omega_3 & 0 & -\omega_1 \\ -\omega_2 & \omega_1 & 0 \end{bmatrix} \tag{5.35}$$

where $\mathbf{e}$ is the permutation symbol. The mathematical expansion of the rotation tensor is

$$\mathbf{R}^c = \exp\left(\operatorname{spn}\left(\boldsymbol{\omega}\right)\right) = \cos\left(\omega\right)\mathbf{I} + \frac{\sin\left(\omega\right)}{\omega}\operatorname{spn}\left(\boldsymbol{\omega}\right) + \frac{1-\cos\left(\omega\right)}{\omega^2}\boldsymbol{\omega}\otimes\boldsymbol{\omega} \tag{5.36}$$

In a small rotation framework, the rotation matrix, $\mathbf{R}^c$, is approximately expressed by

$$\mathbf{R}^c \cong \mathbf{I} + \operatorname{spn}\left(\boldsymbol{\omega}\right) = \begin{bmatrix} 1 & -\omega_3 & \omega_2 \\ \omega_3 & 1 & -\omega_1 \\ -\omega_2 & \omega_1 & 1 \end{bmatrix} \tag{5.37}$$

5.2.2.3 Strain and micro-curvature of a micropolar continuum

For a three-dimensional micropolar point, the microrotation can result in the production of micro-torsion curvature in the corresponding axis and micro-bending curvatures in other two axes. Thus there are a total of 18 components in the generalized strain vector $\boldsymbol{\varepsilon}$,

$$\boldsymbol{\varepsilon} = \left[\varepsilon_{xx}\ \varepsilon_{yy}\ \varepsilon_{zz}\ \varepsilon_{xy}\ \varepsilon_{yx}\ \varepsilon_{yz}\ \varepsilon_{zy}\ \varepsilon_{zx}\ \varepsilon_{xz}\ \kappa_{xx}l_t\ \ \kappa_{yy}l_t\ \ \kappa_{zz}l_t\ \ \kappa_{xy}l_b\ \ \kappa_{xz}l_b\ \ \kappa_{yx}l_b\ \ \kappa_{yz}l_b\ \ \kappa_{zx}l_b\ \ \kappa_{zy}l_b\right]^T \tag{5.38}$$

in which l_b and l_t are two new added micro–length scale parameters. l_b and l_t are related to the bending couple stress and the torsion couple stress, respectively.

The micropolar strain can be formulated in indicial notation as

$$\varepsilon_{ij} = u_{j,i} - e_{ijk}\omega_k \tag{5.39}$$

Micro-curvature is a third-order tensor and is mathematically defined as

$$\kappa_{ijs} = R_{ik}^{c} R_{ik,s}^{c} \tag{5.40}$$

Because the third-order curvature is antisymmetric with respect to the interchange of the first two indices, it can be reduced to a second-order tensor per the following notation:

$$\kappa_{ls} = \frac{1}{2}\left(e_{lij} R_{ik}^{c} R_{jk,s}^{c}\right) \tag{5.41}$$

Substituting Eq. (5.37) in the above equation and ignoring any higher-order terms of rotation supplies the second-order curvature tensor:

$$\kappa = \begin{bmatrix} \kappa_{11} & \kappa_{12} & \kappa_{13} \\ \kappa_{21} & \kappa_{22} & \kappa_{23} \\ \kappa_{31} & \kappa_{32} & \kappa_{33} \end{bmatrix} = \omega_{i,j} \tag{5.42}$$

Thus the micropolar strain and micro-curvature components in (*x, y, z*) coordinate space can be expressed by

$$\begin{cases} \varepsilon_{xx} = \dfrac{\partial u_x}{\partial x}, \varepsilon_{yy} = \dfrac{\partial u_y}{\partial y}, \varepsilon_{zz} = \dfrac{\partial u_z}{\partial z} & \kappa_{xx} = \dfrac{\partial \omega_x}{\partial x}, \kappa_{yy} = \dfrac{\partial \omega_y}{\partial y}, \kappa_{zz} = \dfrac{\partial \omega_z}{\partial z} \\ \varepsilon_{xy} = \dfrac{\partial u_y}{\partial x} - \omega_z, \varepsilon_{yx} = \dfrac{\partial u_x}{\partial y} + \omega_z & \kappa_{xy} = \dfrac{\partial \omega_y}{\partial x}, \kappa_{xz} = \dfrac{\partial \omega_x}{\partial z} \\ \varepsilon_{yz} = \dfrac{\partial u_z}{\partial y} - \omega_x, \varepsilon_{zy} = \dfrac{\partial u_y}{\partial z} + \omega_x & \kappa_{yx} = \dfrac{\partial \omega_y}{\partial x}, \kappa_{yz} = \dfrac{\partial \omega_y}{\partial z} \\ \varepsilon_{zx} = \dfrac{\partial u_x}{\partial z} - \omega_y, \varepsilon_{xz} = \dfrac{\partial u_z}{\partial x} + \omega_y & \kappa_{zx} = \dfrac{\partial \omega_z}{\partial x}, \kappa_{zy} = \dfrac{\partial \omega_z}{\partial y} \end{cases} \tag{5.43}$$

5.2.3 Force stress and moment stress of a micropolar continuum

Similarly, there are also a total of 18 components in the generalized stress vector $\boldsymbol{\sigma}$. Apart from the components identical to the classical ones, the stress vector also includes the micro-couple components (moments) energetically conjugated with the micro-bending and torsion curvatures:

$$\boldsymbol{\sigma} = \left[\sigma_{xx}\ \sigma_{yy}\ \sigma_{zz}\ \sigma_{xy}\ \sigma_{yx}\ \sigma_{yz}\ \sigma_{zy}\ \sigma_{zx}\ \sigma_{xz}\ \frac{m_{xx}}{l_t}\ \frac{m_{yy}}{l_t}\ \frac{m_{zz}}{l_t}\ \frac{m_{xy}}{l_b}\ \frac{m_{xz}}{l_b}\ \frac{m_{yx}}{l_b}\ \frac{m_{yz}}{l_b}\ \frac{m_{zx}}{l_b}\ \frac{m_{zy}}{l_b}\right]^T \tag{5.44}$$

Figure 5-3 shows all the stress components acting on a 3D micropolar continuum. The first subscript of the force stress refers to the direction of the surface normal pertinent to the surface on

which the force stress acts. The second subscript of the force stress refers to the direction on which the stress acts. The first subscript of couple stress refers to the axis around which it rotates, whereas the second subscript denotes the surface on which the couple stress acts.

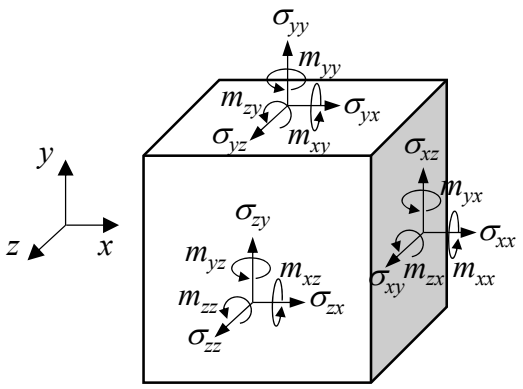

Figure 5-3 Stress components acting on a 3D micro polar continuum

5.2.4 Constitutive equations for a micropolar elasticity

In the constitutive relations of a 3D micropolar elasticity, two assumptions have been made: first, there is no coupling between the force stress and couple stress components; second, to relate couple stress to curvature, there is no interaction between bending and torsion couple stresses. Just as with classical constitutive relations, the generalized strain vector and stress vector are related by the linear elastic operator $\mathbf{D}^{\mathbf{e}}$,

$$\boldsymbol{\sigma} = \mathbf{D}^{\mathbf{e}}\boldsymbol{\varepsilon} \tag{5.45}$$

where $\mathbf{D}^{\mathbf{e}}$ is defined by

$$\mathbf{D}^{\mathbf{e}} = \begin{bmatrix} \mathbf{D}_{u} & \mathbf{D}_{u\omega} \\ \mathbf{D}_{\omega u} & \mathbf{D}_{\omega} \end{bmatrix} \tag{5.46}$$

Removing the interaction between force stress and couple stress so that $\mathbf{D}_{\omega u} = \mathbf{D}_{u\omega} = 0$, the remaining two submatrices are formulated as (Liu et al., 2007; Khoei et al., 2010; Tang and Hu, 2017)

$$\mathbf{D}_u = \begin{bmatrix} \lambda+2G & \lambda & \lambda & 0 & 0 & 0 & 0 & 0 & 0 \\ \lambda & \lambda+2G & \lambda & 0 & 0 & 0 & 0 & 0 & 0 \\ \lambda & \lambda & \lambda+2G & 0 & 0 & 0 & 0 & 0 & 0 \\ 0 & 0 & 0 & G+G_c & G-G_c & 0 & 0 & 0 & 0 \\ 0 & 0 & 0 & G-G_c & G+G_c & 0 & 0 & 0 & 0 \\ 0 & 0 & 0 & 0 & 0 & G+G_c & G-G_c & 0 & 0 \\ 0 & 0 & 0 & 0 & 0 & G-G_c & G+G_c & 0 & 0 \\ 0 & 0 & 0 & 0 & 0 & 0 & 0 & G+G_c & G-G_c \\ 0 & 0 & 0 & 0 & 0 & 0 & 0 & G-G_c & G+G_c \end{bmatrix} \quad (5.47)$$

and

$$\mathbf{D}_\omega = \begin{bmatrix} 2G & 0 & 0 & 0 & 0 & 0 & 0 & 0 & 0 \\ 0 & 2G & 0 & 0 & 0 & 0 & 0 & 0 & 0 \\ 0 & 0 & 2G & 0 & 0 & 0 & 0 & 0 & 0 \\ 0 & 0 & 0 & 2G & 0 & 0 & 0 & 0 & 0 \\ 0 & 0 & 0 & 0 & 2G & 0 & 0 & 0 & 0 \\ 0 & 0 & 0 & 0 & 0 & 2G & 0 & 0 & 0 \\ 0 & 0 & 0 & 0 & 0 & 0 & 2G & 0 & 0 \\ 0 & 0 & 0 & 0 & 0 & 0 & 0 & 2G & 0 \\ 0 & 0 & 0 & 0 & 0 & 0 & 0 & 0 & 2G \end{bmatrix} \quad (5.48)$$

with the Lame constant $\lambda = 2G/(1-2\upsilon)$; G and υ are the classical shear modulus and Poisson's ratio, respectively. G_c denotes the micropolar shear modulus.

5.3 Finite element formulations

5.3.1 Equilibrium equations

The equilibrium governing equations in micropolar theory can be written in the indicial notation forms

$$\begin{cases} \sigma_{ij,i} + f_j = 0 \\ m_{kj,j} + e_{kij}\sigma_{ij} + c_k = 0 \end{cases} \quad (5.49)$$

where **f** and **c** denote the body force and body couple moment, and **σ** and **m** are the micro polar force stress and micro couple stress, respectively. The first sub-equation is completely analogous to the

equilibrium equation of classical continuum, and the second sub-equation is the additional condition for a micropolar continuum.

5.3.2 Kinematics equations

The relations between the generalized deformation vector and strain vector in Eq. (5.43) can be connected by an operator matrix **L**

$$\boldsymbol{\varepsilon} = \mathbf{L}\mathbf{u} \tag{5.50}$$

where the operator matrix **L** is defined as

$$\mathbf{L} = \begin{bmatrix} \mathbf{L}_1 \\ \mathbf{L}_2 \end{bmatrix} \tag{5.51}$$

in which $\mathbf{L}_1$ and $\mathbf{L}_2$ are formulated as

$$\mathbf{L}_1 = \begin{bmatrix} \frac{\partial}{\partial x} & 0 & 0 & 0 & 0 & 0 \\ 0 & \frac{\partial}{\partial \mathrm{y}} & 0 & 0 & 0 & 0 \\ 0 & 0 & \frac{\partial}{\partial z} & 0 & 0 & 0 \\ 0 & \frac{\partial}{\partial x} & 0 & 0 & 0 & -1 \\ \frac{\partial}{\partial y} & 0 & 0 & 0 & 0 & 1 \\ 0 & 0 & \frac{\partial}{\partial y} & -1 & 0 & 0 \\ 0 & \frac{\partial}{\partial z} & 0 & 1 & 0 & 0 \\ \frac{\partial}{\partial z} & 0 & 0 & 0 & -1 & 0 \\ 0 & 0 & \frac{\partial}{\partial x} & 0 & 1 & 0 \end{bmatrix}, \mathbf{L}_2 = \begin{bmatrix} 0 & 0 & 0 & l_t \frac{\partial}{\partial x} & 0 & 0 \\ 0 & 0 & 0 & 0 & l_t \frac{\partial}{\partial y} & 0 \\ 0 & 0 & 0 & 0 & 0 & l_t \frac{\partial}{\partial z} \\ 0 & 0 & 0 & l_b \frac{\partial}{\partial y} & 0 & 0 \\ 0 & 0 & 0 & l_b \frac{\partial}{\partial z} & 0 & 0 \\ 0 & 0 & 0 & 0 & l_b \frac{\partial}{\partial x} & 0 \\ 0 & 0 & 0 & 0 & l_b \frac{\partial}{\partial z} & 0 \\ 0 & 0 & 0 & 0 & 0 & l_b \frac{\partial}{\partial x} \\ 0 & 0 & 0 & 0 & 0 & l_b \frac{\partial}{\partial y} \end{bmatrix} \tag{5.52}$$

5.3.3 Finite element discretization

To avoid the volumetric locking associated with incompressible materials and the hourglass phenomenon caused by reduced integration in the low-order cubic element (Reduced integration

does not work in 4 noded quadrilateral elements or 8 noded brick elements. The error occurs because the stiffness matrix is nearly singular and the system of equations includes a weakly constrained deformation mode. This phenomenon is known as 'hourglassing' because of the characteristic shape of the spurious deformation mode (Bower, 2009)), the cubic solid element of higher order shown in Figure 5-4 has been adopted. Because the higher-order element has a higher level of continuity, it performs well when simulating incompressible and nonlinear materials, in this way, it is suitable to simulate the strain localization phenomena in boundary value problems (Brown, 1997; Schwarzbach et al., 2011; Belytschko et al., 2013).

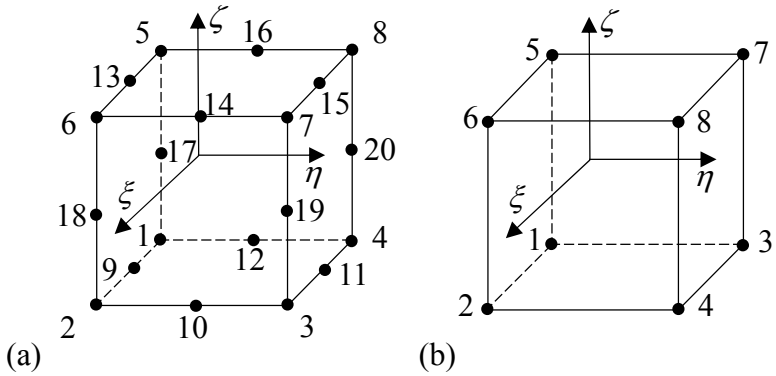

Figure 5-4 Element of 3D micro polar continuum: (a) 20-node solid element; (b) integration points

For the 20-node cubic isoparametric element depicted in Figure 5-4, each node possesses six degrees of freedom: three translational and three rotational. The displacements and rotations of the element can be calculated by the interpolation approximation of all the nodes

$$\mathbf{u} = \mathbf{N}\boldsymbol{\delta}^{\mathbf{e}} \tag{5.53}$$

where **N** is the interpolation function matrix:

$$\mathbf{N} = \left[\mathbf{I}N_1\ \mathbf{I}N_2\ \mathbf{I}N_3 \cdots\cdots \mathbf{I}N_{20}\right], \mathbf{I} = \begin{bmatrix} 1 & 0 & 0 & 0 & 0 & 0 \\ 0 & 1 & 0 & 0 & 0 & 0 \\ 0 & 0 & 1 & 0 & 0 & 0 \\ 0 & 0 & 0 & 1 & 0 & 0 \\ 0 & 0 & 0 & 0 & 1 & 0 \\ 0 & 0 & 0 & 0 & 0 & 1 \end{bmatrix} \tag{5.54}$$

The shape function of each node in Figure 5-4 is expressed in the space of the natural coordinates:

$$
\begin{cases}
N_j = \frac{1}{8}\left(1+\xi_j\xi\right)\left(1+\eta_j\eta\right)\left(1+\zeta_j\zeta\right)\left(\xi_j\xi+\eta_j\eta+\zeta_j\zeta-2\right) & j=1,2,\cdots 8; \\
N_j = \frac{1}{4}\left(1-\xi^2\right)\left(1+\eta_j\eta\right)\left(1+\zeta_j\zeta\right) & j=9,11,13,15; \\
N_j = \frac{1}{4}\left(1-\eta^2\right)\left(1+\xi_j\xi\right)\left(1+\zeta_j\zeta\right) & j=10,12,14,16; \\
N_j = \frac{1}{4}\left(1-\zeta^2\right)\left(1+\xi_j\xi\right)\left(1+\eta_j\eta\right) & j=17,18,19,20;
\end{cases}
\tag{5.55}
$$

and $\boldsymbol{\delta}^{\mathbf{e}}$ is the generalized displacement vector:

$$
\boldsymbol{\delta}^{\mathbf{e}} = \begin{Bmatrix} \delta_1 \\ \delta_2 \\ \vdots \\ \vdots \\ \vdots \\ \delta_{20} \end{Bmatrix}, \delta_i = \begin{Bmatrix} u_{xi} \\ u_{yi} \\ u_{zi} \\ \omega_{xi} \\ \omega_{yi} \\ \omega_{zi} \end{Bmatrix} \left(\mathrm{i}=1,2,...,20\right)
\tag{5.56}
$$

Accordingly, we have

$$
\boldsymbol{\varepsilon} = \mathbf{Lu} = \mathbf{LN}\boldsymbol{\delta}^{\mathbf{e}} = \mathbf{B}\boldsymbol{\delta}^{\mathbf{e}}
\tag{5.57}
$$

where **B = LN** is the strain matrix.

The total potential energy of a structure is formulated as the summation of all elements,

$$
\begin{aligned}
\Pi_p = \sum_e \Pi_p^e = \sum_e \left((\boldsymbol{\delta}^{\mathbf{e}})^{\mathrm{T}} \int_{V_e} \frac{1}{2} \mathbf{B}^T \mathbf{D}^{\mathbf{ep}} \mathbf{B} dV \boldsymbol{\delta}^{\mathbf{e}} \right) \\
- \sum_e \left(\int_{V_e} (\boldsymbol{\delta}^{\mathbf{e}})^{\mathrm{T}} \mathbf{u}^T \mathbf{f} dV \right) - \sum_e \left(\int_{S_e} (\boldsymbol{\delta}^{\mathbf{e}})^{\mathrm{T}} \mathbf{N}^T \mathbf{T} ds \right)
\end{aligned}
\tag{5.58}
$$

where **f** is the body force vector in the inner of the element and **T** is the surface force vector exerted on the boundary. Based on the minimum potential energy principle and the randomness of the virtual displacement, the partial differential $\frac{\partial \Pi_p}{\partial \boldsymbol{\delta}^{\mathbf{e}}} = 0$ must be satisfied, after which the discretized governing field equations of finite element analysis can be obtained,

$$
\mathbf{K}^e \boldsymbol{\delta}^{\mathbf{e}} = \mathbf{P}^e
\tag{5.59}
$$

with the element stiffness matrix $\mathbf{K}^{\mathrm{e}}$ and element node load vector $\mathbf{P}^{\mathrm{e}}$ expressed as

$$\mathbf{K}^e = \int_{V_e} \frac{1}{2}\mathbf{B}^T\mathbf{D}^{\mathbf{ep}}\mathbf{B}dV,\ \mathbf{P}^e = \int_{V_e} \mathbf{u}^T\mathbf{f}dV + \int_{S_e} \mathbf{N}^T\mathbf{T}ds \tag{5.60}$$

Finally, the Newton–Raphson technique is used to fulfill the static equilibrium iteration of the nonlinear problems, and the Gauss integration method is adopted when performing the integral operation. Take the element stiffness matrix, for example,

$$\mathbf{K}^e = \int_{V_e} \mathbf{B}^T\mathbf{D}^{\mathbf{ep}}\mathbf{B}dV = \int_{-1}^{1}\int_{-1}^{1}\int_{-1}^{1} \mathbf{B}^T\mathbf{D}^{\mathbf{ep}}\mathbf{B}\,|\mathbf{J}|d\xi d\eta d\zeta = \sum_{k=1}^{l}\sum_{i=1}^{m}\sum_{j=1}^{n} H_k H_i H_j \mathbf{B}^T\mathbf{D}^{\mathbf{ep}}\mathbf{B}\,|\mathbf{J}| \tag{5.61}$$

in which $m = n = l = 2$, H_i, H_j, and H_k are the corresponding weight factors of each integration point and the Jacobian matrix is expressed as

$$[\mathbf{J}] = \begin{bmatrix} \frac{\partial x}{\partial \xi} & \frac{\partial y}{\partial \xi} & \frac{\partial z}{\partial \xi} \\ \frac{\partial x}{\partial \eta} & \frac{\partial y}{\partial \eta} & \frac{\partial z}{\partial \eta} \\ \frac{\partial x}{\partial \zeta} & \frac{\partial y}{\partial \zeta} & \frac{\partial z}{\partial \zeta} \end{bmatrix} \tag{5.62}$$

5.4 FE implementation of the 3D critical state–based micropolar model

Compared with the initial SIMSAND model, the stress and strain invariants in the 3D micropolar SIMSAND model have been augmented by considering micro-curvatures and corresponding energetically conjugated couple stresses. According to de Borst et al. (1987; 1991; 1991), the strain and stress invariants can be formulated as

$$\dot{\varepsilon}_d^p = \left[b_1 \dot{e}_{ij}^p \dot{e}_{ij}^p + b_2 \dot{e}_{ij}^p \dot{e}_{ji}^p + b_3 \dot{\kappa}_{ij}^p \dot{\kappa}_{ij}^p l_c^2 \right]^{\frac{1}{2}} \tag{5.63}$$

$$J_2 = a_1 s_{ij} s_{ij} + a_2 s_{ij} s_{ji} + a_3 m_{ij} m_{ji} / l_c^2 \tag{5.64}$$

where $\dot{e}_{ij}^p$ is the plastic deviatoric strain rate tensor, $\dot{\kappa}_{ij}^p$ is the plastic micro-curvature rate tensor, s_{ij} is the deviatoric stress tensor, m_{ij} is the micro-moment tensor, and the internal length scale parameter l_c can be either l_t or l_b. The summation convention for repeated indices has been adopted. In the absence of microcurvatures and the energetically conjugated couple stresses—that is, $\dot{\kappa}_{ij}^p = 0$, $\dot{e}_{ij}^p = \dot{e}_{ji}^p$ and $m_{ij} = 0$, $s_{ij} = s_{ji}$—the strain and stress invariants are expressed as

$$\dot{\varepsilon}_d^p = \left[b_1 \dot{e}_{ij}^p \dot{e}_{ij}^p + b_2 \dot{e}_{ij}^p \dot{e}_{ij}^p \right]^{\frac{1}{2}} \tag{5.65}$$

$$J_2 = \left(a_1 + a_2\right) s_{ij} s_{ij} \tag{5.66}$$

To ensure proper retrieval of the classical continuum expressions for the invariants, the choices $a_1 = a_2 = 1/4$, $a_3 = 1/2$ and $b_1 = b_2 = 1/3$, $b_3 = 2/3$ have been used in most cases (de Borst, 1990; de Borst, 1991; de Borst and Sluys, 1991). Thus the deviatoric stress q in the 3D micropolar SIMSAND model should be calculated by the new stress invariant $\sqrt{3J_2}$. To arrive at a compact matrix–vector notation, the formulation of q is expressed as

$$q = \sqrt{\frac{1}{2}\boldsymbol{\sigma}^{\mathrm{T}}\mathbf{P}\boldsymbol{\sigma}} \tag{5.67}$$

where **P** is the plastic potential matrix (Li and Tang, 2005; Khoei et al., 2006; Khoei et al., 2010):

$$\mathbf{P} = \begin{bmatrix} \mathbf{P}_1 & \mathbf{0} & \mathbf{0} \\ \mathbf{0} & \mathbf{P}_2 & \mathbf{0} \\ \mathbf{0} & \mathbf{0} & \mathbf{P}_3 \end{bmatrix} \tag{5.68}$$

where $\mathbf{P}_1$, $\mathbf{P}_2$, and $\mathbf{P}_3$ can be expressed as

$$\mathbf{P}_1 = \begin{bmatrix} 2 & -1 & -1 \\ -1 & 2 & -1 \\ -1 & -1 & 2 \end{bmatrix}, \mathbf{P}_2 = \begin{bmatrix} \frac{3}{2} & \frac{3}{2} & 0 & 0 & 0 & 0 \\ \frac{3}{2} & \frac{3}{2} & 0 & 0 & 0 & 0 \\ 0 & 0 & \frac{3}{2} & \frac{3}{2} & 0 & 0 \\ 0 & 0 & \frac{3}{2} & \frac{3}{2} & 0 & 0 \\ 0 & 0 & 0 & 0 & \frac{3}{2} & \frac{3}{2} \\ 0 & 0 & 0 & 0 & \frac{3}{2} & \frac{3}{2} \end{bmatrix}$$

$$\mathbf{P}_3 = \begin{bmatrix} 3 & 0 & 0 & 0 & 0 & 0 & 0 & 0 & 0 \\ 0 & 3 & 0 & 0 & 0 & 0 & 0 & 0 & 0 \\ 0 & 0 & 3 & 0 & 0 & 0 & 0 & 0 & 0 \\ 0 & 0 & 0 & 3 & 0 & 0 & 0 & 0 & 0 \\ 0 & 0 & 0 & 0 & 3 & 0 & 0 & 0 & 0 \\ 0 & 0 & 0 & 0 & 0 & 3 & 0 & 0 & 0 \\ 0 & 0 & 0 & 0 & 0 & 0 & 3 & 0 & 0 \\ 0 & 0 & 0 & 0 & 0 & 0 & 0 & 3 & 0 \\ 0 & 0 & 0 & 0 & 0 & 0 & 0 & 0 & 3 \end{bmatrix} \tag{5.69}$$

Similarly, the equivalent plastic strain ε_d^p can be expressed in a compact matrix–vector notation as

$$\varepsilon_d^p = \sqrt{\frac{2}{3}\left(\boldsymbol{\varepsilon}^{\mathbf{p}}\right)^{\mathbf{T}} \mathbf{Q}\, \boldsymbol{\varepsilon}^{\mathbf{p}}} \tag{5.70}$$

where matrix **Q** is defined as

$$\mathbf{Q} = \begin{bmatrix} \mathbf{Q}_1 & \mathbf{0} & \mathbf{0} \\ \mathbf{0} & \mathbf{Q}_2 & \mathbf{0} \\ \mathbf{0} & \mathbf{0} & \mathbf{Q}_3 \end{bmatrix} \tag{5.71}$$

where $\mathbf{Q}_1$, $\mathbf{Q}_2$, and $\mathbf{Q}_3$ can be expressed as

$$\mathbf{Q}_1 = \begin{bmatrix} \frac{2}{3} & -\frac{1}{3} & -\frac{1}{3} \\ -\frac{1}{3} & \frac{2}{3} & -\frac{1}{3} \\ -\frac{1}{3} & -\frac{1}{3} & \frac{2}{3} \end{bmatrix}, \mathbf{Q}_2 = \begin{bmatrix} \frac{1}{2} & \frac{1}{2} & 0 & 0 & 0 & 0 \\ \frac{1}{2} & \frac{1}{2} & 0 & 0 & 0 & 0 \\ 0 & 0 & \frac{1}{2} & \frac{1}{2} & 0 & 0 \\ 0 & 0 & \frac{1}{2} & \frac{1}{2} & 0 & 0 \\ 0 & 0 & 0 & 0 & \frac{1}{2} & \frac{1}{2} \\ 0 & 0 & 0 & 0 & \frac{1}{2} & \frac{1}{2} \end{bmatrix}$$

$$\mathbf{Q}_3 = \begin{bmatrix} 1 & 0 & 0 & 0 & 0 & 0 & 0 & 0 & 0 \\ 0 & 1 & 0 & 0 & 0 & 0 & 0 & 0 & 0 \\ 0 & 0 & 1 & 0 & 0 & 0 & 0 & 0 & 0 \\ 0 & 0 & 0 & 1 & 0 & 0 & 0 & 0 & 0 \\ 0 & 0 & 0 & 0 & 1 & 0 & 0 & 0 & 0 \\ 0 & 0 & 0 & 0 & 0 & 1 & 0 & 0 & 0 \\ 0 & 0 & 0 & 0 & 0 & 0 & 1 & 0 & 0 \\ 0 & 0 & 0 & 0 & 0 & 0 & 0 & 1 & 0 \\ 0 & 0 & 0 & 0 & 0 & 0 & 0 & 0 & 1 \end{bmatrix} \tag{5.72}$$

As can be seen from the foregoing formulations, when extending a classical constitutive model to a micropolar model at stress–strain level, the stress and strain vectors need merely to be augmented to incorporate the micro-moment stresses and microcurvatures. Consequently, the stress and strain invariants also need to be defined based on generalized stress and strain components. For the particular SIMSAND model, only the second stress invariant J_2 and second plastic strain invariant ε_d^p

should be redefined, but in some constitutive models, including the third stress invariant J_3, J_3 should be also redefined as (Liu et al., 2007)

$$J_3 = \frac{1}{3}\left(s_{ij}s_{jk}s_{ik} + m_{ij}m_{jk}m_{ik}\right) \tag{5.73}$$

When conducting numerical simulations with the micropolar model, if the independent rotational degrees of freedom are constrained, all the micro-qualities become null values, and the micropolar model is retrieved to the classical one. The 3D polarized SIMSAND model has been numerically implemented via the user-defined element introduced in the previous section. For the integration algorithm within the constitutive model, the cutting plane technique was also adopted as illustrated in detail in chapter 2.

5.5 Numerical simulations and discussions

5.5.1 Element validation

To ensure the correctness of the three-dimensional user-developed element and the polarized elastoplastic model, element validation is essential. In this section, simulations of drained and undrained triaxial tests and drained and undrained biaxial tests for both loose and dense Toyoura sand were conducted using the 3D micropolar SIMSAND model, which were compared and verified by the results from IPP. The comparisons were presented hereafter, from Figure 5-5 to Figure 5-8. In the comparing figures, each subfigure denotes a relationship: (a) axial strain versus deviatoric stress, (b) mean effective stress versus deviatoric stress, (c) axial strain versus void ratio, (d) mean effective stress versus deviatoric stress. From the comparisons, it could be found that the simulated results obtained from 3D micropolar SIMSAND model coincide exactly with those obtained through IPP, proving the correctness of the implementation of the 3D polarized model. Note, however, that the micropolar quantities were nulls in element tests.

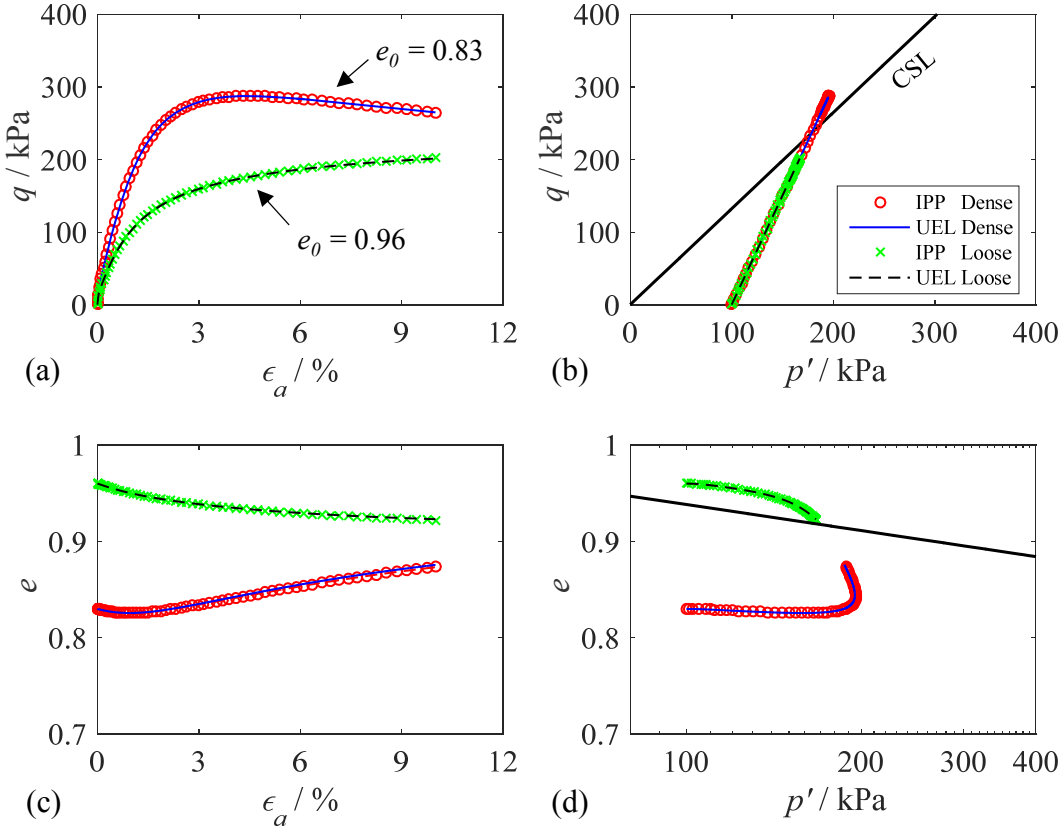

Figure 5-5 Comparisons between IPP and 3D UEL in simulating triaxial drained test

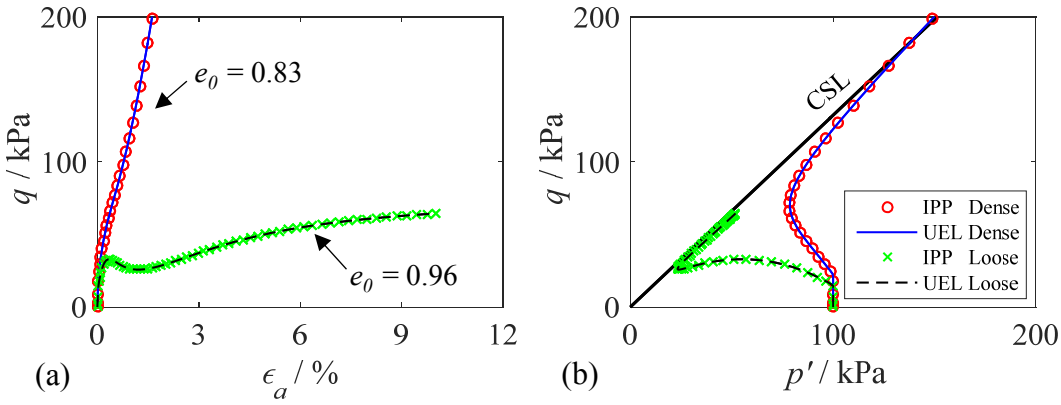

Figure 5-6 Comparisons between IPP and 3D UEL in simulating triaxial undrained test

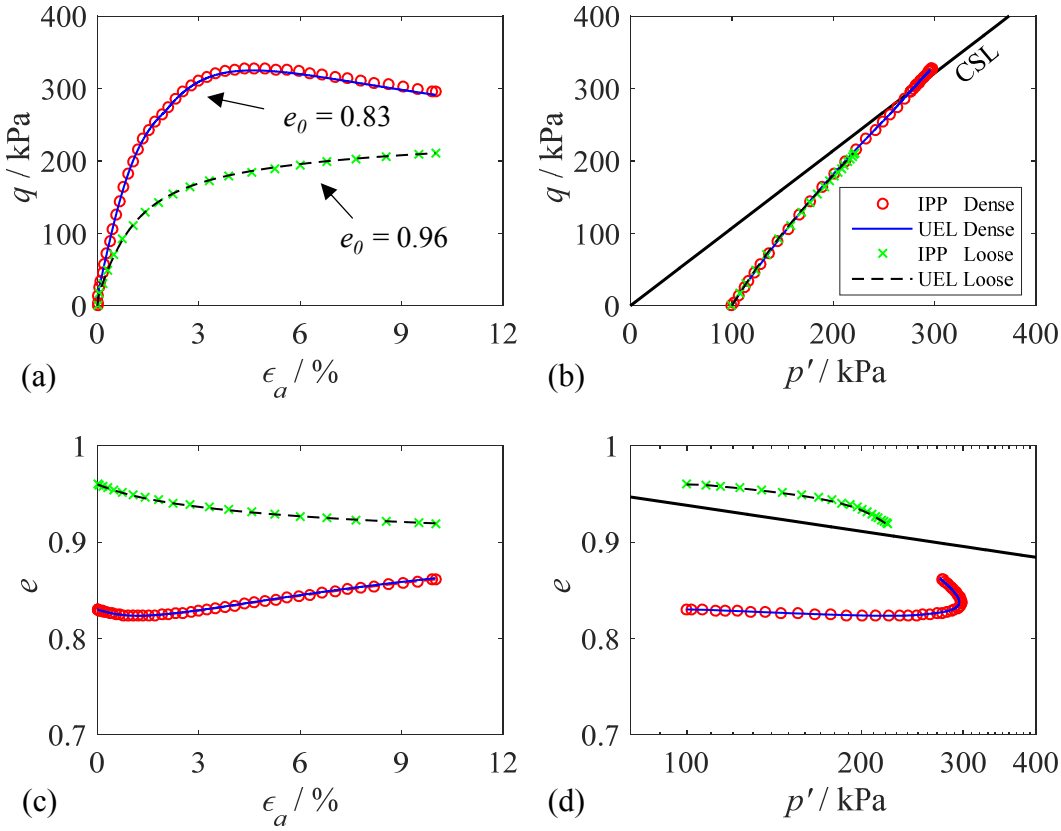

Figure 5-7 Comparisons between IPP and 3D UEL in simulating biaxial drained

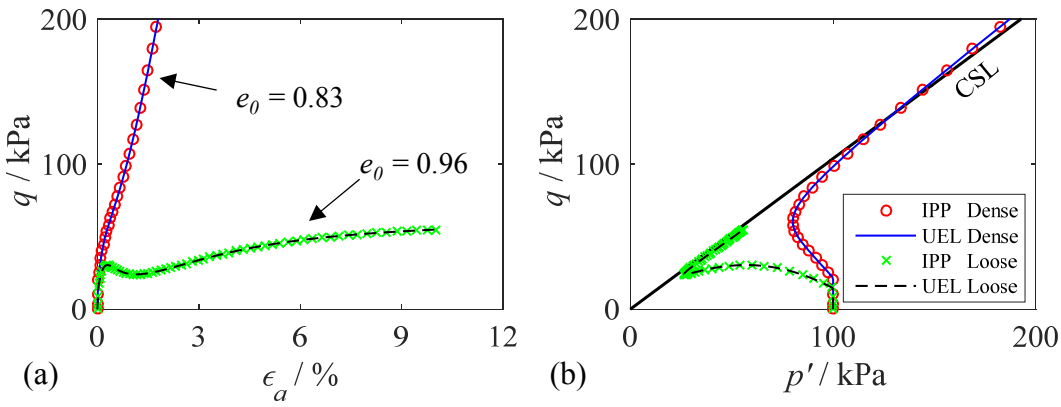

Figure 5-8 Comparisons between IPP and 3D UEL in simulating biaxial undrained

5.5.2 Boundary value problems in plane strain condition

We know that in element tests, all simulations are confined in a homogeneous state without strain localization phenomena. However, micro polar technique can be activated only with the onset of strain localization, which is accompanied by particle rotations in the strain-localized region and a lessening of the structure's strength. Accordingly, simulations of strain localization phenomena in boundary value problems, such as shear bands in biaxial tests, should be performed with the 3D micropolar SIMSAND model.

To validate the correctness, the simulations of biaxial tests as had been done in previous Chapter were conducted again within a three-dimensional framework by the polarized SIMSAND model, and all material parameters were kept the same as those used in a 2D condition. In these simulations, the three internal length scale parameters were set the same: $l_b = l_t = l_c$.

In doing so, the conditions of the biaxial test were revisited. A specimen, with a width of 10 cm, a height of 20 cm, and a thickness of 1 cm, was considered—different from that seen in the two-dimensional condition, in which the default thickness is 1 m. The test included two steps, and the mixed loading control was adopted. The first step was isotropic compression with a confining pressure of 100 kPa, and the second was shear loading produced by controlling the displacement of the top surface (up to a total axial strain of 5%). To trigger the strain localization easily, the lateral deformations of the top and bottom surfaces of the specimen were constrained.

5.5.2.1 Mesh dependency using the classical SIMSAND model

Considering that there is no obvious shear band in the 30×60×1 mesh as a result of poor convergence within the framework of classical continuum theory, shear bands identified by the equivalent plastic strain distribution of three different discretizations—mesh sizes of 10×20×1, 15×30×1, and 20×40×1—are shown in Figure 5-9, with the corresponding load versus displacement curves plotted in Figure 5-10. From the contours and the load–displacement curves, it can be found that the simulations for relative coarse meshes, such as 10×20×1 and 15×30×1, are completely finished, whereas the calculation stops just after the onset of bifurcation point for a fine mesh of 20×40×1. The bearing peak of the coarse 10×20×1 mesh is slightly higher and more delayed than the others.

Additionally, the specimen displays a stiffer behavior during the softening regime with a coarse mesh than that with a fine mesh. All the observations obtained using a 3D framework are in accordance with those by using a 2D framework, indicating the presence of serious mesh dependency problems for a classical continuum when simulating strain localization problems.

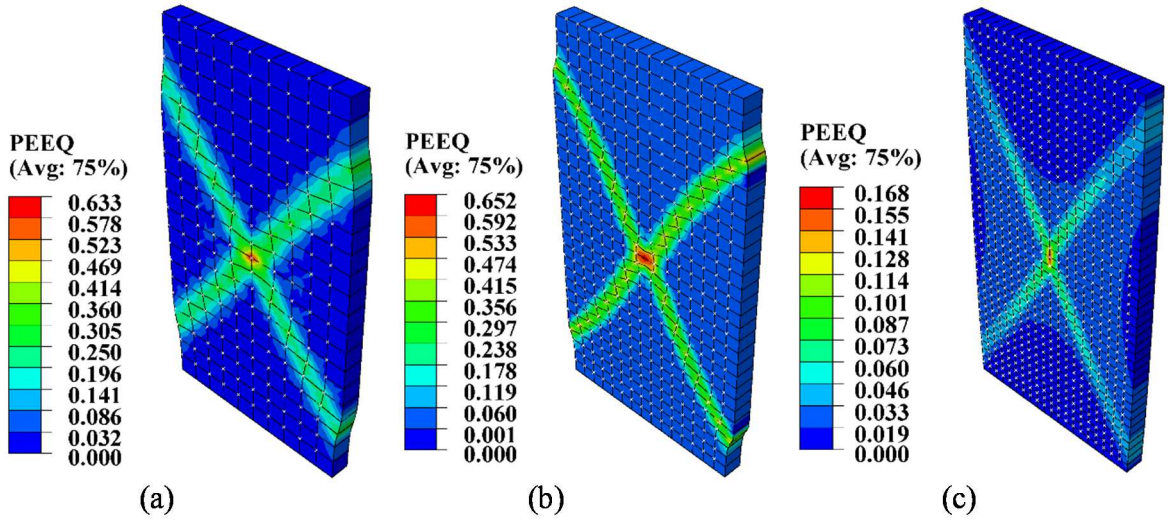

Figure 5-9 Shear bands of three different mesh sizes using the 3D classical model: (a) mesh 10×20×1; (b) mesh 15×30×1; (c) mesh 20×40×1

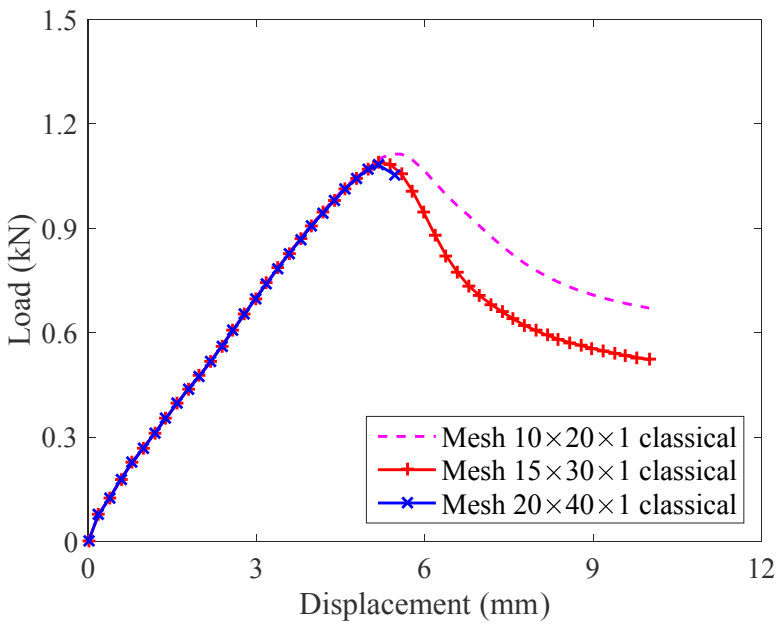

Figure 5-10 Load–displacement of three different mesh sizes using the 3D classical model

5.5.2.2 Mesh independency using the 3D micropolar SIMSAND model

To demonstrate the regularization capability of the micropolar technique, the same simulations of biaxial tests as in previous section were conducted once more using the 3D polarized model, with the parameters kept the same as before and the two newly incorporated length scale parameters $l_b = l_t = l_c$ and the micro polar shear modulus G_c was set identically to the one in the 2D condition. The shear bands identified by plastic strain for four different discretizations are shown in Figure 5-11. Unlike for calculations within the framework of classical continuum theory, all four simulations could be entirely finished without any numerical convergence problem, and from a first glimpse at shear band thickness, the mesh independency for the four different discretizations is found easily. Load–displacement curves for the four simulations are presented in Figure 5-12, showing that the pink curve of mesh 10×20×1 is a little stiffer than the other three curves during the softening regime. However, the load–displacement curves of the other three fine meshes coincide with each other and display mesh independency. In this sense, the existence of the effective regularization ratio of internal length to element size is verified again.

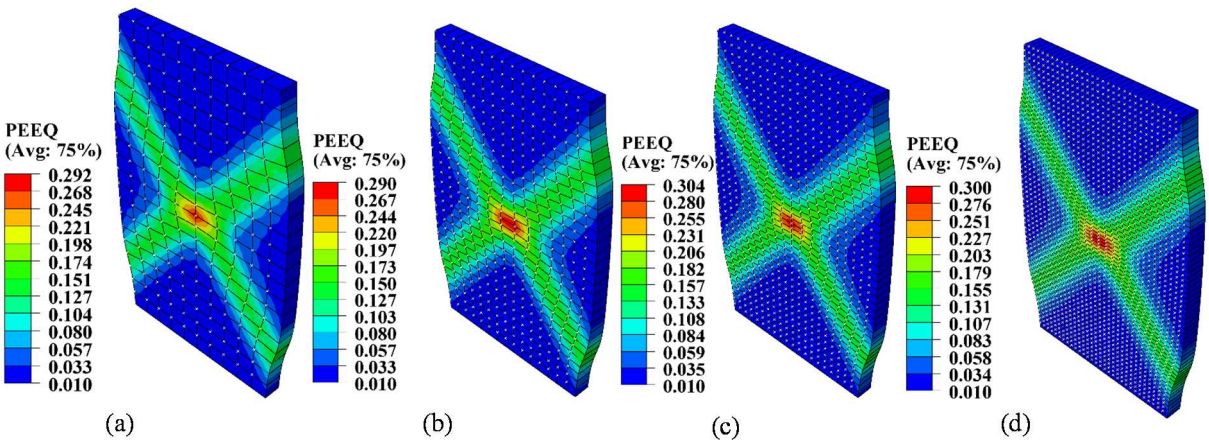

Figure 5-11 Shear bands of four different mesh sizes using the3D micropolar model: (a) mesh 10×20×1; (b) mesh 15×30×1; (c) mesh 20×40×1; (d) mesh 30×60×1

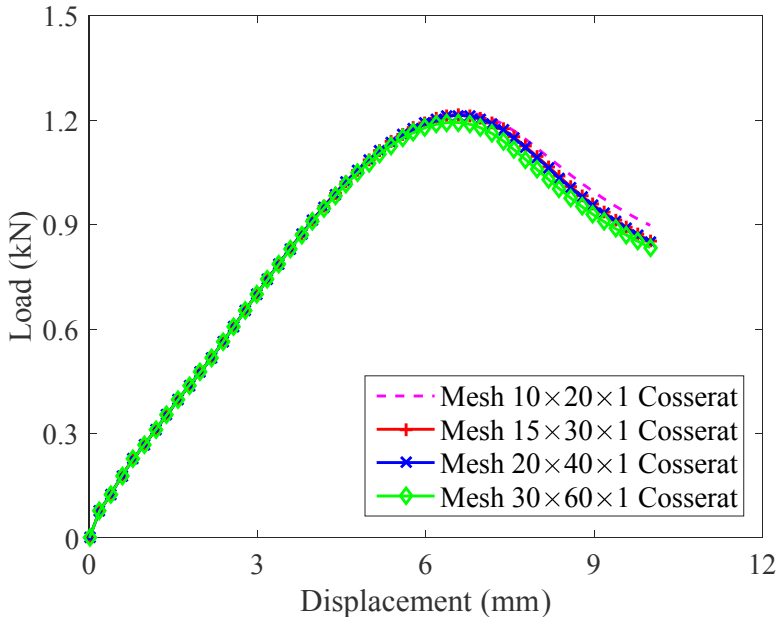

Figure 5-12 Load–displacement of four different mesh sizes using the3D micro polar model

5.5.2.3 Influence of the internal length scales

The incorporation of the internal length scale is required to preserve the ellipticity of the partial differential equations for boundary values problems. Through the regularization mechanism of the micro polar approach, the mesh dependency problems have been amply solved. Undoubtedly, the internal length scales will greatly influence the material behavior as well as the shear band pattern.

Shear band contours with the fixed mesh size for a classical continuum and a micropolar continuum with three different values of the internal length scales are shown in Figure 5-13 ($l_b = l_t = l_c$). The relatively thin shear bands are observed for a zero or small internal length, whereas the shear bands are thicker for the larger internal length scales.

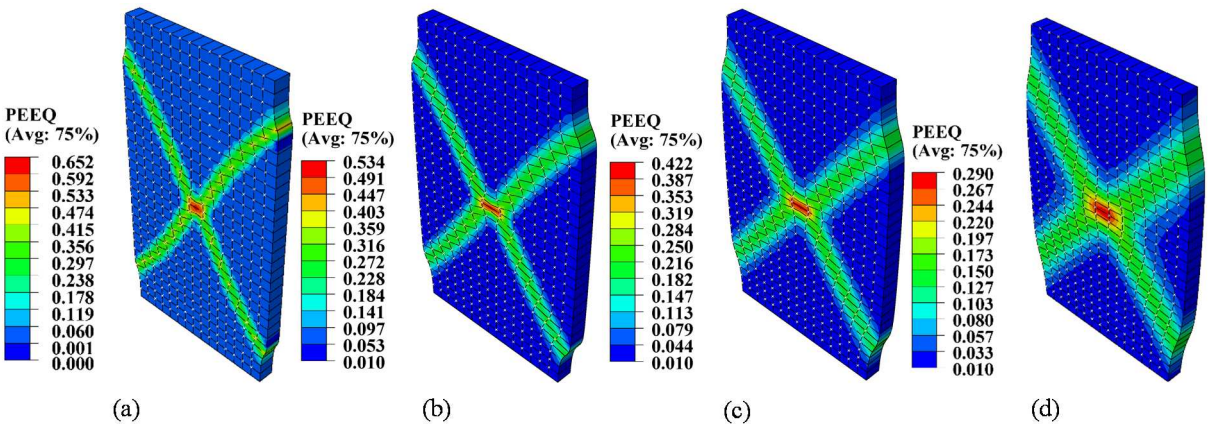

Figure 5-13 Influence of internal length scale l_c on shear band thickness: (a) l_c = 0mm; (b) l_c = 1mm; (c) l_c = 1.5mm; (c) l_c = 2mm;

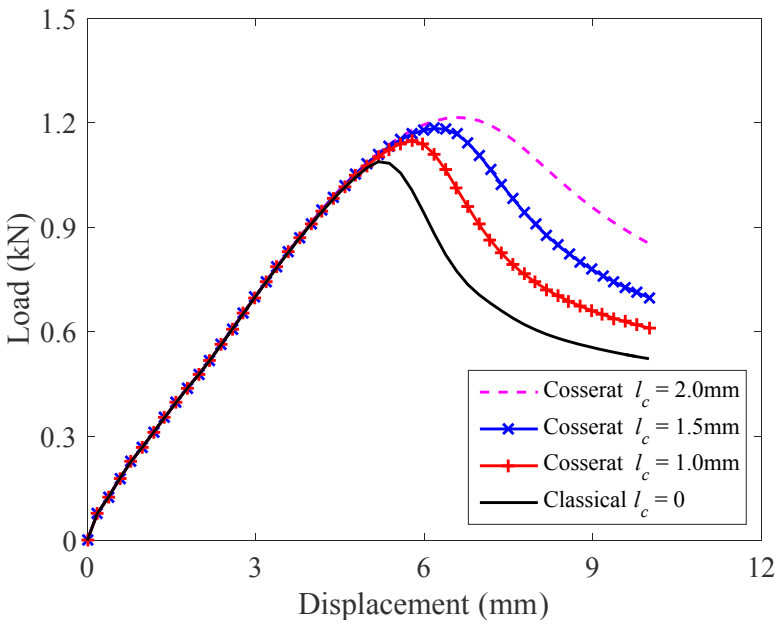

Figure 5-14 Influence of internal length scale l_c on load–displacement curves

The load–displacement curves of four different l_c with a fixed mesh size (mesh 15×30×1) have been illustrated in Figure 5-14. The load–displacement curves show that the load peak depends on the internal length scale and increases with l_c. In addition, larger values of l_c require a larger axial strain to arrive at the peak load, indicating that the increased l_c is able to delay the bifurcation point of a structure. During the softening stage, material having a larger l_c also demonstrates stiffer behaviors.

5.5.2.4 Validation of the simulated results

According to the simulated results heretofore related, the 3D micropolar model has demonstrated a significant ability to overcome convergence difficulties and alleviate mesh dependency problems. However, these results can be persuasive only after validation. The correctness of the 3D micropolar model is validated by comparing the results from the 2D micropolar, which are assumed to be right ones by default.

First, the results from the retrieved classical model should be compared. The shear bands using a 2D classical model for three different mesh sizes are shown in Figure 5-15, allowing us to note that the shear band patterns from a 3D model, shown in Figure 5-9, are precisely the same as these obtained by using a 2D model. The comparisons of the load–displacement curves between 2D and 3D classical models are presented in Figure 5-16, showing that the curves from the 3D model coincide exactly with those from the 2D model. Notably, the strength of the 3D model should be multiplied by 100 considering the unit depth (100 cm) of 2D models.

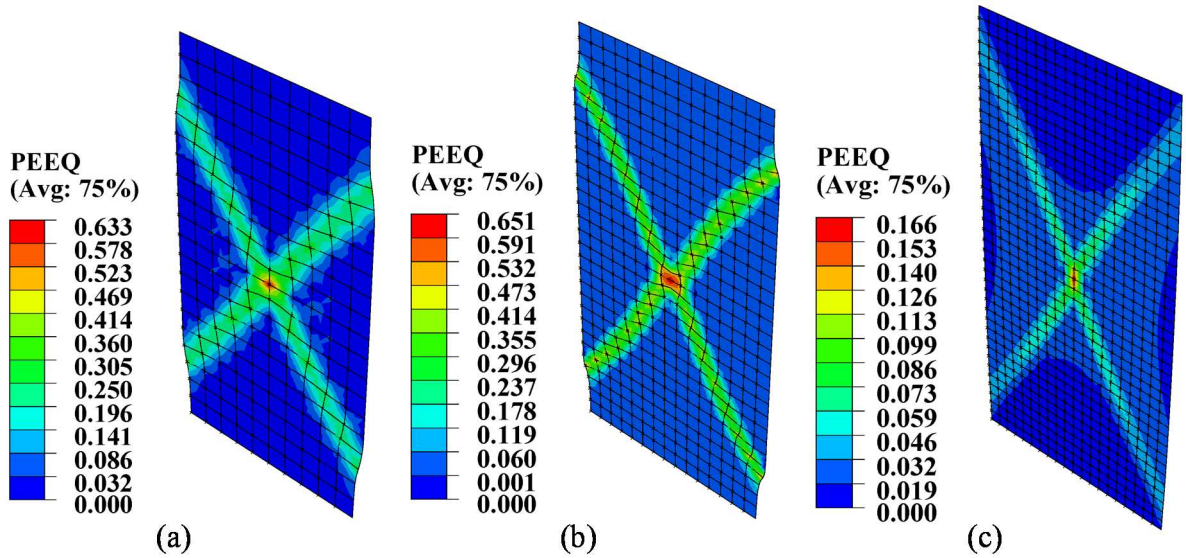

Figure 5-15 Shear bands of three different mesh sizes using the 2D classical model: (a) mesh 10×20; (b) mesh 15×30; (c) mesh 20×40

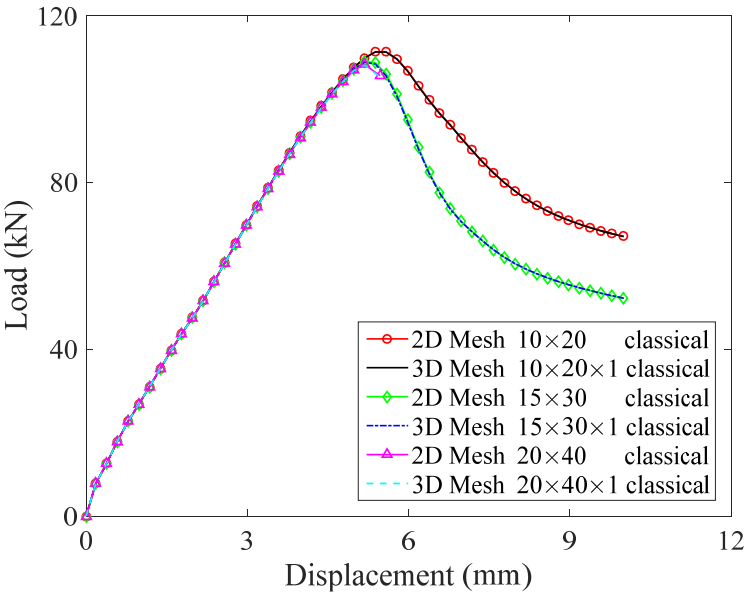

Figure 5-16 Comparisons of load–displacement curves between 2D and 3D classical SIMSAND model

Second, the results obtained by using the micropolar model should be validated. The shear bands obtained by using a 2D micropolar model for four different mesh sizes are shown in Figure 5-17, allowing us to note that the shear bands obtained by using a 3D micropolar model, shown in Figure 5-11, are identical to those obtained by using a 2D model. The comparisons of the load–displacement curves between 2D and 3D micropolar models are presented in Figure 5-18, which indicates that the curves from 3D and 2D micropolar models are consistent with each other and are all also mesh-independent.

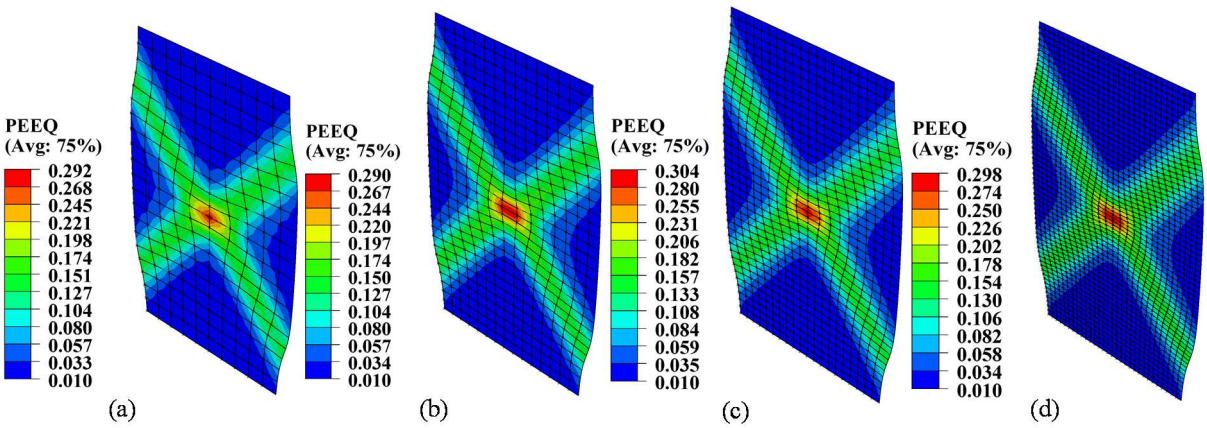

Figure 5-17 Shear bands of four different mesh sizes using the 2D micro polar model: (a) mesh 10×20; (b) mesh 15×30; (c) mesh 20×40; (d) mesh 30×60

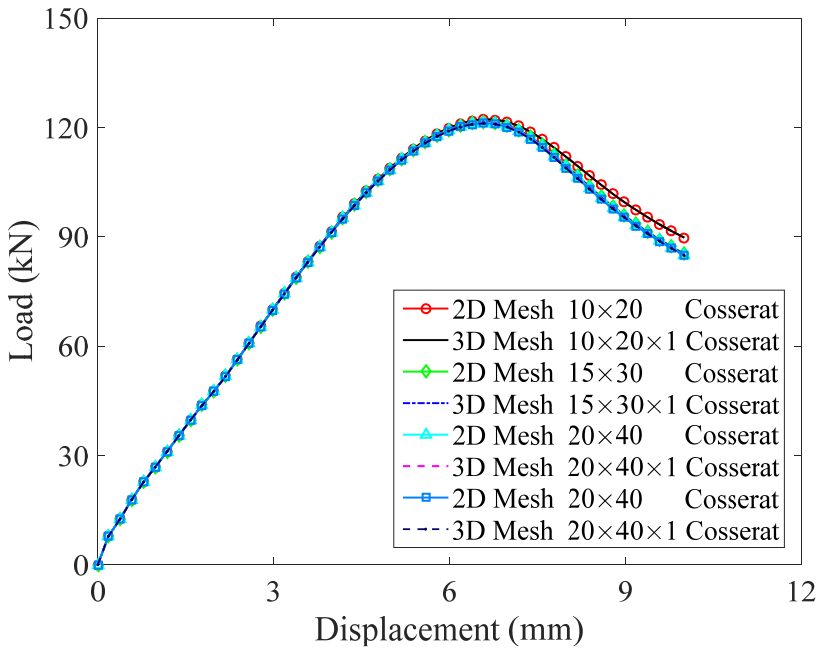

Figure 5-18 Comparisons of load–displacement curves between 2D and 3D micropolar SIMSAND model

5.5.3 Boundary value problems in a real 3D condition

To illustrate the regularization effectiveness of the 3D polarized SIMSAND model, a real 3D problem was simulated in this section. The geometry and the boundary conditions of the model were presented in Figure 5-19(a), showing a vertical cut of 10×10×10 cm was subjected to the prescribed loading in y direction at its corner on the top surface. The loading was controlled by the incremental displacement of a rigid square panel of 2.5×2.5 cm, which was roughly located on the corner. All the translational and rotational degrees of freedom of the bottom side were fixed totally, while two side surfaces on the left side and back side were restrained in their perpendicular directions. Accordingly, a localized region would form under the panel as shown in Figure 5-19(b). All the material parameters were referred to the calibrated ones from Ottawa sand in Appendix E, with the internal length scales $l_b = l_t = l_c = 1$mm and micropolar shear modulus $G_c = 0.5G$.

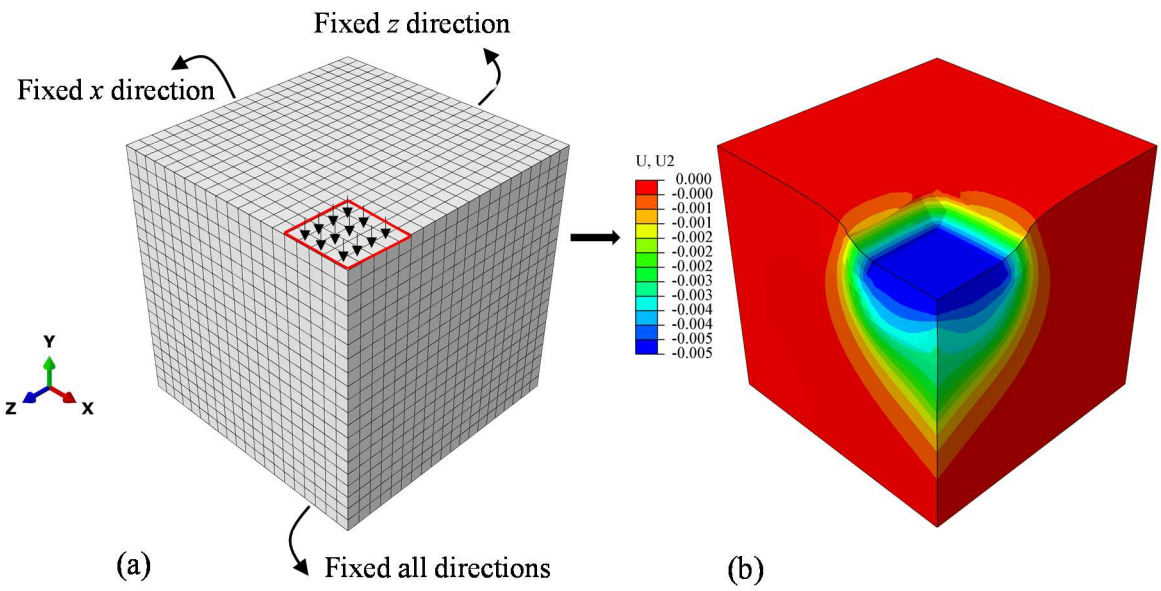

Figure 5-19 Boundary conditions and final schematic of the model

5.5.3.1 Simulations using the classical 3D model

First, the simulations were conducted within the framework of classical continuum mechanics. Three different mesh sizes—16×16×16, 20×20×20, 24×24×24—were adopted. The strain localized regions identified by the equivalent plastic strain were shown in Figure 5-20. It was evident that the width of shear band was determined by the element size. Similarly, the mesh dependency problems of the classical model could also be illustrated by the load-displacement curves of three different simulations. Although the differences of the three different element sizes were not so large, the load-displacement curves in post-peak regime still could not coincide with each other.

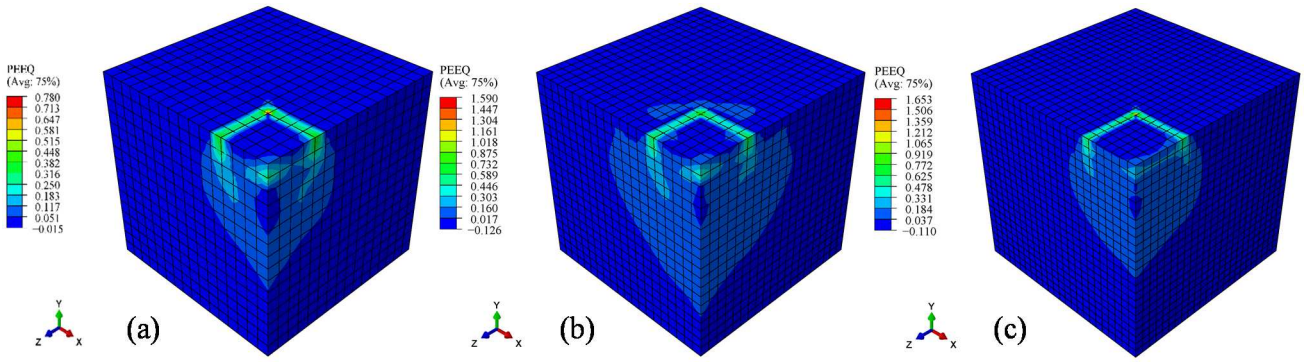

Figure 5-20 Shear bands in 3D foundations using classical model

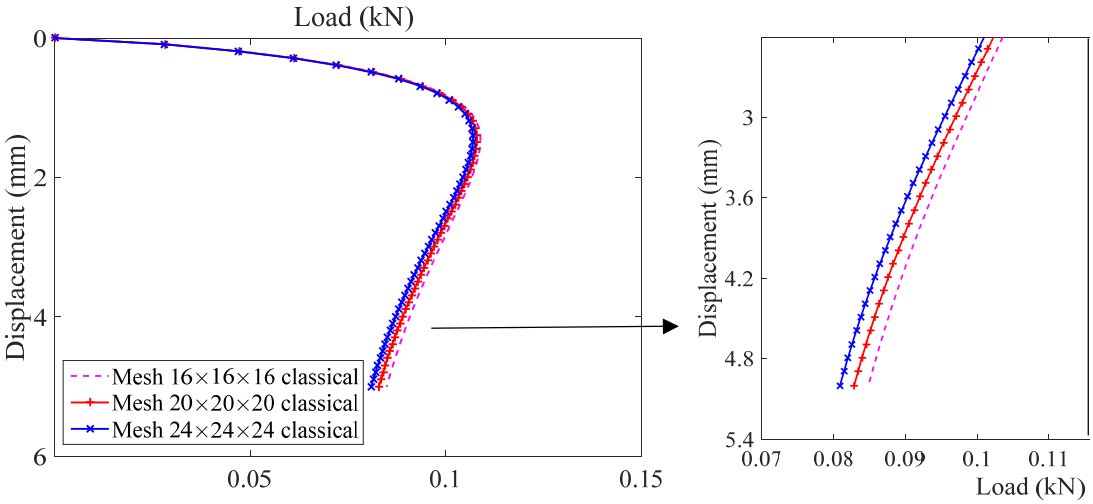

Figure 5-21 Load-displacement of three different meshes using the classical model

5.5.3.2 Simulations using the micropolar 3D model

After that, the simulations were conducted again with the 3D micropolar model. Different from the classical one, micropolar approach had regularized the localized region, and the width of shear band of three different meshes displayed mesh independency as shown in Figure 5-22. Moreover, the mesh dependency problems of load-displacement curves were absolutely relieved as shown in Figure 5-23.

From the comparisons of the mechanical responses between classical and micropolar simulations as shown in Figure 5-24, it could be easily found that micropolar technique, being able to preserving the property of differential governing equation in finite element analysis, made materials stiffer and enabled to delay the bifurcation point.

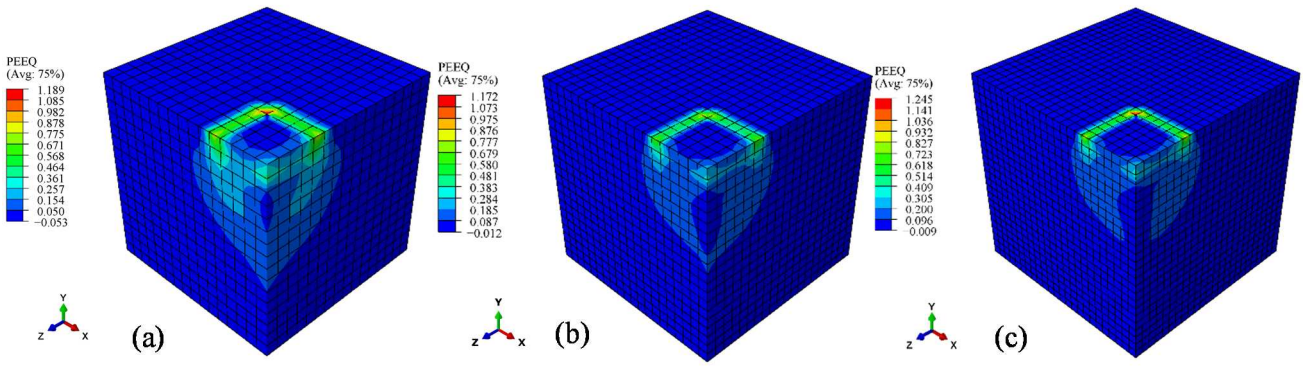

Figure 5-22 Shear bands in 3D foundations using micropolar model

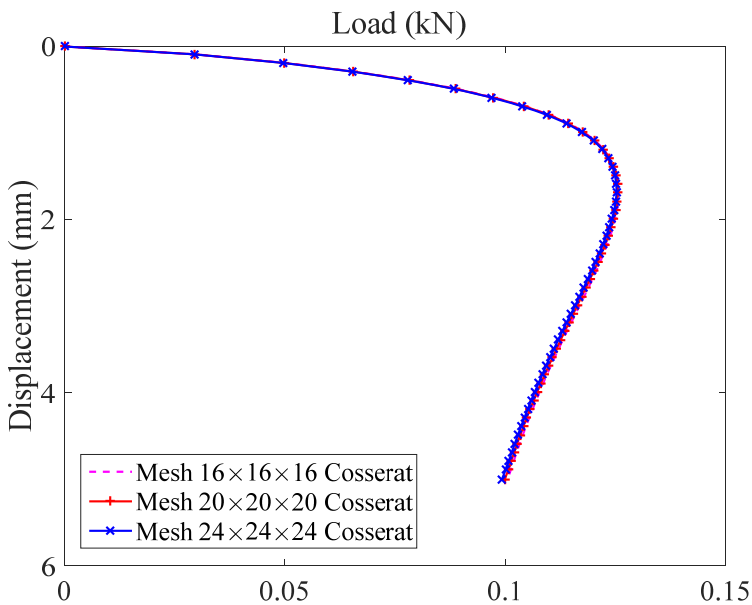

Figure 5-23 Load-displacement of three different meshes using the micropolar model

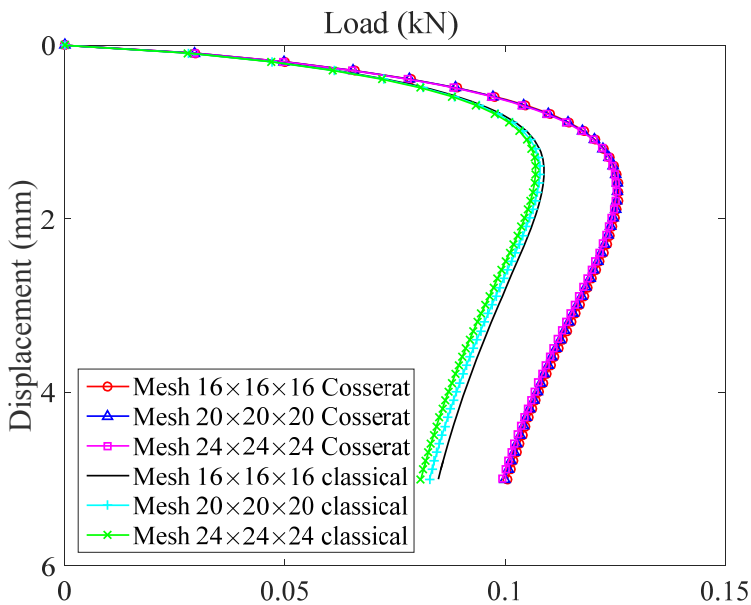

Figure 5-24 Comparisons of the mechanical property between classical and Cosserat simulations

5.6 Conclusions

In this chapter, the micropolar theory within a 3D framework was demonstrated in detail. A high-order 20-node cubic solid element having six degrees of freedom (three translational and three rotational), was developed via the user-defined interface of ABAQUS, and a reduced integration was adopted that successfully avoids the volumetric and shear locking associated with incompressible

materials and the hourglass phenomena for low-order element when using reduced integration. Furthermore, a finite element implementation of the 3D micropolar model was performed. Through simulation of element tests, the 3D micropolar model has been proven to be correct when modeling a homogeneous stress state.

The regularization abilities of the 3D micropolar model were exhibited by simulating boundary value problems in the context of strain localization phenomena under both plane strain condition and real three-dimensional conditions. Simulations of biaxial tests using the 3D polarized critical state–based model were compared with the results obtained by using a 2D micropolar model, thereby validating the correctness of the 3D micropolar model as well as its ability to overcome numerical difficulties and alleviate mesh dependency problems for strain localization phenomena during finite element analysis. Similarly, simulation of a three-dimensional foundation for different mesh sizes has demonstrated the regularization abilities of the 3D micropolar model. However, more work should be further continued on the 3D model.

Conclusions and Perspectives

Conclusions

As for investigating the strain localization phenomena in geotechnical engineering, main results of the thesis can be concluded as follows:

(1) Considering the fact that great rearrangements and rotations occur inside shear band, the micropolar approach with clearer physical sense among other regularization theories, was favored in current study to deal with the mesh dependency problems.

(2) A simple critical-state based sand model has been formulated within the micropolar theory and numerically implemented into a finite element code for dealing with 2D and 3D static and quasi-static problems, with which the convergence difficulties and the mesh dependency problems faced with the classical continuum theory based models were effectively relieved.

(3) With the micropolar model, the comprehensive study of shear band has been conducted. Based on serious simulations, a regularization effective ratio of the internal length to element size was proposed to absolutely deal with the mesh dependency problems. Various factors' influences on the shear band patterns and the regularization efficiencies have been investigated, showing that a larger l_c corresponds to more ductile of material in the softening regime, and shear band thickness increases with internal length scale l_c; another micropolar parameter G_c has nearly no influence on the shear band patterns and the regularization effective ratio; peak load carrying capacity increases with initial density, confining pressure, critical friction angle ϕ_u, strength parameter n_p, and deformation parameter n_d, however, the impact of each factor varies.

(4) The second-order work, as instability criterion, has been newly defined within the micropolar theory. After considering the contribution of couple stresses and conjugated curvatures, the vanishing of second-order work has been obviously delayed. Moreover, the vanished values of second-order work become meaningful in a micropolar continuum. Therefore, the envelope diagrams of the local vanishing of second-order work can be used to characterize the failure domain.

Perspectives

Although the micropolar theory has demonstrated more physical meaning and great ability in dealing with mesh dependency problems in finite element analysis, its regularization efficiency was still affected by the element size. In this sense, the application of micropolar theory in simulating the very large geotechnical structures is still on the way. Based on the current study, the perspectives are looked forward to as follows.

(1) The sensitivity of the results of the finite element simulations to the mesh size has been illustrated, while, the influences of the mesh alignment have not been discussed. Therefore, besides the rectangular element, more types of the user defined element, e.g. triangle element, should be developed for the mesh sensitive study.

(2) The discussions of the internal length scales in micropolar theory are still an opening question. Therefore, the further study about the physical meaning should be continued in the future.

(3) The other regularization approaches should have also been numerically implemented and compared with the micropolar theory, which may be an interesting direction and will be tried in the future. Considering the advantages and the scope of applications of each regularization technique, the combined regularization approach may be proposed to become more powerful to deal with the mesh dependency problems. What's more, the attempts can also be done to implement other advance techniques, such as SPH, MPM, in the near future.

(4) Current finite element simulations were conducted with the implicit algorithm in ABAQUS, which limited the problems in a static or quasi-static domain. Using the explicit method to study the dynamic problems is a tendency.

(5) Although the 2D and 3D micropolar model has been implemented and validated successfully, the calculation efficiency was not so powerful to obtain a solution rapidly. As a result, more advanced algorithms should be adopted to face the volume interlocking and hourglass problems in low-order element.

Appendix A: Numerical Pathological Solutions

Ill-posedness of static loading problems

From a mathematical point of view, material instability results in changes to the properties of a partial differential equation. For simplicity, a one-dimensional uniaxial compression or tension test is first taken as an example in context of which to discuss the instability of static loading problems under the framework of classical continuum theory. As we know, the total strain of a material point can be decomposed into the elastic part and plastic part:

$$\varepsilon = \varepsilon^e + \varepsilon^p \tag{A-1}$$

The elastic part can be calculated by the Hooke's Law,

$$\varepsilon^e = \frac{\sigma}{E} \tag{A-2}$$

where σ and E are the axial stress and Young's modulus, respectively. It is assumed that the material belongs to the typical plastic category and that stress rate will decrease linearly with plastic strain rate after entering into the softening regime, after which the current stress can be expressed as

$$\sigma = \sigma_0 + h_p \varepsilon^p \tag{A-3}$$

where σ and σ_0 are the current stress and initial yield stress, respectively; h_p is the plastic hardening (softening) modulus. Thus the plastic part can be calculated from Eq. (A-3):

$$\varepsilon^p = \frac{\sigma - \sigma_0}{h_p} \tag{A-4}$$

Combining Eqs. (A-1), (A-2) and (A-4), we get the total strain rate:

$$\dot{\varepsilon} = \dot{\varepsilon}^e + \dot{\varepsilon}^p = \frac{\dot{\sigma}}{E} + \frac{\dot{\sigma}}{h_p} = \frac{E + h_p}{E h_p} \dot{\sigma} \tag{A-5}$$

Alternatively, the stress rate can be expressed as a function of total strain rate:

$$\dot{\sigma} = \frac{E h_p}{E + h_p} \dot{\varepsilon} \tag{A-6}$$

The absolute value of softening parameter is less than the Young's modulus by default. If the elastoplastic modulus is changed from $E h_p / \left(E + h_p\right) > 0$ to $E h_p / \left(E + h_p\right) < 0$ (h_p from positive

to negative), then the second-order work density $\dot{\varepsilon}\dot{\sigma} = \dot{\varepsilon}^2 E h_p \big/ \left(E + h_p\right) < 0$, and the material goes into instability. The rate form of the partial differential equation for one-dimensional static problem is expressed as

$$\frac{\partial \dot{\sigma}}{\partial x} = \dot{f} \tag{A-7}$$

where f is the body force. From Eq. (A-6) and Eq. (A-7), we can get

$$\frac{\partial \dot{\sigma}}{\partial x} = \frac{E h_p}{E + h_p} \frac{\partial^2 u}{\partial x^2} = \dot{f} \tag{A-8}$$

The property of the partial differential equation for static loading problems, it is universally acknowledged, must be kept elliptical. When the condition of $E > -h_p > 0$ is satisfied, the property of the governing field equation will change from ellipticity to hyperbolicity, and material stability is lost. What's more, the solutions become pathological.

Ill-posedness of dynamic loading problems

To aid discussion of the instability and ill-posedness of dynamic loading problems under the framework of classical continuum theory, we take a one-dimensional wave equation as an example,

$$\frac{\partial \dot{\sigma}}{\partial x} = \rho \frac{\partial^2 \dot{u}}{\partial t^2} \tag{A-9}$$

where ρ, $\dot{\sigma}$, $\dot{u}$, and t are the density of the medium, the stress rate, the spread speed, and the time. Reconsidering the relationship between stress rate and strain rate as Eq. (A-6), the wave expressed in Eq. (A-9) can also be expressed as

$$\frac{E + h_p}{C^2} \frac{\partial^2 \dot{u}}{\partial t^2} - h_p \frac{\partial^2 \dot{u}}{\partial x^2} = 0 \tag{A-10}$$

where $C = \sqrt{E/\rho}$, the property of the foregoing partial differential equation, is hyperbolic when $h_p > 0$ and, conversely, is elliptic when $0 < -h_p < E$. To illustrate the problems more clearly, we conduct a characteristic analysis of the foregoing wave equation, calculating the first-order derivatives of the spread speed $\dot{u}$ in the x–t plane:

$$d\left(\frac{\partial \dot{u}}{dt}\right) = \frac{\partial^2 \dot{u}}{\partial t^2} dt + \frac{\partial^2 \dot{u}}{\partial x \partial t} dx \tag{A-11}$$

$$d\left(\frac{\partial \dot{u}}{dx}\right)=\frac{\partial^2 \dot{u}}{\partial x \partial t}dt+\frac{\partial^2 \dot{u}}{\partial x^2}dx \tag{A-12}$$

Based on Eq. (A-10), Eq. (A-11), and Eq. (A-12), we can obtain a matrix equation in which $\frac{\partial^2 \dot{u}}{\partial x^2}$, $\frac{\partial^2 \dot{u}}{\partial t^2}$, and $\frac{\partial^2 \dot{u}}{\partial x \partial t}$ are taken as unknowns.

$$\begin{bmatrix} \frac{E+h_p}{C^2} & 0 & -h_p \\ dt & dx & 0 \\ 0 & dt & dx \end{bmatrix} \begin{Bmatrix} \frac{\partial^2 \dot{u}}{\partial t^2} \\ \frac{\partial^2 \dot{u}}{\partial x \partial t} \\ \frac{\partial^2 \dot{u}}{\partial x^2} \end{Bmatrix} = \begin{Bmatrix} 0 \\ d\left(\frac{\partial \dot{u}}{dt}\right) \\ d\left(\frac{\partial \dot{u}}{dt}\right) \end{Bmatrix} \tag{A-13}$$

The multiplier matrix is noted to be **A**, after which we can obtain the characteristic functions from the condition det(**A**) = 0:

$$\frac{dx}{dt}=\pm C\sqrt{\frac{h_p}{E+h_p}} \tag{A-14}$$

The foregoing equation means that the wave spreads with a speed of $C\sqrt{h_p/\left(E+h_p\right)}$ when $h_p/\left(E+h_p\right)<0$, as well as that the wave speed is an imaginary number. Furthermore, the wave will become a standing wave, unable to spread any more.

From the foregoing discussions, we can conclude that the property of partial differential equations used in dynamic loading problems will vary from hyperbolic to elliptic in response to strain softening behaviors within the framework of classical continuum theory. When the wave speed in the strain localization region becomes an imaginary number, the wave will become a standing wave and lose the ability to spread further.

Appendix B: Mesh Dependency Problem within Classical Continuum Theory

Mesh dependency phenomenon can be observed by revisiting an example, the uniaxial tension test of a bar, conducted by Crisfield and de Borst (1982, 1986), in which a softening plasticity model was adopted.

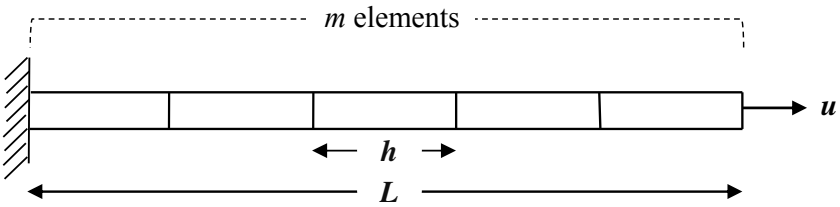

Figure B-1 Uniaxial tension test of a bar

In Figure B-1, a bar of length L is divided uniformly into m elements, with each element having a length h, so that $L = m \cdot h$. Moreover, it is assumed that one element has been set as an imperfection and has a tensile strength limit σ_y that is slightly weaker than other $m - 1$ elements. A tension load is performed in the right side of the bar, and the final displacement is u. An approximation of the measured load–displacement relation is plotted in Figure B-2. During the first stage, before reaching the tensile yield stress of the weak element, all the elements' response is elastic until the yield stress σ_y, with a linear relation assumed between the stress σ and the strain $\varepsilon = \varepsilon^e$ ($\varepsilon^p = 0$) during this stage, defined as

$$\sigma = E\varepsilon^e, \quad (\text{if } \varepsilon \le \sigma_y / E) \tag{B-1}$$

A softening stage ensues. In this second stage, on reaching the yield strength σ_y of the imperfect element, its current stress begins to reduce with further tension because of the material's softening behavior. However, this condition has not exceeded other elements' yield strength, meaning that they will unload elastically to maintain the equilibrium of the system. It is also assumed that the descending slope is a constant (i.e., that the softening parameter H does not vary with the inelastic strain). In the softening stage, then,

$$\sigma = \sigma_y - H(\varepsilon - \varepsilon^e), \quad (\text{if } \varepsilon > \sigma_y / E) \tag{B-2}$$

The relation of the average strain of the bar and the evolution of current stress is plotted in Figure B-3, which indicates that the results depend entirely on the discretization of the bar. The finite

element method simply manages to capture the failure zone in a single element thickness, irrespective of the size of the element:

$$\bar{\varepsilon} = \frac{u}{L} = \frac{\varepsilon^e hm + h\varepsilon^p}{mh} = \varepsilon^e + \frac{\varepsilon^p}{m} = \frac{\sigma}{E} - \frac{\sigma - \sigma_y}{mH}, \quad (\sigma \geq \sigma_y) \tag{B-3}$$

From the preceding mathematical derivation, it can be easily found that $\bar{\varepsilon}$ depends on the element number *m*: after the onset of strain softening $(\sigma \geq \sigma_y)$ the solution is entirely determined by the discretization. When the imperfect element is totally exhausted, and current stress σ becomes zero. It is obvious from Figure B-3 that when the bar is infinitely divided, *m* tends toward an infinite value, with the post-peak curve receding absolutely along the original loading path. A major problem, however, is that because the constitutive model has always been illustrated in terms of a stress–strain law and not as a force-displacement relation, when the average strain becomes zero upon mesh refinement and the failure area also becomes zero, energy dissipation also tends to become zero. From a physical point of view, this is unacceptable. We must either rephrase our constitutive model in terms of force–displacement relations, which implies the use of special interface element (Rots, 1988), or enrich the continuum description by adding higher-order terms that can accommodate narrow zones of highly localized deformation (de Borst and Mühlhaus, 1991).

It can be judged from Figure B-3 to obtain a meaningful solution for elastoplastic materials. It is compulsory to set $m < \sigma_y/H$.

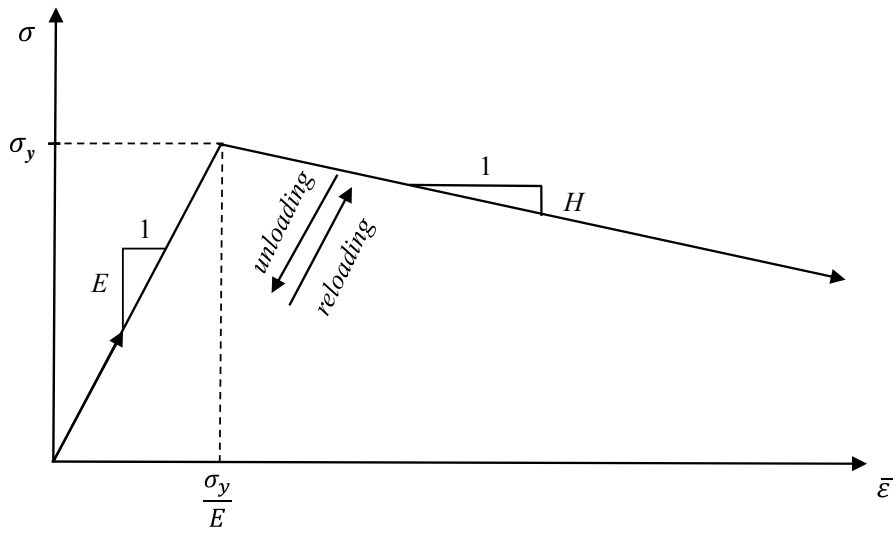

Figure B-2 Softening response in stress-strain

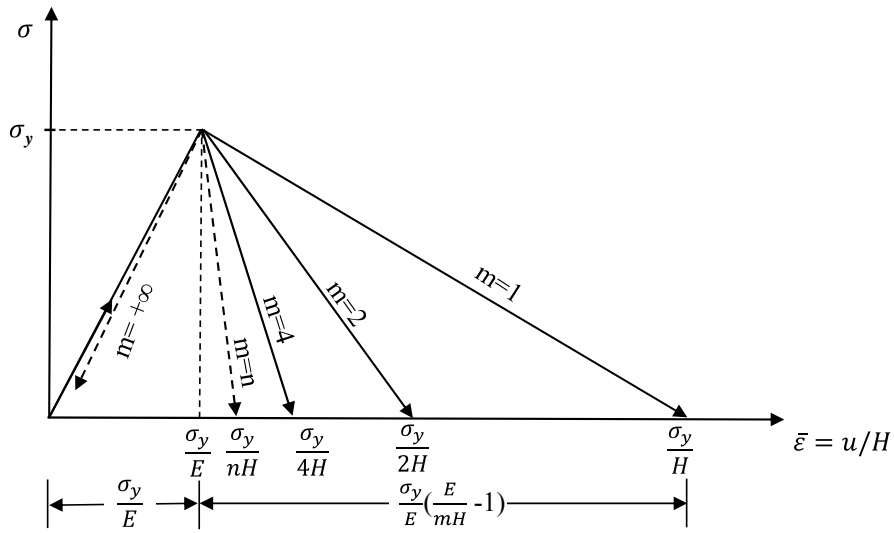

Figure B-3 Solution dependency on the discretization for a bar in uniaxial test

The mechanism of these mesh dependency problems has been demonstrated clearly from a mathematical and analytical point of view. Similarly, mesh dependency problems exist with the softening of constitutive models within the framework of the classical continuum theory in general 2D or 3D cases, especially when the failure analysis is performed by the finite element method.

Appendix C: Full Formulations of Micropolar Theory

Issues of strain localization in failure analysis of geotechnical structures are of great importance in geotechnical engineering. Considering the numerical difficulties of finite element method in modeling strain localization phenomena within the framework of classical Cauchy–Boltzmann continuum mechanics, various approaches have been proposed to overcome these difficulties. For example, methods based on micropolar continuum theory, gradient-enhanced constitutive laws, embedded weak or strong discontinuities, or the nonlocal integral constitutive equations have been under intensive investigation in recent years, as mentioned in the previous chapter.

The pioneering work of the Delft University of Technology (de Borst, 1991; de Borst and Mühlhaus, 1991; de Borst and Sluys, 1991; de Borst, 1993) was based on a reappraisal of the mechanics of generalized continua developed in the 1960s (Kröner, 1967; Forest et al., 2001). Generalized continua can be classified into three main groups:

(1) micropolar continua are endowed with additional degrees of freedom in addition to the usual displacement field (Cosserat and micro-orphic theories, according to (Eringen, 1976);

(2) higher-grade continua introduce higher space derivatives of the displacement field than the usual deformation gradient (second gradient theory, according to (Mindlin and Eshel, 1968), and this class of theories also incorporates the gradients of some selected internal variables that play significant roles in the balance and constitutive relations (Aifantis, 1987);

(3) the third or last class contains fully nonlocal media for which integral relations relate stress and strain evolutions (Eringen, 1976; Pijaudier-Cabot and Bažant, 1987).

Among these three approaches, micropolar theory is particularly attractive for its relative ease of implementation and its suitability in capturing shear-dominated modes of failure. Furthermore, the micropolar theory, in which the grain rotations and couple stresses arise naturally and can be easily explained from a point of view of physics, has been adopted in present study.

In contrast to micropolar theory, classical continuum mechanics considers only the interaction of microstructures of material through global displacements of material points. However, in reality, interactions of grains may include micro-rotations and consequently produced micro-curvatures and corresponding conjugated couple stresses. Accordingly, extending the classical continuum to a

generalized micropolar continuum that considers micro-rotations has become a popular topic among those attempting to explain the micro-scale effects.

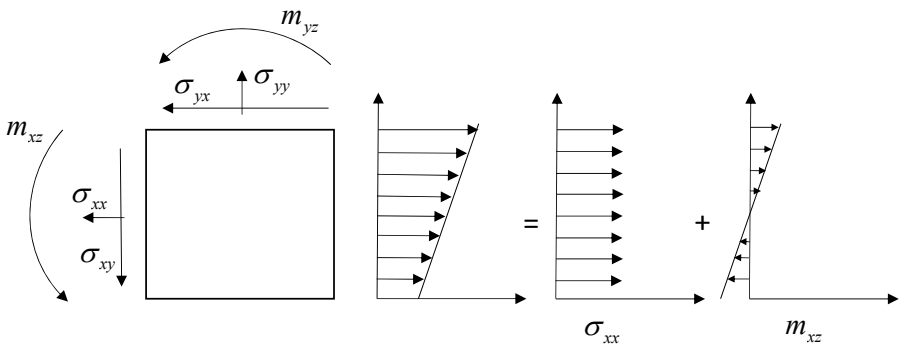

Figure C-1 Asymmetry stress distribution in micro polar theory

Classical continuum models, not having any internal length scale parameter, suffer from pathological mesh dependency when modeling strain localization in failure analysis. A potential reason for this defect is that the governing field equations of the constitutive model within the framework of classical theory will convert from the elliptic property into the hyperbolic one under static loading conditions when a localization zone sees excessive development. For half a century, micropolar theory with high-order terms has been used as a regularization approach to preserve the ellipticity.

Two-dimensional plane strain problems are first taken into consideration for the introduction of micropolar theory. There are three generalized displacement degrees of freedom for each micro-element.

$$\mathbf{u} = \left[u_x \; u_y \; \omega_z \right]^T \tag{C-1}$$

As Figure C-1, after an additional rotational degree of freedom for a micro-element has been introduced in the constitutive model for two-dimensional problems, the stress distributions of a micro plane element become asymmetric.

Different from Cauchy stress and Cauchy strain based on classical continuum mechanics theory, the stress and strain vectors in micropolar continua are generalized to consider micro-curvatures and micro-moments,

$$\boldsymbol{\varepsilon} = \left[\varepsilon_{xx} \; \varepsilon_{yy} \; \varepsilon_{zz} \; \varepsilon_{xy} \; \varepsilon_{yx} \; \kappa_{zx} l_c \; \kappa_{zy} l_c \right]^T \tag{C-2}$$

$$\boldsymbol{\sigma} = \left[\sigma_{xx} \; \sigma_{yy} \; \sigma_{zz} \; \sigma_{xy} \; \sigma_{yx} \; m_{zx}/l_c \; m_{zy}/l_c \right]^T \tag{C-3}$$

where κ_{zx} and κ_{zy} are introduced as micro-curvatures in micropolar theory, derived from the gradients of rotational quantity ω_z in directions x and y; m_{zx} and m_{zy} are couple stresses energy conjugated to the curvatures κ_{zx} and κ_{zy}; and l_c, a material bending length, may be taken as an internal length. The value of internal length l_c, however, is still an open question. Many researchers imbue this parameter with more physical meaning and then take the mean grain size d_{50} as the internal length scale parameter.

When considering the additional components of stress and strain, it must be noted that the stress tensor is non-symmetric and that the couple stress are noticeable in the shear zones. However, the stress tensor is symmetric, and the couple stresses disappear outside the shear zones. The occurrence of non-symmetry in the stress tensor and the appearance of the couple stresses take place immediately after the onset of the strain localization. Accordingly, when interests are limited to strain localization phenomena, the equilibrium equations, compatibility equations, and constitutive laws in micropolar continua mechanics must be revised by considering the additional components of stress and strain on the basis of classic continua mechanics, as will be illustrated in detail in the following sections.

Equilibrium equations

Static equilibrium

With the incorporated couple stresses as already discussed, the equilibrium of a micro plane element having a very small size of dx in x direction and dy in y direction is considered while ignoring the body force and body moment. The thickness of the micro-element is assumed to be one unit. As shown in Figure C-2, the stress distribution on the right side is slightly different from that on the left side, and the up side is different from the down side in the x and y directions.

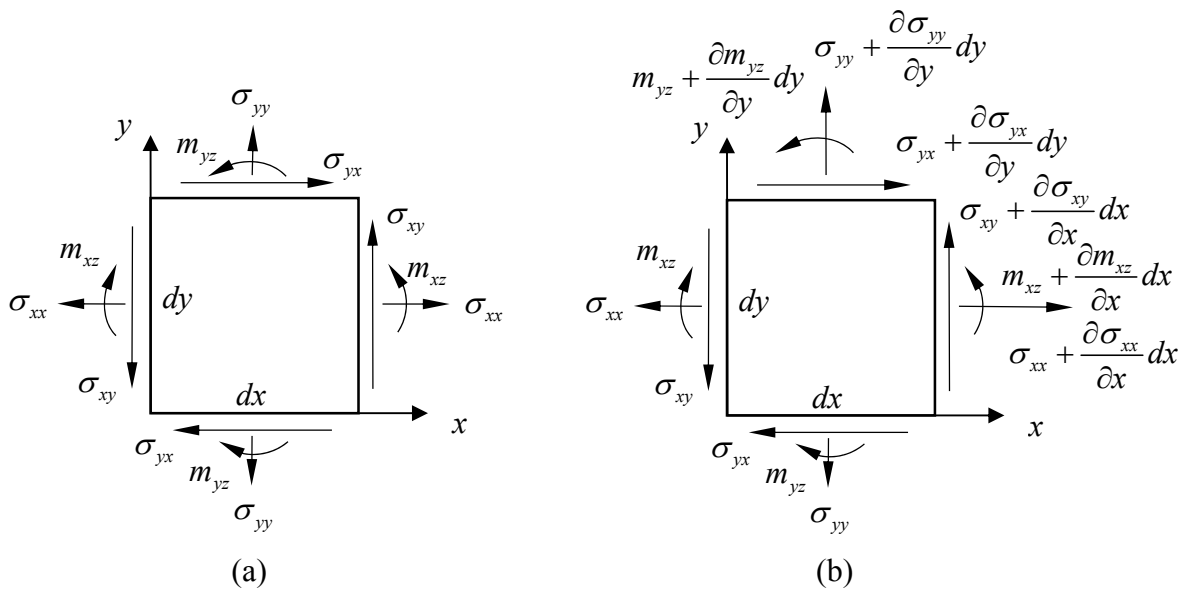

Figure C-2 Micropolar plane element: (a) ideal stress distribution of a micro polar element; (b) considering the slight difference caused by micro size

Based on the static equilibrium conditions: $\sum F_x = 0$, $\sum F_y = 0$, $\sum M_o = 0$ (o is the centroid of the element), three equilibrium equations can be obtained:

$$\begin{cases} \left(-\sigma_{xx} + \sigma_{xx} + \dfrac{\partial \sigma_{xx}}{\partial x} dx\right) dy + \left(-\sigma_{yx} + \sigma_{yx} + \dfrac{\partial \sigma_{yx}}{\partial y} dy\right) dx = 0 \\ \left(-\sigma_{yy} + -\sigma_{yy} + \dfrac{\partial \sigma_{yy}}{\partial y} dy\right) dx + \left(-\sigma_{xy} + \sigma_{xy} + \dfrac{\partial \sigma_{xy}}{\partial x} dx\right) dy = 0 \\ \left(-m_{xz} + m_{xz} + \dfrac{\partial m_{xz}}{\partial x} dx\right) dy + \left(-m_{yz} + m_{yz} + \dfrac{\partial m_{yz}}{\partial y} dy\right) dx + \\ \quad \left(-\sigma_{xy} + \sigma_{xy} + \dfrac{\partial \sigma_{xy}}{\partial x} dx\right) dy \cdot \dfrac{1}{2} dx - \left(\sigma_{yx} + \sigma_{yx} + \dfrac{\partial \sigma_{yx}}{\partial y} dy\right) dx \cdot \dfrac{1}{2} dy = 0 \end{cases} \tag{C-4}$$

It is assumed that the element size is rather small (dx and dy are the infinitesimal quantities), which means that the higher-order terms can be ignored. Consequently, if the body force and body moment are also ignored, the foregoing equilibrium equations can be simplified in the form

$$\begin{cases} \dfrac{\partial \sigma_{xx}}{\partial x} + \dfrac{\partial \sigma_{yx}}{\partial y} = 0 \\ \dfrac{\partial \sigma_{yy}}{\partial y} + \dfrac{\partial \sigma_{xy}}{\partial x} = 0 \\ \sigma_{xy} - \sigma_{yx} + \dfrac{\partial m_{xz}}{\partial x} + \dfrac{\partial m_{yz}}{\partial y} = 0 \end{cases} \tag{C-5}$$

The first two sub-equations of Eq. (C-5) are the same as in the classical continuum theory. The third sub-equation is a particular case of micropolar theory from which we can observe that the theorem of conjugate shearing stress is no longer true owing to the appearance of the couple stresses. In geotechnical engineering, the shear stresses are categorized into the symmetric part and skew symmetric part based on the roles they play on the micro-element. The symmetric part $\tau_S = \left(\sigma_{xy} + \sigma_{yx}\right)/2$ produces the shear strain, whereas the skew symmetric part $\tau_A = \left(\sigma_{xy} - \sigma_{yx}\right)/2$ only induces the independent rotation of the micro-element and has nothing to do with the shear strain. If the skew symmetric part disappears ($\tau_A = 0$, $\tau_S = \sigma_{xy} = \sigma_{yx}$), it satisfies the theorem of conjugate shearing stress, and the micropolar theory is totally retrieved to the classical continuum mechanics theory.

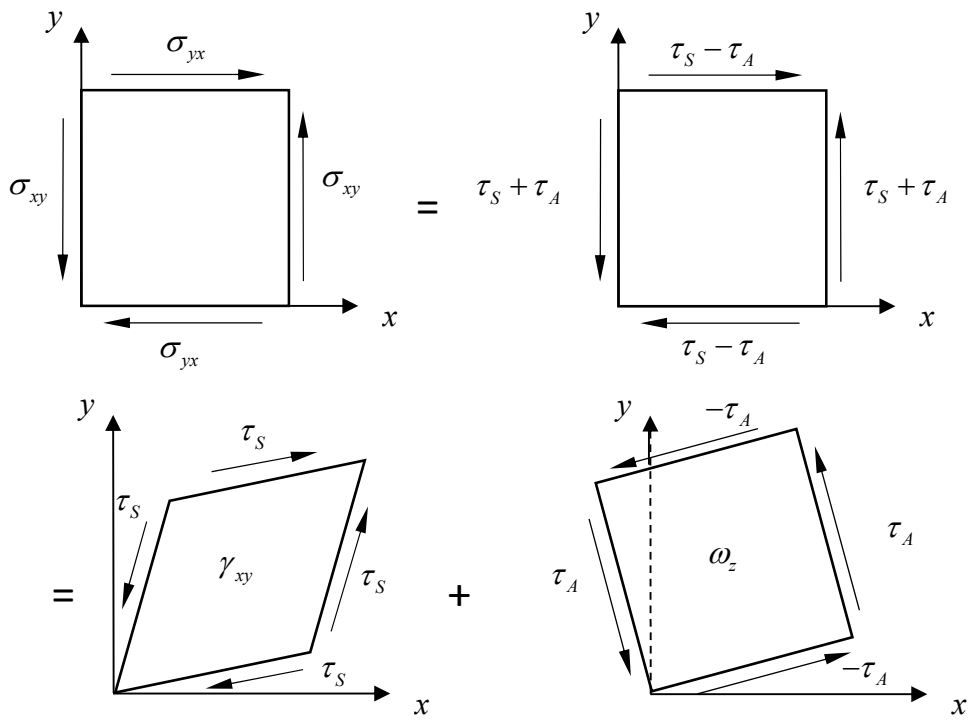

Figure C-3 Symmetric part and the skew symmetric part of the shear stress in micro polar theory

Dynamic equilibrium

For dynamic problems, apart from the conventional way, linear inertia terms, the rotational or spin inertia are also taken into account in a micropolar continuum for which the form of equilibrium equations is similar to those of static ones,

$$\begin{cases} \dfrac{\partial \sigma_{xx}}{\partial x} + \dfrac{\partial \sigma_{yx}}{\partial y} = \rho \dfrac{\partial^2 u_x}{\partial t^2} \\ \dfrac{\partial \sigma_{yy}}{\partial y} + \dfrac{\partial \sigma_{xy}}{\partial x} = \rho \dfrac{\partial^2 u_y}{\partial t^2} \\ \sigma_{xy} - \sigma_{yx} + \dfrac{\partial m_{xz}}{\partial x} + \dfrac{\partial m_{yz}}{\partial y} = \Theta \dfrac{\partial^2 \omega_z}{\partial t^2} \end{cases} \tag{C-6}$$

where ρ is the mass density, t denotes time, and Θ represents spin inertia per unit volume. The first two sub-equations in Eq. (C-6) are the equilibrium equations of forces, and the third responds to the moment equilibrium. The value for Θ depends on the size of the micro-elements and on the density ρ. The micro-elements have been assumed to be cubes having edges of length $2d$ (de Borst and Sluys, 1991), as shown in Figure **C-4**. In two dimensions, the spin inertia of such a micro-element can be calculated:

$$\Theta_{cube} = \int_{-d}^{d} \int_{-d}^{d} \rho \left(x^2 + y^2 \right) 2d \; dxdy \tag{C-7}$$

Carrying out the spatial integration with respect to x and to y results in

$$\Theta_{cube} = \frac{16}{3} \rho d^5 \tag{C-8}$$

so the spin inertia per unit volume in z direction is given by

$$\Theta = \frac{\Theta_{cube}}{V} = \frac{2}{3} \rho d^2 \tag{C-9}$$

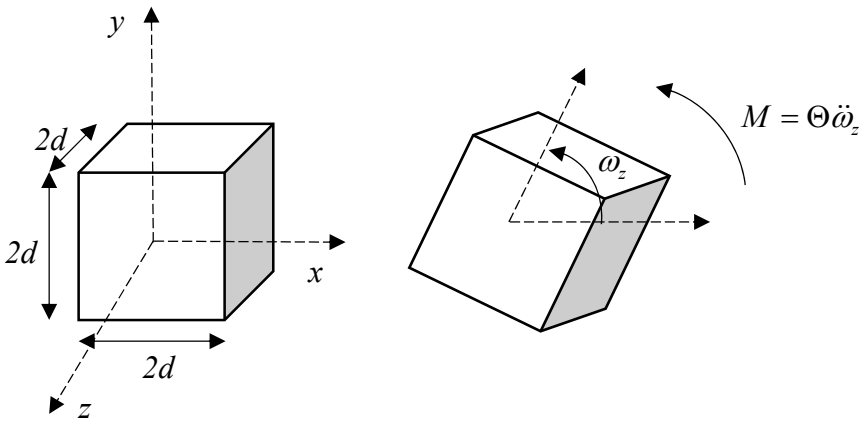

Figure C-4 Cube micro element and spin inertia

Considering a spin moment acting on the micro-element:

$$M_{xz} = \frac{1}{6} G(1+\upsilon)(2d)^4 \kappa_{xz} \tag{C-10}$$

For the couple stress m_{xz}, then, we can get

$$m_{xz} = \frac{M_{xz}}{(2d)^2} = \frac{2}{3} G(1+\upsilon) d^2 \kappa_{xz} \tag{C-11}$$

If the elastic relation is assumed (see Eq. (C-21) in the section 3), the micro-moment can be calculated by the corresponding micro-curvature:

$$m_{xz} = 2G\kappa_{xz} l_c^{\,2} \tag{C-12}$$

The internal length scale l_c is then directly related to the element size $2d$:

$$d^2 = \frac{3}{1+\upsilon} l_c^{\,2} \tag{C-13}$$

Substitution of this relation into Eq. (C-9) results in

$$\Theta = 2\frac{\rho}{1+\upsilon} l_c^{\,2} \tag{C-14}$$

From all the foregoing formulations, it can be easily found for dynamic problems that only density ρ is a new added parameter compared with static problem.

Kinematics equations

In micropolar theory, apart from the translational degrees of freedom inherited from the classical continuum theory, an additional rotational degree of freedom appears and results in an independent micro-rotation different from the macro-rotation caused by shear strain. The micropolar theory thus requires two independent kinematical fields: The first aims to obtain the conventional strain tensor, and the second is used to get the curvatures or the rotation gradients. That is to say, the micro-rotation may be an arbitrary value with $\omega_z \neq \frac{1}{2}\left(\frac{\partial u_y}{\partial x} - \frac{\partial u_x}{\partial y}\right)$. For the components of the strain vector in Eq. (C-2), the normal strain ε_{xx} and ε_{yy} can be still calculated by using the same classical continuum theory, whereas the curvatures κ_{xz} and κ_{yz} conjugated with the couple stresses m_{xz} and m_{yz} are related to the micro-rotation ... From Figure C-5, the geometric relationship between curvatures and the micro-rotation can be formulated as follows:

$$\kappa_{xz} = \frac{\partial \omega_z}{\partial x}, \kappa_{yz} = \frac{\partial \omega_z}{\partial y} \tag{C-15}$$

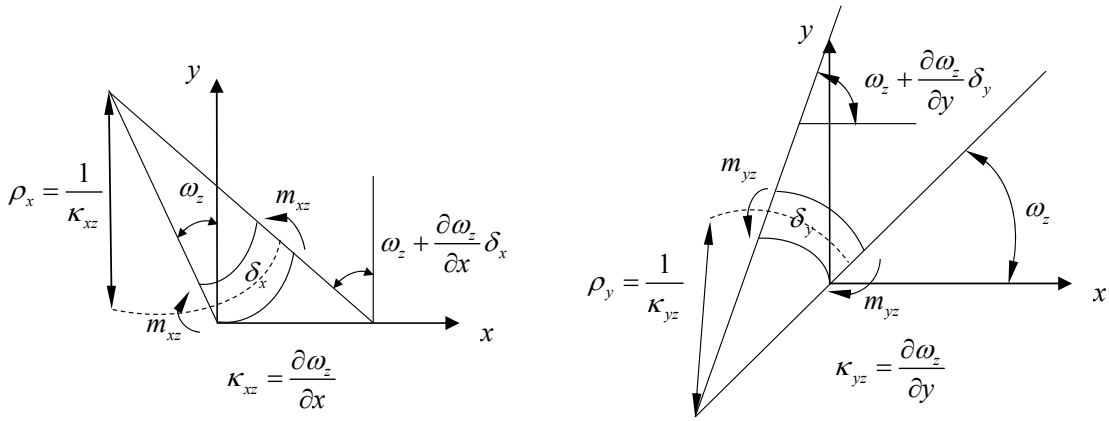

Figure C-5 Bending curvatures and couple stresses of a micropolar element

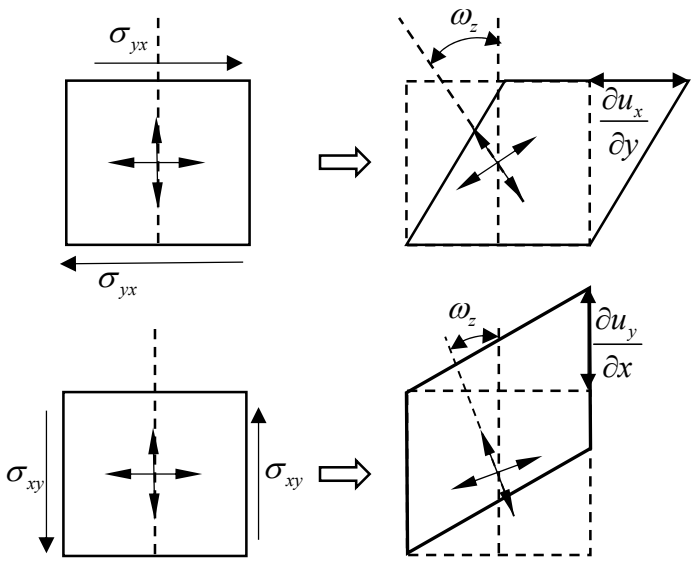

Figure C-6 Shear strains in micropolar theory

Considering the shearing of a micro-element (one reduced material point inside the element is assumed) in micropolar theory depicted in Figure C-6, as well as its independent rotation, we can find that the shear strain components in micropolar theory are related not only to the translational deformation but also to the micro-rotation. Then the shear strain components can be derived:

$$\varepsilon_{xy} = \frac{\partial u_y}{\partial x} - \omega_z, \varepsilon_{yx} = \frac{\partial u_x}{\partial y} + \omega_z \tag{C-16}$$

To summarize, the geometric equations of the plane strain problems in micropolar continuum theory are formulated as follows:

$$\begin{cases} \varepsilon_{xx} = \dfrac{\partial u_x}{\partial x}, \varepsilon_{yy} = \dfrac{\partial u_y}{\partial y} \\ \varepsilon_{xy} = \dfrac{\partial u_y}{\partial x} - \omega_z, \varepsilon_{yx} = \dfrac{\partial u_x}{\partial y} + \omega_z \\ \varepsilon_{zz} = 0 \\ \kappa_{xz} = \dfrac{\partial \omega_z}{\partial x}, \kappa_{yz} = \dfrac{\partial \omega_z}{\partial y} \end{cases} \tag{C-17}$$

Constitutive laws

To summarize the two foregoing subsections, a similar process has been found for the micropolar continuum theory as for the classical continuum mechanics theory, which must necessarily obey the kinematic and equilibrium equations. The foregoing equations can be written in matrix–vector forms for simplification,

$$\boldsymbol{\varepsilon} = \mathbf{L}\mathbf{u} \tag{C-18}$$

$$\mathbf{L}^T\boldsymbol{\sigma} + \mathbf{f} = 0 \tag{C-19}$$

where **f** denotes body force vector (including body moment) and the displacement-strain operator matrix **L** is defined as

$$\mathbf{L}^T = \begin{bmatrix} \dfrac{\partial}{\partial x} & 0 & 0 & 0 & \dfrac{\partial}{\partial y} & 0 & 0 \\ 0 & \dfrac{\partial}{\partial y} & 0 & \dfrac{\partial}{\partial x} & 0 & 0 & 0 \\ 0 & 0 & 0 & -1 & 1 & l_c\dfrac{\partial}{\partial x} & l_c\dfrac{\partial}{\partial y} \end{bmatrix} \tag{C-20}$$

Elastic models

For the constitutive relation of elastic materials, the stress rate is linearly related to elastic strain rate by the elastic stiffness matrix

$$\dot{\boldsymbol{\sigma}} = \mathbf{D}^e\dot{\boldsymbol{\varepsilon}}^e \tag{C-21}$$

in which

$$\mathbf{D}^e = \begin{bmatrix} \lambda+2G & \lambda & \lambda & 0 & 0 & 0 & 0 \\ \lambda & \lambda+2G & \lambda & 0 & 0 & 0 & 0 \\ \lambda & \lambda & \lambda+2G & 0 & 0 & 0 & 0 \\ 0 & 0 & 0 & G+G_c & G-G_c & 0 & 0 \\ 0 & 0 & 0 & G-G_c & G+G_c & 0 & 0 \\ 0 & 0 & 0 & 0 & 0 & 2G & 0 \\ 0 & 0 & 0 & 0 & 0 & 0 & 2G \end{bmatrix} \tag{C-22}$$

where Lamé constant $\lambda=2G\upsilon/(1-2\upsilon)$, G and υ are the conventional shear modulus and Poisson's ratio, respectively, and G_c is the micropolar shear modulus affecting the asymmetric degree of shear stress. The coefficient 2 has been introduced in the terms $\mathbf{D}^e(6, 6)$ and $\mathbf{D}^e(7, 7)$ so as to arrive at a convenient form of the inelastic constitutive equations (de Borst, 1991; de Borst and Mühlhaus, 1991; de Borst and Sluys, 1991; de Borst, 1993). Obviously, the total bending stiffness $2Gl_c^2$, which sets the relation between the micro-curvatures and the couple stresses, is determined by the value of the internal length scale parameter l_c.

Elastoplastic models

For the formulation of a general elastoplastic micropolar continuum, the hypothesis that strain rate can be decomposed into both elastic and plastic parts for small–strain plasticity is adopted:

$$\dot{\boldsymbol{\varepsilon}} = \dot{\boldsymbol{\varepsilon}}^{\mathbf{e}} + \dot{\boldsymbol{\varepsilon}}^{\mathbf{p}} \tag{C-23}$$

Combining Eq. (C-23) and Eq. (C-21) results in

$$\dot{\boldsymbol{\sigma}} = \mathbf{D}^e(\dot{\boldsymbol{\varepsilon}} - \dot{\boldsymbol{\varepsilon}}^{\mathbf{p}}) \tag{C-24}$$

Furthermore, the plastic strain is given by

$$\dot{\boldsymbol{\varepsilon}}^{\mathbf{p}} = \dot{\lambda}\mathbf{m}, \quad \text{with} \quad \mathbf{m} = \frac{\partial \mathbf{Q}}{\partial \boldsymbol{\sigma}} \tag{C-25}$$

where $\mathbf{Q}$ is the potential function, $\dot{\lambda}$ denotes the plastic multiplier, and $\mathbf{m}$ determines the direction of plastic flow. For a general elastoplastic yield function

$$F(\boldsymbol{\sigma}, \boldsymbol{\kappa}) = \phi(\boldsymbol{\sigma}) - \bar{\sigma}(\boldsymbol{\kappa}) = 0 \tag{C-26}$$

in which $\boldsymbol{\sigma}$ represents the current stress state and $\boldsymbol{\kappa}$ is a vector containing the hardening variables, the Kuhn–Tucker conditions must be satisfied:

$$\begin{cases} \dot{\lambda} \geq 0 \\ F \leq 0 \\ \dot{\lambda} F = 0 \end{cases} \tag{C-27}$$

which means the multiplier is a nonnegative value, current stress must located within or on the yield surface and the consistency condition must be satisfied. The plastic flow is governed by the consistency condition

$$\dot{F} = \mathbf{n}^T \dot{\boldsymbol{\sigma}} - h\dot{\lambda} = 0 \tag{C-28}$$

where the gradient to the yield function and the hardening modulus can be calculated as

$$\mathbf{n} = \frac{\partial \mathbf{F}}{\partial \boldsymbol{\sigma}} \tag{C-29}$$

and

$$h = -\frac{\dot{\boldsymbol{\kappa}}}{\dot{\lambda}} \frac{\partial \mathbf{F}}{\partial \boldsymbol{\kappa}} \tag{C-30}$$

respectively. Combining Eq. (C-24) and Eq. (C-28), we obtain the elastoplastic relationship of stress rate and strain rate:

$$\dot{\boldsymbol{\sigma}} = \left[\mathbf{D}^e - \frac{\mathbf{D}^e \mathbf{m} \mathbf{n}^{\mathrm{T}} \mathbf{D}^e}{h + \mathbf{n}^{\mathrm{T}} \mathbf{D}^e \mathbf{m}} \right] \dot{\boldsymbol{\varepsilon}} \tag{C-31}$$

The stress and strain rate are the generalized vectors of a micropolar continuum defined in Eq. (C-2) and Eq. (C-3). The elastoplastic stiffness matrix can be defined as

$$\mathbf{D}^{ep} = \mathbf{D}^e - \frac{\mathbf{D}^e \mathbf{m} \mathbf{n}^{\mathrm{T}} \mathbf{D}^e}{h + \mathbf{n}^{\mathrm{T}} \mathbf{D}^e \mathbf{m}} \tag{C-32}$$

Appendix D: Brief Introduction of UMAT and Validation

Introduction of UMAT

User defined material (UMAT) is one of the functions of the commercial FE software—ABAQUS. The UMAT subroutine, with specific format is shown in Figure D-1, needs to be coded to define the mechanical behavior of a material. The specific interface is able to realize data transference and data sharing between different subroutines of ABAQUS. Various constitutive models can be numerically implemented as alternatives to become the built-in ABAQUS models. UMAT greatly increases the power of ABAQUS, allowing it to contain more and more materials with arbitrary complexity.

When programming a UMAT, users can still take the advantages of ABAQUS's pre-processing and post-processing platforms, making implementation easy. All that users need to do is completely incorporate the constitutive law into the subroutine. In the UMAT subroutine, certain indispensable arrays, such as the current strain *STRAN*(*NTENS*), the strain increment *DSTRAN*(*NTENS*) and initial input parameters *PROPS*(*NPROPS*), and the current stress *STRESS*(*NTENS*), must be defined. Some other variables, such as the Jacobian matrix *DDSDDE*(*NTENS*,*NTENS*), stress *STRESS*(*NTENS*), and state variables *STATEV*(*STATV*), need to be updated and saved at the end of the subroutine, after which all updated arrays will be returned into UMAT subroutine as a current new state for further calculation. A detailed description of UMAT can be found in the ABAQUS documentation. The process for defining a user-defined material is briefly demonstrated in flowchart in Figure D-2. The integration method, cutting plane algorithm, in the flowchart has been illustrated in Chapter 2.

```
C-----------------User defined Material subroutine--------------C

      SUBROUTINE UMAT(STRESS, STATEV, DDSDDE, SSE, SPD, SCD,
     1 RPL, DDSDDT, DRPLDE, DRPLDT,
     2 STRAN, DSTRAN, TIME, DTIME, TEMP, DTEMP, PREDEF, DPRED, CMNAME,
     3 NDI, NSHR, NTENS, NSTATV, PROPS, NPROPS, COORDS, DROT, PNEWDT,
     4 CELENT, DFGRD0, DFGRD1, NOEL, NPT, LAYER, KSPT, KSTEP, KINC)
C
      INCLUDE 'ABA_PARAM.INC'
C
      CHARACTER*80 CMNAME
      DIMENSION STRESS(NTENS), STATEV(NSTATV),
     1 DDSDDE(NTENS,NTENS), DDSDDT(NTENS), DRPLDE(NTENS),
     2 STRAN(NTENS), DSTRAN(NTENS), TIME(2), PREDEF(1), DPRED(1),
     3 PROPS(NPROPS), COORDS(3), DROT(3,3), DFGRD0(3,3), DFGRD1(3,3)


      user coding to define DDSDDE, STRESS, STATEV, SSE, SPD, SCD
      and, if necessary, RPL, DDSDDT, DRPLDE, DRPLDT, PNEWDT


      RETURN
      END

C-----------------------------------------------------------------C
```

Figure D-1 Subroutine interface of UMAT

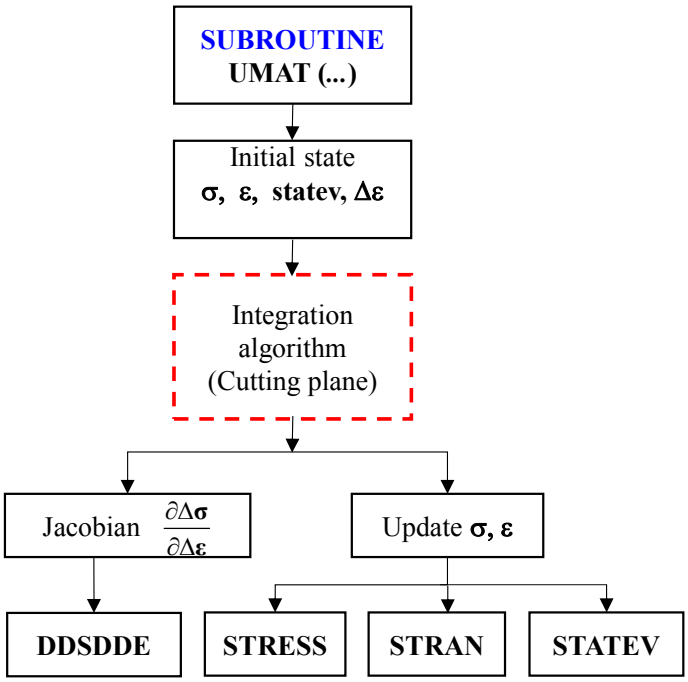

Figure D-2 Flowchart of UMAT

Verification of UMAT

Guaranteeing the correctness of an implementation of the UMAT program requires numerical validation: comparison of finite element numerical results from UMAT with those from the integration point program (IPP), whose constitutive relations are limited only in stress–strain level. It

is assumed the results from the stress–strain level (one Gauss point) are the correct and objective ones by default.

UMAT simulations of the typical laboratory tests with the SIMSAND model, including drained and undrained triaxial tests and drained and undrained biaxial tests for both loose and dense Toyoura sand (Jin et al., 2016; Wu et al., 2017), were compared with those from IPP. It is worth noting that all results are based on the assumption that specimens are sustained in a homogeneous state from beginning to end. For drained tests, there were two steps: the first step was isotropic compression, and the second one was the shear loading by the strain control of the top side of specimen, mean while keeping the confining pressure constant. Differently, for undrained tests, the specimen volume was kept constant by controlling the axial and lateral strain at the same time in the second shear loading step.

The comparisons of IPP and UMAT simulations of drained and undrained for both dense and loose Toyoura sand were shown from Figure D-3 to Figure D-6. In all the figures, each subfigure denotes different meaning: (a) axial strain versus deviatoric stress, (b) mean effective stress versus deviatoric stress, (c) axial strain versus void ratio, and (d) mean effective stress versus deviatoric stress. From the comparisons, it can be found that the simulated results produced by UMAT are absolutely consistent with those produced by IPP, thus amply verifying the correctness of the UMAT implementation. The successful implementation of UMAT in ABAQUS will lay a solid foundation for further implementation of a UEL.

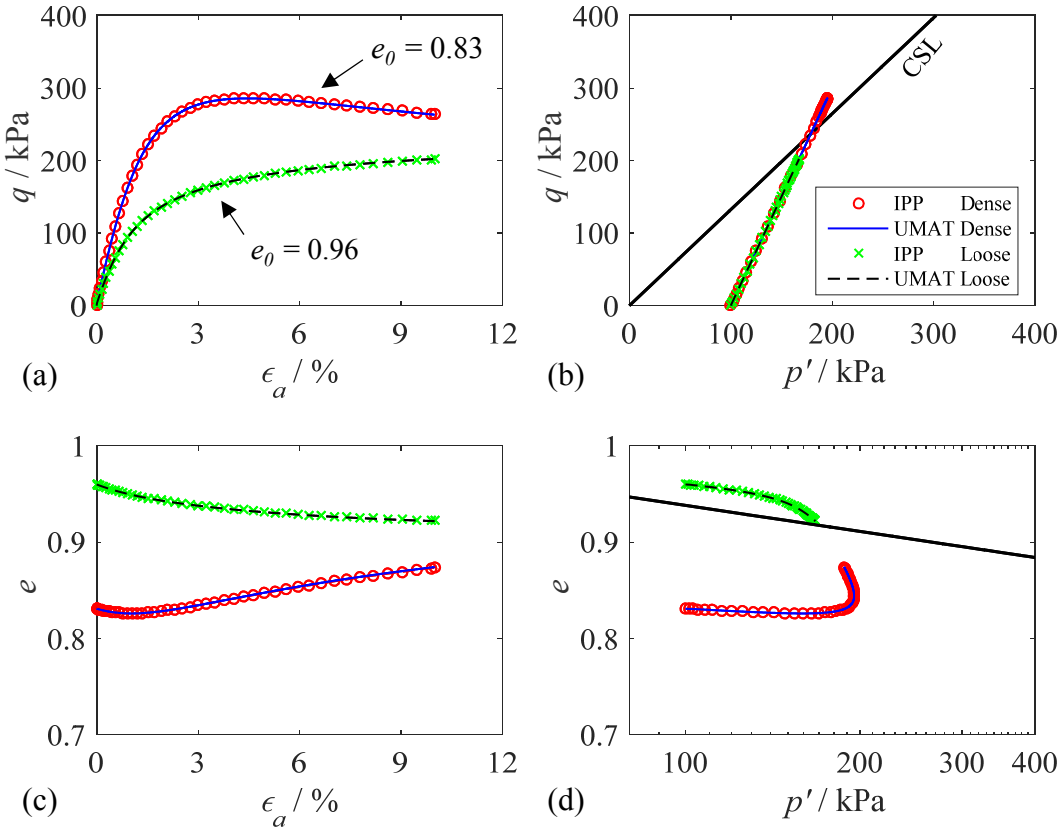

Figure D-3 Comparisons between IPP and UMAT in simulating triaxial drained test

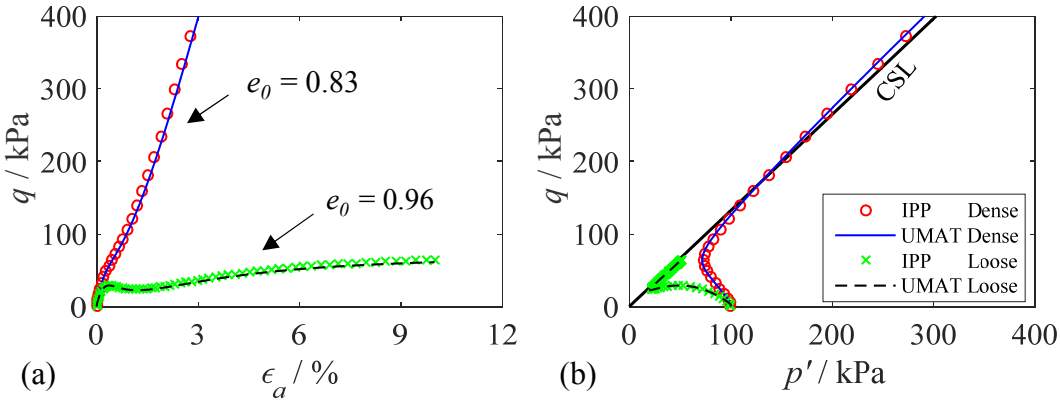

Figure D-4 Comparisons between IPP and UMAT in simulating triaxial undrained test

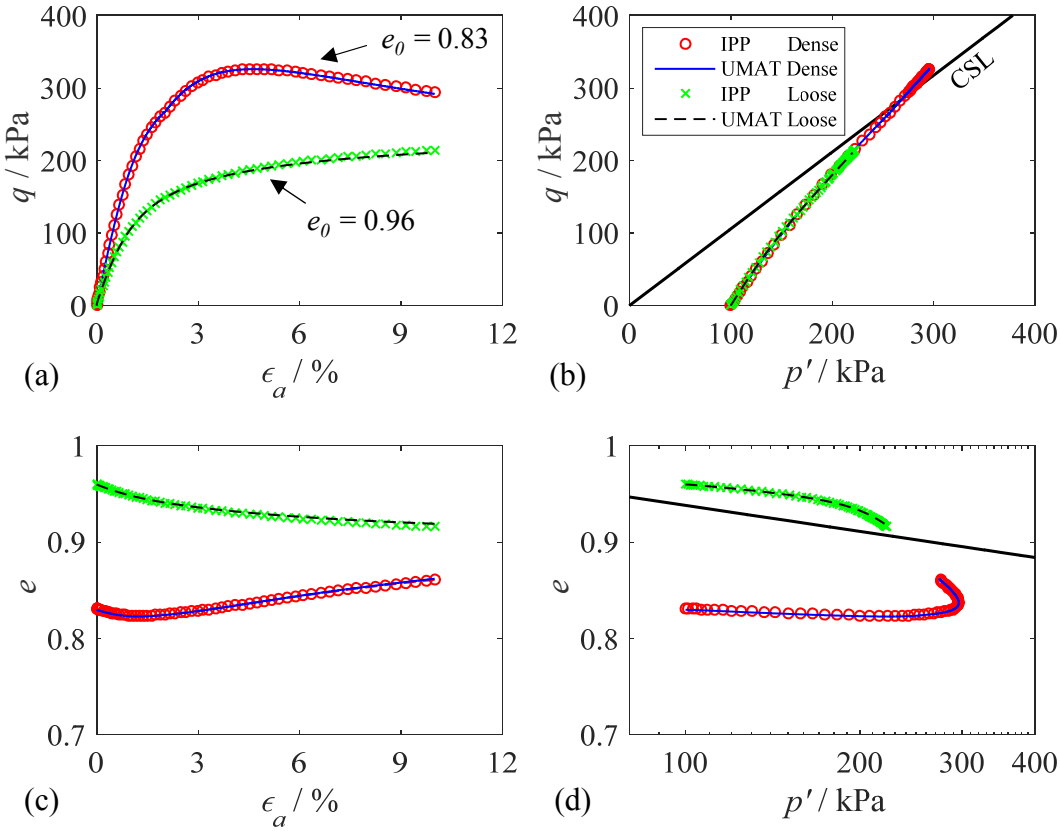

Figure D-5 Comparisons between IPP and UMAT in simulating biaxial drained test

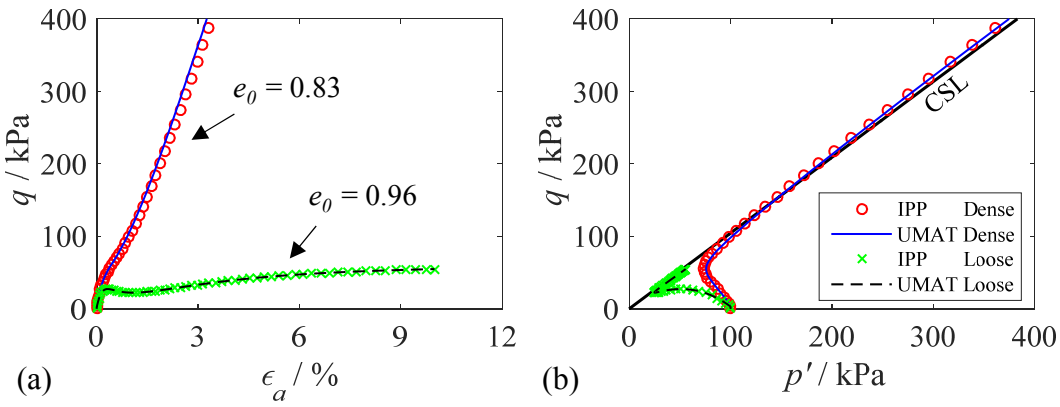

Figure D-6 Comparisons between IPP and UMAT in simulating biaxial undrained test

Appendix E: Calibration with Optimization Method

After the detailed description of all the parameters for the micropolar constitutive model in chapter 2, their estimation process has been illustrated in this section. From the description of these parameters in the previous section, we know that certain of them, such as l_c and υ, can be assumed at the beginning; the micropolar shear modulus G_c can be set to depend on the shear modulus G; the elasticity-related parameters K_0, ζ can be identified by fitting the isotropic compression test; and the critical state-related parameters ϕ_u, e_{ref}, and λ and plastic interlocking parameters k_p, A_d, n_p, and n_d can be identified by a series of triaxial tests. The genetic optimization method was used to search for these parameters, and the process for finding the optimized solutions is displayed hereafter. For more information about the optimization technique, please consult Jin et al. (2016).

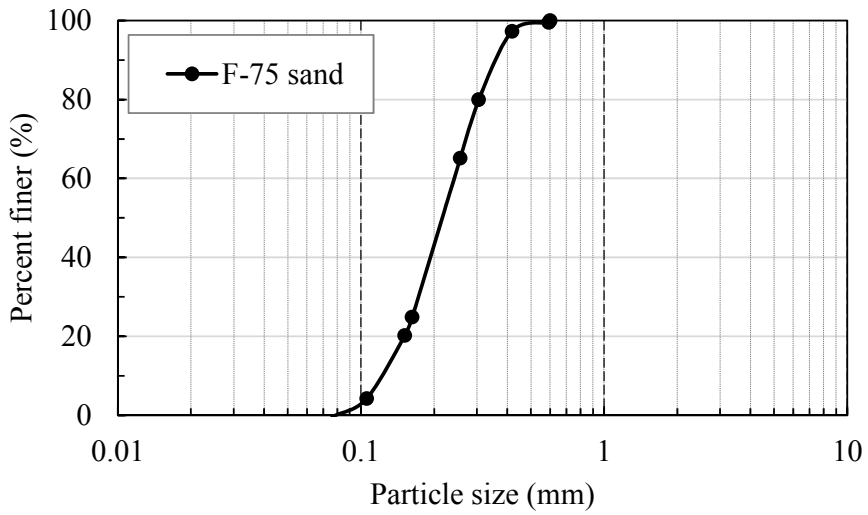

Figure E-1 Particle size distribution of F-75 sand

Laboratory tests on Ottawa sand was chosen to demonstrate the process of calibrating the parameters of the SIMSAND model. F-75 Ottawa sand, as seen in Figure E-1, is fine-grained, rounded, and uniform white sand obtained from Ottawa Industrial Silica (d_{50} = 0.22 mm, G_s = 2.65, e_{min} = 0.486, e_{max} = 0.805). The data from one isotropic compression test on Ottawa sand (Omar, 2010), and five different drained triaxial tests on medium-density Ottawa F-75 sand with three different values of confining pressure p'_0 and three different initial void ratios e_0 (Alshibli et al., 2003), were selected to be the fitting objects. It was assumed that the elasticity-related parameters are the same for Ottawa sand of different densities; thus these parameters, as obtained from the isotropic

compression test, were also suitable for triaxial tests. Nine independent parameters needed to be identified by experimental data, and another three parameters could be assumed in advance (l_c and υ) or set to depend on other parameters (G_c). Because many researchers (Roscoe, 1970; Vardoulakis et al., 1978; Mühlhaus and Vardoulakis, 1987; Desrues, 1990; Alshibli and Sture, 1999, 2000b; Yoshida et al., 1994; Tatsuoka et al.,1997; Tejchman et al., 1999; Viggiani et al., 2001; Alshibli et al., 2002; Alsaleh, 2004; Desrues and Viggiani, 2004) have found that the thickness of the shear band is linearly related to the mean grain size from biaxial tests, and because the thickness of the shear band has also been found to be linearly related to the internal length scale l_c in numerical simulations, in the present study, l_c, reflecting the microstructure, was regarded as the mean grain size by default, and there was no need to identify it by fitting the experimental curves. For a more specific value of l_c, it can also be decided by reproducing the thickness of the shear band (as in the biaxial test).

The adopted parameter estimation procedure is divided into three steps: First, the elasticity parameters can be determined based on the isotropic compression test; then, the critical state parameters can be inversely searched for, based on at least three drained triaxial tests; and finally, the interlocking related parameters can be defined based on at least one drained triaxial test. The optimization technique assists in finding a more accurate model parameter that is capable of adequately describing the sand behavior. The detailed procedures are presented in the following sections. Using the genetic optimization technique, the optimized parameters were found and are summarized below. Thereafter, the comparisons between the laboratory data and simulated results with the optimized parameters will be displayed.

Table E-1 Optimized values of constitutive parameters

Parameters	K_0	ζ	ϕ_u	e_{ref}	λ	k_p	A_d	n_p	n_d
Values	60	0.63	35.8	0.776	0.015	0.004	0.4	1	2

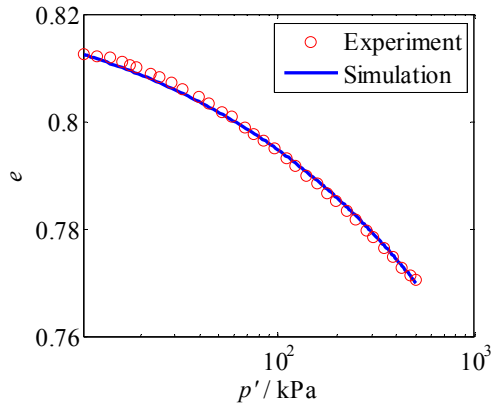

(a)

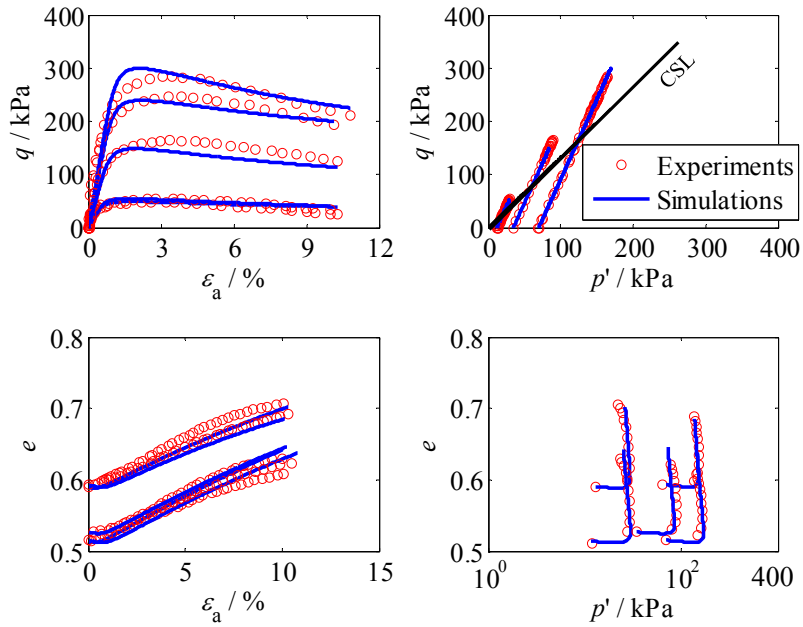

(b)

Figure E-2 Calibration of parameters with isotropic compression and triaxial drained tests of F-75 sand: (a) one isotropic compression test; (b) five different triaxial drained tests with different confining pressure

Based on these comparisons between the simulations and the experimental results, we can discern that the optimized parameters for the critical state–based model are able to adequately describe the sand behaviors in the isotropic compression and triaxial drained tests. By means of the calibration process, we can deeply understand the model and its parameters.

Micropolar theory is mainly used to reflect the micro-size effect and deal with the mesh dependency problems by regularizing the governing field's equations in finite element analysis. Thus, the influences on the final results caused by the internal length scale l_c were observed and detailed

discussed in the chapter 3 and chapter 5, when the program have been numerically implemented in the finite element code in the commercial software ABAQUS. It should be noted that only when the rotational degree of freedom is activated (inhomogeneous deformation) can l_c play a significant role in regularizing the field equations in finite element analysis.

References

Adeosun, A., 1968. Lateral forces and failure patterns in the cutting of sands. Research Project, University of Cambridge.

Adhikary, D., Dyskin, A., 1997. A Cosserat continuum model for layered materials. Computers and Geotechnics 20, 15-45.

Adhikary, D., Mühlhaus, H., Dyskin, A., 1999. Modelling the large deformations in stratified media—the Cosserat continuum approach. Mechanics of Cohesive - frictional Materials 4, 195-213.

Aifantis, E.C., 1984. On the microstructural origin of certain inelastic models. ASME J. Eng. Mater. Technol 106, 326-330.

Aifantis, E.C., 1987. The physics of plastic deformation. International journal of plasticity 3, 211-247.

Aifantis, E.C., 1999. Strain gradient interpretation of size effects. International Journal of Fracture 95, 299-314.

Al-Rub, R.K.A., Voyiadjis, G.Z., 2004. Analytical and experimental determination of the material intrinsic length scale of strain gradient plasticity theory from micro-and nano-indentation experiments. International journal of plasticity 20, 1139-1182.

Allersma, H., 1994a. Development of miniature equipment for a small geotechnical centrifuge. Transportation research record 1432, 99.

Allersma, H., 1994b. The University of Delft geotechnical centrifuge, Proc. Int. Conf.

Allersma, H., 2002. Application of a Small Beam Centrifuge in Offshore Foundation Engineering, The Twelfth International Offshore and Polar Engineering Conference. International Society of Offshore and Polar Engineers.

Alsaleh, M.I., 2004. Numerical modeling of strain localization in granular materials using Cosserat theory enhanced with microfabric properties. Jordan University of Science and Technology, Jordan, 1998.

Alsaleh, M.I., Voyiadjis, G.Z., Alshibli, K.A., 2006. Modelling strain localization in granular materials using micropolar theory: mathematical formulations. International Journal for Numerical and Analytical Methods in Geomechanics 30, 1501-1524.

Alshibli, K.A., Alsaleh, M.I., Voyiadjis, G.Z., 2006. Modelling strain localization in granular materials using micropolar theory: numerical implementation and verification. International Journal for Numerical and Analytical Methods in Geomechanics 30, 1525-1544.

Alshibli, K.A., Batiste, S.N., Sture, S., 2003. Strain localization in sand: plane strain versus triaxial compression. Journal of Geotechnical and Geoenvironmental Engineering 129, 483-494.

Alshibli, K.A., Batiste, S.N., Sture, S., Curreri, P.A., 2002. Experimental Observations of Localization Phenomena in Sands: Plane Strain Versus Triaxial Compression Conditions.

Alshibli, K.A., Sture, S., 1999. Sand shear band thickness measurements by digital imaging techniques. Journal of computing in civil engineering 13, 103-109.

Alshibli, K.A., Sture, S., 2000. Shear band formation in plane strain experiments of sand. Journal of Geotechnical and Geoenvironmental Engineering 126, 495-503.

Altenbach, H., Eremeyev, V.A., 2012. Generalized Continua-from the Theory to Engineering Applications. Springer.

Andrade, F.X.C., 2013. Non-local modelling of ductile damage: formulation and numerical issues.

Ari, N., Eringen, A.C., 1980. Nonlocal Stress Field at Griffith Crack. DTIC Document.

Arslan, H., Sture, S., 2008a. Evaluation of a physical length scale for granular materials. Computational Materials Science 42, 525-530.

Arslan, H., Sture, S., 2008b. Finite element analysis of localization and micro–macro structure relation in granular materials. Part II: Implementation and simulations. Acta Mechanica 197, 153-171.

Arthur, J., 1962. Strains and lateral force in sand. PhD Thesis, University of Cambridge.

Arthur, J., Dunstan, T., Al-Ani, Q., Assadi, A., 1977. Plastic deformation and failure in granular media. Geotechnique 27, 53-74.

Bésuelle, P., Rudnicki, J.W., 2004. Localization: shear bands and compaction bands. INTERNATIONAL GEOPHYSICS SERIES. 89, 219-322.

Bardet, J., Proubet, J., 1991. Numerical investigation of the structure of persistent shear bands in granular media. Geotechnique 41, 599-613.

Bauer, E., 1999. Analysis of shear band bifurcation with a hypoplastic model for a pressure and density sensitive granular material. Mechanics of materials 31, 597-609.

Bažant, Z.P., Belytschko, T.B., Chang, T.-P., 1984. Continuum theory for strain-softening. Journal of engineering mechanics 110, 1666-1692.

Bažant, Z.P., Lin, F.B., 1988. Non - local yield limit degradation. International Journal for Numerical Methods in Engineering 26, 1805-1823.

Belytschko, T., Liu, W.K., Moran, B., Elkhodary, K., 2013. Nonlinear finite elements for continua and structures. John wiley & sons.

Benvenuti, E., Tralli, A., 2003. Iterative LCP solvers for non - local loading–unloading conditions. International Journal for Numerical Methods in Engineering 58, 2343-2370.

Bobinski, J., Tejchman, J., 2004. Numerical simulations of localization of deformation in quasi-brittle materials within non-local softening plasticity. Computers and Concrete 1, 433-455.

Borino, G., Failla, B., 2000. 'Thermodynamically consistent plasticity models with local and nonlocal internal variables. Proc., European Congr. on Computational Methods in Applied Sciences and Engineering, ECCOMAS.

Borja, R.I., 2002. Bifurcation of elastoplastic solids to shear band mode at finite strain. Computer Methods in Applied Mechanics and Engineering 191, 5287-5314.

Bower, A.F., 2009. Applied mechanics of solids. CRC press.

Bransby, P.L., 1968. Stress and strain in sand caused by rotation of a model wall. University of Cambridge.

Brown, J., 1997. Characterization of MSC/NASTRAN & MSC/ABAQUS elements for turbine engine blade frequency analysis, Proc. MSC Aerospace Users' Conference. Citeseer.

Chambon, R., Caillerie, D., Matsuchima, T., 2001. Plastic continuum with microstructure, local second gradient theories for geomaterials: localization studies. International Journal of solids and Structures 38, 8503-8527.

Chang, C., Hicher, P.-Y., 2005. An elasto-plastic model for granular materials with microstructural consideration. International Journal of solids and Structures 42, 4258-4277.

Cheng, S., Ariaratnam, S., Dubey, R., 1971. Axisymmetric bifurcation in an elastic-plastic cylinder under axial load and lateral hydrostatic pressure. Quarterly of applied mathematics 29, 41-51.

Chikazawa, Y., Koshizuka, S., Oka, Y., 2001. A particle method for elastic and visco-plastic structures and fluid-structure interactions. Computational Mechanics 27, 97-106.

Coleman, B.D., Hodgdon, M.L., 1985. On shear bands in ductile materials. Archive for Rational Mechanics and analysis 90, 219-247.

Cosserat, E., Cosserat, F., Brocato, M., Chatzis, K., 1909. Théorie des corps déformables.

Cowin, S.C., 1969. Singular stress concentrations in plane Cosserat elasticity. Zeitschrift für Angewandte Mathematik und Physik (ZAMP) 20, 979-982.

Crisfield, S., 1982. Local instabilities in the non-linear analysis of reinforced concrete beams and slabs, Institution of Civil Engineers, Proceedings, Pt2.

Cundall, P.A., Strack, O.D., 1979. A discrete numerical model for granular assemblies. Geotechnique 29, 47-65.

Daouadji, A., AlGali, H., Darve, F., Zeghloul, A., 2009. Instability in granular materials: experimental evidence of diffuse mode of failure for loose sands. Journal of engineering mechanics 136, 575-588.

Daouadji, A., Jrad, M., Prunier, F., Sibille, L., Nicot, F., Laouafa, F., Darve, F., 2012. Divergence instability and diffuse failure in granular media. Procedia IUTAM 3, 115-140.

Darve, F., Chau, B., 1987. Constitutive instabilities in incrementally non-linear modelling. Constitutive laws for engineering materials, 301-310.

Darve, F., Flavigny, E., Meghachou, M., 1995. Constitutive modelling and instabilities of soil behaviour. Computers and Geotechnics 17, 203-224.

Darve, F., Laouafa, F., 2000. Instabilities in granular materials and application to landslides. Mechanics of Cohesive‐frictional Materials 5, 627-652.

Darve, F., Servant, G., Laouafa, F., Khoa, H., 2004. Failure in geomaterials: continuous and discrete analyses. Computer Methods in Applied Mechanics and Engineering 193, 3057-3085.

De Angelis, F., 2007. A variationally consistent formulation of nonlocal plasticity. International Journal for Multiscale Computational Engineering 5.

de Borst, R., 1986. Non-linear analysis of frictional materials. na.

de Borst, R., 1990. Simulation of localisation using Cosserat theory, Computer Aided Analysis and Design of Concrete Structures, Pineridge Press, Swansea United Kingdom, Proceedings of SCI-C 1990 Second International Conference held in Zell am See Austria, pp. 931-943.

de Borst, R., 1991. Simulation of strain localization: a reappraisal of the Cosserat continuum. Engineering computations 8, 317-332.

de Borst, R., 1993. A generalisation of J2-flow theory for polar continua. Computer Methods in Applied Mechanics and Engineering 103, 347-362.

de Borst, R., Mühlhaus, H., 1991. Continuum models for discontinuous media, Fracture processes in concrete, rock and ceramics. Proceedings of the international rilem/esis conference, noordwijk, the netherlands, June 19-21 2, 601-618. (1991).

de Borst, R., Mühlhaus, H., 1992. Gradient‐dependent plasticity: Formulation and algorithmic aspects. International Journal for Numerical Methods in Engineering 35, 521-539.

de Borst, R., Pamin, J., 1996. Some novel developments in finite element procedures for gradient-dependent plasticity. International Journal for Numerical Methods in Engineering 39, 2477-2505.

de Borst, R., Sluys, L.J., 1991. Localisation in a Cosserat continuum under static and dynamic loading conditions. Computer Methods in Applied Mechanics and Engineering 90, 805-827.

de Borst, R., Sluys, L.J., Muhlhaus, H., Pamin, J., 1993. Fundamental issues in finite element analyses of localization of deformation. Engineering computations 10, 99-121.

Desrues, J., 1984. La localisation de la déformation dans les milieux granulaires. Université Joseph-Fourier-Grenoble I.

Desrues, J., 1990. Shear band initiation in granular materials: Experimentation and theory. Geomaterials Constitutive Equations and Modelling, 283-310.

Desrues, J., Bésuelle, P., Lewis, H., 2007. Strain localization in geomaterials. Geological Society, London, Special Publications 289, 47-73.

Desrues, J., Chambon, R., Mokni, M., Mazerolle, F., 1996. Void ratio evolution inside shear bands in triaxial sand specimens studied by computed tomography. Geotechnique 46, 529-546.

Desrues, J., Nguyen, T., Combe, G., Caillerie, D., 2015. FEM× DEM multi-scale analysis of boundary value problems involving strain localization, Bifurcation and degradation of geomaterials in the new millennium. Springer, pp. 259-265.

Desrues, J., Viggiani, G., 2004. Strain localization in sand: an overview of the experimental results obtained in Grenoble using stereophotogrammetry. International Journal for Numerical and Analytical Methods in Geomechanics 28, 279-321.

Desrues, J., Viggiani, G., Besuelle, P., 2010. Advances in X-ray Tomography for Geomaterials. John Wiley & Sons.

Dias da Silva, V., 2004. A simple model for viscous regularization of elasto‐plastic constitutive laws with softening. International Journal for Numerical Methods in Biomedical Engineering 20, 547-568.

Dietsche, A., Willam, K., 1997. Boundary effects in elasto-plastic Cosserat continua. International Journal of solids and Structures 34, 877-893.

Dorgan, R.J., Voyiadjis, G.Z., 2003. Nonlocal dislocation based plasticity incorporating gradients of hardening. Mechanics of materials 35, 721-732.

Drucker, D.C., 1957. A definition of stable inelastic material. BROWN UNIV PROVIDENCE RI.

Duvaut, G., Lions, J.L., 1972. Les inéquations en mécanique et en physique.

Ehlers, W., Diebels, S., Ellsiepen, P., Volk, W., 1997. 'Localization Phenomena in Liquid-Saturated Soils, Proc. NAFEMS World Congress 1997, pp. 287-298.

Ehlers, W., Volk, W., 1997a. On shear band localization phenomena induced by elasto-plastic consolidation of fluidsaturated soils. Computational Plasticity-Fundamentals and Applications 2, 1657-1664.

Ehlers, W., Volk, W., 1997b. On shear band localization phenomena of liquid‐saturated granular elastoplastic porous solid materials accounting for fluid viscosity and micropolar solid rotations. Mechanics of Cohesive‐frictional Materials 2, 301-320.

Ehlers, W., Volk, W., 1998. On theoretical and numerical methods in the theory of porous media based on polar and non-polar elasto-plastic solid materials. International Journal of solids and Structures 35, 4597-4617.

Engelen, R.A., Geers, M.G., Baaijens, F.P., 2003. Nonlocal implicit gradient-enhanced elasto-plasticity for the modelling of softening behaviour. International journal of plasticity 19, 403-433.

Eringen, A.C., 1966. A unified theory of thermomechanical materials. International Journal of Engineering Science 4, 179-202.

Eringen, A.C., 1972a. Linear theory of nonlocal elasticity and dispersion of plane waves. International Journal of Engineering Science 10, 425-435.

Eringen, A.C., 1972b. Nonlocal polar elastic continua. International Journal of Engineering Science 10, 1-16.

Eringen, A.C., 1976. Nonlocal polar field theories. Continuum physics 4, 205-264.

Eringen, A.C., 1981. On nonlocal plasticity. International Journal of Engineering Science 19, 1461-1474.

Eringen, A.C., 1983. Theories of nonlocal plasticity. International Journal of Engineering Science 21, 741-751.

Eringen, A.C., 1999. Theory of micropolar elasticity, Microcontinuum field theories. Springer, pp. 101-248.

Eringen, A.C., Edelen, D., 1972. On nonlocal elasticity. International Journal of Engineering Science 10, 233-248.

Etse, G., Willam, K., 1994. Fracture energy formulation for inelastic behavior of plain concrete. Journal of engineering mechanics 120, 1983-2011.

Finno, R.J., Harris, W., Mooney, M.A., Viggiani, G., 1997. Shear bands in plane strain compression of loose sand. Geotechnique 47, 149-165.

Forest, S., Boubidi, P., Sievert, R., 2001. Strain localization patterns at a crack tip in generalized single crystal plasticity. Scripta Materialia 44, 953-958.

Fuschi, P., Polizzotto, C., 1999. A thermodynamic approach to nonlocal plasticity and related variational principles.

Gajo, A., Wood, M., 1999. Severn–Trent sand: a kinematic-hardening constitutive model: the q–p formulation. Geotechnique 49, 595-614.

Gudehus, G., Nübel, K., 2004. Evolution of shear bands in sand. Geotechnique 54, 187-201.

Guo, N., Zhao, J., 2014. A coupled FEM/DEM approach for hierarchical multiscale modelling of granular media. International Journal for Numerical Methods in Engineering 99, 789-818.

Guo, N., Zhao, J., 2015. A multiscale investigation of strain localization in cohesionless sand, Bifurcation and Degradation of Geomaterials in the New Millennium. Springer, pp. 121-126.

Guo, N., Zhao, J., 2016. 3D multiscale modeling of strain localization in granular media. Computers and Geotechnics 80, 360-372.

Hadda, N., Nicot, F., Bourrier, F., Sibille, L., Radjai, F., Darve, F., 2013. Micromechanical analysis of second order work in granular media. Granular matter 15, 221-235.

Hadda, N., Sibille, L., Nicot, F., Wan, R., Darve, F., 2016. Failure in granular media from an energy viewpoint. Granular matter 18, 1-17.

Han, C., Drescher, A., 1993. Shear bands in biaxial tests on dry coarse sand. Soils and Foundations 33, 118-132.

Hardin, B.O., 1985. Crushing of soil particles. Journal of Geotechnical Engineering 111, 1177-1192.

Hicher, P., Wahyudi, H., Tessier, D., 1994. Microstructural analysis of strain localisation in clay. Computers and Geotechnics 16, 205-222.

Hill, R., 1958. A general theory of uniqueness and stability in elastic-plastic solids. Journal of the Mechanics and Physics of Solids 6, 236-249.

Hill, R., 1961. Bifurcation and uniqueness in non-linear mechanics of continua. Problems of Continuum Mechanics, 155-164.

Hossain, Z., Indraratna, B., Darve, F., Thakur, P., 2007. DEM analysis of angular ballast breakage under cyclic loading. Geomechanics and Geoengineering: An International Journal 2, 175-181.

Huang, M., Chen, Z., Lu, X., Gu, X., 2017. Theoretical Prediction of Strain Localization in Anisotropic Sand by Non-coaxial Elasto-Plasticity, in: Papamichos, E., Papanastasiou, P., Pasternak, E., Dyskin, A. (Eds.), Bifurcation and Degradation of Geomaterials with Engineering Applications: Proceedings of the 11th International Workshop on Bifurcation and Degradation in Geomaterials dedicated to Hans Muhlhaus, Limassol, Cyprus, 21-25 May 2017. Springer International Publishing, Cham, pp. 89-95.

Huang, M., Lu, X., Qian, J., Wang, W., 2009. Prediction of the onset of strain localization in non-coaxial plasticity, Proceedings of the 17th International Conference on Soil Mechanics and Geotechnical Engineering, Alexandria, Egypt, IOS, pp. 574-577.

Huang, W., Bauer, E., 2003. Numerical investigations of shear localization in a micro‐polar hypoplastic material. International Journal for Numerical and Analytical Methods in Geomechanics 27, 325-352.

Huang, W., Hjiaj, M., Sloan, S.W., 2005. Bifurcation analysis for shear localization in non-polar and micro-polar hypoplastic continua. Journal of engineering mathematics 52, 167-184.

Huang, W., Nübel, K., Bauer, E., 2002. Polar extension of a hypoplastic model for granular materials with shear localization. Mechanics of materials 34, 563-576.

Huang, W., Sloan, S.W., Sheng, D., 2014. Analysis of plane Couette shear test of granular media in a Cosserat continuum approach. Mechanics of materials 69, 106-115.

Huang, W., Xu, K., 2015. Characteristic lengths in Cosserat continuum modeling of granular materials. Engineering computations 32, 973-984.

Iwashita, K., Oda, M., 1999. Mechanics of granular materials: an introduction. CRC Press.

Jackiewicz, J., 2000. Numerical aspects of non-local modeling of the damage evolution in elastic–plastic materials. Computational Materials Science 19, 235-251.

Jackiewicz, J., Kuna, M., 2003. Non-local regularization for FE simulation of damage in ductile materials. Computational Materials Science 28, 684-695.

James, R., 1965. Stress and strain fields in sand. University of Cambridge.

Janbu, N., 1959. Stability analysis of slopes with dimensionless parameters. Harvard University, Division of Engineering and Applied Physics.

Jefferies, M., 1993. Nor-Sand: a simple critical state model for sand. Geotechnique 43, 91-103.

Jiang, M.-J., Liu, J.-D., Sun, Y.-G., Yin, Z.-Y., 2013a. Investigation into macroscopic and microscopic behaviors of bonded sands using distinct element method. Soils and Foundations 53, 804-819.

Jiang, M.-J., Murakami, A., 2012. Distinct element method analyses of idealized bonded-granulate cut slope. Granular matter 14, 393.

Jiang, M.-J., Yan, H., Zhu, H.-H., Utili, S., 2011. Modeling shear behavior and strain localization in cemented sands by two-dimensional distinct element method analyses. Computers and Geotechnics 38, 14-29.

Jiang, M.-J., Yu, H.S., Harris, D., 2006. Discrete element modelling of deep penetration in granular soils. International Journal for Numerical and Analytical Methods in Geomechanics 30, 335-361.

Jiang, M.-J., Zhang, W.-C., 2015. DEM analyses of shear band in granular materials. Engineering computations 32, 985-1005.

Jiang, M.-J., Zhang, W.-C., Sun, Y.-G., Utili, S., 2013b. An investigation on loose cemented granular materials via DEM analyses. Granular matter 15, 65-84.

Jiang, M.-J., Zhu, H.-H., Li, X.-M., 2010. Strain localization analyses of idealized sands in biaxial tests by distinct element method. Frontiers of Architecture and Civil Engineering in China 4, 208-222.

Jin, Y.-F., Yin, Z.-Y., Shen, S.-L., Hicher, P.-Y., 2016. Investigation into MOGA for identifying parameters of a critical-state-based sand model and parameters correlation by factor analysis. Acta Geotechnica 11, 1131-1145.

Jirásek, M., 1998. Nonlocal models for damage and fracture: comparison of approaches. International Journal of solids and Structures 35, 4133-4145.

Jirásek, M., Rolshoven, S., 2003. Comparison of integral-type nonlocal plasticity models for strain-softening materials. International Journal of Engineering Science 41, 1553-1602.

Khoei, A., Yadegari, S., Anahid, M., 2006. Three-dimensional modeling of strain localization in Cosserat continuum theory.

Khoei, A., Yadegari, S., Biabanaki, S., 2010. 3D finite element modeling of shear band localization via the micro-polar Cosserat continuum theory. Computational Materials Science 49, 720-733.

Koiter, W., 1969. Couple-stresses in the theory of elasticity, I & II.

Kondo, E., 2010. Characterizing the evolving internal length scale in strain localization for cosserat media. Ph. D. Thesis) Delft University of Technology, Delft.

Kröner, E., 1967. Elasticity theory of materials with long range cohesive forces. International Journal of solids and Structures 3, 731-742.

Kröner, E., 2012. Continuum mechanics and range of atomic cohesion forces, ICF1, Japan 1965.

Kuhn, M.R., 1999. Structured deformation in granular materials. Mechanics of materials 31, 407-429.

Kulesh, M., Matveenko, V., Shardakov, I., 2006. Propagation of surface elastic waves in the Cosserat medium. Acoustical Physics 52, 186-193.

Kunin, I., 1966. Theory of elasticity with spatial dispersion one-dimensional complex structure. Journal of Applied Mathematics and Mechanics 30, 1025-1034.

Labuz, J.F., Zang, A., 2012. Mohr–Coulomb failure criterion, The ISRM Suggested Methods for Rock Characterization, Testing and Monitoring: 2007-2014. Springer, pp. 227-231.

Lade, P., Yamamuro, J.A., Skyers, B.D., 1996. Effects of shear band formation in triaxial extension tests.

Lakes, R., 1995. Experimental methods for study of Cosserat elastic solids and other generalized elastic continua. Continuum models for materials with microstructure, 1-25.

Lee, K.L., 1970. Comparison of plane strain and triaxial tests on sand. Journal of the Soil Mechanics and Foundations Division 96, 901-923.

Leśniewska, D., 2000. Analysis of shear band pattern formation in soil. IBW PAN.

Li, X.-K., Tang, H.-X., 2005. A consistent return mapping algorithm for pressure-dependent elastoplastic Cosserat continua and modelling of strain localisation. Computers & Structures 83, 1-10.

LI, X.-K., ZHANG, J.-B., ZHANG, H.-W., 2002. INSTABILITY AND DISPERSIVITY OF WAVE PROPAGATION IN INELASTIC SATURATED/UNSATURATED POROUS MEDIA. Appl. Math. Mech. -Engl. Ed. 23, 35-52.

Li, X.-S., Wang, Y., 1998. Linear representation of steady-state line for sand. Journal of Geotechnical and Geoenvironmental Engineering 124, 1215-1217.

Lin, J., Wu, W., 2016. A comparative study between DEM and micropolar hypoplasticity. Powder Technology 293, 121-129.

Liu, X., Scarpas, A., Kasbergen, C., 2007. A micropolar formulation of the Desai hierarchical model for elastoplastic porous media. International Journal of solids and Structures 44, 2695-2714.

Liu, X., Scarpas, A., Kasbergen, C., Kondo, E., 2011. Characterizing the Influence of the Evolution of Length scale on the Strain Localization in Cosserat Media, Instrumentation, Testing, and Modeling of Soil and Rock Behavior, pp. 62-69.

Lord, J., 1969. Stresses and strains in an earth pressure problem. University of Cambridge.

Lucia, J., 1966. Passive earth pressure and failure in sand. Research project report, Mechanical Sciences Tripos, Part IIA, University of Cambridge.

Lyapunov, A., 1907. Problème général de la stabilité de mouvement. Annal.Facult.Sci.Toulous 9, 203-274.

Mühlhaus, H., 1989. Application of Cosserat theory in numerical solutions of limit load problems. Archive of Applied Mechanics 59, 124-137.

Mühlhaus, H., Alfantis, E., 1991. A variational principle for gradient plasticity. International Journal of solids and Structures 28, 845-857.

Mühlhaus, H., Vardoulakis, I., 1987. The thickness of shear bands in granular materials. Geotechnique 37, 271-283.

Maier, G., Hueckel, T., 1979. Nonassociated and coupled flow rules of elastoplasticity for rock-like materials, International Journal of Rock Mechanics and Mining Sciences & Geomechanics Abstracts. Elsevier, pp. 77-92.

Manzari, M.T., 2004. Application of micropolar plasticity to post failure analysis in geomechanics. International Journal for Numerical and Analytical Methods in Geomechanics 28, 1011-1032.

Manzari, M.T., Dafalias, Y., 2005. A critical state two-surface micropolar plasticity model for sands, Proceedings of 11th International Conference on Fracture, Torino, Italy.

Manzari, M.T., Yonten, K., 2011. Analysis of post-failure response of sands using a critical state micropolar plasticity model. Interaction and multiscale mechanics 4, 187-206.

Marachi, N.D., Duncan, J., Chan, C., Seed, H., 1981. Plane-strain testing of sand, Laboratory shear strength of soil. ASTM International.

May, J., 1967. A pilot project on the cutting of soils. Res. Rep. Soil Mech. Lab.

Michalowski, R.L., 1995. Stability of slopes: limit analysis approach. Reviews in Engineering Geology 10, 51-62.

Milligan, G., 1974. The Behaviour of Rigid and Flexible Retaining Walls in Sand. University of Cambridge.

Mindlin, R.D., 1963. Influence of couple-stresses on stress concentrations. Experimental mechanics 3, 1-7.

Mindlin, R.D., 1964. Micro-structure in linear elasticity. Archive for Rational Mechanics and analysis 16, 51-78.

Mindlin, R.D., Eshel, N., 1968. On first strain-gradient theories in linear elasticity. International Journal of solids and Structures 4, 109-124.

Mindlin, R.D., Tiersten, H., 1962. Effects of couple-stresses in linear elasticity. Archive for Rational Mechanics and analysis 11, 415-448.

Mokni, M., Desrues, J., 1999. Strain localization measurements in undrained plane-strain biaxial tests on Hostun RF sand. Mechanics of Cohesive‐frictional Materials 4, 419-441.

Nübel, K., Huang, W., 2004. A study of localized deformation pattern in granular media. Computer Methods in Applied Mechanics and Engineering 193, 2719-2743.

Needleman, A., 1988. Material rate dependence and mesh sensitivity in localization problems. Computer Methods in Applied Mechanics and Engineering 67, 69-85.

Needleman, A., Ortiz, M., 1991. Effect of boundaries and interfaces on shear-band localization. International Journal of solids and Structures 28, 859-877.

Needleman, A., Tvergaard, V., 1998. Dynamic crack growth in a nonlocal progressively cavitating solid. European Journal of Mechanics-A/Solids 17, 421-438.

Nicot, F., Challamel, N., Lerbet, J., Prunier, F., Darve, F., 2012a. Some insights into structure instability and the second-order work criterion. International Journal of solids and Structures 49, 132-142.

Nicot, F., Daouadji, A., Laouafa, F., Darve, F., 2011. Second-order work, kinetic energy and diffuse failure in granular materials. Granular matter 13, 19-28.

Nicot, F., Darve, F., 2007. A micro-mechanical investigation of bifurcation in granular materials. International Journal of solids and Structures 44, 6630-6652.

Nicot, F., Darve, F., 2011. Diffuse and localized failure modes: two competing mechanisms. International Journal for Numerical and Analytical Methods in Geomechanics 35, 586-601.

Nicot, F., Darve, F., 2015. Describing failure in geomaterials using second-order work approach. Water Science and Engineering 8, 89-95.

Nicot, F., Darve, F., Dat Vu Khoa, H., 2007. Bifurcation and second‐order work in geomaterials. International Journal for Numerical and Analytical Methods in Geomechanics 31, 1007-1032.

Nicot, F., Hadda, N., Bourrier, F., Sibille, L., Wan, R., Darve, F., 2012b. Inertia effects as a possible missing link between micro and macro second-order work in granular media. International Journal of solids and Structures 49, 1252-1258.

Nicot, F., Hadda, N., Darve, F., 2013. Second‐order work analysis for granular materials using a multiscale approach. International Journal for Numerical and Analytical Methods in Geomechanics 37, 2987-3007.

Nicot, F., Lerbet, J., Darve, F., 2017. Second-order work criterion: from material point to boundary value problems. Acta Mechanica, 1-16.

Nicot, F., Sibille, L., Darve, F., 2009. Bifurcation in granular materials: An attempt for a unified framework. International Journal of solids and Structures 46, 3938-3947.

Nilsson, C., 1997. Nonlocal strain softening bar revisited. International Journal of solids and Structures 34, 4399-4419.

Nilsson, C., 1998. On nonlocal rate-independent plasticity. International journal of plasticity 14, 551-575.

Nitka, M., Bilbie, B., Combe, G., Dascalu, C., Desrues, J., 2009a. A micro–macro (DEM–FEM) model of the behavior of granular solids, 1st International Symposium on Computational Geomechanics (ComGeo I), Juan-les-Pins, France, pp. 38-48.

Nitka, M., Bilbie, G., Combe, G., Dascalu, C., Desrues, J., 2009b. A DEM—FEM two scale approach of the behaviour of granular materials, AIP Conference Proceedings. AIP, pp. 443-446.

Nitka, M., Combe, G., Dascalu, C., Desrues, J., 2011. Two-scale modeling of granular materials: a DEM-FEM approach. Granular matter 13, 277-281.

Nova, R., 1994. Controllability of the incremental response of soil specimens subjected to arbitrary loading programmes. Journal of the Mechanical behavior of Materials 5, 193-202.

Nova, R., 2003. The failure concept in soil mechanics revisited. Swets and Zeitlinger, Lisse, Netherlands.

O'Sullivan, C., 2011. Particulate discrete element modelling: a geomechanics perspective. Taylor & Francis.

Oda, M., Iwashita, K., Kazama, H., 1997. Micro-structure developed in shear bands of dense granular soils and its computer simulation—mechanism of dilatancy and failure—, IUTAM Symposium on Mechanics of Granular and Porous Materials. Springer, pp. 353-364.

Oda, M., Kazama, H., 1998. Microstructure of shear bands and its relation to the mechanisms of dilatancy and failure of dense granular soils. Geotechnique 48, 465-481.

Oda, M., Konishi, J., Nemat-Nasser, S., 1982. Experimental micromechanical evaluation of strength of granular materials: effects of particle rolling. Mechanics of materials 1, 269-283.

Oka, F., Higo, Y., Kimoto, S., 2002. Effect of dilatancy on the strain localization of water-saturated elasto-viscoplastic soil. International Journal of solids and Structures 39, 3625-3647.

Oka, F., Yashima, A., Sawada, K., Aifantis, E., 2000. Instability of gradient-dependent elastoviscoplastic model for clay and strain localization analysis. Computer Methods in Applied Mechanics and Engineering 183, 67-86.

Omar, T., 2010. Specimen size effect on shear behavior of loose sand in triaxial testing. The University of Western Ontario.

Ortiz, M., Simo, J., 1986. An analysis of a new class of integration algorithms for elastoplastic constitutive relations. International Journal for Numerical Methods in Engineering 23, 353-366.

Pamin, J., 1994. Gradient-dependent plasticity in numerical simulation of localization phenomena.

Papamichos, E., Vardoulakis, I., 1995. Shear band formation in sand according to non-coaxial plasticity model. Geotechnique 45, 649-661.

Papanastasiou, P.C., Vardoulakis, I., 1989. Bifurcation analysis of deep boreholes: II. Scale effect. International Journal for Numerical and Analytical Methods in Geomechanics 13, 183-198.

Pasternak, E., Mühlhaus, H., 2001. Cosserat continuum modelling of granulate materials. Computational Mechanics–new frontiers for new Millennium, 1189-1194.

Perrin, G., Devaux, J., 1994. Bifurcation effects in ductile metals with nonlocal damage.
Perzyna, P., 1963. The constitutive equations for rate sensitive plastic materials. Quarterly of applied mathematics 20, 321-332.
Perzyna, P., 1966. Fundamental problems in viscoplasticity. Advances in applied mechanics 9, 243-377.
Pijaudier-Cabot, G., Bažant, Z.P., 1987. Nonlocal damage theory. Journal of engineering mechanics 113, 1512-1533.
Pradhan, T., 1997. Characteristics of shear band in plane strain compression test of sands. Deformation and Progressive Failure in Geomechanics, 241-246.
QIAN, J., HUANG, M., YANG, J., 2006. Effect of non-coaxial plasticity on onset strain localization in soils under 3D stress condition. Chinese J. Geot. Eng. 28, 510-515.
Randow, C., Gray, G., Costanzo, F., 2006. A directed continuum model of micro-and nano-scale thin films. International Journal of solids and Structures 43, 1253-1275.
Riahi, A., Curran, J., 2010. Comparison of the Cosserat Continuum approach with finite element interface models in a simulation of layered materials. Scientia Iranica. Transaction A, Civil Engineering 17, 39.
Riahi, A., Curran, J., Bidhendi, H., 2009. Buckling analysis of 3D layered structures using a Cosserat continuum approach. Computers and Geotechnics 36, 1101-1112.
Riahi, A., Curran, J.H., 2009. Full 3D finite element Cosserat formulation with application in layered structures. Applied mathematical modelling 33, 3450-3464.
Richart, F.E., Hall, J.R., Woods, R.D., 1970. Vibrations of soils and foundations.
Ristinmaa, M., Vecchi, M., 1996. Use of couple-stress theory in elasto-plasticity. Computer Methods in Applied Mechanics and Engineering 136, 205-224.
Rolshoven, S., 2003. Nonlocal plasticity models for localized failure. Institut de structures section de génie civil pour l'obtention du grade de docteur ès sciences par dipling. Physikalische Ingenieurwissenschaft, TU Berlin.
Roscoe, K.H., 1970. The Influence of Strains in Soil Mechanics. Geotechnique 20, 129-170.
Rots, J.G., 1988. Computational modeling of concrete fracture.
Rowe, P.W., 1962. The stress-dilatancy relation for static equilibrium of an assembly of particles in contact, Proceedings of the royal society of London a: mathematical, physical and engineering sciences. The Royal Society, pp. 500-527.
Rudnicki, J.W., Rice, J., 1975. Conditions for the localization of deformation in pressure-sensitive dilatant materials. Journal of the Mechanics and Physics of Solids 23, 371-394.
Saada, A., Liang, L., Figueroa, J., Cope, C., 1999. Bifurcation and shear band propagation in sands. Geotechnique 49, 367-385.
Scarpelli, G., Wood, D.M., 1982. Experimental observations of shear patterns in direct shear tests. NASA STI/Recon Technical Report N 83.
Schofield, A., Wroth, P., 1968. Critical state soil mechanics. McGraw-Hill London.
Schwarzbach, C., Börner, R.-U., Spitzer, K., 2011. Three-dimensional adaptive higher order finite element simulation for geo-electromagnetics—a marine CSEM example. Geophysical Journal International 187, 63-74.
Shahin, G., Desrues, J., Pont, S.D., Combe, G., Argilaga, A., 2016. A study of the influence of REV variability in double‐scale FEM× DEM analysis. International Journal for Numerical Methods in Engineering 107, 882-900.

Shao, L.-t., Sun, Y.-z., Wang, Z.-p., LIU, Y.-l., 2006. Application of digital image processing technique to triaxial test in soil mechanics. ROCK AND SOIL MECHANICS-WUHAN-27, 29.

Sharbati, E., Naghdabadi, R., 2006. Computational aspects of the Cosserat finite element analysis of localization phenomena. Computational Materials Science 38, 303-315.

Shawki, T., Clifton, R., 1989. Shear band formation in thermal viscoplastic materials. Mechanics of materials 8, 13-43.

Simo, J., Kennedy, J., Taylor, R., 1989. Complementary mixed finite element formulations for elastoplasticity. Computer Methods in Applied Mechanics and Engineering 74, 177-206.

Sluys, L.J., 1992. Wave propagation, localisation and dispersion in softening solids.

Sluys, L.J., de Borst, R., 1991. Rate-dependent modelling of concrete fracture. Heron 36, 3-15.

Sluys, L.J., de Borst, R., 1992. Wave propagation and localization in a rate-dependent cracked medium—model formulation and one-dimensional examples. International Journal of solids and Structures 29, 2945-2958.

Smith, I.A.A., 1972. Stress and stain in a sand mass adjacent to a model wall. University of Cambridge.

Sternberg, E., Muki, R., 1967. The effect of couple-stresses on the stress concentration around a crack. International Journal of solids and Structures 3, 69-95.

Strömberg, L., Ristinmaa, M., 1996. FE-formulation of a nonlocal plasticity theory. Computer Methods in Applied Mechanics and Engineering 136, 127-144.

Sulem, J., Vardoulakis, I., 1990. Bifurcation analysis of the triaxial test on rock specimens. A theoretical model for shape and size effect. Acta Mechanica 83, 195-212.

Taiebat, M., Dafalias, Y.F., 2008. SANISAND: Simple anisotropic sand plasticity model. International Journal for Numerical and Analytical Methods in Geomechanics 32, 915-948.

Takemura, T., Oda, M., Takahashi, M., 2004. Microstructure observation in deformed geomaterials using microfocus X-ray computed tomography. X-ray CT for Geomaterials, 299-304.

Tang, H.-X., Hu, Z.-L., 2017. Application of the Cosserat continua to numerical studies on the properties of the materials. Mechanics of Advanced Materials and Structures 24, 797-808.

Tang, H.-X., Hu, Z.-L., Li, X.-K., 2013. Three-dimensional pressure-dependent elastoplastic Cosserat continuum model and finite element simulation of strain localization. International Journal of Applied Mechanics 5, 1350030.

Tang, H.-X., LI, X.-K., 2007. The Biot-Cosserat continuum model for coupled hydro-dynamic analysis in saturated porous media and finite element simulation of strain localization. Engineering Mechanics 9, 005.

Tang, H., Li, X., 2008. Numerical analysis for the effects of constitutive parameters in Cosserat continuum model on the simulation results of the strain localization. Chinese Journal of Computational Mechanics 25, 676-681.

Tejchman, J., 2002. Patterns of shear zones in granular bodies within a polar hypoplastic continuum. Acta Mechanica 155, 71-94.

Tejchman, J., 2008. Shear localization in granular bodies with micro-polar hypoplasticity. Springer Science & Business Media.

Tejchman, J., 2010. Effect of grain crushing on shear localization in granular bodies within micro-polar hypoplasticity. Using DEM. Arch. Hydro-Eng. Environ. Mech 57, 3-30.

Tejchman, J., Bauer, E., 1996. Numerical simulation of shear band formation with a polar hypoplastic constitutive model. Computers and Geotechnics 19, 221-244.
Tejchman, J., Gudehus, G., 2001. Shearing of a narrow granular layer with polar quantities. International Journal for Numerical and Analytical Methods in Geomechanics 25, 1-28.
Tejchman, J., Herle, I., Wehr, J., 1999. FE - studies on the influence of initial void ratio, pressure level and mean grain diameter on shear localization. International Journal for Numerical and Analytical Methods in Geomechanics 23, 2045-2074.
Tejchman, J., Niemunis, A., 2006. FE-studies on shear localization in an anistropic micro-polar hypoplastic granular material. Granular matter 8, 205.
Tejchman, J., Wu, W., 1993. Numerical study on patterning of shear bands in a Cosserat continuum. Acta Mechanica 99, 61-74.
Tejchman, J., Wu, W., 1995. Experimental and numerical study of sand–steel interfaces. International Journal for Numerical and Analytical Methods in Geomechanics 19, 513-536.
Tejchman, J., Wu, W., 1996. Numerical simulation of shear band formation with a hypoplastic constitutive model. Computers and Geotechnics 18, 71-84.
Vardoulakis, I., 1979. Bifurcation analysis of the triaxial test on sand samples. Acta Mechanica 32, 35-54.
Vardoulakis, I., 1980. Shear band inclination and shear modulus of sand in biaxial tests. International Journal for Numerical and Analytical Methods in Geomechanics 4, 103-119.
Vardoulakis, I., 1983. Rigid granular plasticity model and bifurcation in the triaxial test. Acta Mechanica 49, 57-79.
Vardoulakis, I., 1998. Strain localization in granular materials. Springer.
Vardoulakis, I., Aifantis, E., 1989. Gradient dependent dilatancy and its implications in shear banding and liquefaction. Ingenieur-Archiv 59, 197-208.
Vardoulakis, I., Aifantis, E., 1991. A gradient flow theory of plasticity for granular materials. Acta Mechanica 87, 197-217.
Vardoulakis, I., Goldscheider, M., Gudehus, G., 1978. Formation of shear bands in sand bodies as a bifurcation problem. International Journal for Numerical and Analytical Methods in Geomechanics 2, 99-128.
Vardoulakis, I., Sulem, J., 1995. Bifurcation analysis in geomechanics. hapman & Hall. London.
Vermeer, P., 1978. A double hardening model for sand. Geotechnique 28, 413-433.
Vermeer, P., 1982. A simple shear-band analysis using compilances.
Viggiani, G., Bésuelle, P., Hall, S., Desrues, J., 2010. Imaging sand deformation at the grain scale, EPJ Web of Conferences. EDP Sciences, p. 22021.
Viggiani, G., Kuntz, M., Desrues, J., 2001. An experimental investigation of the relationships between grain size distribution and shear banding in sand. LECTURE NOTES IN PHYSICS-NEW YORK THEN BERLIN-, 111-128.
Viggiani, G., Lenoir, N., Bésuelle, P., Di Michiel, M., Marello, S., Desrues, J., Kretzschmer, M., 2004. X-ray microtomography for studying localized deformation in fine-grained geomaterials under triaxial compression. Comptes rendus Mécanique 332, 819-826.
Voigt, W., 1887. Theoretische studien über die elasticitätsverhältnisse der krystalle. in der Dieterichschen Buchhandlung.
Voyiadjis, G.Z., Alsaleh, M.I., Alshibli, K.A., 2005. Evolving internal length scales in plastic strain localization for granular materials. International journal of plasticity 21, 2000-2024.

Voyiadjis, G.Z., Song, C.R., 2002. Multi-scale non-local approach for geomaterials. Mechanics Research Communications 29, 121-129.

Wan, R., Pinheiro, M., Daouadji, A., Jrad, M., Darve, F., 2013. Diffuse instabilities with transition to localization in loose granular materials. International Journal for Numerical and Analytical Methods in Geomechanics 37, 1292-1311.

Wang, J., Dove, J., Gutierrez, M., 2007. Discrete-continuum analysis of shear banding in the direct shear test. Geotechnique 57, 513-526.

Wang, J., Gutierrez, M., 2010. Discrete element simulations of direct shear specimen scale effects. Geotechnique 60, 395-409.

Wang, W., Askes, H., Sluys, L.J., 1998. Gradient viscoplastic modelling of material instabilities in metals. Metals and Materials International 4, 537-542.

Wang, W., Sluys, L.J., de Borst, R., 1997. Viscoplasticity for instabilities due to strain softening and strain-rate softening. International Journal for Numerical Methods in Engineering 40, 3839-3864.

Wu, F., Freund, L., 1984. Deformation trapping due to thermoplastic instability in one-dimensional wave propagation. Journal of the Mechanics and Physics of Solids 32, 119-132.

Wu, Z.-X., Yin, Z.-Y., Jin, Y.-F., Geng, X.-Y., 2017. A straightforward procedure of parameters determination for sand: a bridge from critical state based constitutive modelling to finite element analysis. European Journal of Environmental and Civil Engineering, 1-23.

Yatomi, C., Yashima, A., Iizuka, A., SANO, I., 1989. General theory of shear bands formation by a non-coaxial Cam-clay model. Soils and Foundations 29, 41-53.

Yin, Z.-Y., Chang, C.S., Hicher, P.-Y., 2010. Micromechanical modelling for effect of inherent anisotropy on cyclic behaviour of sand. International Journal of solids and Structures 47, 1933-1951.

Yin, Z.-Y., Zhao, J., Hicher, P.-Y., 2014. A micromechanics-based model for sand-silt mixtures. International Journal of solids and Structures 51, 1350-1363.

Yin, Z.-Y., Chang, C. S., Karstunen, M., & Hicher, P.-Y. (2010a). An anisotropic elastic–viscoplastic model for soft clays. International Journal of solids and Structures, 47(5), 665-677.

Yin, Z. Y., & Hicher, P. Y. (2008). Identifying parameters controlling soil delayed behaviour from laboratory and in situ pressuremeter testing. International Journal for Numerical and Analytical Methods in Geomechanics, 32(12), 1515-1535.

Yin, Z.-Y., Jin, Y.-F., Shen, S.-L., & Huang, H.-W. (2017). An efficient optimization method for identifying parameters of soft structured clay by an enhanced genetic algorithm and elastic–viscoplastic model. Acta Geotechnica, 12(4), 849-867.

Yin, Z.-Y., & Karstunen, M. (2011). Modelling strain-rate-dependency of natural soft clays combined with anisotropy and destructuration. Acta Mechanica Solida Sinica, 24(3), 216-230.

Yin, Z.-Y., Karstunen, M., Chang, C. S., Koskinen, M., & Lojander, M. (2011). Modeling time-dependent behavior of soft sensitive clay. Journal of Geotechnical and Geoenvironmental Engineering, 137(11), 1103-1113.

Yin, Z.-Y., Karstunen, M., & Hicher, P.-Y. (2010b). Evaluation of the influence of elasto-viscoplastic scaling functions on modelling time-dependent behaviour of natural clays. Soils and Foundations, 50(2), 203-214.

Yin, Z.-Y., Xu, Q., & Yu, C. (2015a). Elastic-viscoplastic modeling for natural soft clays considering nonlinear creep. International Journal of Geomechanics, 15(5), A6014001.

Yin, Z.-Y., Yin, J.-H., & Huang, H.-W. (2015b). Rate-dependent and long-term yield stress and strength of soft Wenzhou marine clay: experiments and modeling. Marine Georesources & Geotechnology, 33(1), 79-91.

Yin, Z.-Y., Zhu, Q.-Y., & Zhang, D.-M. (2018). Comparison of two creep degradation modeling approaches for soft structured soils. Acta Geotechnica, DOI: 10.1007/s11440-017-0556-y.

Zhang, H.-W., 2003. A discussion on some relationships between two different material models related with strain localization analysis [J]. Acta Mechanica Sinica 1, 013.

Zhang, H.-W., Sheng, Z., Jianmin, Q., 2004. Discussion on interaction between different intrinsic length scale parameters for material strain localization analysis [J]. Chinese Journal of Rock Mechanics and Engineering 19, 008.

Zhang, Q.-H., Zhao, X.-H., 2000. An influence on shear band formation of the rotations of principal stress directions [J]. Rock and Soil Mechanics 1, 011.

Zhang, W., Wang, J., Jiang, M., 2013. DEM-aided discovery of the relationship between energy dissipation and shear band formation considering the effects of particle rolling resistance. Journal of Geotechnical and Geoenvironmental Engineering 139, 1512-1527.

Thèse de Doctorat

Jiangxin LIU

Titre de la thèse : Etude numérique de la localisation des déformations en géotechnique dans le cadre de la théorie micro

Title of thesis : Numerical investigations of the strain localization in geotechnical engineering within the framework of micropolar theory

Résumé

La plupart des ruptures des structures géotechniques sont associées aux phénomènes de localisation des déformations, qui s'accompagnent toujours d'un adoucissement de la résistance. De nombreuses observations expérimentales montrent que d'importants réarrangements et rotations de particules se produisent à l'intérieur des bandes de cisaillement. Cette thèse vise à étudier numériquement les phénomènes de localisation des déformations dans les matériaux granulaires. Considérant les problèmes de dépendance au maillage dans l'analyse par éléments finis dans le cadre de la modélisation continue classique, un modèle de sable basé sur l'état critique a été formulé dans le cadre de la théorie micropolaire. Un code d'éléments finis pour les problèmes bidimensionnels a été développé dans ce cadre. Ensuite, les simulations d'essais biaxiaux ont permis d'étudier en profondeur les caractéristiques des bande de cisaillement en termes d'apparition, d'épaisseur, d'orientation, etc … Dans le même temps, l'efficacité de l'approche micropolaire, en tant que technique de régularisation, a été discutée. L'analyse de l'instabilité dans un continuum micropolaire basé sur le travail du second-ordre a également été effectuée. Enfin, pour une application plus large dans la simulation des défaillances en ingénierie géotechnique, le modèle 2D a été étendu à un modèle 3D. Sur la base de l'étude, les modèles 2D et 3D ont démontré leurs capacités de régularisation pour éviter les problèmes de dépendance au maillage et reproduire raisonnablement les bandes de cisaillement dans les géostructures.

Mots-clés
Sol granulaire, bande de cisaillement, méthode des éléments finis, dépendance au maillage, théorie micropolaire, instabilité.

Abstract

Most of the progressive failures of geotechnical structures are associated with the strain localization phenomenon, which is generally accompanied by strength softening. Many experimental observations show that significant rearrangements and rotations of particles occur inside the shear bands. The aim of this thesis is to investigate numerically the strain localization phenomena of granular materials. Considering the mesh dependency problems in finite element analysis caused by strain softening within the classical continuum framework, a sand model based on critical-state has been formulated within the framework of the micropolar theory, taking into account the micro rotations, and implemented into a finite element code for two dimensional problems. Then, the simulations of the shear band in biaxial tests are comprehensively studied in terms of onset, thickness, orientation, etc. At the same time, the efficiency of the micropolar approach, as a regularization technique, is discussed. This is followed by an instability analysis using the second-order work based on the micropolar continuum theory. Finally, for a wider application in simulating failures in geotechnical engineering, the 2D model has been extended to 3D model. Based on the entire study, both the 2D and 3D model demonstrate obvious regularization ability to relieve the mesh dependency problems and to reproduce reasonably the shear bands in geostructures.

Key Words
Granular soils, shear band, finite element method, mesh dependency, micropolar theory, instability.

UNIVERSITÉ BRETAGNE LOIRE